THEORETICAL PREDICTION OF COUNTER-ROTATING PROPELLER NOISE

by

ANTHONY BRIAN PARRY

Being an account of research carried out in the
Department of Applied Mathematical Studies, University
of Leeds, under the supervision of Professor D. G. Crighton

Submitted in accordance with the requirements
for the degree of Doctor of Philosophy

February, 1988

ABSTRACT

A theoretical prediction scheme has been developed for the tone noise generated by a counter-rotation propeller.

We start by deriving formulae for the harmonic components of the far acoustic field generated by the thickness and steady loading noise sources. Excellent agreement is shown between theory and measurements. Asymptotic approximation techniques are described which enable us to simplify considerably the complex radiation formulae, whilst retaining all of their important characteristics, and thus save, typically, 95% of computer processing time.

Next we derive formulae for the radiated sound field generated by aerodynamic interactions between the blade rows. Here, however, the inputs to the formulae include a knowledge of the fluctuating blade pressure fields which cannot generally be assumed given and must therefore be calculated within the prediction scheme.

In the case of viscous wake interactions we consider various models for the wake profile which is written as a series of harmonic gusts. The fluctuating pressure distribution on the downstream blades can then be calculated in the high frequency limit. Comparisons are made between measurements and predictions for a counter-rotation propeller and for rotor/stator interaction on a model fan rig.

For potential field interactions we describe the flow fields due to blade circulation and blade thickness in terms of harmonic gusts with the flow assumed incompressible. The blade response is calculated for both finite and semi-infinite airfoils. Some important differences between these two cases are noted in both high and low frequency limits. Predicted noise levels are much improved over those obtained using only the viscous wake model. The inclusion of compressibility, in both flow field and airfoil

response calculations, provides a further improvement in the predicted noise levels. The discrepancy between measurements and predictions at this stage is, typically, 2 or 3 dB.

ACKNOWLEDGEMENTS

First and foremost I would like to express sincere thanks to Professor D. G. Crighton for his insuperable help, encouragement and enthusiasm. During the three years it has taken to prepare this thesis, I found our regular discussion sessions to be most stimulating; these discussions managed to rekindle in me an appetite for applied mathematics that I thought I had left behind in the sixth form. For this I shall always be grateful.

I would like to thanks Rolls-Royce plc. for allowing me to pursue my studies, and for releasing some experimental data.

In addition, my colleagues at Rolls-Royce plc. deserve a mention. In particular, I am indebted to Dr. A. J. Kempton for many helpful discussions, and to Dr. A. M. Cargill for a number of invaluable suggestions relating to the work in chapters 5, 6 and 7.

The financial support of the S.E.R.C., through the award of an Industrial Studentship, and of Rolls-Royce plc., is also gratefully acknowledged.

Finally, I must compliment Mrs. L. Trundle on her meticulous typing, of both text and formulae, and Mr. C. J. Knighton on his handiwork in preparing the figures.

TO

DEANA, JENNIFER AND KATE

CONTENTS

LIST OF FIGURES

1. INTRODUCTION

Interest has recently been revived in the use of the propeller as a propulsor for modern day aircraft. However, current aircraft are designed to cruise at Mach numbers in the range 0.7-0.9 where the efficiency of conventional propellers drops rapidly. A solution to this problem was put forward many years ago by Brady (1951) who suggested using thin blades and/or swept blades to maintain high propeller efficiency at transonic or supersonic speeds. However, because of low fuel costs and the advent of the turbofan this idea was not pursued.

In the mid-1970's the oil embargo led to rocketing fuel prices, and Hamilton Standard and N.A.S.A. started to consider alternative fuel efficient powerplants. Rohrbach & Metzger (1975) introduced the Prop-Fan which is a small diameter, highly loaded, multi-bladed, variable pitch unducted propulsor whose blades incorporate thin advanced airfoil sections with tip sweep. The Prop-Fan had potential for significant fuel savings, and it was suggested that community noise levels would be lower than those with current turbofan powered aircraft and that cabin noise levels should be much the same as on current turbofan-propelled aircraft. In addition, the Prop-Fan could be used in both commercial and military applications (see Jackson & Gatzen (1976) and, more recently, Lange (1984)).

Following the introduction of the Prop-Fan many aerospace companies initiated major research programmes to develop Prop-Fan technology and to examine its viability: N.A.S.A.'s technology status has been reviewed by Dugan et al. (1977, 1978) and Mitchell & Mikkelson (1982); Hamilton Standard's by Holbrook & Rosen (1978), Metzger (1980, 1984) and Gatzen

(1982); and Pratt and Whitney's by Banach & Reynolds (1981) and Godston & Reynolds* (1985).

The review of Mitchell & Mikkelson (1982) also suggested that propulsive efficiency could be increased by a further 7-11% by introducing a second Prop-Fan behind the first which rotates in the opposite direction and hence removes the swirl created by the forward row: this device is known as a counter-rotation propeller.

These suggestions were further substantiated by the analytical study of Strack et al. (1982) who took into account performance, acoustics, vibration, weight, cost and maintenance and concluded that the counter-rotation propeller provided 8% higher propulsive efficiency than an equivalent single-rotation propeller.

The Prop-Fan has now achieved the status of a full scale powerplant. Sagerser & Ludemann (1985) describe in detail the progress on the N.A.S.A./ Hamilton Standard large scale advanced propeller (L.A.P.) and Prop-Fan test assessment program (P.T.A.), which comprises a complete powerplant (single-rotation propeller) and flight tests. The General Electric unducted fan (U.D.F. counter-rotation propeller) has also been flight tested recently: a full description is given by Harris & Cuthbertson (1987).

It is important to note that all of the Prop-Fan designs currently being flight tested by airframe manufacturers are counter-rotation propellers, as opposed to single rotation propellers†. The suggestion of Rohrbach & Metzger (1975), who considered only single-rotation propellers, that noise should not be a problem for advanced propellers,

---

FOOTNOTES

* In particular, Godston & Reynolds discussed the state of technology readiness for both tractor - and pusher-propeller configurations.

† Boeing have carried out flight tests on the U.D.F. (Harris & Cuthbertson 1987) and McDonnell-Douglas have carried out flight tests on both the U.D.F. and the Pratt and Whitney/Allison geared counter-rotation propeller.

is therefore not applicable because of the additional noise sources due to aerodynamic interactions between the blade rows.

Consequently, it is important to be able to predict the noise from counter-rotation propellers in order to advise on the optimum (acoustic) propeller configuration. The work described here is therefore aimed at providing a prediction technique for counter-rotation propeller noise: in particular, we have concentrated on far field noise, since any new Prop-Fan powered aircraft must automatically comply with the stringent community noise rules* in order to achieve certification. However, we note that there is currently some concern over the cabin noise nuisance associated with Prop-Fans.

For single-rotation propellers the main noise sources, in linear theory, are generated by blade loading and volume displacement. In chapter 2 we derive mathematical descriptions of these sources and their radiated fields, and show comparisons between measurement and theory.

Since the whole aim of the work is to provide predictions for engineering purposes, we must be able to consider the whole of the audible frequency range and to obtain predictions relatively quickly and cheaply. With this in mind we describe, in chapter 3, asymptotic approximation techniques which enable us to simplify considerably the formulae derived in chapter 2, whilst retaining all of their important characteristics, and thus save, typically, 95% of computer processing time.

In chapter 4 we describe the framework for prediction of noise radiation from counter-rotation propellers due to aerodynamic interactions between the blade rows. Here, however, the inputs to the radiation

---

FOOTNOTE

* Federal Aviation Regulations (F.A.R.) Part 36 Stage III.

formulae include a knowledge of the fluctuating blade pressure fields which, unlike the steady lift forces, cannot generally be assumed given.

In chapter 5 we consider the aerodynamic interactions due to the viscous wakes shed from the upstream blades. Various models are described for the wake profile, which is rewritten as a series of harmonic gusts. The fluctuating pressure distribution on the downstream blades can then be calculated in the high frequency limit*. Comparisons are made between measured and predicted levels for a counter-rotation propeller and for rotor/ stator interactions on a model turbofan rig.

Additional interaction sources are produced by the bound potential fields about each blade row. In chapter 6 we describe models for the potential flow fields due to blade thickness and blade circulation, assuming the flow to be incompressible. As before, the velocity fields are written in terms of harmonic gusts. The response of the adjacent blade row (upstream or downstream) is calculated assuming the blades to be semi-infinite flat plates. Since, in incompressible flow, the response of a finite flat plate airfoil can be calculated exactly, we also discuss some important differences between the semi-infinite and the finite airfoil response calculations in the high and low frequency limits. Comparisons are shown between measured and predicted far-field noise levels; here the predictions are much improved over those obtained when only the wake interaction is included.

In chapter 7 we extend the model for potential interactions to include compressibility effects which become important at the higher Mach numbers typical of Prop-Fan operating conditions. Here we update the

---

FOOTNOTE

* Even for the lowest frequency interaction on a typical counter-rotation propeller the reduced frequency is greater than unity. The high frequency approximation is therefore the most appropriate.

descriptions of both the potential flow field around the blades and the high frequency airfoil response. It is shown that there is a further improvement in the predicted noise levels, as compared with measurements, when the compressibility effects are included.

Finally, in chapter 8, we discuss ways in which the prediction scheme can be improved or extended to include additional effects.

Literature surveys and historial reviews are provided in the introductory sections to each chapter.

Throughout we have tried to develop a prediction scheme which is reasonably robust, can be used for engineering purposes, provides an insight into the underlying physics, does not rely on large quantities of computer processing time, and - first and foremost - is based on rational analytical models of all the fluid mechanical and acoustic processes involved.

2. SINGLE ROTATION PROPELLER NOISE

2.1 Introduction

In this chapter we will derive, theoretically, expressions for the acoustic field of a single-rotation propeller, using linear theory. Within this framework the sources of noise are blade loading (doublet or dipole) and blade thickness (simple source or monopole). These sources are discussed in sections 2.2 and 2.3 respectively.

In order to gain confidence in the expressions, a comparison is made in section 2.4 between predictions and measured data for the case of a subsonic conventional propeller.

Although the whole of this work is based on linear theory we do, in section 2.5, discuss the possible importance of nonlinear or quadrupole effects, making reference to the existing literature.

2.2 Steady Loading Noise

The propeller blades have a pressure, or force, distribution which is steady in blade-fixed coordinates (hence the term 'steady loading noise'). For a fixed observer this means that the fluid forces fluctuate at blade passing frequency, resulting in acoustic dipole radiation (see below).

Apart from some early work by Lynam & Webb (1919) and Bryan (1920) the first complete description of propeller steady loading noise was given by Gutin (1936), for the case of a stationary propeller, who utilised Lamb's (1932) expression for concentrated point force radiation. Descriptions of Gutin's analysis are now standard in acoustics textbooks: see, for example, Morse & Ingard (1968), Sharland & Leverton (1968), Pierce (1981), Glegg (1982) and Goldstein (1976).

Gutin's analysis was extended to include the effects of forward speed by Garrick & Watkins (1954) who generalised Lamb's expression to the case of a concentrated point force moving uniformly at subsonic speeds. In addition, consideration of acoustic chordwise noncompactness effects was provided by Watkins & Durling (1956). Their analysis differs from ours in that they projected the propeller blades forward onto a disc, while in our approach we allow the blades to twist between hub and tip.

Lowson (1965) showed that there are two terms contributing to the sound field of a fluctuating point force in motion. One term is due to the fluctuation of the force and the other is due to the fluctuation of the convection velocity. In the far field the fluctuating force produces a sound field of dipole character, as would be expected, and the fluctuating convection velocity produces a sound field of quadrupole character. Lowson applied the analysis

to the case of a static propeller, with the forces assumed to be concentrated at an effective radius. Switching to a Fourier series representation he obtained precisely the same result as Gutin (1936). The 'thrust' force is constant in strength and, due to motion in a circle, has fluctuating convection velocity, thus resulting in radiation of quadrupole character. The 'torque' force, or at least its component in a particular direction, fluctuates due to rotation thus resulting in radiation of dipole character; see also Lowson (1966). (A description of the directivities of the different sources is provided by Sharland & Leverton (1968).) This shows that we must take care when referring to loading sources as dipoles.

Our starting point is the Ffowcs Williams-Hawkings (1969a) equation (an extension of Lighthill's (1952) theory of aerodynamic sound and Curle's (1955) work on solid boundaries to include the effects of motion). This shows that the acoustic pressure dp due to a moving point force $d\underline{F}$ is given by

$$dp(\underline{x},t) = - \nabla \cdot \left[\frac{d\underline{F}(\underline{y},\tau)}{4\pi R(1-M)} \right] \qquad (2.2.1)$$

where τ represents the source time, R the distance of the observer $\underline{x}$ from the source $\underline{y}$ at the source time τ and M the Mach number of the source (at τ) in the direction of the observer. Source time can be simply related to observer time t, as shown in the general case by Morfey (1972) and for the case of rotating blades by Hawkings & Lowson (1975). The relationship is

$$\tau = \frac{t - R/c_o}{1 - M_x \cos\theta} \qquad (2.2.2)$$

where M_x is the flight Mach number and θ is the angle of the observer to the flight axis at time τ (see Figure 2.1).

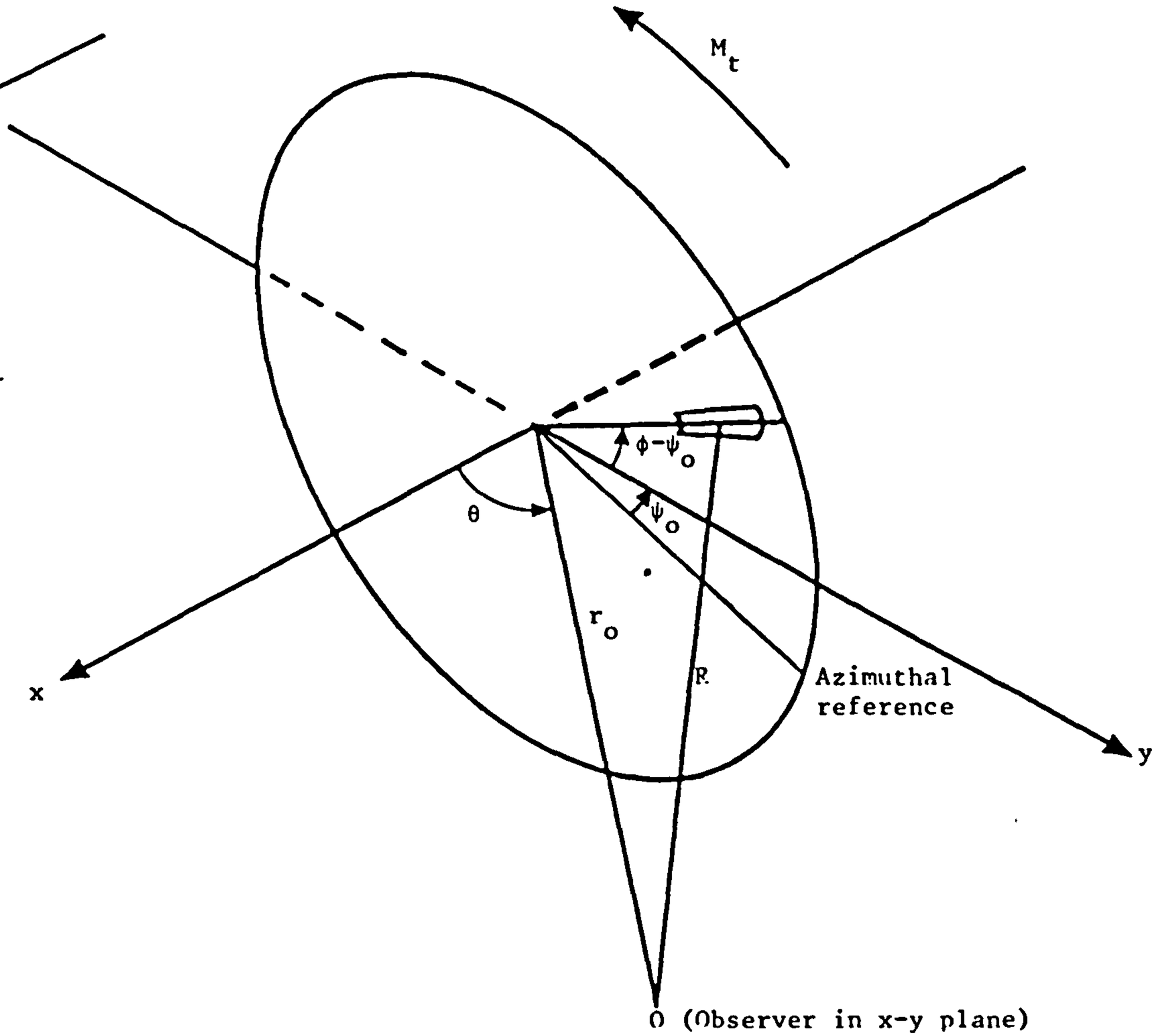

Figure 2.1 The nominal propeller disc plane.

The lift acting across a blade section of span dr is

$$\tfrac{1}{2}\rho\, U_r^2 C_L c\,dr \qquad (2.2.3)$$

where c is the local chord, U_r is the blade section speed and C_L is the local lift coefficient. In (2.2.3) U_r is given by

$$M_r = \frac{U_r}{c_o} \qquad (2.2.4)$$

where M_r is the section relative Mach number,

$$M_r = (M_x^2 + z^2 M_t^2)^{\frac{1}{2}} \ . \qquad (2.2.5)$$

In (2.2.5) z is a normalised radius,

$$z = \frac{r}{R_t} \qquad (2.2.6)$$

where r is the local radius, $R_t = D/2$ is the propeller tip radius, and M_t is the tip rotational Mach number. We will introduce the function $F_L(X)$ to represent the distribution of lift along the local blade chord†. The coordinate X is measured parallel to the local chord and is normalised by the chord length so that $X = -\frac{1}{2}$ at the blade loading edge and $X = \frac{1}{2}$ at the trailing edge. The function $F_L(X)$ is also normalised so that

$$\int_{-\frac{1}{2}}^{\frac{1}{2}} F_L(X)\, dX = 1 \ . \qquad (2.2.7)$$

FOOTNOTE

† The specification of the lift distribution along the chord is necessary if we are to take account of acoustic chordwise non-compactness effects.

The force acting across a blade element of span dr and chord cdX is then

$$dL = \tfrac{1}{2}\rho U_r^2 C_L F_L(X)dr\ cdX\ . \qquad (2.2.8)$$

The blades are assumed to be thin† so that the points of action can be represented by Dirac delta functions (cf. Glegg (1982)). Then the force exerted on the fluid, by a blade element, in a direction normal to the blade sections, at radius r, axial station X and azimuthal angle ϕ is given by

$$dF = -dL = -\tfrac{1}{2}\rho U_r^2 C_L F_L(X)dr\ cdX \sum_{m=-\infty}^{\infty} \delta\left[\frac{2\pi m}{B} + \Omega\tau - \phi\right], \qquad (2.2.9)$$

where Ω is the propeller angular speed and B is the number of blades. We can rewrite (2.2.9) in Fourier series form as

$$dF = -\tfrac{1}{2}\rho U_r^2 C_L F_L(X)dr\ cdX \frac{B}{2\pi} \sum_{m=-\infty}^{\infty} e^{imB(\Omega\tau - \phi)}\ . \qquad (2.2.10)$$

From Figure 2.2 we can see that the components of fluid force acting on a blade section are given by

$$dF_x(r,X,\phi) = dF \sin\alpha, \qquad (2.2.11a)$$

$$dF_y(r,X,\phi) = dF \cos\alpha \sin(\phi-\psi_o-\psi), \qquad (2.2.11b)$$

$$dF_z(r,X,\phi) = -dF \cos\alpha \cos(\phi-\psi_o-\psi), \qquad (2.2.11c)$$

FOOTNOTE

† The thin blade assumption is quite reasonable since advanced propellers are likely to have thickness/chord ratios of about 0.02.

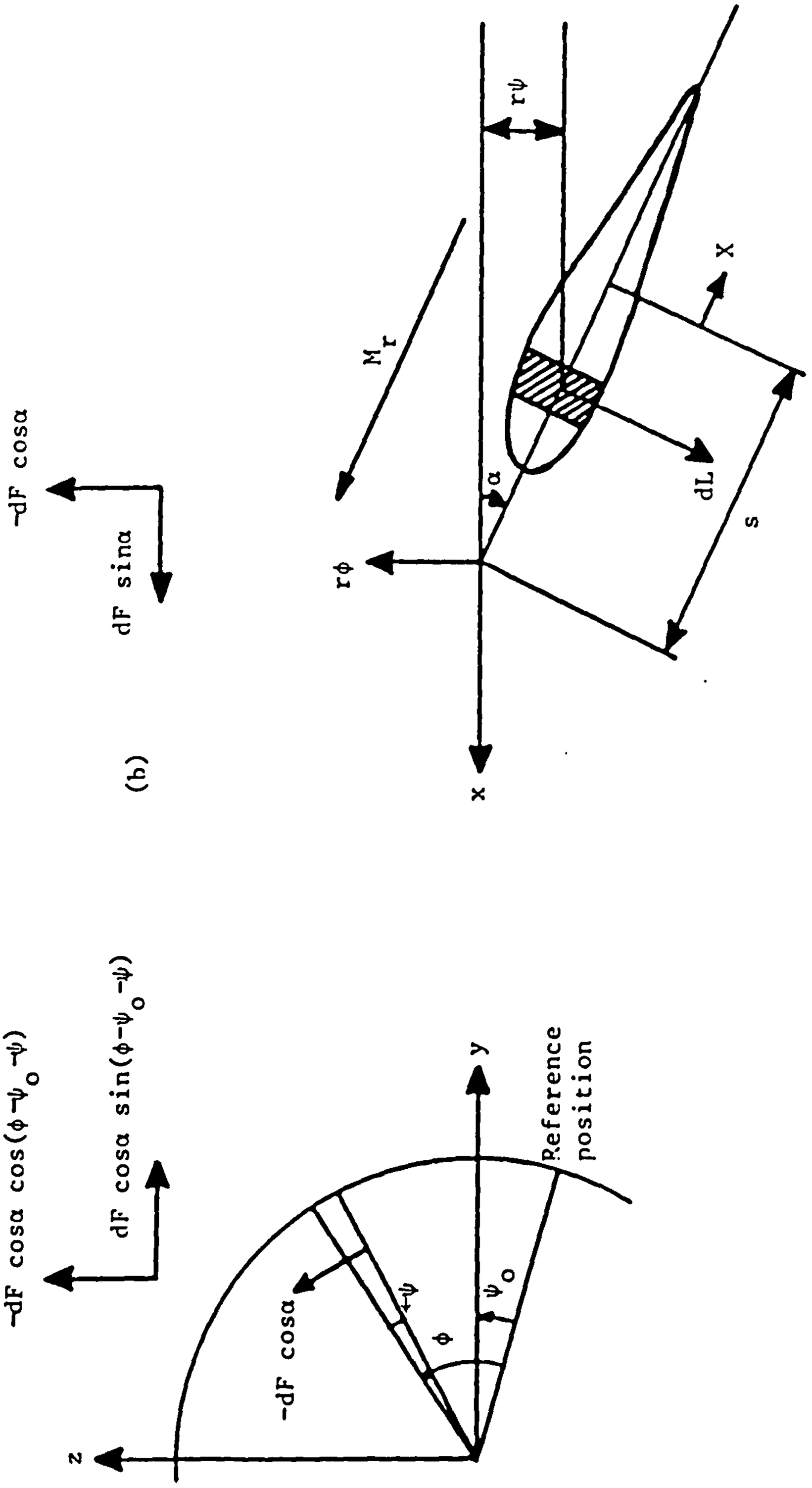

Figure 2.2 Propeller geometry: (a) the nominal disc plane; (b) a single blade element.

where α is the local blade stagger angle, obtained from the local velocity triangle as[†]

$$\alpha = \tan^{-1}\left(\frac{zM_t}{M_x}\right) . \qquad (2.2.12)$$

In (2.2.11b) and (2.2.11c) ψ_o is the (azimuthal) angle of the observer from the reference point (see Figure 2.2) and ψ represents the variation in azimuthal angle as X varies between $-\frac{1}{2}$ and $\frac{1}{2}$. From Figure 2.2 we can see that

$$r\psi = (s + cX) \sin\alpha \qquad (2.2.13)$$

or, from (2.2.5) and (2.2.12),

$$r\psi = (s + cX)\frac{zM_t}{M_r} \qquad (2.2.14)$$

where s is the distance the blade mid-chord has been swept back, along a helical path, from the pitch change axis.

In the far field the distance of the observer from an element at (r,X,ϕ) can be approximated by

$$R \sim r_o - r\sin\theta\cos(\phi-\psi_o-\psi) + (s+cX)\cos\alpha\cos\theta, \qquad (2.2.15)$$

where r_o is the distance of the observer from the centre of the propeller disc and

---

FOOTNOTE

† Note, from (2.2.5) and (2.2.12), that we have taken the blade to lie parallel to the local flow direction.

$$\frac{s}{r_o} << 1, \quad \frac{c}{r_o} << 1, \quad \frac{R_t}{r_o} << 1. \tag{2.2.16}$$

The approximation (2.2.15) will be used in phase terms involving R; however, it is sufficient to replace the 1/R amplitude term by $1/r_o$. The far field acoustic pressure, (2.2.1), is given by

$$dp = \frac{-1}{4\pi r_o(1-M_x\cos\theta)} \nabla\cdot[dF(\tau)] \, . \tag{2.2.17}$$

From (2.2) and (2.10) we can see that the spatial dependence of $d\underline{F}$, where

$$d\underline{F} = (dF_x, dF_y, dF_z) \tag{2.2.18}$$

is, for each value of m, $\exp[-imB\Omega r_o/c_o(1-M_x\cos\theta)]$. The far field acoustic pressure is then given by*

$$dp = \frac{imB\Omega}{4\pi r_o c_o(1-M_x\cos\theta)^2} (dF_x\cos\theta + dF_y\sin\theta) \tag{2.2.19}$$

Combining equations (2.2.10), (2.2.11), (2.2.15) and (2.2.19) and integrating over ϕ, X and r we find that the far field acoustic pressure is given by

$$p = \sum_{m=-\infty}^{\infty} \frac{-imB^2\Omega\rho\, c_o D}{16\pi^2 r_o(1-M_x\cos\theta)^2} \exp\left[\frac{imB\Omega(t-r_o/c_o}{1-M_x\cos\theta}\right]$$

$$\int_{R_h}^{R_t}\int_{-\frac{1}{2}}^{\frac{1}{2}}\int_{0}^{2\pi} M_r^2 C_L F_L(X) \frac{c}{D} [\cos\theta\, \sin\alpha + \sin\theta\, \cos\alpha\, \sin(\phi-\psi_o-\psi)] \tag{2.2.20}$$

$$\exp\left\{\frac{imB\Omega}{(1-M_x\cos\theta)c_o}[r\, \sin\theta\, \cos(\phi-\psi_o-\psi) - (s+cX)\cos\alpha\, \cos\theta]-imB\phi\right\} d\phi dX dr,$$

---

* This result agrees with equation (8) of Lighthill (1972) for the far field of a dipole in a moving fluid.

where R_h is the propeller hub radius. In the integral over ϕ in (2.2.20), I_ϕ say, we replace $(\phi-\psi_o-\psi)$ with ϕ_1, whence

$$I_\phi = e^{-imB\psi_o - imB\psi} \int_0^{2\pi} (\cos\theta \sin\alpha + \sin\theta \cos\alpha \sin\phi_1) \tag{2.2.21}$$

$$\exp\left[\frac{imB\Omega r \sin\theta}{(1-M_x\cos\theta)c_o}\cos\phi_1 - imB\phi_1\right] d\phi_1,$$

where the same limits of integration have been retained due to the periodicity of the integrand. This integral can be performed analytically in terms of Bessel functions (see Watson (1952)). We then have

$$I_\phi = 2\pi e^{imB(\pi/2-\psi_o-\psi)} \left[\cos\theta \sin\alpha - \frac{(1-M_x\cos\theta)\cos\alpha}{\Omega r/c_o}\right] J_{mB}\left[\frac{mB\Omega r \sin\theta}{(1-M_x\cos\theta)c_o}\right]. \tag{2.2.22}$$

From equations (2.2.5), (2.2.6), (2.2.12), (2.2.14) and (2.2.22) we see that (2.2.20) reduces to

$$p = \sum_{m=-\infty}^{\infty} \frac{-imB^2\rho c_o^2 D}{8\pi r_o (1-M_x\cos\theta)^2} \exp\left[\frac{imB\Omega}{(1-M_x\cos\theta)}(t-r_o/c_o) + imB(\pi/2-\psi_o)\right]$$

$$\int_{z_o}^{1}\int_{-\frac{1}{2}}^{\frac{1}{2}} M_r^2 C_L F_L(X) \frac{c}{D}\left[\frac{M_r^2\cos\theta - M_x}{zM_r}\right] J_{mB}\left[\frac{mBM_t z \sin\theta}{1-M_x\cos\theta}\right] \tag{2.2.23}$$

$$\exp\left[-\frac{i2mB}{(1-M_x\cos\theta)}\frac{(s+cX)}{D}\frac{M_t}{M_r}\right] dXdz$$

where z_o is the propeller hub/tip ratio.

In order to compare our result with that of Hanson (1980a), we define a phase term

$$\phi_s = \frac{2mB\ s/D\ M_t}{(1-M_x\cos\theta)M_r}, \tag{2.2.24}$$

non-dimensional wavenumbers

$$k_x = \frac{2mB\ c/DM_t}{(1-M_x\cos\theta)M_r}, \tag{2.2.25}$$

$$k_y = \frac{2mB\ c/D\ (M_r^2\cos\theta - M_x)}{(1-M_x\cos\theta)zM_r}, \tag{2.2.26}$$

and a noncompactness factor

$$\Psi_L(k_x) = \int_{-\frac{1}{2}}^{\frac{1}{2}} F_L(X)e^{-ik_xX}\,dX. \tag{2.2.27}$$

Using (2.2.24) to (2.2.27) we can rewrite (2.2.23) in the form

$$p = \sum_{m=-\infty}^{\infty} \frac{-\rho c_o^2 DB}{8\pi r_o(1-M_x\cos\theta)} \exp\left[\frac{imB\Omega}{(1-M_x\cos\theta)}(t - \frac{r_o}{c_o}) + imB(\frac{\pi}{2} - \psi_o)\right] \tag{2.2.28}$$

$$\int_{z_o}^{1} M_r^2 e^{-i\phi_s} J_{mB}\left[\frac{mBM_t z\ \sin\theta}{1-M_x\cos\theta}\right](ik_y\ \frac{C_L}{2})\Psi_L(k_x)\,dz\ .$$

Equation (2.2.28) is the complex conjugate of Hanson's (1980a) result for steady loading noise, corresponding to the fact that we chose a time dependence $e^{i\omega t}$ whereas Hanson chose $e^{-i\omega t}$.

2.3 Thickness Noise

The rotating propeller blades have finite thickness, which results in a continuous extraction and injection of fluid across the boundary of any control volume. For a fixed observer this volume displacement effect generates acoustic monopole radiation (see below) which fluctuates at blade passing frequency.

A first description of thickness noise, for a stationary propeller with symmetrical sections, was provided by Deming (1937, 1938), who used Rayleigh's (1877) expression for the velocity potential due to a source in a wall of infinite extent. This work suggested that thickness noise was not an important noise source.

A description of the sound field for a simple source in motion was provided by Oestreicher (1951) who later pointed out the occurrence of a dipole addition to the sound field (Oestreicher 1957). Lowson (1965) derived a more complete expression which showed, in fact, that the sound field of a simple source consists of three terms: a monopole effect due to the double rate of change of mass introduction, a dipole effect due to the convection of the displaced mass, and a quadrupole effect due to the acceleration. This shows again, as we commented for steady loading noise in the previous section, that care must be taken when referring to the thickness noise source as a pure monopole.

Diprose (1955) extended Deming's analysis to include the effects of forward speed and showed that thickness noise assumes greater importance, in relation to steady loading noise, as the blade speeds are increased. Further work on thickness noise was also provided by Van de Vooren & Zandbergen (1963) who used an acceleration potential technique for a propeller in forward flight. Their results showed that the thickness and steady loading noise components could be of the same order of magnitude. In addition Lyon (1971) and Lyon et al.(1973)

showed the importance of thickness noise for airfoils with section relative Mach number close to unity.

Our starting point for thickness noise is again the Ffowcs Williams-Hawkings equation (1969a). This shows that the acoustic pressure p due to a blade element of thickness $\bar{h}(X)$ is given by

$$p = \frac{\partial}{\partial t}\left\{\frac{1}{c}\frac{\partial}{\partial X}\left[\frac{\rho \bar{h}(X) U_r}{4\pi R(1-M)}\right]\right\} \qquad (2.3.1)$$

where the sign is different to that used by Ffowcs Williams & Hawkings since here the X coordinate points in the direction opposite to the blade motion (see Figure 2.2). We now normalise the thickness function by the maximum section thickness b so that

$$\bar{h}(X) = b h(X) \ . \qquad (2.3.2)$$

To extend the result (2.3.1) to the case of B propeller blades rotating with angular velocity Ω we proceed as in section 2.1 and replace the normalised thickness function h(X) by

$$h(X) \sum_{m=-\infty}^{\infty} \delta\left(\frac{2\pi m}{B} + \Omega\tau - \phi\right) \ . \qquad (2.3.3)$$

Using the far field approximation, (2.3.1) then becomes

$$p = \frac{\rho c_o M_r}{4\pi r_o (1-M_x \cos\theta) c} \frac{b}{\partial X} \frac{\partial h}{2\pi} \frac{B}{\partial t} \frac{\partial}{\partial t}\left\{\sum_{m=-\infty}^{\infty} e^{imB(\Omega\tau-\phi)}\right\} \qquad (2.3.4)$$

where we have used the Fourier series form of (2.3.3). Then, using

(2.2.2) and (2.2.5) and integrating over ϕ, X and r we find that the far field acoustic pressure is given by

$$p = \sum_{m=-\infty}^{\infty} \frac{imB^2\Omega\rho c_o}{8\pi^2 r_o(1-M_x\cos\theta)^2} \exp\left[\frac{imB\Omega}{(1-M_x\cos\theta)}(t-r_o/c_o)\right]$$

$$\int_{R_h}^{R_t}\int_{-\frac{1}{2}}^{\frac{1}{2}}\int_{0}^{2\pi} \exp\left[-imB\phi + \frac{imB\Omega r\,\sin\theta\cos(\phi-\psi_o-\psi)}{c_o(1-M_x\cos\theta)} \frac{-imB\Omega(s+cX)\cos\alpha\cos\theta}{c_o(1-M_x\cos\theta)}\right] \tag{2.3.5}$$

$$M_r \frac{b}{c}\frac{\partial h}{\partial X}\, d\phi c dX dr\ .$$

The integral over ϕ can be evaluated analytically in terms of Bessel functions, as in (2.2.21) and (2.2.22) of the previous section, whence

$$p = \sum_{m=-\infty}^{\infty} \frac{imB^2\Omega\rho c_o}{4\pi r_o(1-M_x\cos\theta)^2} \exp\left[\frac{imB\Omega(t-r_o/c_o)}{(1-M_x\cos\theta)} + imB(\pi/2-\psi_o)\right]$$

(2.3.6)

$$\int_{z_o}^{1}\int_{-\frac{1}{2}}^{\frac{1}{2}} \exp\left[\frac{-i2mB}{(1-M_x\cos\theta)}\frac{(s+cX)}{D}\frac{M_t}{M_r}\right] M_r \frac{b}{c}\frac{\partial h}{\partial X} J_{mB}\left[\frac{mBzM_t\sin\theta}{1-M_x\cos\theta}\right] c dX R_t dz,$$

where we have used (2.2.12) and (2.2.14). The integral over X can now be evaluated by parts to give.

$$p = \sum_{m=-\infty}^{\infty} \frac{-\rho\, c_o^2 DB}{8\pi r_o(1-M_x\cos\theta)} \exp\left[\frac{imB\Omega(t-r_o/c_o)}{(1-M_x\cos\theta)} + imB(\pi/2 - \psi_o)\right]$$

$$\int_{z_o}^{1} M_r^2\, e^{-i\phi_s}\, J_{mB}\left\{\frac{mBzM_t\sin\theta}{1-M_x\cos\theta}\right\} k_x^2 \frac{b}{c} \Psi_v(k_x)\, dz \qquad (2.3.7)$$

where Ψ_v is the noncompactness factor defined by

$$\Psi_v = \int_{-\frac{1}{2}}^{\frac{1}{2}} h(X) e^{-ik_x X}\, dX \quad . \qquad (2.3.8)$$

The result (2.3.7) again agrees precisely with Hanson's (1980a) expression for thickness noise when we allow for the different time dependences.

2.4 Comparison with Measurements

In order to gain confidence in the expressions we have derived, we need to compare predictions with measured data. The data we shall use in the comparison have been acquired by Rolls-Royce during a series of flyover tests with a Fairey Gannet aircraft. Although the Gannet is powered by a counter-rotation propeller it was possible, because of the design of the double Mamba engine, to run the two rows at slightly different speeds so that the "rotor-alone" tones of the front and rear rows, and the tones generated by the aerodynamic interactions between the two rows, are separated in terms of frequency and so can be examined independently, as shown by Bradley (1986). The problem of Doppler frequency shifting, inherent in flyover tests, has been removed by using the Rolls-Royce de-Dopplerisation technique; see Howell et al.(1986). As a result it is possible to produce directivity plots for the rotor alone tones and for the interaction tones.

Figures 2.3 and 2.4 show the measured and predicted levels, as a function of angle, for the first two harmonics of blade-passing frequency (for the forward row). As can be seen, the predictions are dominated by the steady loading component*, and it is clear that the agreement between the measured data and the predictions is excellent. The loading and thickness distribution inputs, as a function of radius, for equations (2.2.28) and (2.3.7) are required for the prediction. These were supplied to Rolls-Royce by Dowty Rotol, manufacturers of the Gannet propeller. However, since the flight Mach number of the Gannet is very modest (less than 0.3), the chordwise

FOOTNOTE

* This result is to be expected at subsonic speeds, as was commented in section 2.2, and has been shown previously by Deming (1937, 1938), Regier & Hubbard (1953), Diprose (1955) and Lyon (1971).

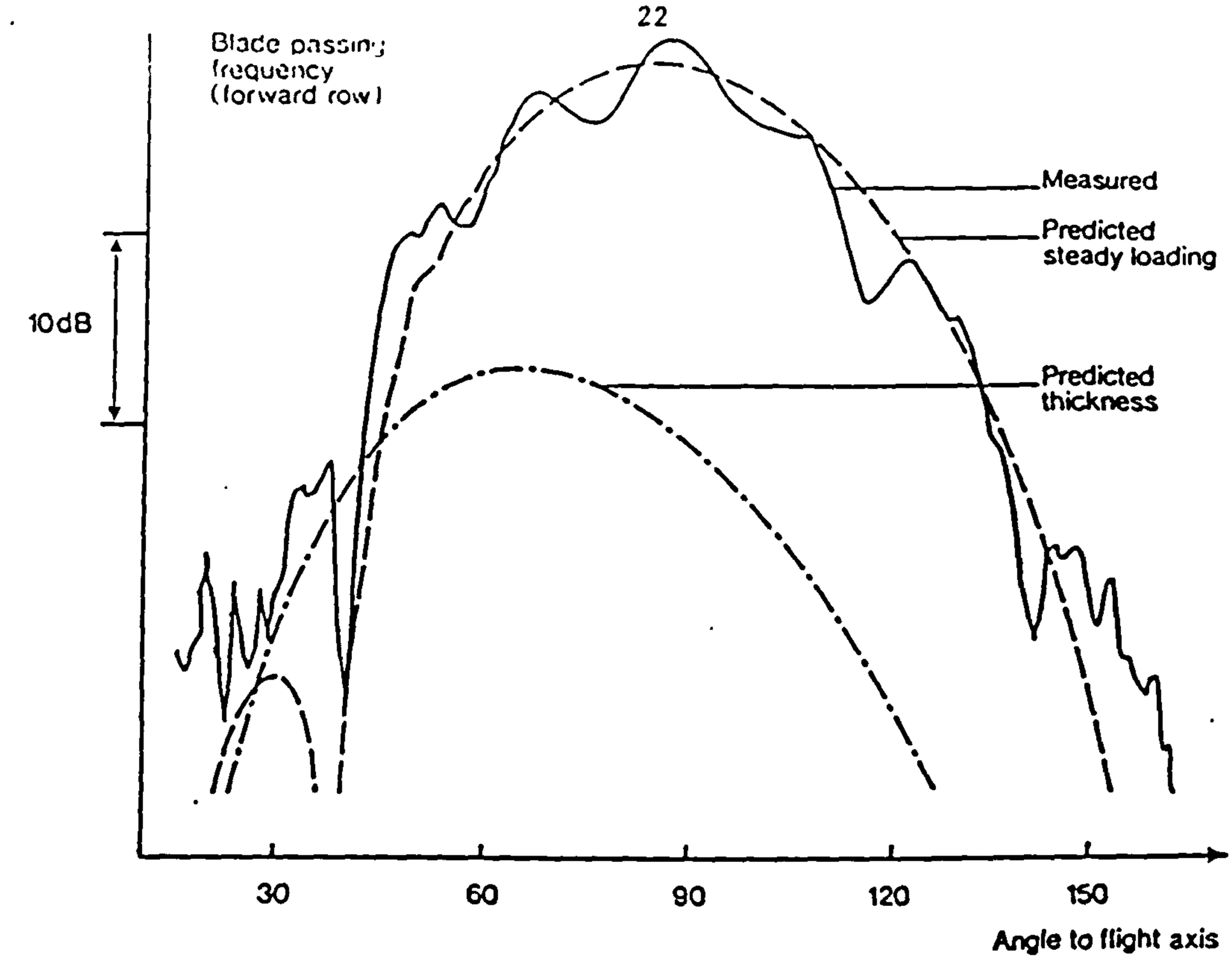

Figure 2.3 Gannet measurements vs predictions.

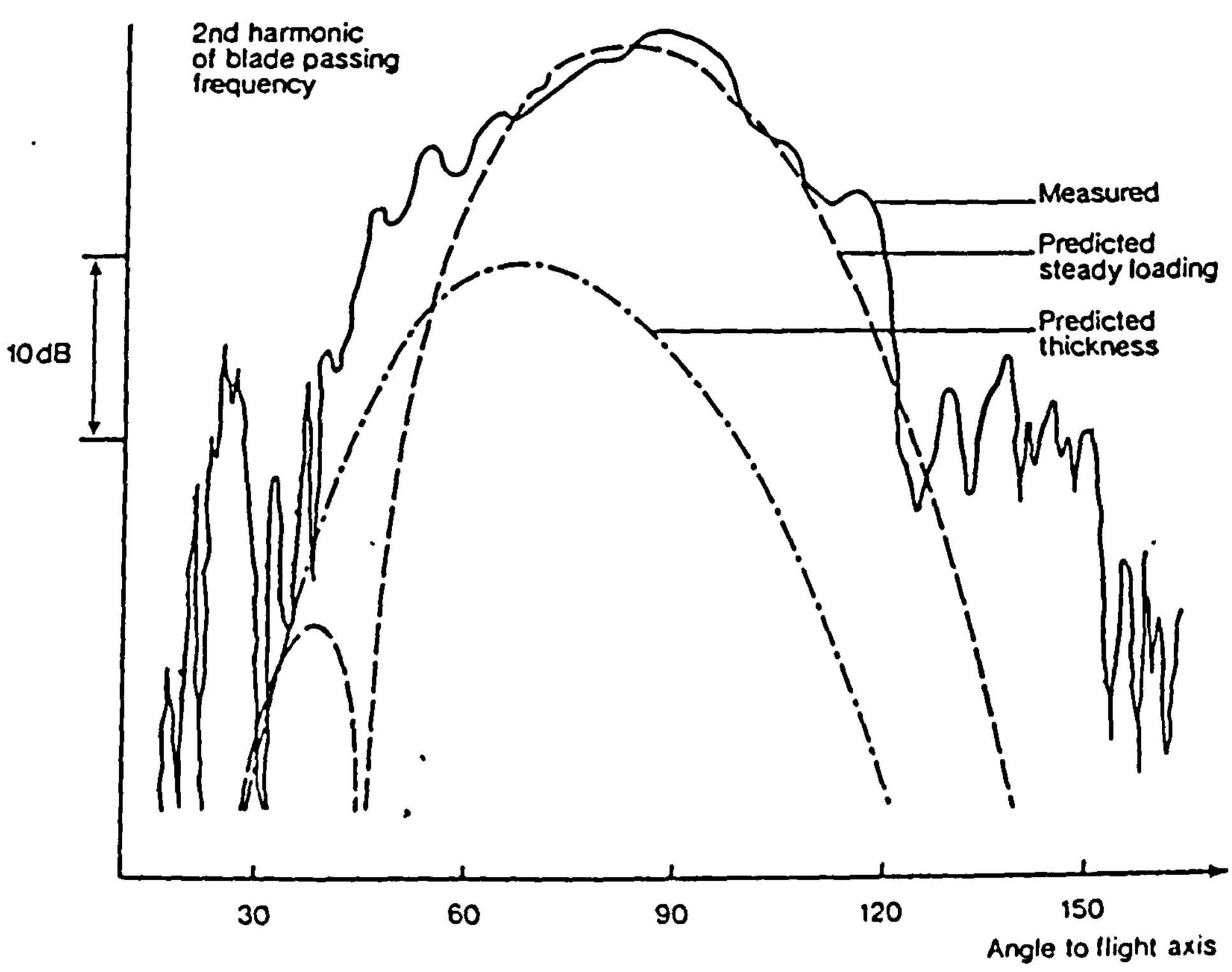

Figure 2.4 Gannet measurements vs predictions.

wavenumber is small for the first few harmonics of blade passing frequency and hence the noncompactness factors are approximately equal to 1, i.e. it is not necessary to input the chordwise distributions of loading and thickness but only the spanwise distributions.

2.5 Nonlinear Effects

The steady loading and thickness components, described in sections 2.1 and 2.2, represent the linear content of the sound field. In addition to these there are also quadrupole, or nonlinear, components which become important, in relation to the linear sound field, when the perturbation velocities in the flow can no longer be considered small. Although nonlinear effects are not, in general, covered in our analysis* it is worth discussing their importance in relation to the linear terms. This will be done by reference to the literature.

The nonlinear effects depend not only on the hydrodynamic flow around the blades but also on the resultant acoustic field generated. This means that there are essentially two effects: first, nonlinear source effects and second, nonlinear propagation effects; although it is not possible to separate the two either conceptually or in practice.

An approach which implicitly includes both source and propagation effects has been provided by Hawkings (1979) who, instead of using the acoustic analogy (Ffowcs Williams & Hawkings 1969a) as is usual, used the transonic small disturbance theory of Caradonna & Isom (1972). This approach, however, involves solving the Caradonna-Isom equation numerically to obtain the near aerodynamic field, and then using Kirchoff's theorem to obtain the far acoustic field. The latter stage is effected by the numerical evaluation of a surface integral. The extensiveness of the calculations obviously makes this approach unattractive for a prediction scheme. More recently Morgan (1982) has argued that, by means of an ingenious transformation, the leading

FOOTNOTE

* Note, however, that the asymptotic analysis described in later chapters is applicable to any source, linear or nonlinear. All that is required is knowledge of the source strength.

nonlinear term in the Caradonna-Isom equation can be incorporated into the linear wave equation.

The importance of quadrupole source terms in rotating machinery, particularly for multibladed high speed rotors was first pointed out by Ffowcs Williams & Hawkings (1969b). In addition, for ducted rotors, Morfey & Fisher (1970) showed the inadequacies of linear theory in the supersonic operating regime, these inadequacies being due to the development of shocks on the rotors. Hanson & Fink (1979) also discussed the quadrupole source terms and showed that they were only important at transonic blade speeds. The incorporation of blade sweep into the propeller design can effectively remove this transonic phenomenon; see Hanson (1979) and Metzger & Rohrbach (1979). It should therefore be possible to neglect the quadrupole source term for propfans.

Instead of considering the nonlinear effects as source terms, Ffowcs Williams (1979) has argued that the role of the quadrupole is more that of modifying the propagation speed of the acoustic wave. This effect is generally discussed in the literature by way of Whitham's (1956, 1974) weak shock theory. Hawkings & Lowson (1974) have used the Whitham technique to account for some of the discrepancy between linear predictions and measurements when the pressure signature was assumed to be an N-wave. However Barger (1980) argued that for subsonic or low supersonic tip speeds the pressure signature never attains an N-wave form. His approach showed that nonlinear distortion can result in shock formation after short propagation distances for straight bladed propellers (NASA SR-2 propeller blades for example) and that shocks form at much greater distances for subsonic or swept

propellers. In addition Tam & Salikuddin (1986), who used weak shock theory, have pointed out that at high forward speeds, where cabin noise (rather than far-field community noise) is the major concern and the propagation distance is small, nonlinear effects can be important* since the propagation time is increased, for waves propagating upstream, due to the high speed of the convected flow in the opposite direction. The cumulative nonlinear process thus has sufficient time to take effect.

There are, however, a number of reasons for wishing to ignore nonlinear effects in the development of a prediction technique. The first is that the incorporation of nonlinear effects into a computer program inevitably results in much greater computer running time and, in many cases, the difference between the linear and the nonlinear solutions is only 2 or 3 dB (Hawkings & Lowson 1974, Tam & Salikuddin 1986). This seems to be the case when weak shock theory is used to correct the linear solution. When a more complete nonlinear prediction is required, it is necessary to link an aerodynamic flowfield program with an acoustics program and the end result can in fact be no better than the simple linear prediction. For example Korkan et al.(1986) used the NASPROP-E code to generate the aerodynamic flowfield around an SR-3 propeller. The description of the flowfield was then used as input to a noise prediction program based on the Ffowcs Williams-Hawkings equation in order to predict the radiated noise. The predictions agreed with measurements in the subsonic regime but were typically 5dB in error in the supersonic regime. Since our aim is to provide a relatively straightforward prediction scheme we will therefore remain within a linear framework.

FOOTNOTE

* A configuration with rear-mounted propfan engines is in mind here.

3. ASYMPTOTIC APPROXIMATIONS FOR ROTOR ALONE NOISE

3.1 Introduction

In chapter 2 we showed that linear acoustic theory, using only the thickness monopoles and force dipoles and completely ignoring any quadrupole effects, produces accurate results - at any rate, over the parameter range represented by flight tests of the Gannet aircraft. However the formulae, equations (2.2.28) and (2.3.7), involve numerical integration along the blade span and the integrand includes a complicated Bessel function as a factor. Furthermore, at conditions where noncompactness effects become important, an additional numerical integration is required along the blade chord. Since results are likely to be required for several harmonics, a range of observer positions, various operating conditions and different propeller configurations, numerical evaluation of the formulae can become a relatively cumbersome procedure. It is therefore useful to have available much simpler approximate formulae from which trends, scaling laws and possibly even absolute values, can be quickly obtained. The current chapter will address the problem of obtaining suitable approximate formulae.

For conventional subsonic propellers it has been standard for many years to use the Gutin (1936) point force approximation, which was shown by Deming (1940) to be accurate for low values of mB. However Hicks & Hubbard (1947), Kurbjun (1955) and more recently Trebble et al. (1981) have all shown, for propellers, that the Gutin approximation underpredicts, relative to measured levels, for high values of mB. The work of Trillo (1966) on hovercraft propellers, Filleul (1966) on axial flow fans and Stuckey & Goddard (1967) on helicopters has also shown that the Gutin formula underpredicts compared to measured data, for high

mB. In the last case, comparison was also made with predictions from the Deuce computer program of Dodd & Roper (1958), which includes numerical integration along the blade span and limited chordwise noncompactness effects; the Gutin results were much lower than the computed results at high values of mB. Since the advanced propellers of interest today have relatively large numbers of blades the Gutin approximation is therefore likely to prove inaccurate.

Alternative approximations have been derived by Tanna & Morfey (1971) for the simple source (thickness) component and by Morfey & Tanna (1971) for the doublet (force) component. However these expressions relate to power spectral density and therefore do not retain the full character of expressions for sound pressure level, all phase information having been discarded.

A Mach number scaling law for helicopter rotors has been derived by Aravamudan et al. (1978) in terms of power spectral density. In their work, however, they neglected the variation in the Bessel function with tip speed which, as we shall show below, is the most important part of the formulation and of the phenomenon it describes.

3.2 Subsonic Operating Conditions

3.2.1 A Straight Bladed Propeller

In this section we will derive asymptotic results for the far-field harmonic components of the radiated sound field. We start with the case of a straight bladed propeller operating at low forward speeds. The effects of acoustic chordwise noncompactness are more important at supersonic and high subsonic speeds, since the non-dimensional chordwise wavenumber k_x, defined in (2.2.25), is much larger there because of the effect of the Doppler factor. Accordingly, noncompactness effects

are considered in section 3.3.3 which discusses propellers operating at supersonic conditions (although the results derived there are applicable at both subsonic and supersonic speeds). We will therefore now set

$$\left.\begin{aligned} \phi_s &= 0, \\ \Psi_L &= 1, \\ \Psi_v &= 1. \end{aligned}\right\} \tag{3.2.1}$$

In order to consider different sources together we will write the harmonic components of the sound field in the form

$$P_m = \int_{z_o}^{1} S(z) J_{mB}\left\{\frac{mBzM_t \sin\theta}{1-M_x\cos\theta}\right\} dz \ , \tag{3.2.2}$$

where P_m represents a typical term in the summation in either (2.2.28) or (2.3.7) after a factor

$$\frac{-\rho c_o^2 B}{8\pi \frac{r_o}{D}(1-M_x\cos\theta)} \exp\left[\frac{imB\Omega}{(1-M_x\cos\theta)}(t - r_o/c_o) + imB(\tfrac{\pi}{2} - \psi_o)\right]$$

has been removed. Factors representing interference effects will be inserted to multiply the source strength S(z) when we come to consider those effects in later sections. Thus S(z) represents the variation in source strength with spanwise/radial station (note that S also depends on harmonic, blade number and the propeller operating parameters) and the Bessel function represents the radiation efficiency of sources rotating in the nominal disc plane.

For a propeller operating at subsonic* conditions the argument of the Bessel function will always be less than the order. If we consider the order of the Bessel function mB, representing the product of harmonic and blade number, to be large we can use the Debye approximation (see, for example, Abramowitz & Stegun (1965))

$$J_{mB}(mB\,\mathrm{sech}\beta) \sim \frac{\exp[mB(\tanh\beta-\beta)]}{(2\pi mB\tanh\beta)^{\frac{1}{2}}} \quad , \tag{3.2.3}$$

where

$$\mathrm{sech}\beta = \frac{zM_t\sin\theta}{1-M_x\cos\theta} \quad . \tag{3.2.4}$$

Note that this is quite different from the approximation used by Goldstein (1976) and others, in which the argument of the Bessel function is assumed small and the order fixed. We would suggest that that approximation is generally quite inappropriate in propeller noise theory. All experience with Bessel function asymptotics suggests that mB = 4 is quite sufficient to permit accurate results using the large mB limit, and that even mB = 2 (lowest harmonic of a 2-bladed propeller) is better approached through the limit $mB \to \infty$ as opposed to the small argument, fixed order limit.

Since mB has been assumed large we see, from the form of (3.2.3) and (3.2.4), that the Bessel function, and hence the integrand of (3.2.2) because S(z) contains no terms which vary exponentially rapidly with mB, increases rapidly towards the tip. We can therefore evaluate (3.2.2) using Laplace's method for integrals (see, for example, Murray (1974)).

FOOTNOTE

* A propeller is said to be operating at subsonic conditions when the blade tip relative Mach number is less than unity.

We will put

$$S(z) \sim \bar{S}(1 - z)^{\nu} \quad \text{as} \quad z \to 1 \ . \tag{3.2.5}$$

If the source strength is finite at the propeller tips, then

$$\left.\begin{aligned} \bar{S} &= S(1) \\ \nu &= 0 \ . \end{aligned}\right\} \tag{3.2.6}$$

Equation (3.2.2) then reduces to

$$P_m \sim \frac{\bar{S}\ \exp[mB(\tanh\beta_t - \beta_t)]}{(2\pi mB\tanh\beta_t)^{\frac{1}{2}}} \int_{-\infty}^{1} (1-z)^{\nu} \exp[-mB(1-z)\tanh\beta_t]dz \tag{3.2.7}$$

where

$$\beta_t = \operatorname{sech}^{-1}\left[\frac{M_t \sin\theta}{1-M_x\cos\theta}\right] \tag{3.2.8}$$

and the suffix t refers to the blade tips. We can then evaluate (3.2.7) to give

$$P_m \sim \frac{\bar{S}\ \exp[mB(\tanh\beta_t - \beta_t)]}{(2\pi mB\ \tanh\beta_t)^{\frac{1}{2}}} \frac{\nu!}{(mB\ \tanh\beta_t)^{\nu+1}} \ . \tag{3.2.9}$$

This equation is much simpler than the full prediction requiring numerical evaluation (equations (2.2.28) and (2.3.7)) and, in addition, retains full dependence on tip rotational Mach number, radiation angle and harmonic number. The essence of (3.2.9) is that it shows precisely

how, under the conditions assumed, single rotation propeller noise at subsonic speeds is tip dominated.

To show the accuracy of (3.2.9) we will compare the full numerical predictions with the asymptotic predictions. This will be done for the steady loading noise source which, as remarked at the start of section 2.1, dominates the sound field at subsonic conditions. The values of $\bar{S}$ and ν are obtained by matching (3.2.5) with the tip variation of the radial loading distribution to be used in the full numerical calculation, Figure 3.1 compares the numerical and the asymptotic solutions for a 12-bladed propeller at first and second harmonics of blade passing frequency. The radiation angle was chosen to be 90°, since it has been known for many years that, for a propeller operating subsonically, the sound level drops rapidly away from the propeller plane: see Paris (1932). The figure shows the variation in sound pressure level with tip rotational Mach number. It is clear that there is close agreement between the two results across the full range of tip rotational Mach numbers examined, particularly at the second harmonic of blade passing frequency.

The asymptotic result, equation (3.2.9), can also be used to explain numerous published results, both experimental and theoretical.

Trebble (1983a, 1983b, 1984), for example, found experimentally that at low helical tip speeds the radiated sound field decayed rapidly with the harmonic of blade passing frequency, whereas at higher (subsonic) helical tip speeds there was only a weak decay in the sound field with harmonic number. The same result had also been found earlier by Hubbard & Lassiter (1952)*. To explain this effect we will take the dominant term

FOOTNOTE

* Although Hubbard and Lassiter's results were primarily for supersonic tip speeds, they also obtained some results at tip rotational Mach numbers of 0.75 and 0.9 for comparative purposes.

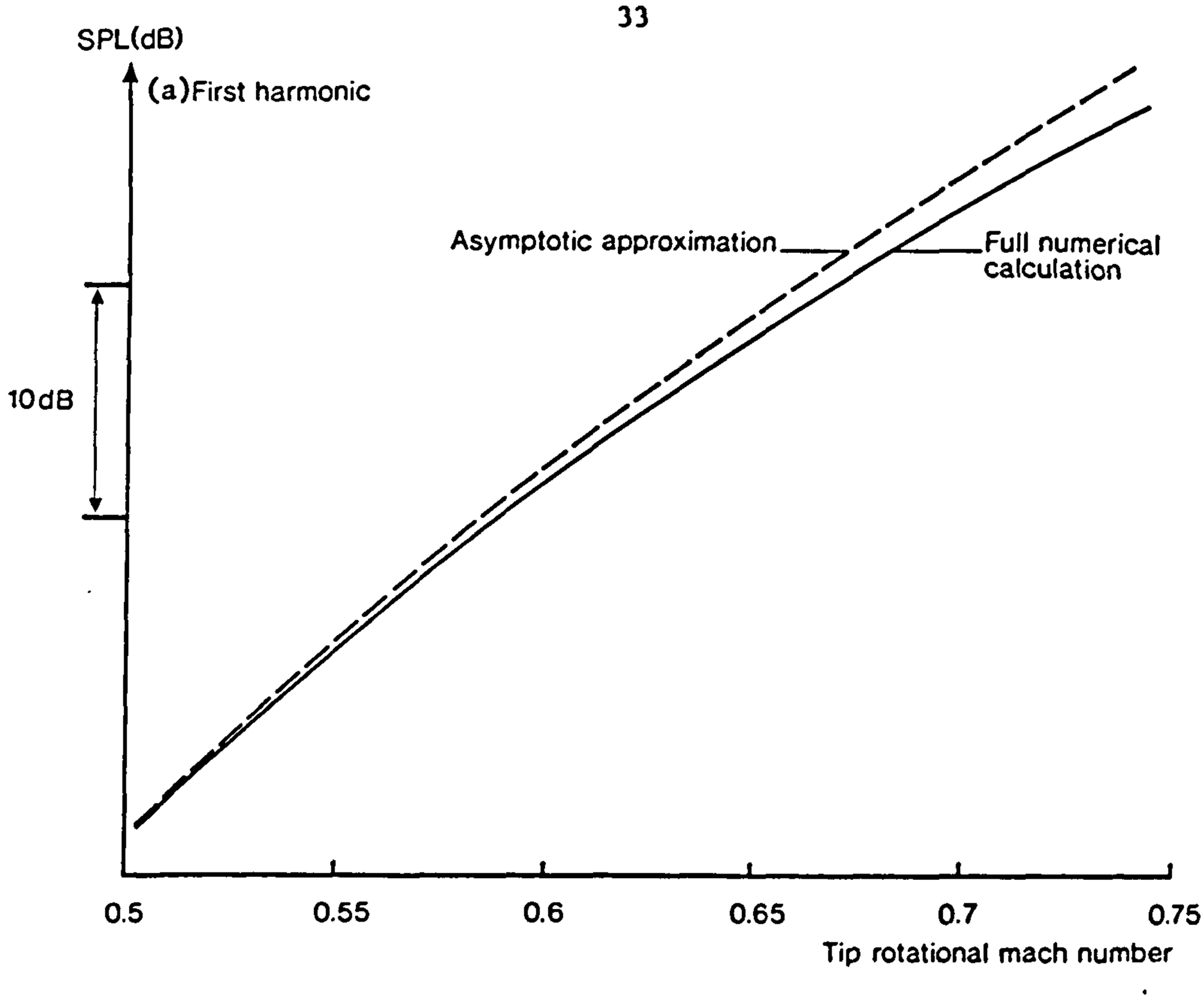

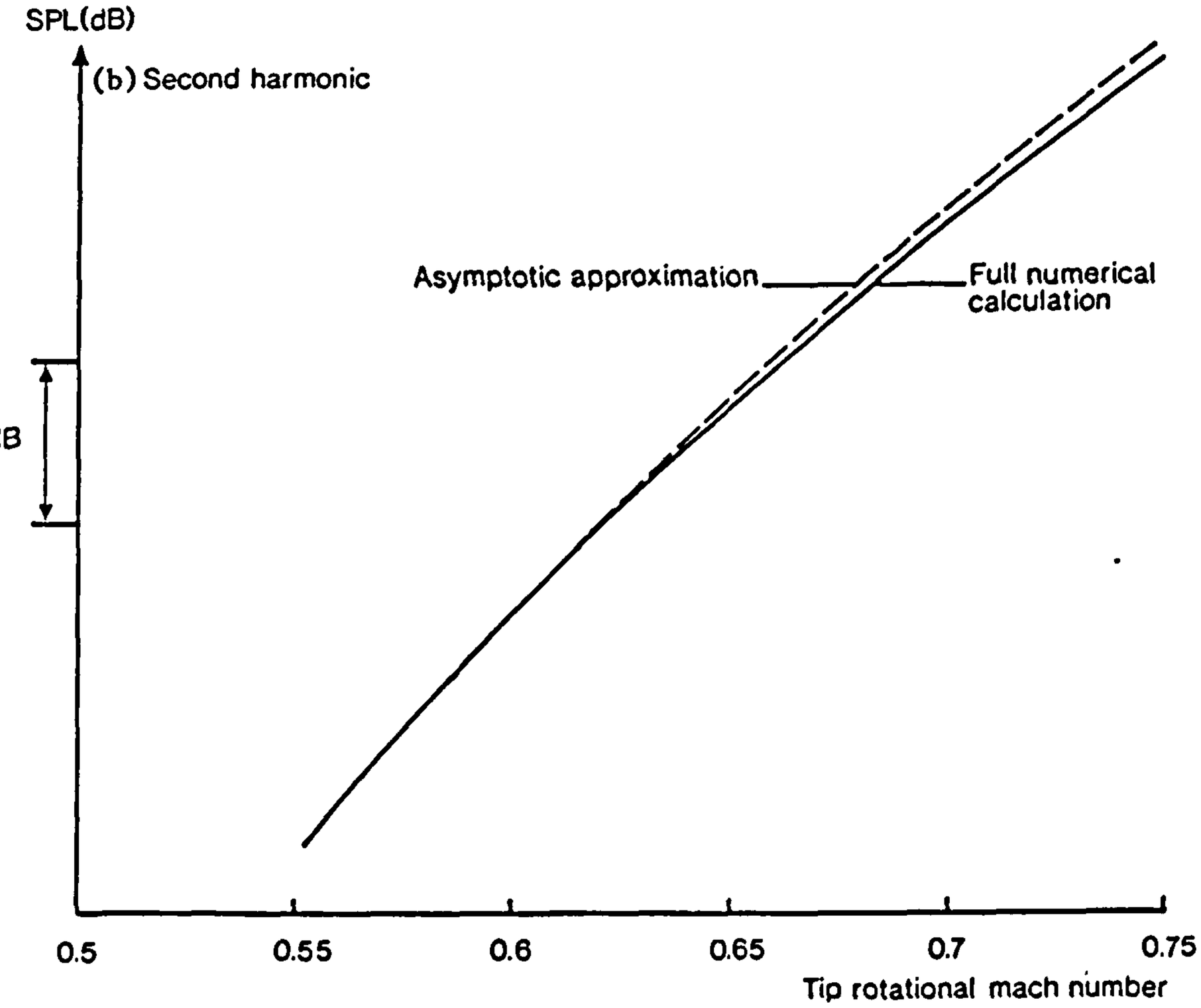

Figure 3.1 Numerical and asymptotic predictions for a subsonic, straight-bladed propeller; B = 12, $\theta = 90^{\circ}$, $M_x = 0.3$.

in (3.2.9), which is

$$E = \exp[-mB(\beta_t - \tanh\beta_t)] \qquad (3.2.10)$$

and we will rewrite (3.2.8) as

$$\operatorname{sech}\beta_t = M_{obs}, \qquad (3.2.11)$$

since M_{obs} represents the component of the blade tip rotational Mach number in the direction of the observer. A plot of M_{obs} against β_t is shown in Figure 3.2. When M_{obs} is small, β_t is large. Since $\tanh\beta_t < 1$ the argument of the exponential in (3.2.10) will be large and negative: in fact, $E \sim \exp(-mB\beta_t)$. It is clear that as the harmonic number m is increased E will decay very rapidly indeed. However as $M_{obs} \to 1$, β_t becomes small and $(\beta_t - \tanh\beta_t) \sim \beta_t^3/3$ which shows that E will decay only weakly with m: in fact, $E \sim \exp(-mB\beta_t^3/3)$.

An early survey by Regier & Hubbard (1953) concluded that propeller noise could best be reduced by increasing the number of blades and decreasing the tip speed. The same results were found more recently by Miller & Sullivan (1985) who carried out a parametric study, using a time domain prediction program, which was aimed at the simultaneous optimisation of both noise and performance. These two proposed changes - reducing the tip speed and increasing the blade number - have effects identical to those discussed above if we note that increasing the number of blades corresponds to increasing the harmonic number.

In addition, Miller & Sullivan found that if the spanwise (radial) distribution of load was altered so that the inboard loading was increased and the loading near the tip reduced whilst the total load was maintained

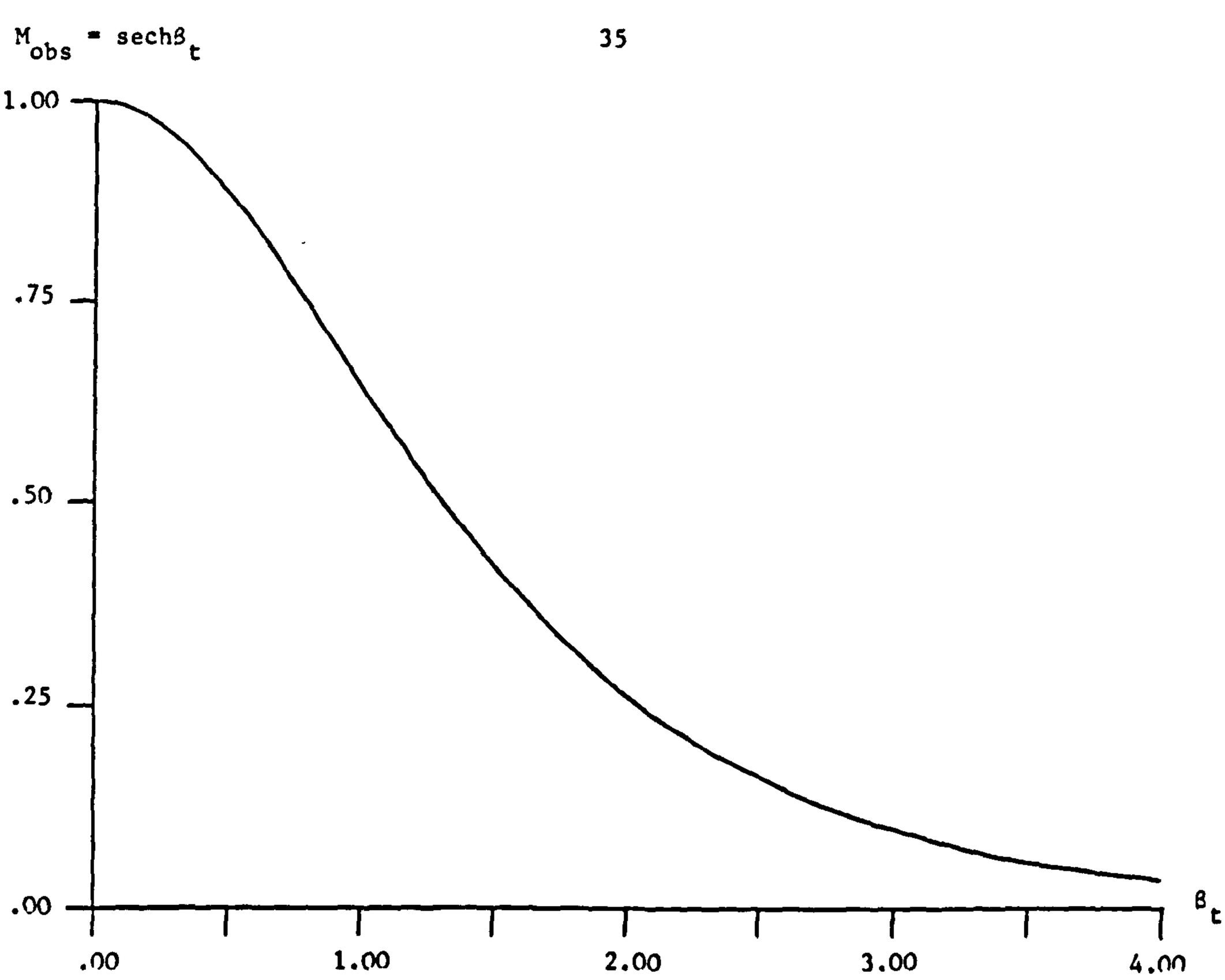

Figure 3.2 The relationship between β_t and M_{obs}.

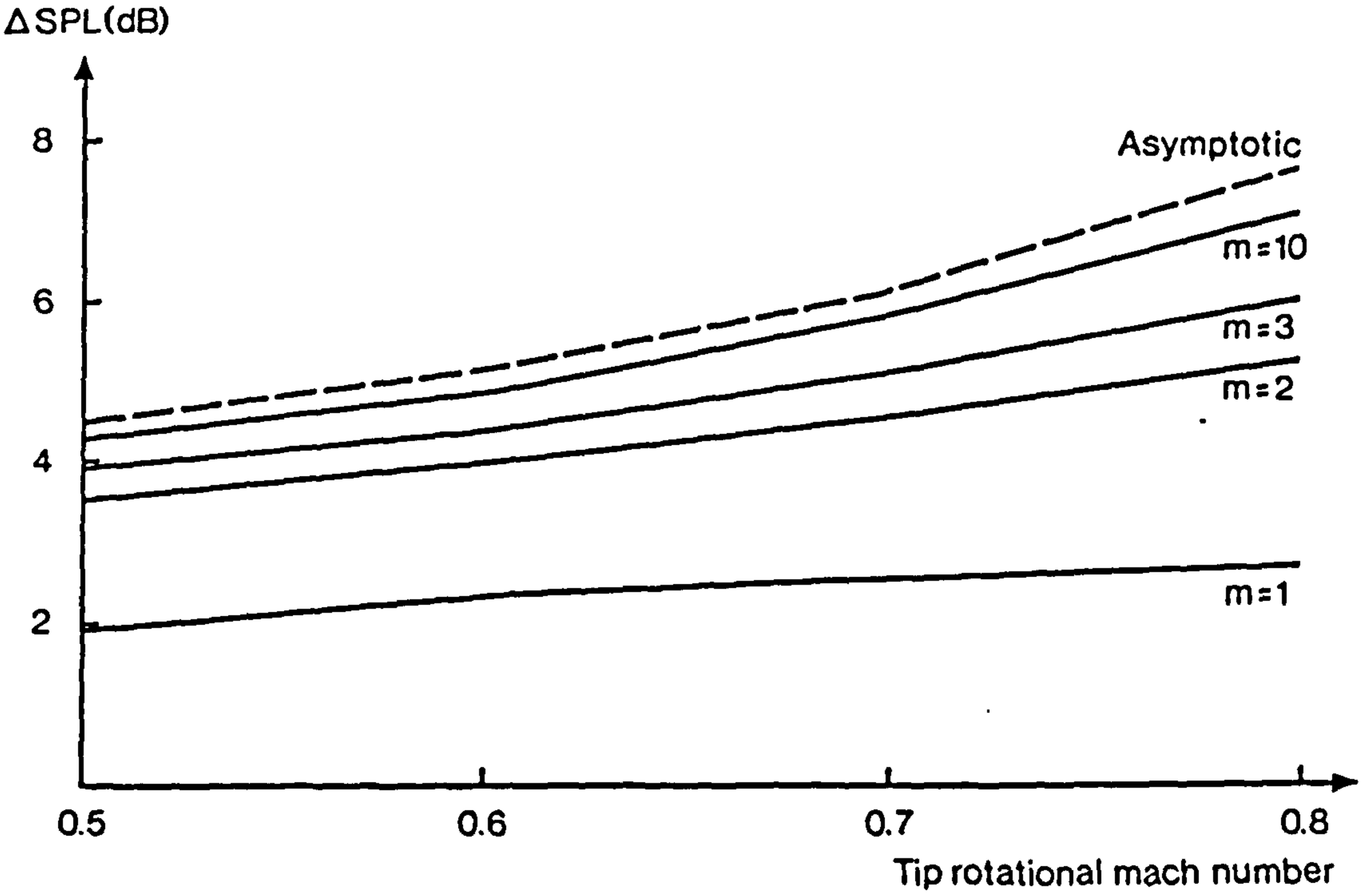

Figure 3.3 Numerical and asymptotic predictions of the effect of blade sweep on a subsonic propeller; $\Lambda_t = 50^o$.

constant, then the radiated noise was reduced*. Since we know from equation (3.2.9) that most of the noise is generated near the blade tip, it is the reduction in loading <u>there</u> that is important. We can see from (3.2.5) that decreasing the loading near the blade tips corresponds to decreasing $\bar{S}$ and/or increasing ν (for the steady loading component). Equation (3.2.9) then shows the precise form of the reduction in the sound field (steady loading component). Dittmar (1984) also used a computer program to look at the effect of moving the loading inboard and found similar results†, as did Succi (1980).

In Gutin's (1936) original work the propeller was modelled by an effective source at the radial station $z = 0.8$. In this case it is still possible to use the asymptotic approximation (3.2.3), but instead of (3.2.10), the dominant term will now be given by

$$E = \exp[-mB(\beta_e - \tanh\beta_e)] \tag{3.2.12}$$

where

$$\operatorname{sech}\beta_e = 0.8M_{obs}. \tag{3.2.13}$$

This shows that β_e will be larger than β_t so that Gutin's approximation will overpredict the reduction of noise with mB, particularly for low tip rotational Mach numbers.

FOOTNOTES

* Note here that, as noted previously, the steady loading component of the sound field is more important than the thickness noise component at subsonic speeds.

† Dittmar's work was specifically aimed at supersonic tip speed propellers. However for off-peak observer angles, M_{obs} will be less than unity (see equation (3.2.11)) and in this region our results above will be valid.

3.2.2 A Swept Propeller

The advanced propellers currently being studied generally incorporate some degree of blade sweep (see, particularly, Metzger & Rohrbach (1979, 1985)). This is mainly for aerodynamic reasons but, in addition, the inclusion of sweep in the blade design produces acoustic benefits because the signals, emitted from different radial stations are partially dephased. Some discussion of this aspect has already been given by Hanson (1980b).

We will now extend the asymptotic analysis, discussed in section 3.2.1, to include the effects of blade sweep. We assume that at subsonic operating conditions, as for straight bladed propellers, most of the noise is generated near the blade tips. We then linearise the section relative Mach number M_r, and the non-dimensional blade sweep s/D (as defined in Figure 2.2), about z = 1, i.e.

$$\frac{s}{D} \sim \frac{s_t}{D} + \frac{(z-1)}{2} \tan \Lambda_t \ , \tag{3.2.14}$$

$$M_r \sim M_{rt} \left[1 + (z-1) \frac{M_t^2}{M_{rt}^2} \right] \tag{3.2.15}$$

where s_t is the blade tip sweep, Λ_t is the blade tip sweep angle and M_{rt} is the tip relative Mach number. This means that the phase exponent ϕ_s, representing the effects of blade sweep, can be approximated by

$$\phi_s \sim \phi_{st} + \frac{2mBM_t}{(1-M_x\cos\theta)M_{rt}} \left(\frac{\tan\Lambda_t}{2} - \frac{s_t M_t^2}{DM_{rt}^2} \right) (z-1) \tag{3.2.16}$$

where ϕ_{st} represents the phase component as calculated at the blade tips,

$$\phi_{st} = \frac{2mBM_t s_t/D}{(1-M_x\cos\theta)M_{rt}} \quad . \tag{3.2.17}$$

If we now include this phase term in (3.2.7) we find that

$$P_m \sim \frac{\bar{S}\ \exp[mB(\tanh\beta_t-\beta_t)]}{(2\pi m\beta\tanh\beta_t)^{\frac{1}{2}}} \int_{-\infty}^{1} (1-z)^{\nu} \tag{3.2.18}$$

$$\exp\left\{mB(z-1)\left[\tanh\beta_t - i\,\frac{2M_t}{(1-M_x\cos\theta)M_{rt}}\left[\frac{\tan\Lambda_t}{2} - \frac{s_t}{D}\frac{M_t^2}{M_{rt}^2}\right]\right]\right\}dz.$$

By evaluating this integral, using (3.2.8), and comparing with the result (3.2.9) for straight bladed propellers, we see that the effect is given by the multiplying factor

$$\frac{P_m(\text{swept})}{P_m(\text{straight})} = \left\{1 + \frac{4M_t^2}{M_{rt}^2[(1-M_x\cos\theta)^2-M_t^2\sin^2\theta]}\left[\frac{\tan\Lambda_t}{2} - \frac{s_t}{D}\frac{M_t^2}{M_{rt}^2}\right]^2\right\}^{-(\nu+1)/2} . \tag{3.2.19}$$

Equation (3.2.19) shows that, asymptotically, the noise benefit achieved by incorporating blade sweep into a propeller design is independent of blade number and harmonic. The predicted noise benefit for a 12-bladed propeller with 50° of tip sweep has been calculated using the full numerical calculation, given by (2.2.28), and the asymptotic approximation (3.2.19). The results are shown in

Figure 3.3, for an observer at 90^{o} radiation angle; the tip rotational Mach number varies between 0.5 and 0.8. The numerical calculations are shown for the first, second, third and tenth harmonics of blade passing frequency. At the first harmonic the noise reduction, as calculated numerically, is less than the asymptotic prediction across the full range of tip rotational Mach numbers examined. However, at higher harmonics the numerical results rapidly approach the asymptotic result. This is in accord with intuition, which suggests that the phase oscillations due to sweep weaken the dominance of the tip region at fixed mB, so that a given level of accuracy can only be achieved by increasing mB. Figure 3.3 indeed shows this behaviour.

To justify the arguments leading to (3.2.19) we refer to pages 121-125 of Olver (1974), where it is proved that the dominant contribution to the integral $\int_a^b \exp[zp(t)]q(t)dt$ when $|z|$ is large comes from the vicinity of the point $t = t_o$ at which $\mathrm{Re}\{zp(t)\}$ attains its maximum value provided t_o coincides with an end point, a or b. That is the case here; the real part of the argument of the exponential is unaffected by blade sweep and (for subsonic conditions) reaches its maximum at the blade tip. The result which justifies (3.2.9) for unswept blades and (3.2.19) for swept is actually (6.19) of Olver (1974), and shows again that subsonic single-rotor noise is tip-dominated. (There is, in particular, no significance in any saddlepoint, at which the complex argument of the exponential is stationary in these circumstances.)

3.3 Supersonic Operating Conditions

3.3.1 A Straight Bladed Propeller

When the propeller blade tips are operating supersonically* M_{obs}, defined by (3.2.8) and (3.2.11), can be greater than unity for certain values of θ. For each such θ there is a section of the blade which approaches the observer at θ with precisely sonic speeds. In this case the blade tips are no longer the most efficient radiators of sound since, for large values of mB, the radiation efficiency, represented by the Bessel function in (2.2.28) and (2.3.7), peaks near the radial station z* where

$$z^* = \frac{1}{M_{obs}} = \frac{1-M_x\cos\theta}{M_t\sin\theta} . \qquad (3.3.1)$$

For the present we will neglect the effects of chordwise noncompactness and blade sweep so that, from (3.2.2), the harmonic components of the radiated sound are given by

$$P_m = \int_{z_o}^{1} S(z)\ J_{mB}(mB\frac{z}{z^*})dz \qquad (3.3.2)$$

where, as in section 3.2, S(z) is used to denote the source strength at radiation station z.

It was shown in (3.2.3) that, for z less than z* and mB large, the Bessel function is exponentially small. For z greater than z* and mB large we can use the asymptotic approximation

---

FOOTNOTE

* Here we mean that M_{rt}, rather than M_t, is greater than 1.

$$J_{mB}(mB\ \sec\beta) \sim \left(\frac{2}{\pi mB\ \tan\beta}\right)^{\frac{1}{2}} \cos(mB\ \tan\beta - mB\beta - \pi/4)\ , \qquad (3.3.3)$$

where $\sec\beta = z/z^*$, showing that the Bessel function oscillates rapidly with slowly changing amplitude. The integral in (3.2.2) will therefore be dominated by contributions from close to $z = z^*$, those from $z < z^*$ being suppressed by exponential smallness of the Bessel function, those from $z > z^*$ being almost self-cancelling because of the rapid oscillations. Consequently, we can make the approximation

$$P_m \sim S(z^*) \int_0^\infty J_{mB}\left(mB\ \frac{z}{z^*}\right) dz \qquad (3.3.4)$$

where the source strength is only evaluated at $z = z^*$ and the lower and upper limits of integration have been extended to zero and infinity respectively. The integral in (3.3.4) can easily be evaluated* to give

$$P_m \sim S(z^*)\ \frac{z^*}{|mB|}\ . \qquad (3.3.5)$$

Interpretation of this result is most important. If, for given θ, there exists a section $z = z^*$ on the blade for which $M_{obs} z^* = 1$, then the radiation in direction θ is dominated by contributions from the immediate vicinity of $z = z^*$ rather than the tip. If $S(z)$ is independent of mB then the decay of those contributions from $z = z^*$ with mB is as $|mB|^{-1}$, and the harmonic series in this case converges to a function with logarithmic singularities in the time domain. However, from section 2.2 we see, from the definition of k_y in (2.2.26), that the

---

FOOTNOTE

* We note that, for helicopter rotors, Hawkings & Lowson (1974) used stationary phase techniques to simplify the integration over the blade surface, for high values of mB. They also found that the "sonic radius" provided the dominant contribution to the radiated sound field.

force component of S(z) increases as mB in which case the harmonic series represents a waveform containing (pole) singularities of order 1. For the volume component, from the definition of k_x in (2.2.25), S(z) increases as $(mB)^2$ so that the harmonic series represents a waveform containing (pole) singularities of order 2. (A detailed discussion of the harmonic series results is given in appendix 3.1). Taking account of the finite chordwise dimension reduces the order of these singularities, as will be shown in section 3.3.2. It is thus seen that the present spectral approach is able, quite naturally, to pick up distinctive features characteristic of the real time waveform - such as singularities - whenever these exist. Any power law decay with m gives a singularity in some derivative of p(t), while if P_m vanishes faster than any inverse power of m, p(t) is infinitely differentiable - and has no special character.

In Figure 3.4 a comparison is shown between a full numerical calculation and the asymptotic approximation for a 12-bladed propeller operating at a range of supersonic helical tip speeds. The results are shown for an observer in the plane of the propeller, and for the first two harmonics of blade passing frequency. It is clear that the simple asymptotic approximation, (3.3.5), agrees well with the full numerical calculation over the range of tip rotational Mach numbers examined. The plots show that there are small oscillations in the numerical predictions as the tip rotational Mach number is varied. This is because, as the tip rotational Mach number is increased, the radial integral will be altered by a small amount, either positive or negative, due to the Bessel function oscillations. These oscillations are associated with the next term in the asymptotic development, of relative order $(mB)^{-\frac{1}{2}}$, containing a sinusoidal term and dominated by contributions from the tip. We will return to this point in section 3.4.

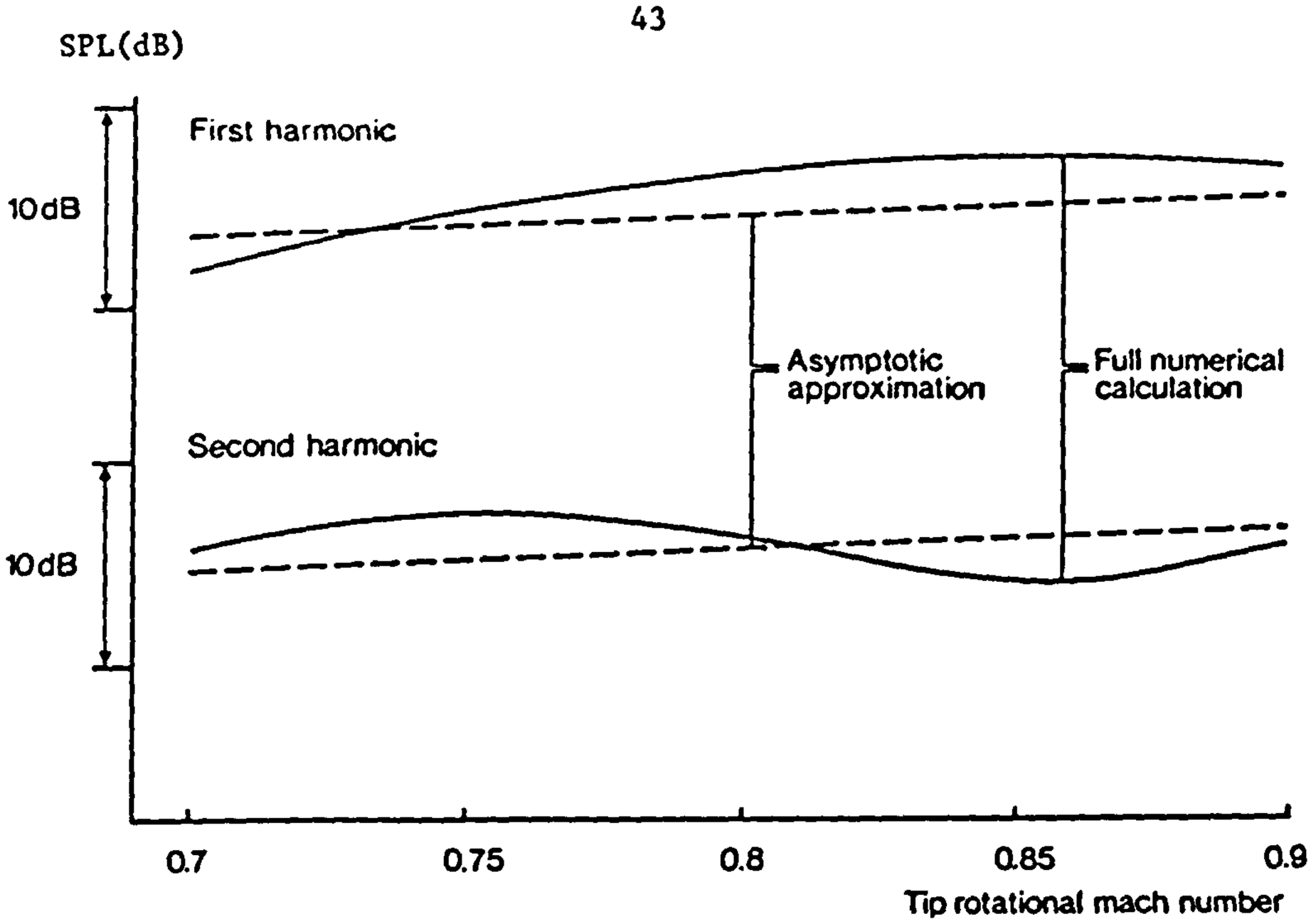

Figure 3.4 Comparisons between numerical and asymptotic predictions for a supersonic, straight-bladed propeller.

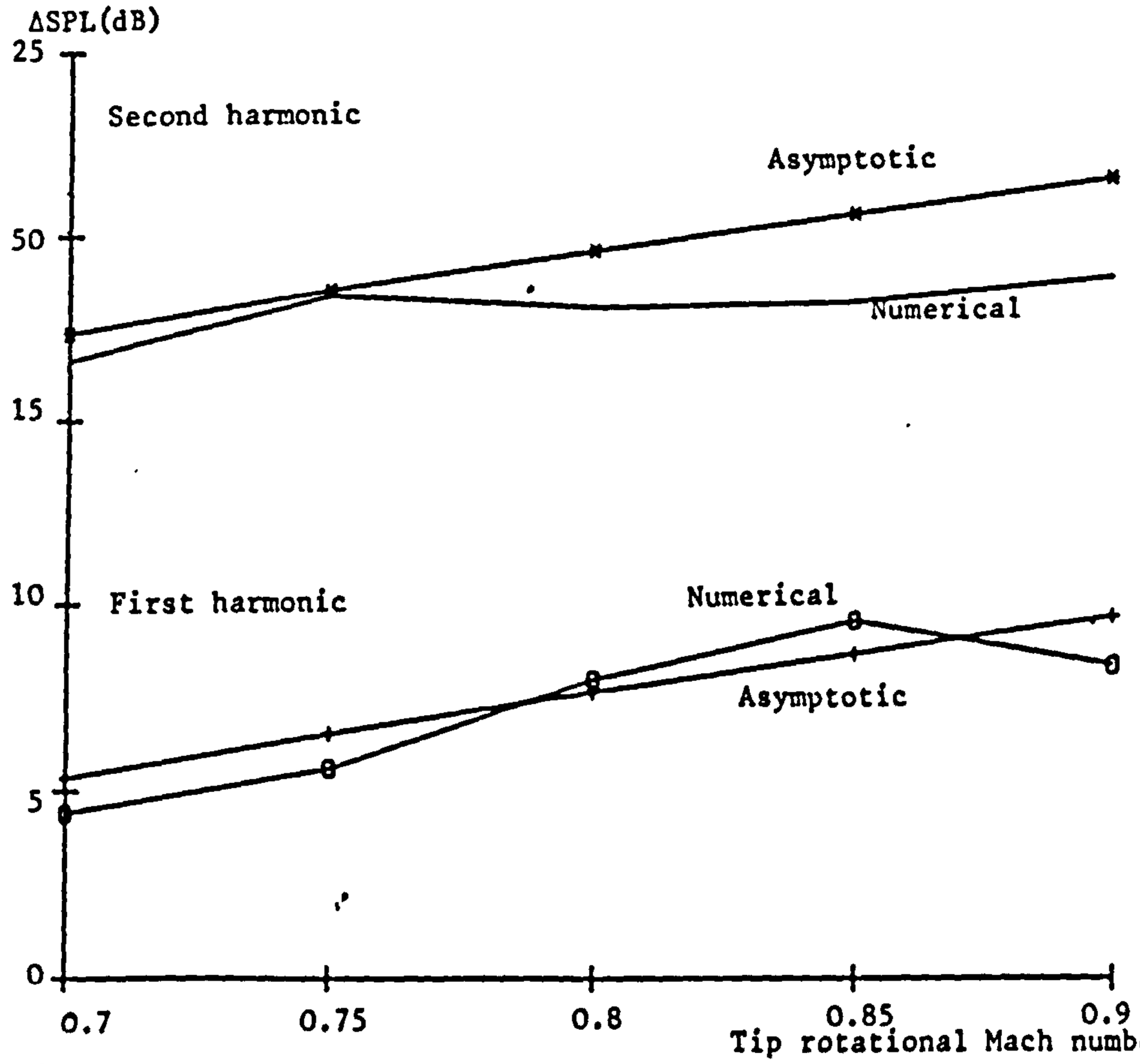

Figure 3.5 Numerical and asymptotic predictions of the effect of chordwise noncompactness.

3.3.2 Chordwise Noncompactness Effects

When the chordwise wavenumber k_x of (2.2.25) exceeds unity the effects of chordwise noncompactness can become significant. These effects will be most important at high forward speeds where the Doppler factor can produce a considerable increase in k_x.

From (2.2.27) and (2.3.8) we see that noncompactness at each radial station z can be represented by the factor

$$\Psi = \int_{-\frac{1}{2}}^{\frac{1}{2}} f(X) e^{-ik_x X} \, dX \,, \tag{3.3.6}$$

where $f(X)$ is a general chordwise shape function corresponding either to $F(X)$, which represents the blade loading, or $h(X)$, which represents the blade thickness. We rewrite (3.3.6) in the form of a Fourier transform

$$\Psi = \int_{-\infty}^{\infty} f(X)[H(X + \tfrac{1}{2}) - H(X - \tfrac{1}{2})] e^{-ik_x X} \, dX \,, \tag{3.3.7}$$

where H is the Heaviside unit function. Since the shape functions are always of algebraic form in the region of the blade leading and trailing edges we can put*

$$\left.\begin{aligned} f(X) &\sim \alpha_L(\tfrac{1}{2} + X)^{\nu_L} \quad \text{as} \quad X \to -\tfrac{1}{2} \,, \\ f(X) &\sim \alpha_T(\tfrac{1}{2} - X)^{\nu_T} \quad \text{as} \quad X \to \tfrac{1}{2} \,. \end{aligned}\right\} \tag{3.3.8}$$

Here we have used the suffices L and T to denote leading and trailing edge values respectively. As in previous sections, mB is assumed to be

---

FOOTNOTE

* An integrable singularity in the leading edge loading can, as usual, be tolerated, corresponding to $-1 < \nu_L < 0$.

large so that, from (2.2.25), k_x is also large. We can then evaluate (3.3.7) asymptotically, using the methods outlined in chapter 4 of Lighthill (1958), leading to

$$\Psi \sim \frac{\alpha_L \nu_L!\, \exp[\pm i|k_x|/2 \mp i(\nu_L + 1)\pi/2]}{|k_x|^{\nu_L + 1}} - \frac{\alpha_T \nu_T!\, \exp[\mp i|k_x|/2 \mp i(\nu_T + 1)\pi/2]}{|k_x|^{\nu_T + 1}} \qquad (3.3.9)$$

where the upper or lower signs are used according as m, the harmonic index, is positive or negative. We will consider first the case where ν_L is less than ν_T. This means that the shape function, f(X), is weighted towards the leading edge. The first term in (3.3.9) is then dominant so that the noise generated by a blade section will decay with increasing k_x as

$$\Psi \sim \frac{\alpha_L \nu_L!}{|k_x|^{\nu_L+1}} \exp[\pm i|k_x|/2 \mp i(\nu_L + 1)\pi/2] \,. \qquad (3.3.10)$$

When the chordwise shape function is symmetric we have that

$$\left.\begin{aligned} &\alpha_L = \alpha_T = \alpha \\ \text{and} \qquad &\\ &\nu_L = \nu_T = \nu, \text{ say} \end{aligned}\right\} \qquad (3.3.11)$$

so that (3.3.9) reduces to

$$\Psi \sim \frac{\pm\, 2\alpha\nu!}{|k_x|^{\nu+1}} \sin(k_x/2) e^{\mp i\nu\pi/2} \quad . \tag{3.3.12}$$

In this case the noise level will oscillate as k_x is increased due to the factor $\sin(k_x/2)$ in (3.3.12), and the envelope of the oscillations will reduce in level as $|k_x|^{-\nu-1}$. The two results, (3.3.10) and (3.3.12), provide a simple description of the results found by Hanson (1980b; see, in particular, Figure 9) who examined three types of shape function for loading noise. Of these, two were leading-edge-dominated and had almost identical monotonic algebraic decay of Ψ with increasing k_x, differing only in a constant corresponding to different values of α_L, the distributions elsewhere over the chord being irrelevant. The third was essentially symmetric about the mid-chord and gave oscillatory behaviour in Ψ due to correlated comparable leading and trailing edge effects, with algebraic envelope decay similar to that of the first two.

The importance of our expressions (3.3.10) and (3.3.12) is that (i) they show how noncompactness effects at each station are dominated by leading or trailing edge behaviour, and (ii) they form a basis for subsequent evaluation of the spanwise integral which is needed in order to determine the overall acoustic benefit of noncompactness. This overall benefit cannot be assessed by examining a single blade section (as was done in Figure 9 of Hanson (1980b)).

We will now assume that the noncompactness factor is given asymptotically by (3.3.10), i.e. the shape function f(X) is weighted towards the leading edge. Then, from (3.3.2) and (3.3.10),

$$P_m \sim \alpha_L \nu_L!\, \exp\left[\mp\, i(\nu_L + 1)\frac{\pi}{2}\right] \int_{z_o}^{1} \frac{S(z)}{|k_x|^{\nu_L+1}} J_{mB}(mB\frac{z}{z^*}) e^{\pm i|k_x|/2}\, dz. \tag{3.3.13}$$

The form of the integral in (3.3.13) is similar to that in (3.3.2) except for the additional phase term. If, for the present, we assume k_x to be approximately constant with radius* (we will return to this point later) then we can proceed as in section 3.3.1, and arrive at

$$P_m \sim \frac{\alpha_L \nu_L!\ S(z^*)z^*}{|mB|\,|k_x^*|^{\nu_L+1}} \exp\left[\mp\, i(\nu_L + 1)\frac{\pi}{2} \pm \frac{i|k_x^*|}{2}\right] \qquad (3.3.14)$$

where k_x^* is the value of k_x at $z = z^*$.

Equation (3.3.14) is superficially similar to (3.3.5) which, we observed, corresponded to the production of logarithmic singularities at the condition $M_{obs}z^* = 1$. However, taking into account the dependence of S(z) and k_x on mB, we find that (3.3.14) decays as $|mB|^{-\nu_L-1}$ for the force component of the sound field and as $|mB|^{-\nu_L}$ for the volume component. (The actual dependence on mB is more complex than this; a full description of the harmonic components, and the associated waveforms, is given in appendix 3.2). We examine loading noise first and consider three types of loading distribution. When there is an integrable singularity in the leading edge loading, corresponding to $-1 < \nu_L < 0$, there are weak algebraic singularities in the real time waveform; when the leading edge loading is constant, corresponding to $\nu_L = 0$, logarithmic singularities are generated; finally, when the leading edge loading is zero, corresponding to $\nu_L > 0$, there are no singularities generated (though there are singularities in some derivative of the pressure).

FOOTNOTE

* For k_x to be constant with radius we are assuming, essentially, that the projection of the chord, onto a line parallel to the engine axis, is constant with radius. There are thus no spanwise interference effects which are analogous to the effect of sweep.

We now examine thickness noise where the harmonic decay is controlled by the shape of the leading edge. For a blunt leading edge, corresponding to $0 < \nu_L < 1$, there are weak algebraic singularities in the real time waveform; for a wedge shaped leading edge, corresponding to $\nu_L = 1$, logarithmic singularities are generated; finally, for a cusp shaped leading edge, corresponding to $\nu_L > 1$, there are no singularities in the waveform. The results for thickness noise in the case of a blunt leading edge agree with those obtained previously by Tam (1983).

It is interesting to note the variations with tip rotational Mach number M_t*. For loading noise, from (2.2.25), (2.2.26), (2.2.28), (3.3.1) and (3.3.14), we find that P_m varies as $M_t^{-\nu_L-1}$. Since, for loading, ν_L is always greater than -1 this means that P_m is a <u>decreasing function</u> of M_t. For thickness noise, from (2.2.25), (2.3.7), (3.3.1) and (3.3.14), we find that P_m varies as $M_t^{-\nu_L}$. Since, for blade thickness, ν_L is always greater than 0 this shows, again, that P_m is a decreasing function of M_t. This <u>algebraic decrease</u> contrasts markedly with the <u>exponential increase</u> at subsonic tip speeds which was discussed in section 3.2.

In Figure 3.5 a comparison is shown between a full numerical calculation and the asymptotic approximation (3.3.14) for a 12-bladed propeller of constant chord. The plot shows the noise reduction due to noncompactness for the first two harmonics of blade passing frequency. The values of α_L and ν_L were determined from the form of the full chordwise shape function in the region of the leading edge. The shape function was chosen so that $\nu_L = 1$ and $\nu_T = 2$. From Figure 3.5 it can be

---

<u>FOOTNOTE</u>

* Here we must take account, through (3.3.1), of the variation of z^* with M_t. Note that at $z = z^*$ we have $M_r = M_r^* = 1$.

seen that the asymptotic approximation agrees well with the full numerical calculation over the range of tip speeds examined. At second harmonic there is very close agreement between the two calculations at the lower tip speeds, but there is some discrepancy at higher tip speeds. Since the approximate calculation is asymptotic in mB we would generally expect the results at second harmonic to be more accurate than those at first. However, in deriving (3.3.14) we neglected the variation of the phase term $e^{ik_x/2}$ in (3.3.13) and assumed k_x to be approximately constant with z. From (2.2.25) we find that, for a propeller of constant chord,

$$\frac{d}{dz}\left(\frac{k_x}{2}\right) = -\frac{mBM_t^3\, zc/D}{(1 - M_x\cos\theta)M_r^3} \,. \tag{3.3.15}$$

At first harmonic, for the case under consideration, $(d/dz)(k_x/2)$ is less than 1 for the range of tip speeds examined. This means that, to a first approximation, the variations in phase across the blade span can be neglected, as can be seen from the agreement, at first harmonic, between the asymptotic and numerical predictions in Figure 3.5. However, at higher harmonics the phase variations along the blade span will be significant and the asymptotic approximation (3.3.14) will be inaccurate, particularly at higher tip speeds. This is confirmed by the second harmonic results in Figure 3.5.

The variations in phase along the blade span due to noncompactness are analogous to the effects of blade sweep. To account for spanwise interference effects due to phase variations we can no longer assume that the radiated noise is dominated solely by contributions from z = z*

and must consider, instead, the whole blade span. In the following sections we develop uniform asymptotic approximations in which amplitude and phase effects are accounted for.

3.4 Uniform Asymptotic Approximations

In sections 3.2 and 3.3 we described asymptotic approximations for propellers operating at subsonic and supersonic conditions. However, these approximations were not uniform - in fact the subsonic approximation becomes singular as the blade helical tip speed approaches unity (at $M_{obs} = 1$ we have, from (3.2.8) and (3.2.11), that $\beta_t = 0$ and hence, in (3.2.9), $\tanh\beta_t = 0$). In Figure 3.6 we show a plot of propeller noise against tip rotational Mach number as calculated using the asymptotic approximations in sections 3.2 and 3.3. Here, we switch from the subsonic approximation to the supersonic approximation at $M_{obs} = 1$; it is clear that at this point the curve is discontinuous. In order to rectify this problem we will develop approximations which change smoothly between subsonic and supersonic operating conditions.

3.4.1 Bessel Function Approximations

Since the Bessel function tends, in general, to dominate the radial integrations, (2.2.28) and (2.3.7), we consider asymptotic approximations for $J_\nu(\nu\sigma)$ which are uniform in σ as $\nu \to \infty$.

First we suppose that $\sigma < 1$ and $\sigma = O(1)$. We can then write

$$\sigma = \operatorname{sech}\beta \tag{3.4.1}$$

and use the Debye asymptotic approximation which is given in section 9.3.7 of Abramowitz & Stegun (1965) as

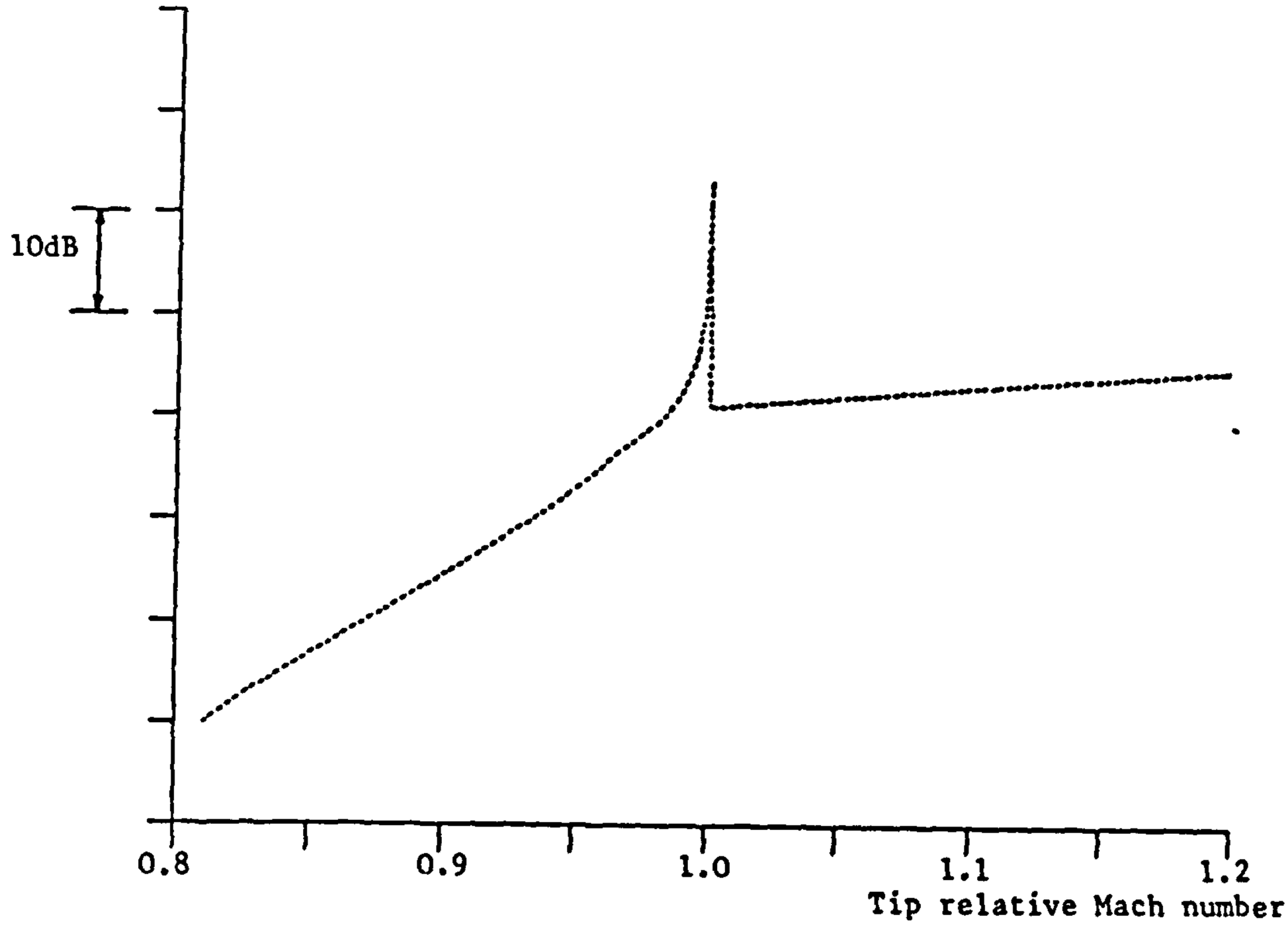

Figure 3.6 Asymptotic calculation of propeller noise vs tip relative Mach number. For $M_{rt} < 1$ we use (3.2.9) and for $M_{rt} \geq 1$ we use (3.3.5).

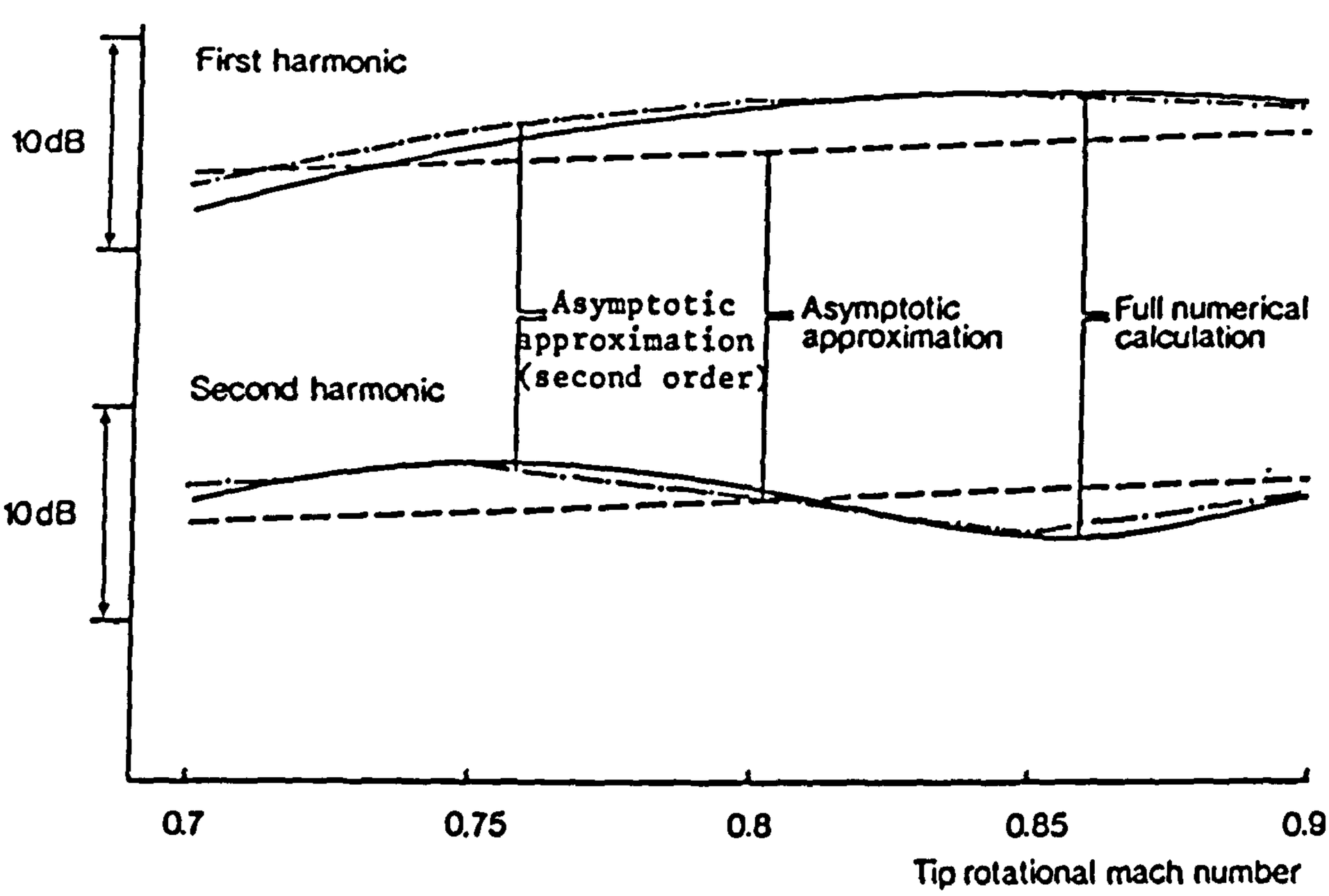

Figure 3.7 Comparisons between first and second order asymptotic predictions and numerical calculations for a supersonic, straight-bladed propeller.

$$J_\nu(\nu\,\mathrm{sech}\beta) \sim \frac{\exp[\nu(\tanh\beta-\beta)]}{(2\pi\nu\tanh\beta)^{\frac{1}{2}}}\left[1 + \sum_{k=1}^{\infty} \frac{u_k(\coth\beta)}{\nu^k}\right] \tag{3.4.2}$$

where

$$u_1(t) = \frac{3t - 5t^3}{24} \tag{3.4.3}$$

and, in general, $u_n(t) \sim t^{3n}$ as $t \to \infty$. The series (3.4.2) is non-uniform as $\beta \to 0$ since then $t = \coth\beta \sim \beta^{-1}$ and

$$\frac{u_1(\coth\beta)}{\nu} \sim \frac{1}{\beta^3\nu} \quad . \tag{3.4.4}$$

The series (3.4.2) is thus nonuniform when $\beta = O(\nu^{-1/3})$. However, for $\beta >> \nu^{-1/3}$ we can use the approximation

$$J_\nu(\nu\sigma) \sim \frac{\exp[\nu(\tanh\beta-\beta)]}{(2\pi\nu\tanh\beta)^{\frac{1}{2}}} \tag{3.4.5}$$

where β is defined by (3.4.1).

We now suppose that $\beta = O(\nu^{-1/3})$ and put

$$\beta = \kappa\nu^{-1/3} \tag{3.4.6}$$

where $\kappa = O(1)$. Since β is small we can use the approximation

$$\mathrm{sech}\beta \sim 1 - \frac{\beta^2}{2} = 1 - \frac{\kappa^2}{2\nu^{2/3}} \quad . \tag{3.4.7}$$

We then obtain

$$J_\nu(\nu\,\mathrm{sech}\beta) = J_\nu\left[\nu - \nu\frac{\kappa^2}{2\nu^{2/3}} + O(\nu^{-1/3})\right] \tag{3.4.8}$$

$$\sim J_\nu(\nu - \frac{\kappa^2}{2}\,\nu^{1/3}) + O(\nu^{-1}),\ \text{as}\ \nu \to \infty.$$

Here, in order to obtain the next term, we use a Taylor expansion and section 9.3.27 of Abramowitz & Stegun (1965). From section 9.3.23 of Abramowitz & Stegun (1965) we find that (3.4.8) reduces further to

$$J_\nu(\nu\,\mathrm{sech}\beta) \sim \frac{2^{1/3}}{\nu^{1/3}}\ \mathrm{Ai}\ (\frac{\kappa^2}{2^{2/3}}) + O(\nu^{-1}). \tag{3.4.9}$$

In order to use only the leading order term in (3.4.9) we require $\nu^{-2/3} \ll 1$ or, from (3.4.6), that $\beta \ll 1$. From (3.4.1), (3.4.7) and (3.4.9) we can then use the approximation

$$J_\nu(\nu\sigma) \sim \frac{2^{1/3}}{\nu^{1/3}}\ \mathrm{Ai}[2^{1/3}\nu^{2/3}(1-\sigma)]\ . \tag{3.4.10}$$

In appendix 3.3 we show that the two expressions (3.4.5) and (3.4.10), agree in the overlap range $\nu^{-1/3} \ll \beta \ll 1$. It would be possible to use this fact to form a <u>composite</u> smooth approximation which reduces to (3.4.5) or (3.4.9) where appropriate. That leads, however, to a rather complicated expression, and instead we will simply <u>join</u> (3.4.5) and (3.4.10) at the point $\beta = \nu^{-1/6}$, i.e. at

$$\sigma = \sigma_- = 1 - \frac{\nu^{-1/3}}{2}\ . \tag{3.4.11}$$

Then, for $\sigma < \sigma_-$ we use the approximation given by (3.4.5) and for

$\sigma_- < \sigma < 1$ we use (3.4.11). In practice this may lead to a discontinuity in the predicted pressure, but this will be extremely small because $\sigma = \sigma_-$ is well inside the overlap domain.

We now turn to the case where $\sigma > 1$ and $\sigma = O(1)$ so that β is imaginary. Instead of using β we define λ by

$$\sigma = \sec\lambda \ . \tag{3.4.12}$$

The asymptotic expansion for $J_\nu(\nu\sigma)$ is then given in section 9.3.15 of Abramowitz & Stegun (1965) as

$$J_\nu(\nu\sec\lambda) \sim \left[\frac{2}{\pi\nu\tan\lambda}\right]^{\frac{1}{2}} \left\{\cos\Phi\left[1 + O\left(\frac{\cot^6\lambda}{\nu^2}\right)\right] + O\left(\frac{\cot^3\lambda}{\nu}\right)\sin\Phi\right\} \tag{3.4.13}$$

where

$$\Phi = \nu(\tan\lambda - \lambda) - \pi/4 \ . \tag{3.4.14}$$

The series (3.4.13) is again nonuniform when $\lambda = O(\nu^{-1/3})$. However, for $\nu^{-1/3} << \lambda < \pi/2$ we can use the approximation

$$J_\nu(\nu\sigma) \sim \left(\frac{2}{\pi\nu\tan\lambda}\right)^{\frac{1}{2}} \cos[\nu(\tan\lambda - \lambda) - \pi/4] \ . \tag{3.4.15}$$

where λ is defined by (3.4.12).

For $\lambda = O(\nu^{-1/3})$ we now carry out an analysis similar to that used above between (3.4.6) and (3.4.11). For $\lambda << 1$ we find that we can again

use the approximation (3.4.10) with σ defined by (3.4.12). The two expressions, (3.4.10) and (3.4.15) agree in the range $\nu^{-1/3} << \lambda << \pi/2$. We therefore join (3.4.10) and (3.4.15) at the point $\lambda = \nu^{-1/6}$, i.e. at

$$\sigma = \sigma_+ = 1 + \frac{\nu^{-1/3}}{2} \quad . \tag{3.4.16}$$

This may again lead to a discontinuity, but the choice of σ_+ should ensure that any such discontinuity is very small, and that the pressure is in fact continuous.

The Bessel function, corresponding to the radiation efficiency of a blade section, has now been split into three distinct regions: first, a subsonic regime defined by $\sigma < \sigma_-$ in which zM_{obs} is always less than unity and where the Bessel function can be approximated by (3.4.5); second, a transonic regime defined by $\sigma_- < \sigma < \sigma_+$ in which zM_{obs} is always close to unity and where the Bessel function can be approximated by (3.4.10); and finally, a supersonic regime, defined by $\sigma > \sigma_+$, in which zM_{obs} is always greater than unity and where the Bessel function can be approximated by (3.4.15).

We therefore proceed by splitting the blade radially into these predefined subsonic, transonic and supersonic regions and then considering each region separately. The acoustic radiation (with harmonic components $P_m^{(1)}$) from the subsonic region is no different from that discussed in section 3.2 (with appropriate changes from parameter values at the tip to values at $z = \sigma_-/M_{obs}$ defining the upper bound of the subsonic regime) and will not, therefore, be considered further.

3.4.2 The Transonic Regime

We now define a new source strength function $\bar{S}(z)$ which combines the original source strength $S(z)$ introduced in section 3.3.1 and the noncompactness factor Ψ which was discussed in section 3.3.2. If both leading and trailing edge effects are to be considered, as in (3.3.9), then we introduce $S_L(z)$ and $S_T(z)$ and consider each source function independently. The phase factors $e^{\pm ik_x/2}$ are, however, not included in the source strength function; instead we introduce the sweep phase factor $e^{-i\bar{\phi}_s}$ in which the sweep is defined relative to the blade leading or trailing edges.

The source strength at z can be related to the source strength at the 'sonic radius' z^* by a Taylor series, i.e.

$$S(z) = S(z^*) + (z - z^*)\, S'(z^*) + \ldots\ldots \qquad (3.4.17)$$

Here we consider just the first two terms in the series expansion. For a straight-bladed propeller* the harmonic components of the acoustic pressure, radiated from the transonic region of the blades, are given by

$$P_m^{(2)} \sim \bar{S}(z^*) \int_{z_-}^{z_+} J_{mB}(mB\,\frac{z}{z^*})dz + \bar{S}'(z^*) \int_{z_-}^{z_+} (z-z^*) J_{mB}(mB\,\frac{z}{z^*})dz \qquad (3.4.18)$$

where†

$$z_{\pm} = z^*\left[1 \pm \frac{(mB)^{-1/3}}{2}\right] . \qquad (3.4.19)$$

FOOTNOTE

* Here we suppose that $\bar{\phi}_s$ is constant over the transonic region of the blades.

† Here, and throughout this section, mB is taken to mean $|mB|$. The analysis is the same for positive and negative harmonics since $J_{-n}(-nx) = J_n(nx)$ for integer values of n.

We now use the asymptotic approximation (3.4.10) for the Bessel function and introduce the substitution

$$x = 2^{1/3}(mB)^{2/3}\left(\frac{z}{z^*} - 1\right) \tag{3.4.20}$$

whence (3.4.18) reduces to

$$P_m^{(2)} = \frac{z^*}{mB}\,\bar{S}(z^*)\int_{x_-}^{x_+} Ai(-x)dx + \frac{z^{*2}}{2^{1/3}}\,\frac{\bar{S}'(z^*)}{(mB)^{5/3}}\int_{x_-}^{x_+} xAi(-x)dx \tag{3.4.21}$$

where the limits of integration are given by

$$x_{\pm} = \pm\,\frac{(mB)^{1/3}}{2^{2/3}}\,. \tag{3.4.22}$$

Since mB is assumed large we have, from (3.4.22), that $x_{\pm}$ are also large. We can therefore use the asymptotic forms for the first of the two integrals in (3.4.21). These can be found in sections 10.4.82 and 10.4.83 of Abramowitz & Stegun (1965). There follows*

$$\int_{x_-}^{x_+} Ai(-x)dx \sim 1 - \frac{2^{\frac{1}{2}}}{\pi^{\frac{1}{2}}(mB)^{1/4}}\left\{\cos\left[\frac{(mB)^{\frac{1}{2}}}{3} + \frac{\pi}{4}\right] + \frac{1}{2}\exp\left[-\frac{(mB)^{\frac{1}{2}}}{3}\right]\right\} \tag{3.4.23}$$

We now proceed to consider the second integral in (3.4.21). The Airy

---

FOOTNOTE

* The higher order terms in the asymptotic approximation for the Bessel function, (3.4.10), can easily be included in the analysis. The result for the first integral in (3.4.18), currently given by (3.4.23), would then contain an additional term of relative order $(mB)^{-2/3}$.

function is defined in integral form in section 10.4.32 of Abramowitz & Stegun (1965) whence

$$\int_{x_-}^{x_+} x\,\mathrm{Ai}(-x)dx = \frac{1}{\pi}\int_{x_-}^{x_+} x \int_0^{\infty} \cos\left(\frac{t^3}{3}-xt\right)dt\,dx \quad . \tag{3.4.24}$$

On changing the order of integration and evaluating the x-integral in (3.4.24) we obtain

$$\int_{x_-}^{x_+} x\,\mathrm{Ai}(-x)dx = \frac{-x_+}{\pi}\int_0^{\infty} \frac{1}{t}\left[\sin\left(\frac{t^3}{3}-x_+t\right)+\sin\left(\frac{t^3}{3}+x_+t\right)\right]dt$$

$$+\frac{1}{\pi}\int_0^{\infty}\frac{1}{t^2}\left[\cos\left(\frac{t^3}{3}-x_+t\right)-\cos\left(\frac{t^3}{3}+x_+t\right)\right]dt \quad . \tag{3.4.25}$$

Both of the integrals in (3.4.25) can be evaluated, using the method of stationary phase, by setting $t = x_+^{\frac{1}{2}}\tau$. Each integral contributes a term of $O(x_+^{-3/4})$ from the stationary phase point at $\tau = 1$. Since neither of the integrals is, in fact, singular at $t = 0$, the stationary phase contribution provides the correct leading order term. We then have

$$\int_{x_-}^{x_+} x\,\mathrm{Ai}(-x)dx \sim O(x_+^{1/4}) \tag{3.4.26}$$

which, on using (3.4.22), reduces to

$$\int_{x_-}^{x_+} x\,\mathrm{Ai}(-x)dx \sim O[(mB)^{1/12}] \quad . \tag{3.4.27}$$

From (3.4.21), (3.4.23) and (3.4.27) we then find that

$$P_m^{(2)} \sim \frac{z^*}{mB}\,\bar{S}(z^*)\left\{1 - \frac{2^{1/2}}{\pi^{1/2}(mB)^{1/4}}\left[\cos\left[\frac{(mB)^{1/2}}{3} + \frac{\pi}{4}\right] + \frac{1}{2}\exp\left[-\frac{(mB)^{-\frac{1}{2}}}{3}\right]\right]\right.$$

$$\left. + O[(mB)^{-7/12}]\right\} . \qquad (3.4.28)$$

Note that the leading order term in (3.4.28) corresponds to the result obtained in section 3.3.1.

In order to complete the analysis for a straight-bladed propeller we need to consider the supersonic region of the blade. Before proceeding, in the next section, to discuss this region we will, however, first tackle the problem of phase variations across the transonic blade region.

The acoustic pressure radiated from the transonic region is, in his case, given by

$$P_m^{(2)} = \bar{S}(z^*)\int_{z_-}^{z_+} J_{mB}(mB\,\frac{z}{z^*})e^{-i\bar{\phi}_s}\,dz . \qquad (3.4.29)$$

We now linearise the sweep phase term $\bar{\phi}_s$ about the sonic radius, setting

$$\bar{\phi}_s \sim \bar{\phi}_s^* + \alpha_s\,(\frac{z}{z^*} - 1)mB \qquad (3.4.30)$$

where

$$\bar{\phi}_s^* = \frac{2mBM_t\bar{s}^*/D}{(1 - M_x\cos\theta)} , \qquad (3.4.31)$$

$$\alpha_s = \frac{M_t(\tan\Lambda^* - 2z^*M_t^2 s^*/D)}{(1 - M_x\cos\theta)} , \qquad (3.4.32)$$

$\bar{s}^*$ is the leading edge sweep at $z = z^*$ and Λ^* is the leading edge sweep angle at $z = z^*$. Now define

$$x = (mB)^{1/3}\left(\frac{z}{z^*} - 1\right) \tag{3.4.33}$$

and then, on using the asymptotic approximation (3.4.10) for the Bessel function, (3.4.29) reduces to

$$P_m^{(2)} \sim \frac{2^{1/3}}{(mB)^{2/3}} z^* \bar{S}(z^*) e^{-i\bar{\phi}_s^*} \int_{-\frac{1}{2}}^{\frac{1}{2}} Ai[-2^{1/3}(mB)^{1/3}x] e^{-i\alpha_s(mB)^{2/3}x} dx. \tag{3.4.34}$$

Now the Airy function can be expressed in integral form by

$$Ai[-2^{1/3}(mB)^{1/3}x] = \frac{1}{2^{4/3}(mB)^{1/3}\pi} \int_{-\infty}^{\infty} \exp\left\{\frac{it^3}{6mB} - ixt\right\} dt \ . \tag{3.4.35}$$

Inserting this in (3.4.34) we obtain

$$P_m^{(2)} \sim \frac{z^*\bar{S}(z^*)e^{-i\bar{\phi}_s^*}}{2\pi mB} \int_{-\frac{1}{2}}^{\frac{1}{2}} \int_{-\infty}^{\infty} \exp\left[\frac{it^3}{6mB} - ixt - i\alpha_s(mB)^{2/3}x\right] dt\, dx \cdot \tag{3.4.36}$$

We now substitute $t = (mB)^{2/3}\tau$ and interchange the order of integration to give

$$P_m^{(2)} \sim \frac{z^*\bar{S}(z^*)}{mB} \frac{e^{-i\bar{\phi}_s^*(mB)^{2/3}}}{2\pi} \int_{-\infty}^{\infty} \exp\left[\frac{imB\tau^3}{6}\right] \int_{-\frac{1}{2}}^{\frac{1}{2}} \exp[-i(mB)^{2/3}x(\tau + \alpha_s)]dx\, d\tau. \tag{3.4.37}$$

The inner integral in (3.4.37), I_x say, can be evaluated as

$$I_x = \frac{-i}{(mB)^{2/3}(\tau+\alpha_s)} \left\{ \exp\left[\frac{i}{2}(mB)^{2/3}(\tau+\alpha_s)\right] - \exp\left[\frac{-i}{2}(mB)^{2/3}(\tau+\alpha_s)\right] \right\} \tag{3.4.38}$$

whence

$$P_m^{(2)} \sim \sum_{\pm} \pm \frac{z^*\bar{S}(z^*)}{mB} \frac{e^{-i\bar{\phi}_s^*}}{2\pi i} \int_{-\infty}^{\infty} \exp\left[\frac{imB\tau^3}{6} \pm \frac{i(mB)^{2/3}(\tau+\alpha_s)}{2}\right] \frac{d\tau}{(\tau+\alpha_s)} \tag{3.4.39}$$

where the ± terms are to be summed: We now make the substitution

$$\tau = (mB)^{-1/6} T, \tag{3.4.40}$$

so that (3.4.39) becomes

$$P_m^{(2)} \sim \pm \frac{z^*\bar{S}(z^*)}{mB} \exp\left[-i\bar{\phi}_s^* \pm \frac{i(mB)^{2/3}}{2}\alpha_s\right] \frac{1}{2\pi i} \int_{-\infty}^{\infty} \exp\left[\frac{i(mB)^{1/2}}{2}\left(\frac{T^3}{3} \pm T\right)\right] \frac{dT}{[T+(mB)^{1/6}\alpha_s]} \cdot \tag{3.4.41}$$

Now we define the functions

$$f_{\pm}(T) = \frac{T^3}{3} \pm T \ , \tag{3.4.42}$$

which have derivatives

$$f'_{\pm}(T) = T^2 \pm 1 \ . \tag{3.4.43}$$

The function f_- thus has stationary points at $T = \pm 1$ and the function f_+ has no stationary points. We will therefore evaluate (3.4.41) by the method of stationary phase, considering only the contribution from f_- and thereby obtaining

$$P_m^{(2)} \sim - \frac{z^*\bar{S}(z^*)}{mB} \exp\left[-i\bar{\phi}_s^* - \frac{i(mB)^{2/3}}{2}\alpha_s\right] \frac{1}{2\pi i}$$

$$\int_{-\infty}^{\infty} \left\{\exp\left[i(mB)^{1/2}\left\{\frac{(T-1)^2}{2} - \frac{1}{3}\right\}\right] - \exp\left[-i(mB)^{1/2}\left\{\frac{(T+1)^2}{2} - \frac{1}{3}\right\}\right]\right\} dT$$

$$= \frac{z^*\bar{S}(z^*)}{mB}\left(\frac{2}{\pi}\right)^{1/2}(mB)^{-1/4} \sin\left[\frac{(mB)^{1/2}}{3} - \frac{\pi}{4}\right] \exp\left[-i\bar{\phi}_s^* - \frac{i(mB)^{2/3}}{2}\alpha_s\right] . \tag{3.4.44}$$

This suggests that the effect of blade sweep is to reduce the acoustic pressure generated by the transonic region of the blade by $O[(mB)^{-1/4}]$. However, in order to confirm this we must first consider the additional contribution to $P_m^{(2)}$ from the singularity at $T = -(mB)^{1/6}\alpha_s$ in (3.4.41). We use the substitutions

$$\left.\begin{aligned} u &= T + \gamma_s \\ \gamma_s &= (mB)^{1/6}\alpha_s \end{aligned}\right\} \tag{3.4.45}$$

in (3.4.41), whence

$$P_m^{(2)} \sim \frac{z^*\bar{S}(z^*)}{mB} \exp\left\{-i\bar{\phi}_s^* - \frac{imB\alpha_s^3}{6}\right\} (I_+ + I_-) \tag{3.4.46}$$

where the integrals $I_{\pm}$ are given by

$$I_{\pm} = \pm \frac{1}{2\pi i} \int_{-\infty}^{\infty} \exp\left\{ \frac{i(mB)^{1/2}}{2} \left[\frac{u^3}{3} - \gamma_s u^2 + (\gamma_s^2 \pm 1)u \right] \right\} \frac{du}{u} , \qquad (3.4.47)$$

Since we are considering only the contribution from u = 0 we write

$$(\gamma_s^2 \pm 1)u - \gamma_s u^2 + \frac{u^3}{3} = (\gamma_s^2 \pm 1)\omega . \qquad (3.4.48)$$

The inverse of (3.4.48) is given by

$$u = \omega + \frac{\gamma_s}{(\gamma_s^2 \pm 1)} \omega^2 + O(\omega^3) . \qquad (3.4.49)$$

The integrals (3.4.47) then reduce to

$$I_{\pm} \sim \pm \frac{1}{2\pi i} \int_{-\infty}^{\infty} \exp\left[\frac{i(mB)^{1/2}}{2} (\gamma_s^2 \pm 1)\omega \right] \left[\frac{1}{\omega} + \frac{\gamma_s}{(\gamma_s^2 \pm 1)} + O(\omega) \right] d\omega$$

$$= \pm \frac{1}{2} \operatorname{sgn}(\gamma_s^2 \pm 1), \quad \gamma_s^2 \neq 1$$

so that

$$I_+ + I_- = H(1 - \gamma_s^2), \quad \gamma_s^2 \neq 1 . \qquad (3.4.50)$$

This shows that the contribution from the singularity is zero for $|\gamma_s| > 1$ or $|\alpha_s| > (mB)^{-1/6}$ so that the acoustic pressure is given by (3.4.44) to leading order. However, when there is little sweep, corresponding to $|\alpha_s| < (mB)^{-1/6}$, the leading order term is given by (3.4.46) with $(I_+ + I_-) = 1$; this differs from the straight bladed result (3.4.28) only by a phase factor. It would therefore seem appropriate to ensure that $|\alpha_s| > (mB)^{-1/6}$ in propfan designs.

3.4.3 The Supersonic Regime

In the supersonic operating regime the acoustic pressure generated by a straight-bladed propeller is given by

$$P_m^{(3)} \sim \int_{z_+}^{1} S(z) J_{mB}(mB \frac{z}{z^*}) dz \ . \qquad (3.4.51)$$

On using the asymptotic approximation for the Bessel function given by (3.4.15) we obtain

$$P_m^{(3)} \sim \int_{\beta_1}^{\beta_2} S(z^*\sec\beta) \left[\frac{2}{\pi mB\tan\beta}\right]^{\frac{1}{2}} \cos[mB(\tan\beta-\beta) - \pi/4] z^*\sec\beta\tan\beta \, d\beta, \qquad (3.4.52)$$

where

$$\beta_1 = \sec^{-1}\left[1 + \frac{(mB)^{-1/3}}{2}\right] \quad , \quad \beta_2 = \sec^{-1}\left[\frac{1}{z^*}\right] \qquad (3.4.53)$$

and we have used the substitution

$$z = z^* \sec\beta \ . \tag{3.4.54}$$

Since mB is large and the dominant term is purely oscillatory we will evaluate (3.4.52) by the method of stationary phase. Define

$$\left.\begin{aligned} f(\beta) &= \tan\beta - \beta \\ f'(\beta) &= \sec^2\beta - 1 = \tan^2\beta, \end{aligned}\right\} \tag{3.4.55}$$

so that a stationary point exists at $\beta = 0$, corresponding to $z = z^*$. This point, however, lies <u>outside</u> the region of integration so that the leading order terms in (3.4.52) are given by the contributions from the end points, and we obtain

$$P_m^{(3)} \sim \left\{ \left(\frac{2}{\pi mB \tan\beta} \right)^{\frac{1}{2}} \frac{z^* S(z^* \sec\beta)}{mB \sin\beta} \sin[mB(\tan\beta - \beta) - \pi/4] \right\}_{\beta_1}^{\beta_2} + O[(mB)^{-2}]. \tag{3.4.56}$$

It therefore appears, superficially, that the leading order term is $O[(mB)^{-3/2}]$. However, from (3.4.53) we note that, since mB is large,

$$\beta_1 \sim (mB)^{-1/6} \tag{3.4.57}$$

so that

$$P_m^{(3)} \sim - \left[\frac{2}{\pi (mB)^{5/6}} \right]^{1/2} \frac{z^* \, \bar{S}(z_+)}{(mB)^{5/6}} \sin\left[\frac{(mB)^{1/2}}{3} - \frac{\pi}{4} \right]$$

and since $S(z_+) = S(z^*) + O[(mR)^{-1/3}]$ we obtain, to leading order,

$$P_m^{(3)} \sim -\left(\frac{2}{\pi}\right)^{1/2} \frac{1}{(mB)^{1/4}} \sin\left[\frac{(mB)^{1/2}}{3} - \frac{\pi}{4}\right] \frac{z^*\bar{S}(z^*)}{mB} \qquad (3.4.58)$$

which is $O[(mB)^{-1/4}]$ times the leading order result from the transonic blade region. In fact (3.4.58) cancels identically with the cosine term in (3.4.28). The leading order approximation is therefore provided by the contribution from $\beta = \beta_2$ which is

$$P_m^{(3)} \sim \left(\frac{2}{\pi mB\tan\beta_2}\right)^{1/2} \frac{z^*S(1)}{mB\sin\beta_2} \sin[mB(\tan\beta_2 - \beta_2) - \pi/4]. \qquad (3.4.59)$$

When (3.4.59), representing an edge effect, is added on to the leading term in (3.4.28) (cf. (3.3.5)) we find that the asymptotics agree remarkably well with full numerical calculations. This is shown quite clearly in Figure 3.7, an updated version of Figure 3.4.

We now consider the effect of blade sweep on the supersonic portion of the blade. We linearise the sweep phase term $\bar{\phi}_s$ about $z = z_+$ so that

$$\bar{\phi}_s = \bar{\phi}_s^+ + \alpha^+\left(\frac{z}{z^+} - 1\right)mB \qquad (3.4.60)$$

where the definitions of $\bar{\phi}_s^+$ and α^+ are analogous to those given for $\bar{\phi}_s^*$ and α_s in (3.4.31) and (3.4.32). The acoustic pressure is then given by

$$P_m^{(3)} \sim e^{-i\bar{\phi}_s^+} \int_{z_+}^{1} S(z)\left(\frac{2}{\pi mB\tan\beta}\right)^{1/2} \cos[mB(\tan\beta - \beta) - \pi/4\,] \; e^{-i\alpha^+ mB(z/z^+ - 1)}\, dz \; . \qquad (3.4.61)$$

We use the substitution (3.4.54) so that, from (3.4.19),

$$\frac{z}{z^+} = \frac{\sec\beta}{\left[1 + \frac{(mB)^{-1/3}}{2}\right]} \sim \left[1 - \frac{(mB)^{-1/3}}{2}\right]\sec\beta \ , \qquad (3.4.62)$$

and we therefore define

$$\tilde{\alpha}^+ = \alpha^+\left[1 - \frac{(mB)^{-1/3}}{2}\right] \qquad (3.4.63)$$

so that (3.4.61) becomes

$$P_m^{(3)} \sim \frac{z^* e^{-i\bar{\phi}_s^{-+} + i\alpha^+ mB}}{(2\pi mB)^{1/2}} \int_{\beta_1}^{\beta_2} S(z)\sec\beta \tan^{1/2}\beta e^{imB f_{\pm}(\beta) \mp \pi/4} \qquad (3.4.64)$$

where the functions $f_{\pm}(\beta)$ are defined by

$$f_{\pm}(\beta) = \pm(\tan\beta - \beta) - \tilde{\alpha}^+ \sec\beta \qquad (3.4.65)$$

and have derivatives

$$\left.\begin{aligned} f'_{\pm}(\beta) &= \pm\tan^2\beta - \tilde{\alpha}^{+}\ \sec\beta\ \tan\beta\ , \\ f''_{\pm}(\beta) &= \pm 2\tan\beta\ \sec^2\beta - \tilde{\alpha}^{+}(\sec\beta\ \tan^2\beta + \sec^3\beta). \end{aligned}\right\} \qquad (3.4.66)$$

There are therefore stationary points at $\beta = 0$, which lies outside the range of integration, or

$$\tilde{\beta} = \pm\ \sin^{-1}\tilde{\alpha}^{+}\ . \qquad (3.4.67)$$

Note that if $\tilde{\beta}$ is negative then it lies outside the range of integration. Therefore only one of the values given by (3.4.67) represents a valid stationary point, according as $\tilde{\alpha}_{+}$ is positive or negative. Without loss of generality we will suppose that $\tilde{\alpha}^{+}$ is positive. We consider two cases. First suppose that $\beta_1 < \tilde{\beta} < \beta_2$ so that the stationary point lies in the range of integration. The function $f_{+}(\beta)$ is expanded about $\beta = \tilde{\beta}$ as

$$f_{+}(\beta) \sim -\tilde{\beta} + (\beta - \tilde{\beta})^2\ \frac{\tan\tilde{\beta}}{2} \qquad (3.4.68)$$

and, following the standard stationary phase procedure,

$$P_m^{(3)} \sim \frac{z^*S(\tilde{z})}{(2\pi mB)^{1/2}}\ e^{-i\tilde{\phi}_s^{+}+imB(\alpha^{+}-\tilde{\beta})-i\pi/4}\ \sec\tilde{\beta}\ \tan^{1/2}\tilde{\beta}\int_{-\infty}^{\infty} e^{imB(\beta-\tilde{\beta})^2\tan\tilde{\beta}/2}\,d\beta$$

where $\tilde{z}$ is the value of z at $\beta = \tilde{\beta}$, $\tilde{z} = z^*\sec\tilde{\beta}$. On evaluating the above integral we obtain

$$P_m^{(3)} \sim \frac{\tilde{z}S(\tilde{z})}{mB} e^{-i\tilde{\phi}_s^{-+} + imB(\alpha^+ - \tilde{\beta})} . \tag{3.4.69}$$

We now consider the case where $\tilde{\beta} < \beta_1$ or $\tilde{\beta} > \beta_2$. Then the integral (3.4.64) is dominated by contributions from the endpoints β_1 and β_2. However, on using (3.4.57) we find that the leading order contribution comes from β_1 and is

$$P_m^{(3)} \sim - \frac{e^{-i\phi_s^{-+} + imB\alpha^+ + imBf_+(\beta_1)}}{(2\pi)^{1/2}\alpha^+(mB)^{5/12}} \frac{z^*S(z^*)}{mB} \tag{3.4.70}$$

which is smaller than (3.4.69) by a factor of $O[(mB)^{-5/12}]$. Note that in (3.4.70) we have assumed that α^+ is not small. For α^+ small the multiplicative factor is $O[(mB)^{-1/4}]$.

The results obtained here show the remarkable fact that the inclusion of sweep can raise the noise level, generated by the supersonic portion of the blade, by $O[(mB)^{1/2}]$ through the introduction of a stationary phase point. This reduces the rather effective cancellation mechanism that was already previously present. In order to avoid this situation we require $\tilde{\beta} < \beta_1$ or $\tilde{\beta} > \beta_2$. From (3.4.57) and (3.4.67), $\tilde{\beta} < \beta_1$ corresponds to $\alpha^+ < (mB)^{-1/6}$. As α^+ is approximately equal to α_s, since $(z^+ - z^*) \sim O[(mB)^{-1/3}]$, this requirement conflicts with that

specified in section 3.4.2 for the transonic regime. We must therefore choose $\tilde{\beta} > \beta_2$ which, from (3.4.53) and (3.4.67), corresponds to

$$\alpha^+ > \sin(\cos^{-1}z^*) = (1 - z^{*2})^{\frac{1}{2}}. \qquad (3.4.71)$$

On neglecting terms of $O[(mB)^{-1/3}]$ we can replace α^+ with α_s which is defined by (3.4.32). The requirement (3.4.71) for effective cancellation can then be written as

$$M_t \frac{(\tan\Lambda^* - 2z^*M_t^2 s^*/D)}{(1 - M_x\cos\theta)} > (1 - z^{*2})^{\frac{1}{2}}. \qquad (3.4.72)$$

APPENDIX 3.1

Harmonic Series for Straight-Bladed, Chordwise Compact, Supersonic Propellers

On neglecting constant factors we find, from (2.2.28), (2.3.7), (3.2.2) and (3.3.5), that the waveform generated by a straight-bladed propeller operating at supersonic conditions, where noncompactness effects are neglected for the present, is of the form

$$p(t) \sim \sum_{m=-\infty}^{\infty} \exp\left\{ imB \left[\frac{\Omega(t-r_o/c_o)}{(1-M_x\cos\theta)} + \frac{\pi}{2} - \psi_o \right] \right\} \frac{S(z^*)}{|mB|} . \qquad (A3.1.1)$$

We now consider three cases. First, $S(z^*)$ is independent of mB. Second, corresponding to the steady loading noise source, take $S(z^*) \sim mB$. Third, corresponding to the thickness noise source, let $S(z^*) \sim (mB)^2$.

Define the function

$$F(\xi) = B^{\eta}\xi^{\eta}\,\mathrm{sgn}(\xi)\exp[i\xi B(\Omega_D\tau + \alpha)] \qquad (A3.1.2)$$

where Ω_D represents the Doppler shifted angular frequency $\Omega/(1-M_x\cos\theta)$, τ the retarded time $(t - r_o/c_o)$ and $\alpha = \pi/2 - \psi_o$. The parameter η can take the values -1, 0 and 1 corresponding, respectively, to $S(z^*) \sim 1$, $S(z^*) \sim mB$ and $S(z^*) \sim (mB)^2$. The Fourier transform of $F(\xi)$ is, in the notation of Lighthill (1958),

$$G(\chi) = \int_{-\infty}^{\infty} F(\xi)\ \exp(-i2\pi\ \xi\ \chi)d\xi$$

$$B^{\eta} \int_{-\infty}^{\infty} \xi^{\eta} \mathrm{sgn}(\xi) \exp\left\{ i2\pi\xi \left[\frac{B}{2\pi}(\Omega_D \tau + \alpha) - \chi \right] \right\} d\xi \ . \qquad \text{(A3.1.3)}$$

The Fourier transforms are, for the three cases,

$$G(\chi) = \frac{-2}{B} \ell n(\Omega_D \tau + \alpha - \frac{2\pi\chi}{B}), \quad \eta = -1; \qquad \text{(A3.1.4)}$$

$$G(\chi) = \frac{2i}{B}(\Omega_D \tau + \alpha - \frac{2\pi\chi}{B})^{-1}, \quad \eta = 0; \qquad \text{(A3.1.5)}$$

$$G(\chi) = \frac{-2}{B}(\Omega_D \tau + \alpha - \frac{2\pi\chi}{B})^{-2}, \quad \eta = -1. \qquad \text{(A3.1.6)}$$

We now use Poisson's summation formula (this is given as Theorem 28 in Lighthill (1958)) which states that

$$\sum_{m=-\infty}^{\infty} F(m) = \sum_{n=-\infty}^{\infty} G(n) \ . \qquad \text{(A3.1.7)}$$

The waveforms generated in the three cases are then

$$p(t) \sim \frac{-2}{B} \sum_{n=-\infty}^{\infty} \ell n(\Omega_D \tau + \alpha - \frac{2\pi n}{B}), \quad \text{for } S(z^*) \sim 1; \qquad \text{(A3.1.8)}$$

$$p(t) \sim \frac{2i}{B} \sum_{n=-\infty}^{\infty} \left(\Omega_D \tau + \alpha - \frac{2\pi n}{B}\right)^{-1}, \quad \text{for } S(z^*) \sim mB; \tag{A3.1.9}$$

$$p(t) \sim \frac{-2}{B} \sum_{n=-\infty}^{\infty} \left(\Omega_D \tau + \alpha - \frac{2\pi n}{B}\right)^{-2}, \quad \text{for } S(z^*) \sim (mB)^2. \tag{A3.1.10}$$

In each case, each of summed singularities corresponds to the passage of a blade.

APPENDIX 3.2

Harmonic Series for Chordwise Noncompact, Supersonic Propellers

On neglecting constant factors we can, from (3.3.14), write the acoustic waveform as

$$p(t) \sim \sum_{m=-\infty}^{\infty} \frac{S(z^*)}{|mB|^{\nu_L+2}} \exp[imB(\Omega_D\tau + \alpha^*) - i(\nu_L+1)\frac{\pi}{2}\,\mathrm{sgn}(m)] \qquad (A3.2.1)$$

where Ω_D, τ are as defined in appendix 3.1 and $\alpha^* = k_x^*/2mB + \pi/2 - \psi_o$.

We consider first the loading noise source with $-1 < \nu_L < 0$ and define the function

$$F(\xi) = \left\{\cos\left[(\nu_L+1)\frac{\pi}{2}\right] - \mathrm{sgn}(\xi)\sin\left[(\nu_L+1)\frac{\pi}{2}\right]\right\} |\xi|^{-\nu_L-1} \mathrm{sgn}(\xi)\, e^{i\xi B(\Omega_D\tau+\alpha^*)}.$$

(A3.2.2)

We now proceed as in appendix 3.1 and obtain, by Poisson's summation formula,

$$p(t) \sim -2i(-\nu_L-1)!B^{\nu_L} \sum_{m=-\infty}^{\infty} |\Omega_D\tau + \alpha^* - 2\pi m/B|^{\nu_L}$$

(A3.2.3)

$$\left\{\sin(\nu_L\frac{\pi}{2})\cos[(\nu_L+1)\frac{\pi}{2}]\mathrm{sgn}(\Omega_D\tau + \alpha^* - \frac{2\pi m}{B}) + \sin[(\nu_L+1)\frac{\pi}{2}]\cos(\frac{\nu_L\pi}{2})\right\}.$$

The waveform thus contains weak algebraic singularities. Similar analyses for $\nu_L = 0$ and $\nu_L = 1$ produce the real time waveforms

$$p(t) \sim 2i \sum_{m=-\infty}^{\infty} \ell n\left|\Omega_D \tau + \alpha^* - \frac{2\pi m}{B}\right| \tag{A3.2.4}$$

and

$$p(t) \sim 2iB \sum_{m=-\infty}^{\infty} \left(\Omega_D \tau + \alpha^* - \frac{2\pi m}{B}\right) \left[\ell n\left(\frac{B}{2\pi}\right) + \ell n\left(\Omega_D \tau + \alpha^* - \frac{2\pi m}{B}\right)\right], \tag{A3.2.5}$$

respectively. The waveform in (A3.2.4), which is generated by a loading function which is finite at the leading edge, contains periodic logarithmic singularities. In (A3.2.5), representing the waveform generated by a loading function which is zero at the leading edge, the singularities have effectively been removed.

In the case of the thickness noise source we define the function

$$F(\xi) = \left\{\cos\left[(\nu_L+1)\frac{\pi}{2}\right] - i\ \mathrm{sgn}(\xi)\sin\left[(\nu_L+1)\frac{\pi}{2}\right]\right\} |\xi|^{-\nu_L} e^{i\xi B(\Omega_D \tau+\alpha^*)}. \tag{A3.2.6}$$

Then, for $0 < \nu_L < 1$, corresponding to an airfoil with a blunt leading edge, we obtain the real time waveform

$$p(t) \sim 2(-\nu_L)!\, B^{\nu_L-1} \sum_{m=-\infty}^{\infty} \left|\Omega_D\tau + \alpha^* - \frac{2\pi m}{B}\right|^{\nu_L-1}$$

(A3.2.7)

$$\left\{\cos\left[(1+\nu_L)\frac{\pi}{2}\right]\cos\left[(1-\nu_L)\frac{\pi}{2}\right] + \sin\left[(1+\nu_L)\frac{\pi}{2}\right]\sin\left[(1-\nu_L)\frac{\pi}{2}\right]\mathrm{sgn}(\Omega_D\tau + \alpha^* - \frac{2\pi m}{B})\right\}$$

which is of the same form as (A3.2.3) and contains weak algebraic singularities. For $\nu_L = 1$, corresponding to an airfoil with a wedge shaped leading edge, we obtain the waveform

$$p(t) \sim 2 \sum_{m=-\infty}^{\infty} \ell n\left|\Omega_D\tau + \alpha^* - \frac{2\pi m}{B}\right| \qquad \text{(A3.2.8)}$$

which is, basically, identical to (A3.2.4) and contains logarithmic singularities. For $\nu_L > 1$, corresponding to an airfoil with a cusp shaped leading edge, the waveform is given by (A3.2.7) which, since $\nu_L - 1 > 0$, now contains no singularities or discontinuities (except in pressure derivatives).

APPENDIX 3.3

Asymptotic Overlap of Bessel Function Approximations

Here we consider the two Bessel function approximations (3.4.5) and (3.4.10) and show that they have a common limit. The upper limit of (3.4.5) is obtained when $\sigma \to 1-$ or, from (3.4.1), when $\beta \to 0+$. Then

$$\tanh\beta \sim \beta - \frac{\beta^3}{3} + O(\beta^5) \qquad \text{(A3.3.1)}$$

so that the leading order approximation to (3.4.5) is

$$J_\nu(\nu\sigma) \sim \frac{\exp(-\nu\beta^3/3)}{(2\pi\nu\beta)^{1/2}}. \qquad \text{(A3.3.2)}$$

Next we consider the lower limit of (3.4.10) which is obtained when $\sigma \to 0+$. The argument of the Airy function in (3.4.10) is then large and positive and we can therefore use the asymptotic form given in section 10.4.59 of Abramowitz & Stegun (1965). There follows, since $1 - \sigma \sim \beta^2/2$,

$$J_\nu(\nu\sigma) \sim \frac{2^{1/3}}{\nu^{1/3}} \frac{1}{2\pi^{1/2}\left[2^{1/3}\nu^{2/3}\ \frac{\beta^2}{2}\right]^{1/4}} \exp\left\{-\frac{2}{3}\left[2^{1/3}\nu^{2/3}\ \frac{\beta^2}{2}\right]^{3/2}\right\}$$

$$= \frac{1}{(2\pi\nu\beta)^{1/2}} \exp\left(-\frac{1}{3}\nu\beta^3\right)$$

in agreement with (A3.3.2).

The Bessel function approximations for $\sigma > 1$ are given by (3.4.10) and (3.4.15). We consider the limit of (3.4.15) as $\sigma \to 1+$, i.e. as $\lambda \to 0+$. Then

$$\tan\lambda \sim \lambda + \frac{\lambda^3}{3} + O(\lambda^5) \qquad \text{(A3.3.3)}$$

and (3.4.15) reduces to

$$J_\nu(\nu\sigma) \sim \left(\frac{2}{\pi\nu\lambda}\right)^{1/2} \cos\left(\frac{\nu\lambda^3}{3} - \frac{\pi}{4}\right) . \qquad \text{(A3.3.4)}$$

Next we consider the limit of (3.4.10) as $\sigma \to +\infty$ with $1 - \sigma = -\lambda^2/2$. The argument of the Airy function is then large and negative and we can use the asymptotic form given in section 10.4.60 of Abramowitz & Stegun (1965) to otbain

$$J_\nu(\nu\sigma) \sim \frac{2^{1/3}}{\nu^{1/3}} \frac{1}{\pi^{1/2}\left(2^{1/3}\nu^{2/3}\,\frac{\lambda^2}{2}\right)^{1/4}} \sin\left[\frac{2}{3}\left(2^{1/3}\nu^{2/3}\,\frac{\lambda^2}{2}\right)^{3/2} + \frac{\pi}{4}\right]$$

$$= \left(\frac{2}{\pi\nu\lambda}\right)^{1/2} \sin\left(\frac{\nu\lambda^3}{3} + \frac{\pi}{4}\right) ,$$

which agrees with (A3.3.4). This confirms that we have complementary asymptotic expansions (3.4.5) and (3.4.10) for $\sigma < 1$, (3.4.15) and

(3.4.10) for $\sigma > 1$, and that these match to leading order in the strict sense of matched expansion theory (see Van Dyke 1975 p.90). Existence of the overlap is necessary to ensure that our sequence of approximations does in fact cover all values of σ.

4. COUNTER-ROTATION PROPELLER NOISE

4.1 Introduction

We now turn our attention to counter-rotation propellers. The earliest work on this topic appears to be that of Hubbard (1948) who complemented his experiments with an analytical description of rotor-rotor acoustic interference effects which, he showed, produce lobular azimuthal directivities. Following this there seems to have been no published work specifically aimed at counter-rotation propeller noise until the 1980's. However, Young (1951) and Daly (1958) carried out experiments on axial flow fans and showed that counter-rotation configurations were clearly noisier than single rotation configurations. In addition, experiments on open rotor aerodynamic interactions were conducted by Roberts & Beranek (1952) who compared data from a tractor propeller (single-rotation) with data from a pusher propeller (a single-rotation propeller with an upstream pylon): it was found that the pusher configuration produced more uniform overall noise directivity patterns than the tractor configuration and that there was no benefit to be obtained in the pusher configuration by increasing blade numbers - in contrast to the well-known benefits for a tractor configuration.

More recently Hanson (1985a) has provided a frequency domain description of the noise generated by the steady and unsteady forces on the blades of a counter-rotation propeller, based on the application of the acoustic analogy to propellers (see Hanson (1983)). In addition to Hanson's analytical work there has been a substantial amount of experimental work. Block at N.A.S.A. Langley has investigated the noise of both pusher propellers (see Block (1985) and Block & Gentry (1986)) and counter-rotation propellers (see Block (1986a, 1986b) and Block et al. (1986)), concentrating mainly on the differences in directivity compared

with single-rotation propellers. Fujii et al. (1986) and Metzger & Brown (1987) have conducted parametric studies on counter-rotation propellers, where they varied tip speeds (of both front and rear rows independently) and rotor-rotor spacing. Experiments on a counter-rotation propeller at an angle of attack have been carried out by Dittmar (1986) and the effects of a cropped rear blade row were investigated by Dittmar & Stang (1987).

In the current chapter we will derive far-field acoustic radiation formulae for the sound generated by aerodynamic interactions on a counter-rotation propeller in terms of the unsteady forces. These fluctuating forces are present on both upstream and downstream blade rows due to the interaction of each blade row with the unsteady velocity field generated by the adjacent blade row. For the present we take that velocity field to be given in the form of a harmonic series. The precise Fourier coefficients, and the resultant unsteady blade forces, will be calculated in chapters 5 to 7 for the different types of aerodynamic interaction.

The frameworks is entirely general, and allows arbitrary (and differential) blade numbers and rotational speeds. The resulting formulae can therefore be applied either to a counter-rotation propeller or to the pylon-rotor interactions on a single-rotation pusher propeller (the latter case is effected by setting the forward blade number to be 1 and the forward row rotational speed to be zero).

Finally, we show how the asymptotic approximation techniques described in chapter 3 can be simply extended for application to a counter-rotation propeller. In this case the savings in CPU time are particularly important because, at the low tip speeds typical of community noise conditions, up to 5000 combination tones can be generated in the

audible frequency range. Since calculations are required at a range of observer positions and for a number of sources the computation time for a wholly numerical calculation can be horrendous.

4.2 Downstream Interactions

In this section we discuss the interactions between the downstream blade row and the distorted flow generated by the upstream blade row. The blade row configurations are shown in Figure 4.1. The analysis is similar to that used in chapter 2 and we will therefore use the same notation, except that the subscripts 1 and 2 are introduced to denote association with the forward or rearward blade row respectively.

We start by taking the distorted velocity field downstream of the forward blade row and writing it in the Fourier series form*

$$\underline{u} = \sum_{n_1=-\infty}^{\infty} \underline{u}_{n_1} e^{in_1 B_1(\Omega_1 \tau + \phi)} \qquad (4.2.1)$$

where the harmonic velocity components $\underline{u}_{n_1}$ are complex. We now define the unsteady lift coefficients $C_L^{(n_1)}$ in terms of the response of a blade section to a single harmonic gust. A gust

$$\underline{u}_{n_1} e^{in_1 B_1(\Omega_1 \tau + \phi)} = \underline{u}_{n_1} e^{in_1 B_1(\Omega_1 + \Omega_2)\tau + in_1 B_1 \phi_2}, \qquad (4.2.2)$$

where ϕ_2 is the azimuthal angle measured in a coordinate system fixed

---

FOOTNOTE

* The distorted flow fields are discussed in more detail in chapters 5 to 7.

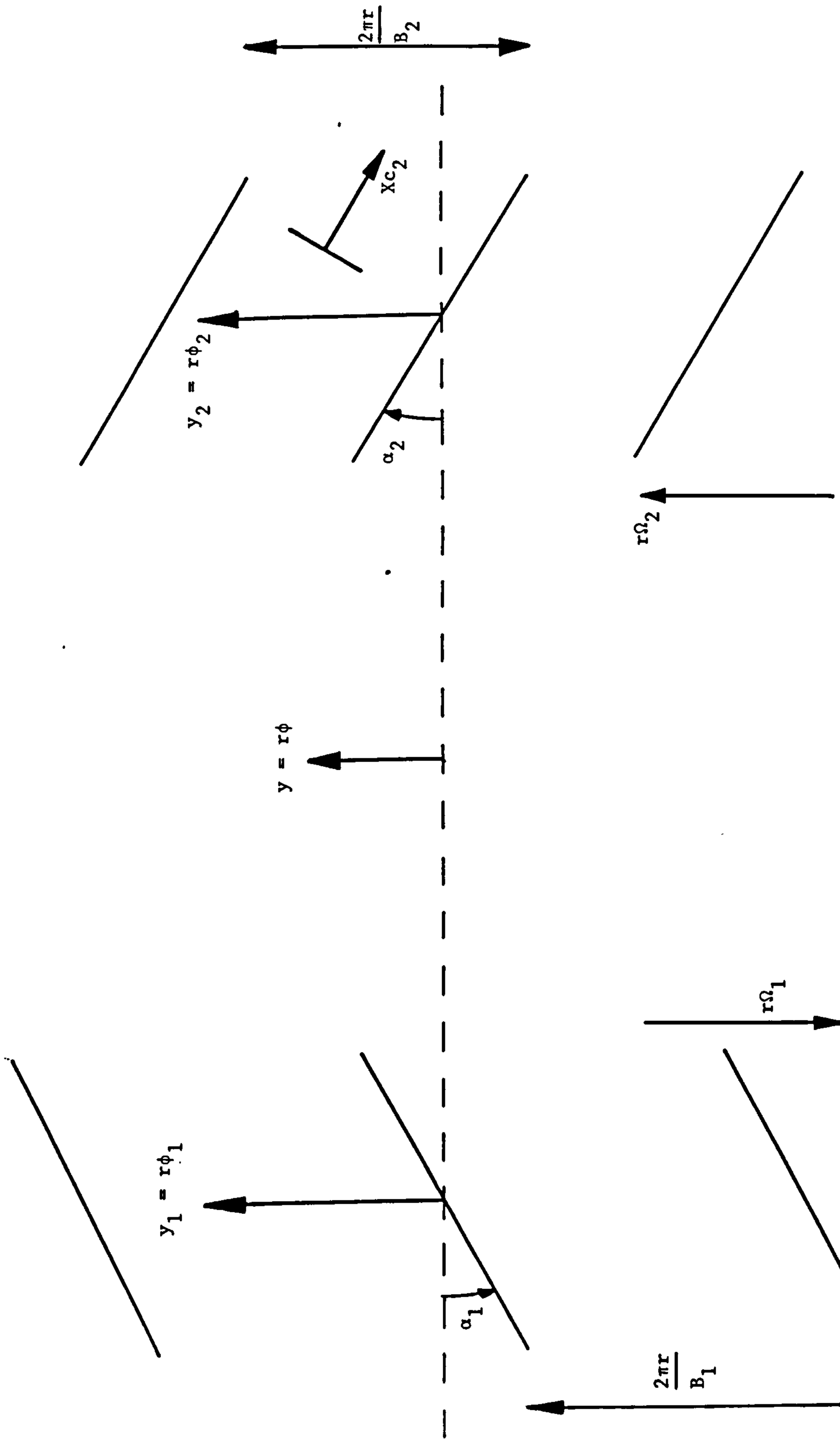

Figure 4.1 Front and rear blade row configurations (at constant radius) on a counter-rotation propeller.

with respect to the rear blade row†, generates an unsteady force

$$dL = \frac{1}{2}\rho U_{r_2}^2 C_L^{(n_1)} f_L^{(n_1)}(X) e^{in_1B_1(\Omega_1+\Omega_2)\tau + in_1B_1\phi_2} drcdX, \tag{4.2.3}$$

where $f_L^{(n_1)}(X)$ is a shape function normalised according to

$$\int_{-\frac{1}{2}}^{\frac{1}{2}} f_L^{(n_1)}(X)\, dX = 1 . \tag{4.2.4}$$

Here $C_L^{(n_1)}$ and $f_L^{(n_1)}$ are both complex. The total elementary force exerted on the fluid by the downstream blades is then given by

$$dF = -dL = -\frac{1}{2}\rho U_{r_2}^2 drcdX \sum_{n_1=-\infty}^{\infty} C_L^{(n_1)} f_L^{(n_1)} e^{in_1B_1(\Omega_1\tau+\phi)} \sum_{n_2=-\infty}^{\infty} \delta\left[\phi-\Omega_2\tau+\frac{2\pi n_2}{B_2}\right]$$

$$= -\frac{\rho U_{r_2}^2 B_2}{4\pi} drcdX \sum_{n_1,n_2=-\infty}^{\infty} C_L^{(n_1)} f_L^{(n_1)} e^{i(n_1B_1\Omega_1+n_2B_2\Omega_2)\tau+i(n_1B_1-n_2B_2)\phi} \tag{4.2.5}$$

where we have followed the approach used in chapter 2. The components of force on the fluid due to a blade element are given by (cf. (2.2.11))

FOOTNOTE

† Specifically, we select $\phi_2 = \phi = 0$ at $\tau = 0$.

$$dF[\sin\alpha_2,\ \cos\alpha_2\ \sin(\phi-\psi_o-\psi),\ -\cos\alpha_2\ \cos(\phi-\psi_o-\psi)]\ , \qquad (4.2.6)$$

where ψ and ψ_o are defined in section 2.2 (see Figure 2.2 and (2.2.14)).

We now proceed exactly as in section 2.2 and, after some manipulation and an analytical integration over ϕ, we obtain the far-field acoustic pressure as

$$p = \sum_{n_1=-\infty}^{\infty} \sum_{n_2=-\infty}^{\infty} \frac{i\rho c_o^2 B_2}{8\pi \frac{r_o}{D}(1-M_x\cos\theta)} \exp\left\{ i\frac{(n_1B_1\Omega_1+n_2B_2\Omega_2)}{(1-M_x\cos\theta)} \left[t - \frac{r_o}{c_o} \right] \right.$$

$$\left. + i(n_1B_1-n_2B_2)(\psi_o + \frac{\pi}{2}) \right\} \qquad (4.2.7)$$

$$\int_{z_o}^{1} M_{r_2}^2 e^{-i\phi_s} J_{n_1B_1-n_2B_2}\left[\frac{(n_1B_1M_{t_1}+n_2B_2M_{t_2})}{(1-M_x\cos\theta)} z\ \sin\theta \right] k_y \frac{C_L^{(n_1)}}{2} \Psi_L^{(n_1)}(k_x)dz$$

where, in order to compare our result with that of Hanson (1985a), we have defined a phase term exponent

$$\phi_s = \frac{2}{M_{r_2}} \left[\frac{(n_1B_1M_{t_1}+n_2B_2M_{t_2})}{(1-M_x\cos\theta)} - n_1B_1(M_{t_1} + M_{t_2}) \right] \frac{s_2}{D}\ , \qquad (4.2.8)$$

nondimensional wavenumbers

$$k_x = \frac{2}{M_{r_2}}\left[\frac{(n_1B_1M_{t_1}+n_2B_2M_{t_2})}{(1-M_x\cos\theta)} - n_1B_1(M_{t_1}+M_{t_2})\right]\frac{c_2}{D} \quad , \tag{4.2.9}$$

$$k_y = \frac{-2}{M_{r_2}}\left[\frac{(n_1B_1M_{t_1}+n_2B_2M_{t_2})}{(1-M_x\cos\theta)}M_{t_2}z\cos\theta + (n_1B_1-n_2B_2)\frac{M_x}{z}\right]\frac{c_2}{D} \quad , \tag{4.2.10}$$

and a noncompactness factor

$$\Psi_L^{(n_1)}(k_x) = \int_{-\frac{1}{2}}^{\frac{1}{2}} f_L^{(n_1)}(X)e^{-ik_xX}\,dX \quad . \tag{4.2.11}$$

Equation (4.2.7) is the complex conjugate of Hanson's (1985a) result since, as in chapter 2, we chose a time dependence $e^{i\omega t}$ and Hanson chose $e^{-i\omega t}$.

4.3 Upstream Interactions

In this section we discuss the interactions between the upstream blade row and the distorted flow generated by the downstream blade row. The analysis is identical to that in section 4.2 so that, by writing the distorted velocity field upstream of the rear blade row in Fourier series form, we obtain

$$p = \sum_{n_1=-\infty}^{\infty} \sum_{n_2=-\infty}^{\infty} \frac{-i\rho c_o^2 B_1}{8\pi \frac{r_o}{D}(1-M_x\cos\theta)} \exp\left\{ i\frac{(n_1B_1\Omega_1+n_2B_2\Omega_2)}{(1-M_x\cos\theta)}\left(t-\frac{r_o}{c_o}\right)\right.$$

$$\left. + i(n_1B_1-n_2B_2)(\psi_o+\pi/2)\right\} \tag{4.3.1}$$

$$\int_{z_o}^{1} {}_{M_{r_1}}^{2} e^{-i\phi_s} J_{n_1B_1-n_2B_2}\left[\frac{(n_1B_1M_{t_1}+n_2B_2M_{t_2})}{(1-M_x\cos\theta)} z\sin\theta\right] k_y \frac{C_L^{(n_2)}}{2} \Psi_L^{(n_2)}(k_x)dz .$$

where here

$$\phi_s = \frac{2}{M_{r_1}}\left[\frac{(n_1B_1M_{t_1}+n_2B_2M_{t_2})}{(1-M_x\cos\theta)} - n_2B_2(M_{t_1}+M_{t_2})\right]\frac{s_1}{D} , \tag{4.3.2}$$

$$k_x = \frac{2}{M_{r_1}}\left[\frac{(n_1B_1M_{t_1}+n_2B_2M_{t_2})}{(1-M_x\cos\theta)} - n_2B_2(M_{t_1}+M_{t_2})\right]\frac{c_1}{D} , \tag{4.3.3}$$

$$k_y = \frac{2}{M_{r_1}}\left[\frac{(n_1B_1M_{t_1}+n_2B_2M_{t_2})}{(1-M_x\cos\theta)}M_{t_1} z\cos\theta - (n_1B_1-n_2B_2)\frac{M_x}{z}\right]\frac{c_1}{D} , \tag{4.3.4}$$

and the noncompactness factor $\Psi_L^{(n_2)}(k_x)$ is defined by (4.2.4) and (4.2.11) with n_1 replaced by n_2 and k_x given by (4.3.3).

Equations (4.2.7) and (4.3.1) are essentially the same with the suffices 1 and 2 interchanged. However, there is a difference in the definitions of k_y in (4.2.10) and (4.3.4); in (4.2.10) the two terms within the square brackets are added whereas in (4.3.4) they are subtracted. This leads to a difference in the far-field directivities of interaction tones generated by the upstream blade row and interaction tones generated by the downstream blade row. Bradley (1986) made use of this fact when appraising data from the Fairey Gannet counter-rotation propeller, and we shall see in chapters 5 to 7 how directivity effects help in determining noise sources.

4.4 Asymptotic Approximations

It is possible to derive asymptotic approximations to the radiation formulae (4.2.7) and (4.3.1) in much the same way as those derived in chapter 3 for rotor alone tones. Here, we define a formally large parameter

$$\nu = n_1B_1 - n_2B_2 \tag{4.4.1}$$

and a sonic radius

$$z^* = \frac{(n_1B_1-n_2B_2)}{(n_1B_1M_{t_1}+n_2B_2M_{t_2})} \frac{(1-M_x\cos\theta)}{\sin\theta} \tag{4.4.2}$$

so that z^* does not necessarily lie on the blade but can be anywhere in the range $0 < z^* < \infty$, depending on the values of the parameters. We

can then proceed as in chapter 3 by defining three regimes corresponding to subsonic, transonic and supersonic mode phase speed*. (This differs from the rotor alone tone case where the field is steady in blade fixed coordinates and the modes are locked to the rotor.) Since the analysis is virtually identical to that in chapter 3 we will not repeat it here. However, in addition to the approximations described in chapter 3 we must consider just one further case, viz. Bessel functions of order zero corresponding to $n_1B_1 = n_2B_2$. Here we use the large argument, fixed order, approximation to the Bessel function given in Abramowitz & Stegun (1965). Then, continuing as in section 3.4.3, for the supersonic portion of a straight bladed S.R.P., we obtain the far-field acoustic pressure as

$$p \sim \left(\frac{2}{\pi}\right)^{\frac{1}{2}} \frac{1}{\eta^{3/2}} \left[S(1)\sin\eta - \frac{S(z_o)}{z_o^{1/2}} \sin(\eta z_o) \right] \qquad (4.4.3)$$

where

$$\eta = \frac{(n_1B_1M_{t_1} + n_2B_2M_{t_2})\sin\theta}{(1-M_x\cos\theta)} \, . \qquad (4.4.4)$$

In (4.4.3) the unsteady source strength S(z) is analogous to the steady source strength defined in chapter 3. The effects of blade sweep and chordwise noncompactness can be included as before .

FOOTNOTE

* Here we refer to the mode generated by the (n_1,n_2) interaction which is defined in the following section.

The sonic radius z* in (4.4.2) depends on n_1B_1 and n_2B_2. We cannot, therefore, use the asymptotic formulae to obtain design rules valid for interaction tones at all frequencies, as we could for rotor alone tones, but we can use the formulae to suggest ways of reducing a particularly noisy or critical interaction tone. Of course, the formulae can also be used to produce large savings in C.P.U. time (of, typically, 95%) when making predictions of interaction noise levels.

4.5 Discussion

In sections 4.2 and 4.3 we provided a framework for the prediction of interaction noise once the unsteady lift coefficients, $C_L^{(n_1)}$ and $C_L^{(n_2)}$, and chordwise shape functions, $f_L^{(n_1)}$ and $f_L^{(n_2)}$, are known. In the following three chapters we will show how the unsteady airfoil response can be calculated, with appropriate approximations, entirely consistent with those of chapters 3 and 4, for different aerodynamic interactions. In each case the chordwise integration can be performed analytically. We therefore calculate the unsteady response, of both upstream and downstream blades, which is acoustically weighted to account for chordwise interference effects, i.e. we calculate

$$\frac{dL_1}{dr} = \frac{1}{2}\rho U_{r_1}^2 c_1 C_L^{(n_2)} \Psi^{(n_2)}(k_x) \qquad (4.5.1)$$

and

$$\frac{dL_2}{dr} = \frac{1}{2}\rho U_{r_2}^2 c_2 C_L^{(n_1)} \Psi^{(n_1)}(k_x). \qquad (4.5.2)$$

The unsteady response values can then be fed into the complete formulae, (4.2.7) or (4.3.1), or into the asymptotic approximations.

From (4.2.7) and (4.3.1) we see that interaction tones are generated at the combination frequencies

$$f_{n_1,n_2} = \frac{(n_1 B_1 \Omega_1 + n_2 B_2 \Omega_2)}{2\pi(1-M_x \cos\theta)} \qquad (4.5.3)$$

where n_1 and n_2 can take any (positive or negative) integer values*. In future chapters we will use the notation (n_1,n_2) to refer to an interaction tone generated at the frequency given by (4.5.3). In the case of interactions between the downstream blades and the wakes or potential flow field generated by the upstream blades, the (n_1,n_2) interaction represents the n_2'th harmonic of the response of the downstream blades to the n_1'th harmonic of the unsteady velocity field. In the case of interactions between the upstream blades and the potential flow field generated by the downstream row, the (n_1,n_2) interaction represents the n_1'th harmonic of the response of the upstream blades to the n_2'th harmonic of the unsteady velocity field. When n_1 and n_2 are of different sign the interaction tone generated (a 'difference tone') has poor radiation efficiency: the mode phase speed is subsonic across the whole span of the blade and the Bessel function in (4.2.7) and (4.3.1) is therefore exponentially small†. We will therefore neglect 'difference

---

FOOTNOTES

* Note that when $n_1 = 0$ we are considering the n_2'th harmonic of rotor alone noise generated by the rear row and when $n_2 = 0$ we are considering the n_1'th harmonic of rotor-alone noise generated by the front row.

† In the case of a ducted rotor, such a mode is called a 'cut-off' mode.

tones' and concentrate only on 'sum tones' for which n_1 and n_2 are of the same sign.

5. WAKE INTERACTIONS

5.1 Introduction

In chapter 4 we provided a framework for the calculation of far-field acoustic radiation due to unsteady blade forces. In this chapter we determine the unsteady lift generated on the downstream blades of a counter-rotation propeller due to interactions with the wakes from the upstream blade row. These unsteady forces can then be inserted into the radiation formulae of chapter 4.

We start by modelling the rotor wakes in section 5.2. Since we are considering counter-rotation propellers which have low blade numbers* we treat each blade in isolation and assume that momentum is conserved on a two-dimensional basis, i.e. at constant blade radius. Two analytical wake models are used which can be derived, with appropriate assumptions, from Prandtl's mixing length theory. An additional wake model based on experimental results is also used.

In section 5.3 we apply the three wake models to the forward row of a counter-rotation propeller. The wake defect velocities for each model are then rewritten in Fourier series form.

Switching to a coordinate system attached to the rear row of the propeller, we calculate the response of the downstream row to each harmonic gust in section 5.4. The flow is taken to be compressible and the airfoil response is assumed to be the same as that on a flat plate extending to downstream infinity (this corresponds to the high frequency response calculation considered by Landahl (1961) and Goldstein (1976)).

Finally, in section 5.5, we compare predictions of far-field noise levels, as calculated using the unsteady blade forces given in the

---

FOOTNOTE

* The blade numbers on a counter-rotation propeller are low when compared with a turbofan, but are still large when compared to a conventional propeller. There is thus no conflict here with the asymptotic calculations discussed in chapters 3 and 4.

current chapter and the radiation formulae in chapter 4, with measured data. We consider both a low blade number counter-rotation propeller and a high blade number model fan rig*. In both cases we discuss the differences in predictions obtained using the different wake models.

5.2 Wake Models

5.2.1 Prandtl's Mixing Length Theory

We start with a brief discussion of Prandtl's mixing length theory which will form the basis for the model of the wake. More detailed discussions of mixing length theory can be found in chapter XIX of Schlichting (1955) and chapter V of Goldstein (1938).

The mean turbulent mixing stress τ is assumed to be locally related to the mean velocity gradient by

$$\tau = A_\tau \frac{d\bar{u}}{dY} , \qquad (5.2.1)$$

where the coordinates (X,Y) are measured parallel and normal to the mean velocity $\bar{u}$. In (5.2.1) A_τ is a mixing coefficient†, corresponding to the viscosity in laminar flow, which is called the eddy viscosity. We also introduce the eddy kinematic viscosity

$$\varepsilon = \frac{A_\tau}{\rho} \qquad (5.2.2)$$

analogous to the kinematic viscosity in laminar flow.

FOOTNOTES

* Here we are considering rotor-stator interaction. This configuration is modelled as a counter-rotation propeller with the rear row speed set to zero.

† The mixing coefficient was introduced by Boussinesq (1877).

Prandtl's mixing length hypothesis asserts that

$$\tau = \rho \ell^2 \left|\frac{d\bar{u}}{dY}\right| \frac{d\bar{u}}{dY} \quad , \tag{5.2.3}$$

where ℓ is known as the mixing length. We now consider the increase in wake width, and decrease in wake velocity, with downstream distance. It is assumed that the mixing length ℓ is proportional to the wake width b, so that

$$\frac{\ell}{b} = \beta \tag{5.2.4}$$

where β is a constant. We also assume that the rate of increase of the wake length b* is proportional to the mean transverse velocity $\bar{v}'$, averaged over one half of the wake, i.e.

$$\frac{Db}{Dt} \sim \frac{1}{b} \left| \int_0^b \bar{v}' \, dy \right| \tag{5.2.5}$$

where D/Dt denotes the convective derivative. Now, following Prandtl (1925) we have that

$$\bar{u}' \sim \bar{v}' \sim \ell \frac{d\bar{u}}{dY} \quad . \tag{5.2.6}$$

FOOTNOTE

* Here b is taken to be the wake half width.

On combining (5.2.4) to (5.2.6) we obtain*

$$\frac{Db}{Dt} \sim \beta \left| \int_0^b \frac{d\bar{u}}{dY} \, dY \right| = \beta \, \bar{u}'_c \qquad (5.2.7)$$

where the prime denotes a perturbation quantity, i.e.

$$\bar{u} = U_\infty - \bar{u}' \qquad (5.2.8)$$

where U_∞ is the flow velocity at infinity, and the suffix c denotes the value at the wake centreline. On using the definition of the convective derivative in (5.2.5), combined with (5.2.6) to (5.2.8), we obtain

$$\frac{db}{dX} \sim \beta \frac{\bar{u}'_c}{U_\infty} \qquad (5.2.9)$$

to leading order in $\bar{u}'/U_\infty$ and $\bar{v}'/U_\infty$.

Now the drag per unit length on the airfoil is related to the momentum by†

FOOTNOTES

* In the case where the wake has no definite edge, b denotes a typical transverse length scale.

† Here we suppose that the static pressure in the wake is approximately equal to that in the freestream. In addition, for application to a blade row, we assume that adjacent blades are far enough apart for each blade to be considered in isolation.

$$\frac{dD}{dr} = \rho \int_{-\infty}^{\infty} \bar{u}(U_\infty - \bar{u})dY \ . \qquad (5.2.10)$$

Using (5.2.8), with $\bar{u}'$ small, we obtain

$$\frac{dD}{dr} = \rho U_\infty^2 \int_{-\infty}^{\infty} \frac{\bar{u}'}{U_\infty} dY \qquad (5.2.11)$$

to leading order in $\bar{u}'/U_\infty$.

We now normalise the transverse coordinate Y by the wake half width b so that

$$Y = b\eta \ . \qquad (5.2.12)$$

In addition we assume that the wake profile shape, normalised on the centreline defect velocity, is independent of X so that

$$\frac{\bar{u}'}{U_\infty} = \frac{\bar{u}'_c}{U_\infty} f_1(\eta) \qquad (5.2.13)$$

where $f_1(\eta)$ is a shape function. Then, from (5.2.11) to (5.2.13),

$$\frac{dD}{dr} = \rho U_\infty^2 \frac{b\bar{u}'_c}{U_\infty} A \qquad (5.2.14)$$

where A is a constant representing the integral of $f_1(\eta)$. The drag coefficient C_D is related to the drag by

$$\frac{dD}{dr} = \frac{1}{2}\rho C_D c U_\infty^2 \qquad (5.2.15)$$

where c is the airfoil chord. Combining (5.2.9), (5.2.14) and (5.2.15) we find that

$$\frac{db}{dX} \sim \beta \frac{C_D c}{2b} \qquad (5.2.16)$$

which can be solved to give

$$b \sim (\beta C_D c X)^{\frac{1}{2}} \quad . \qquad (5.2.17)$$

From (5.2.14) and (5.2.15)

$$\frac{\bar{u}'_c}{U_\infty} = \frac{C_D c}{2bA} \qquad (5.2.18)$$

so that, from (5.2.17), the centreline defect velocity decays with X according to

$$\frac{\bar{u}'_c}{U_\infty} \sim \left(\frac{C_D c}{\beta X}\right)^{\frac{1}{2}} \quad . \qquad (5.2.19)$$

We will now use the above results to obtain wake velocity profiles.

5.2.2 Schlichting Wake Model

We now consider a wake model first investigated by Schlichting (1930) and based on Prandtl's mixing length hypothesis. Detailed derivations are provided in chapter XIII of Goldstein (1938) and chapter XXIV of Schlichting (1955).

With $\bar{u}$ defined by (5.2.8), where $\bar{u}'$ is small, and the transverse velocity $\bar{v}$ equal to $\bar{v}'$, where $\bar{v}'$ is small, the boundary layer equation

$$\frac{\partial \bar{u}}{\partial t} + \bar{u}\frac{\partial \bar{u}}{\partial X} + \bar{v}\frac{\partial \bar{u}}{\partial X} = \frac{1}{\rho}\frac{\partial \tau}{\partial Y} \qquad (5.2.20)$$

reduces, in steady flow, to

$$-U_\infty \frac{\partial \bar{u}'}{\partial X} = \frac{1}{\rho}\frac{\partial \tau}{\partial Y} \qquad (5.2.21)$$

where second order quantities have been neglected. From Prandtl's mixing length hypothesis, (5.2.3), we obtain*

$$-U_\infty \frac{\partial \bar{u}'}{\partial X} = 2\ell^2 \frac{\partial \bar{u}'}{\partial Y}\frac{\partial^2 \bar{u}'}{\partial Y^2} \quad . \qquad (5.2.22)$$

From (5.2.17) and (5.2.19) we put

$$b = B(C_D cX)^{\frac{1}{2}}, \qquad (5.2.23)$$

FOOTNOTE

* Here we use local velocity and not the velocity averaged over the width.

$$\frac{\bar{u}'}{U_\infty} = \left(\frac{C_D c}{X}\right)^{\frac{1}{2}} f_2(\eta) \ , \qquad (5.2.24)$$

where B and the shape function $f_2(\eta)$ are to be determined. On substituting (5.2.23) and (5.2.24) into (5.2.22), with ℓ given by (5.2.4), we obtain

$$\frac{f_2 + \eta f'_2}{2} = 2\,\frac{\beta^2}{B}\, f'_2 f''_2 \qquad (5.2.25)$$

where the primes denote derivatives with respect to argument. The boundary conditions are $u' = 0$, $\partial u'/\partial Y = 0$ at $Y = b$ (or, equivalently, that $f = f' = 0$ at $\eta = 1$). We can integrate (5.2.25) to give

$$\frac{\eta f_2}{2} = \frac{\beta^2}{B}\,(f'_2)^2 \ . \qquad (5.2.26)$$

Since f_2 decreases between $\eta = 0$ and $\eta = 1$ we choose the negative square root, leading to

$$f_2(\eta) = \frac{B}{18\beta^2}\,(1 - \eta^{3/2})^2 \ . \qquad (5.2.27)$$

We now consider the momentum equation which is given by (5.2.14) and (5.2.15). From (5.2.24) the momentum equation reduces to

$$\frac{C_D c}{2} = 2b \left(\frac{C_D c}{X}\right)^{\frac{1}{2}} \int_0^1 f_2(\eta)\, d\eta \ . \qquad (5.2.28)$$

From (5.2.23) and (5.2.27) we obtain $B = \sqrt{10}\beta$ so that

$$\frac{\bar{u}'}{U_\infty} = \frac{\sqrt{10}}{18\beta}\left(\frac{C_D c}{X}\right)^{\frac{1}{2}}\left[1 - \left(\frac{Y}{b}\right)^{3/2}\right]^2 \qquad (5.2.29)$$

and

$$b = \beta(10C_D cX)^{\frac{1}{2}} \ . \qquad (5.2.30)$$

It remains to determine the value of the empirical constant β. Now experiments carried out by Schlichting (1930) and Reichardt (1942)* suggest that

$$b_{\frac{1}{2}} = \frac{(C_D cX)^{\frac{1}{2}}}{4} \qquad (5.2.31)$$

where $b_{\frac{1}{2}}$ is defined as that value of Y such that

$$\left.\frac{\bar{u}'}{U_\infty}\right|_{Y=b_{\frac{1}{2}}} = \frac{1}{2}\frac{\bar{u}'_c}{U_\infty} \ . \qquad (5.2.32)$$

From (5.2.29) we then have

$$b_{\frac{1}{2}} = \frac{(\sqrt{2}-1)^{2/3}}{2^{1/3}}\, b \qquad (5.2.33)$$

FOOTNOTE

* In fact the experiments were carried out on circular cylinders of different diameters. We have assumed the same results to hold for airfoils with the chord as the appropriate length scale.

which, from (5.2.30) and (5.2.31), leads to

$$\beta = \frac{2^{1/3}}{4\sqrt{10}(\sqrt{2}-1)^{2/3}} \approx 0.18 \quad . \tag{5.2.34}$$

In section 5.3 we will apply the "Schlichting wake model" to a counter-rotation propeller and show how the wakes can be rewritten in Fourier series form.

5.2.3 Gaussian Wake Model

Here we consider an alternative wake model which was obtained by Reichardt (1942) and Görtler (1942) and is described in chapter XXIV of Schlichting (1968).

We start by substituting (5.2.1) and (5.2.2) into (5.2.21) whence

$$\frac{\partial \bar{u}'}{\partial X} = \frac{\varepsilon}{U_\infty} \frac{\partial^2 \bar{u}'}{\partial Y^2} \quad , \tag{5.2.35}$$

and if the viscosity ε is now taken as constant (as in laminar flow, though not necessarily with the same numerical value as for laminar flow), this partial differential equation is identical in form to the standard heat equation (see, for example, Chester (1971)). The solution corresponding to a concentration of momentum at the origin is classical, and is given by

$$\frac{\bar{u}'}{U_\infty} = B' \left(\frac{c}{X}\right)^{\frac{1}{2}} \exp\left[-\left(\frac{U_\infty}{4\varepsilon X}\right) Y^2\right] \tag{5.2.36}$$

where the constant of proportionality B' is to be determined. It follows from the momentum equation ((5.2.14) and (5.2.15)) that

$$\frac{C_D c}{2} = B' \left(\frac{c}{X}\right)^{\frac{1}{2}} \int_{-\infty}^{\infty} \exp\left[-\left(\frac{U_\infty}{4\epsilon X}\right) Y^2\right] dY = B' \left(\frac{4\epsilon c \pi}{U_\infty}\right)^{\frac{1}{2}} \qquad (5.2.37)$$

whence

$$\frac{\bar{u}'}{U_\infty} = \frac{cC_D}{4} \left(\frac{U_\infty}{\pi\epsilon X}\right)^{\frac{1}{2}} \exp\left[-\left(\frac{U_\infty}{4\epsilon X}\right) Y^2\right] . \qquad (5.2.38)$$

We now use the empirical formula (5.2.31) which leads to

$$\epsilon = \frac{64 \ell n 2}{U_\infty C_D c} . \qquad (5.2.39)$$

On substituting this into (5.2.38) we obtain

$$\frac{\bar{u}'}{U_\infty} = 2 \left(\frac{\ell n 2}{\pi}\right)^{\frac{1}{2}} \left(\frac{cC_D}{X}\right)^{\frac{1}{2}} \exp\left(-\ell n 2 \frac{Y^2}{b_{\frac{1}{2}}^2}\right) . \qquad (5.2.40)$$

The harmonic components of these Gaussian wakes, as generated by a counter-rotation propeller, will be discussed in section 5.3.

5.2.4 Experiments

To date there is little published information on propfan wakes. The author knows only of the work of Hanson & Patrick (1985), Sundar (1985)

and Sundar & Sullivan (1986). Hanson & Patrick's study was of a qualitative nature and attempted to discriminate between viscous wakes and potential flow fields at different operating conditions; there was insufficient data presented to correlate wake development with downstream distance. Sundar and Sundar & Sullivan's examination of wakes were aimed at determining propeller performance; the downstream development of the wake was therefore not an integral part of the work.

Consequently, we must instead consider wakes behind airfoils or rotors. An early study was provided by Silverstein et al. (1939) on the wakes behind airfoils. This work used experiments to modify a theoretical model*. However, the model did not conserve momentum on a two-dimensional basis and is therefore inappropriate for our use†. (In fact there appeared to be some confusion over near wake and far wake regions where the wake develops at different spatial rates; modifications were made to the far wake model to fit the near wake experimental results. These modifications were inconsistent in that the wake width and wake defect velocity were treated independently.) A detailed discussion of wake models for rotors, both empirical and theoretical, is given by Majjigi & Gliebe (1985). However, this work is aimed at turbofans and is complicated by three dimensional effects. The most appropriate published information appears to be that of Reynolds (1979)†† who studied the

---

FOOTNOTES

* The theoretical model used by Silverstein et al. (1939) was based on Prandtl's mixing length theory and assumes $\bar{u}'/U_\infty \sim X^{-\frac{1}{2}}$ and $b \sim X^{\frac{1}{2}}$. The wake shape is different from the Schlichting and Gaussian profiles and is formed from circular functions.

† All the aerodynamic and response calculations discussed here are carried out on a two dimensional basis.

††See also Raj & Lakshminarayana (1973) and Ravindranath & Lakshminarayana (1981).

wakes behind isolated airfoils, cascades and rotors. In particular, Reynolds examined the wake profile, and the downstream wake development, for different values of section drag coefficient.

Reynolds found that the wake profile correlated well with a Gaussian shape, i.e.

$$f_1(\eta) = \exp(-\ell n2\,\eta^2) = \exp\left[-\ell n2\,\frac{Y^2}{b_{\frac{1}{2}}^2}\right] , \qquad (5.2.41)$$

and that the wake centreline defect velocity decayed according to

$$\frac{\bar{u}'_c}{U_\infty} = C_D^{1/4}\left[\frac{A_1}{\left(\frac{X}{c}-\frac{X_o}{c}\right)^{\frac{1}{2}}} + \frac{A_2}{\left(\frac{X}{c}-\frac{X_o}{c}\right)}\right] \qquad (5.2.42)$$

where X_o represents the virtual wake origin. The values of A_1, A_2 and X_o for different configurations are tabulated in Table 5.1. We will use the values given for the rotor wake.

	Near Wake			Far Wake		
	X_o/c	A_1	A_2	X_o/c	A_1	A_2
Isolated Airfoil	-.193	-.578	.65	-.182	.495	0
Cascade	-.141	.706	.681	-.06	.54	0
Rotor	-.16	.361	.463	-.36	.271	0

Table 5.1 Coefficients for the near wakes and far wakes from isolated airfoils, cascades and rotors.

From the momentum equation we have

$$\frac{C_D c}{2} = \frac{\bar{u}'_c}{U_\infty} \int_{-\infty}^{\infty} \exp\left[-\ell n2 \left(\frac{Y^2}{b_{\frac{1}{2}}^2}\right)\right] dY = \frac{\bar{u}'_c}{U_\infty} \left(\frac{\pi}{\ell n2}\right)^{\frac{1}{2}} b_{\frac{1}{2}}, \qquad (5.2.43)$$

so that, combining (5.2.42) and (5.2.43),

$$b_{\frac{1}{2}} = \frac{c C_D^{3/4}}{2} \left(\frac{\ell n2}{\pi}\right)^{\frac{1}{2}} \left[\frac{A_1}{\left(\frac{X}{c} - \frac{X_o}{c}\right)^{\frac{1}{2}}} + \frac{A_2}{\left(\frac{X}{c} - \frac{X_o}{c}\right)}\right]^{-1} . \qquad (5.2.44)$$

For future reference we will call this wake model the "Reynolds wake model". Note that in the far wake the dependence of b and $\bar{u}'$ on X is the same as in the "Schlichting" and "Gaussian" wake models. However, the dependence on the drag coefficient C_D is different. Here $\bar{u}' \sim C_D^{1/4}$ and $b \sim C_D^{3/4}$ whereas in both the "Schlichting" and "Gaussian" wake models $\bar{u}' \sim C_D^{1/2}$ and $b \sim C_D^{1/2}$. This implies that the "Reynolds" wake profile will have smaller defect velocities but greater width than either the "Schlichting" or "Gaussian" wake profiles. The importance of these differences in wake profile will become clear in section 5.5.

5.3 Harmonic Gusts

In the previous section we described different wake models that may be individually applicable to propfan blades. Here we show how, in each case, the wakes of the complete propfan can be described as a summation of harmonic gusts which then impinge on the rear row of a counter-rotation propeller.

5.3.1 Coordinate System for Wake

We use a coordinate system attached to the forward blade row. The situation is shown in Figure 5.1. The (X, Y) coordinates correspond to those used in section 5.2, with X and Y measured parallel and normal to the airfoil. The (x, y) coordinates correspond to cylindrical polar coordinates (at a fixed radius) with x measured parallel to the propeller axis and y, corresponding to $r\phi_1$ where r is the radius and ϕ_1 is the azimuthal angle, measured in the direction of rotation. The two coordinate systems are related by

$$\left.\begin{aligned} X &= x\ \cos\alpha_1 + y\ \sin\alpha_1 \\ Y &= -x\ \sin\alpha_1 + y\ \cos\alpha_1 \end{aligned}\right\} \qquad (5.3.1)$$

where α_1 represents the local blade stagger angle. Along the wake centre-line Y = 0, so that

$$X = \frac{x}{\cos\alpha_1} \ . \qquad (5.3.2)$$

The wake velocities in the x and y directions are then given by

$$\underline{u} = (u_x, u_y) = -(\cos\alpha_1, \sin\alpha_1)\ \bar{u}'_c \left(\frac{x}{\cos\alpha_1} - X_o\right) f_1 \left[\frac{-x\ \sin\alpha_1 + y\ \cos\alpha_1}{b\left(\frac{x}{\cos\alpha_1} - X_o\right)}\right]. \qquad (5.3.3)$$

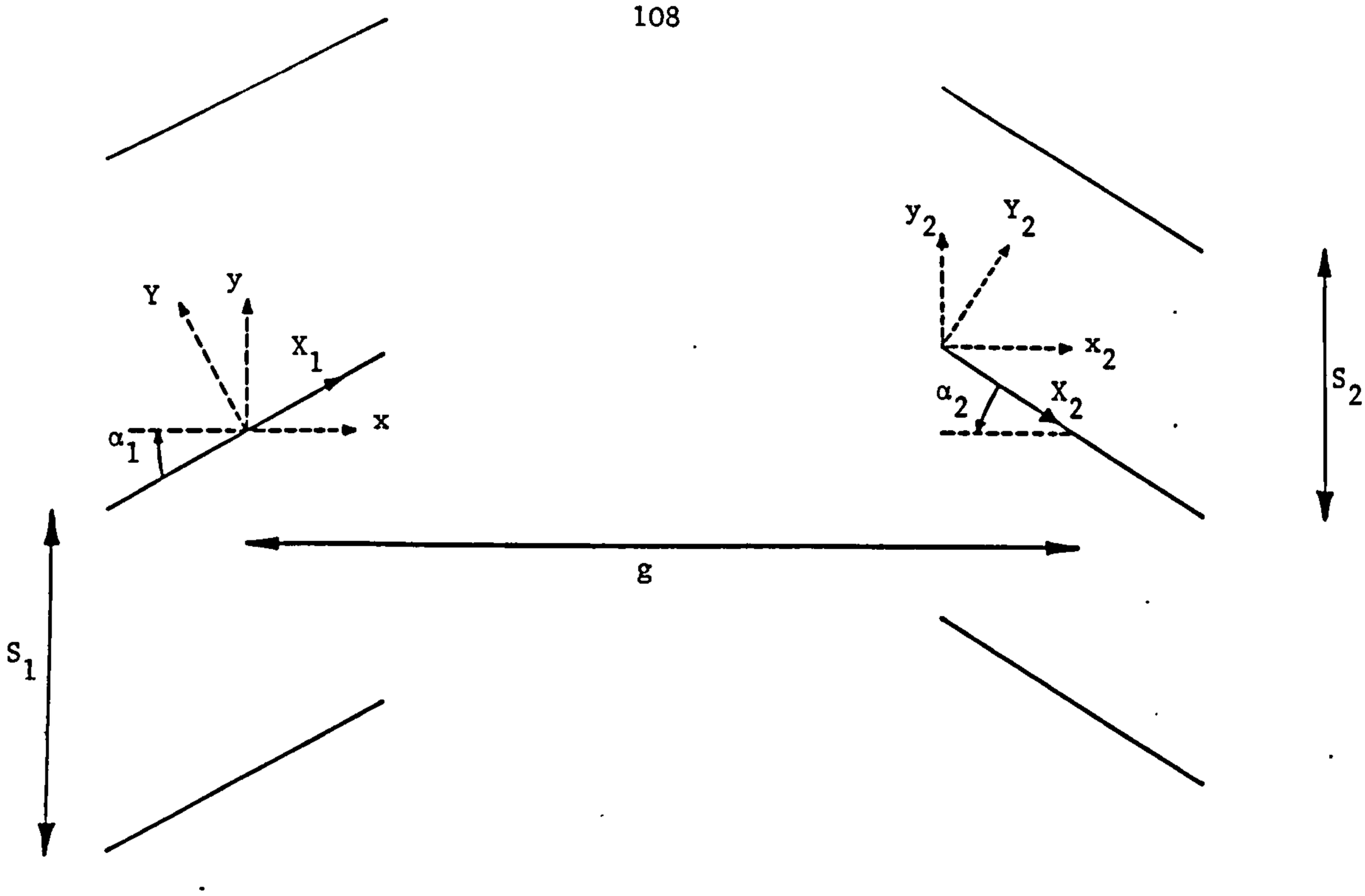

Figure 5.1 Coordinate system for downstream gust interaction.

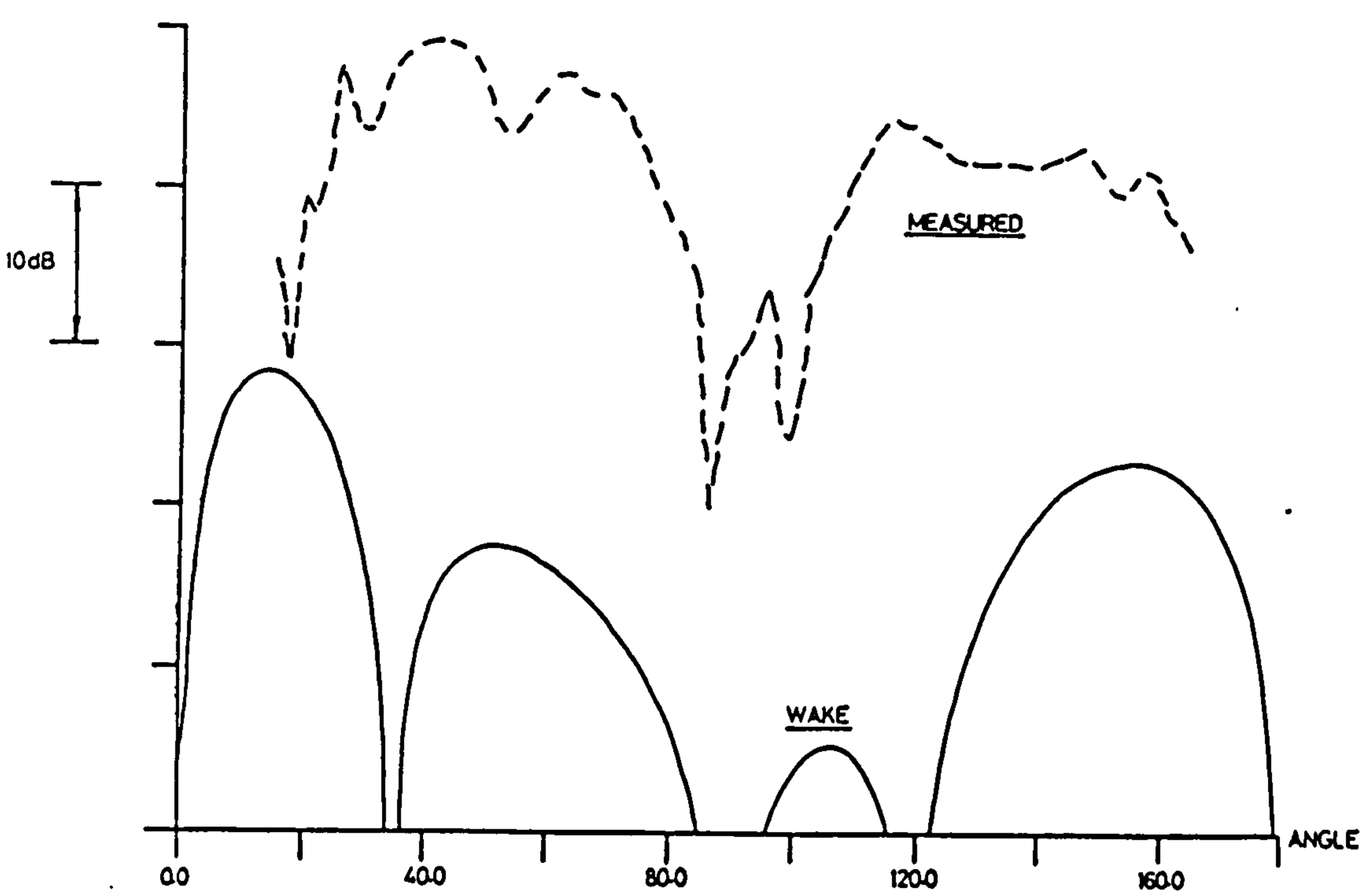

Figure 5.2 Gannet measurements vs predictions for the (1,1) interaction tone.

Since the wake develops relatively slowly in the X direction the wake width in the y direction, b_y, can be related, approximately, to the standard wake width in the Y direction, b, by

$$b_y \sim \frac{b}{\cos\alpha_1} \quad . \tag{5.3.4}$$

We now put $y = r\phi_1$ and decompose the wake into harmonics so that

$$\underline{u} = \sum_{n_1=-\infty}^{\infty} \underline{u}_{n_1} e^{in_1 B_1 \phi_1} \tag{5.3.5}$$

where B_1 is the number of blades on the forward row and $\underline{u}_{n_1}$ is defined by

$$\underline{u}_{n_1} = \frac{B_1}{2\pi} \int_{-\pi/B_1}^{\pi/B_1} \underline{u}(\phi_1) e^{-in_1 B_1 \phi_1} \, d\phi_1 \, . \tag{5.3.6}$$

This analysis will be applied to each wake profile in turn, on the assumption that the <u>isolated</u> blade wake velocity can be used in the integrand of (5.3.6).

5.3.2 <u>Schlichting Wake Model</u>

The defect velocity across the wake is given by (5.2.29). From (5.3.3) and (5.3.6) the harmonic components are given by

$$\underline{u}_{n_1} = -(\cos\alpha_1, \sin\alpha_1)\ \frac{\sqrt{10}}{18\beta}\left(\frac{C_D c_1}{\frac{x}{\cos\alpha_1} - X_o}\right)^{\frac{1}{2}} U_{r_1}$$

$$\int_{\phi_-}^{\phi_+} \left\{1 - \left[\frac{-x\ \sin\alpha_1 + y\ \cos\alpha_1}{b\left(\frac{x}{\cos\alpha_1} - X_o\right)}\right]^{3/2}\right\}^2 e^{-in_1 B_1 \phi_1}\ d\phi_1 \qquad (5.3.7)$$

where U_{r_1} is the relative section flow speed across the upstream blades of local chord length c_1 and $\phi\pm = x\ \tan\alpha_1/r \pm b/r\cos\alpha_1$. On making the substitution

$$\psi = -\frac{-x\ \sin\alpha_1 + r\phi_1 \cos\alpha_1}{b} \qquad (5.3.8)$$

the integral in (5.3.7) can be rewritten as

$$\frac{b}{r\ \cos\alpha_1}\ \exp\left(\frac{-in_1 B_1 x\ \tan\alpha_1}{r}\right) \int_{-1}^{1} (1 - |\psi|^{3/2})^2\ e^{-ik_b\psi}\ d\psi \qquad (5.3.9)$$

where we have defined a wake wavenumber k_b by

$$k_b = \frac{n_1 B_1 b}{r\ \cos\alpha_1}\ . \qquad (5.3.10)$$

The integral in (5.3.9) is evaluated in appendix 5.1. From the definition of the wake width b in (5.2.30), with X given by (5.3.2), we then find,

from (5.3.5), that the defect velocity is given by

$$\underline{u} = -(\cos\alpha_1, \sin\alpha_1) \frac{C_D c_1 U_{r_1}}{2r \cos\alpha_1} \sum_{n_1=-\infty}^{\infty} G(k_b) \exp\left[i n_1 B_1 \left(\Omega_1 t + \phi - \frac{x}{r} \tan\alpha_1\right)\right] \tag{5.3.11}$$

where

$$G(k_b) = \frac{40}{3k_b^4} \left\{ (1 - \cos k_b - k_b \sin k_b) + \frac{k_b^2}{2} \left(\frac{\pi}{2k_b}\right)^{\frac{1}{2}} C\left[\left(\frac{2k_b}{\pi}\right)^{\frac{1}{2}}\right] \right\} \tag{5.3.12}$$

represents the Fourier coefficient, for wavenumber k_b, normalised so that $G(0) = 1$. In (5.3.11) the azimuthal angle ϕ is measured in a stationary frame of reference and is related to ϕ_1 by

$$\phi_1 = \phi + \Omega_1 t \tag{5.3.13}$$

where Ω_1 is the angular shaft speed of the forward row.

5.3.3 Gaussian Wake Model

The wake defect velocity is given in (5.2.40). From (5.3.3) and (5.3.6) we then obtain the harmonic components as

$$\underline{u}_{n_1} = -(\cos\alpha_1, \sin\alpha_1)\, 2 \left(\frac{\ell n 2}{\pi}\right)^{\frac{1}{2}} \left(\frac{c_1 c_D}{\frac{x}{\cos\alpha_1} - X_o}\right)^{\frac{1}{2}} U_{r_1} \int_{-\infty}^{\infty} \exp\left[-\ell n 2 \frac{(-x \sin\alpha_1 + y\cos\alpha_1)^2}{b_{\frac{1}{2}}^2 \left(\frac{x}{\cos\alpha_1} - X_o\right)} - i n_1 B_1 \phi_1\right] d\phi_1 \quad . \tag{5.3.14}$$

Here we have assumed that the wakes are thin so that the limits of integration can be taken as infinite. On using the substitution (5.3.8), with b replaced by $b_{\frac{1}{2}}$, and completing the square in the argument of the exponential we can easily evaluate the integral in (5.3.14). On using the definition of $b_{\frac{1}{2}}$ in (5.2.31) we then obtain the result (5.3.11) with the normalised Fourier coefficients given by

$$G(k_b) = \exp\left[-\frac{k_b^2}{4\ell n2}\right] . \qquad (5.3.15)$$

Here the wake wavenumber k_b, defined by (5.3.10), is based on the width $b_{\frac{1}{2}}$ given in (5.2.31).

5.3.4 Reynolds Wake Model

The wake defect velocity for the Reynolds (empirical) wake model is given in (5.2.42). The analysis is identical to that carried out above for the Gaussian wake model (since the Reynolds wake profile is also of Gaussian form). The defect velocity can be written in the form (5.3.11) with the normalised Fourier coefficients again given by (5.3.15). Here, however, the wake wavenumber k_b is based on the value of $b_{\frac{1}{2}}$ defined by (5.2.44).

5.4 Airfoil Response

5.4.1 Coordinate System for Downstream Blades

We now consider the upwash on a blade of the downstream row. The upstream and downstream blade configurations are shown in Figure 5.1. We define new coordinates (x_2,y_2) measured parallel to the (x_1,y_1) coordinate system but with the origin located at the leading edge of the downstream

reference blade*. The two coordinate systems are related by

$$\left.\begin{aligned} x &= x_2 + g - \frac{c_2}{2}\cos\alpha_2 \\ y &= y_2 + \frac{c_2}{2}\sin\alpha_2 + r(\Omega_1+\Omega_2)t \end{aligned}\right\} \qquad (5.4.1)$$

where α_2 and c_2 represent the local stagger angle and chord, respectively, of the rear blade section. The gap between the upstream and downstream pitch change axes is denoted by g. We also define another coordinate system (X_2,Y_2) where X_2 and Y_2 are measured parallel and normal to the local chord of the downstream reference blade. The origin of this coordinate system is again located at the leading edge of the reference blade (see Figure 5.1). We relate the (X_2,Y_2) coordinates to the (x_2,y_2) coordinates by

$$\left.\begin{aligned} x_2 &= X_2\cos\alpha_2 + Y_2\sin\alpha_2, \\ y_2 &= -X_2\sin\alpha_2 + Y_2\cos\alpha_2. \end{aligned}\right\} \qquad (5.4.2)$$

The upwash normal to the downstream reference blade is given by

$$\hat{u} = u_x\sin\alpha_2 + u_y\cos\alpha_2 \ . \qquad (5.4.3)$$

From (5.3.11) and (5.4.1) to (5.4.3) we then obtain

FOOTNOTE

* The front and rear row reference blades are defined such that $\phi = \phi_1 = \phi_2 = 0$ at $\tau = 0$.

$$\hat{u} = -\sin(\alpha_1 + \alpha_2)\,\frac{C_D c U_{r_1}}{2r\,\cos\alpha_1}\sum_{n_1=-\infty}^{\infty} G(k_b)$$

$$\exp\left\{\frac{in_1B_1}{r\,\cos\alpha_1}\left[\frac{c_2}{2}\sin(\alpha_1 + \alpha_2) - g\,\sin\alpha_1\right] + i\omega_2 t - ik_X X_2 - ik_Y Y_2\right\} \tag{5.4.4}$$

where the angular frequency ω_2 is given by

$$\omega_2 = n_1 B_1(\Omega_1 + \Omega_2) \tag{5.4.5}$$

and the wavenumbers k_X and k_Y are given by

$$\left.\begin{aligned} k_X &= \frac{n_1 B_1 \sin(\alpha_1 + \alpha_2)}{r\,\cos\alpha_1}, \\ k_Y &= \frac{-n_1 B_1 \cos(\alpha_1 + \alpha_2)}{r\,\cos\,\alpha_1}. \end{aligned}\right\} \tag{5.4.6}$$

Recall here that $G(k_b)$ differs for the three different wake models: for the Schlichting wake model $G(k_b)$ is given by (5.3.12) and the wake width b is given by (5.2.30); for both the Gaussian and Reynolds wake models $G(k_b)$ is given by (5.3.15) and k_b is based on $b_{\frac{1}{2}}$, which is defined by (5.2.31) and (5.2.44) for the Gaussian and Reynolds models respectively.

5.4.2 High Frequency Response

We now consider the response of the downstream blades to the fluctuating velocity field described above. Since, for counter-rotation propellers, the blade relative Mach numbers tend to be in the high subsonic regime, we shall take the flow to be compressible. We suppose that the gust is of relatively high frequency; the main reason for this is that the low frequency wake interactions are relatively unimportant - this fact will become clear from the comparisons with measured data in section 5.5. If required, the low frequency airfoil response case can easily be included in the prediction scheme from the published work of Amiet (1973, 1974) who extended an earlier analysis due to Osborne (1973). (A discussion of the low frequency compressible flow solution for non-convected gusts is given in section 7.7. The convected gust result can immediately be obtained from these results by setting the normalised gust frequency equal to the reduced frequency.)

At high frequencies the pressure will oscillate rapidly away from the leading edge of the downstream blades where indeed it will be (integrably) singular. The pressure will be, therefore, to a large part self-cancelling. The trailing edge region should then be relatively unimportant, so that the pressure distribution should be the same as that on a flat plate extending to downstream infinity. We then have a two part boundary value problem which can be solved by the Wiener-Hopf technique (see, for example, Noble (1958) or Crighton (1977)). This method is used in detail in chapter 7 for the case of nonconvected gusts in compressible flow.

We consider one harmonic component of the upwash given by

$$\hat{u}_{n_1} = \hat{v}_{n_1} \exp[ik_x(U_{r_2} t - X_2)] \tag{5.4.7}$$

where the leading edge upwash velocity $\hat{v}_{n_1}$ and the wavenumber k_x are defined in (5.4.4) to (5.4.6). The resulting pressure difference, Δp, across the airfoil (modelled as a semi-infinite flat plate) is given by Landahl (1961) and Goldstein (1976)* as

$$\Delta p(X_2) = \frac{2\rho U_{r_2} \hat{v}_{n_1}}{\left[\pi\sigma_2(1+M_{r_2})2\,\frac{X_2}{c_2}\right]^{\frac{1}{2}}} \exp\left[-\frac{i\pi}{4} - \frac{i\sigma_2 M_{r_2}}{(1+M_{r_2})}\,2\,\frac{X_2}{c_2} + i\omega_2 t\right] \tag{5.4.8}$$

where σ_2 is the reduced frequency defined by

$$\sigma_2 = \frac{\omega_2 c_2}{2U_{r_2}} = k_x \frac{c_2}{2} \tag{5.4.9}$$

and $M_{r_2} = U_{r_2}/c_o$ is the section relative Mach number across the rear blade.

The total lift per unit span on the blade is obtained by integrating (5.4.8) along the chord. We also need to include the phase term $\exp(-ik_x 2X_2/c_2 + ik_x)$ which was introduced in chapter 4† and represents the noncompactness effects. We are therefore calculating the effective

---

FOOTNOTES

* Our solution is the complex conjugate of Goldstein's since he chose a time dependence $e^{-i\omega t}$ and we have used $e^{i\omega t}$. In addition the phase term $e^{i\sigma_2}$ is missing from our result since the gust is referenced to the airfoil leading edge and not the mid-chord.

† Note here that the phase term is referenced to the airfoil leading edge whereas in chapter 4 it was referenced to the mid-chord.

point force which generates the same far acoustic field as the distributed force - the actual unsteady lift per unit span is obtained by setting the chordwise wavenumber k_x equal to zero. The effective unsteady lift per unit span is given by

$$\frac{dL_2}{dr} = \frac{2^{\frac{1}{2}}\rho U_{r_2} \hat{v}_{n_1} c_2 e^{i\omega_2 t + ik_x - i\pi/4}}{\sigma_2^{\frac{1}{2}}(1+M_{r_2})^{\frac{1}{2}}\left[k_x + \frac{\sigma_2 M_{r_2}}{1+M_{r_2}}\right]^{\frac{1}{2}}} E^*\left[\frac{2}{\pi}^{\frac{1}{2}}\left[k_x + \frac{\sigma_2 M_{r_2}}{1+M_{r_2}}\right]^{\frac{1}{2}}\right] \qquad (5.4.10)$$

where E* is the conjugate of the complex Fresnel integral*.

5.5 Measurement vs Prediction

5.5.1 Counter-Rotation Propeller

We now use the unsteady lift calculations described in the current chapter, along with the radiation formulae derived in chapter 4, to predict the noise generated by wake interactions on a counter-rotation propeller. The predictions will be compared with measurements taken from the Fairey Gannet flyover tests which were discussed previously in chapter 2. Since the forward and rearward blade rows on the Gannet were run at slightly different speeds, the interaction tone components could be separated out in terms of frequency thus allowing us to examine each tone individually†.

The first interaction tone generated by the Gannet is the (1,1)

FOOTNOTES

* In the case where $[k_x+\sigma_2 M_{r_2}/(1+M_{r_2})]$ is negative we replace E* with E in (5.4.10) and use $|k_x+\sigma_2 M_{r_2}/(1+M_{r_2})|$.

† A detailed description of the Fairey Gannet flyover tests is given by Bradley (1986).

interaction. The directivity plot for this tone is shown in Figure 5.2. We can see that there is a null at the 90^{o} radiation angle in both the measured and predicted data. This is to be expected since the (1,1) interaction tone generates a plane wave mode (on the Gannet which has equal blade numbers on the forward and rear rows), i.e. $n_1B_1 - n_2B_2 = 0$, which peaks on the propeller axis and is zero in the plane of the rotor. However, the predictions are, typically, 25dB below the measurements.

The next two interaction tones generated by the Gannet are the (2,1) and (1,2) interactions for which directivity plots are shown in Figures 5.3 and 5.4 respectively. For these interaction tones the predictions are at least 10dB below the measurements. In fact, it is not only the levels that are incorrectly predicted but also the directivities: the predictions are 20dB below the measurements for the (1,2) interaction in the forward arc; the predictions are 40dB below the measurements for the (2,1) interaction in the rear arc*.

Bradley (1986) considered the directivities of the interaction tones generated by the Gannet. He showed that, although the measured directivities were similar in level in forward and rear arcs, any noise source on the rear blade row produced only asymmetrical directivities (except for the plane wave case where $n_1 = n_2$). This result suggested that there was a noise source on the forward blade row. In order to generate tones at the (n_1,n_2) interaction tone frequencies the noise source must be that due to the interaction of the forward blade row with the potential field generated by the rear row. Discussion of the potential field interactions is, however, left to chapters 6 and 7.

FOOTNOTE

* Here, we use forward arc and rear arc to denote the angular regions 0^{o} to 90^{o} and 90^{o} to 180^{o} respectively.

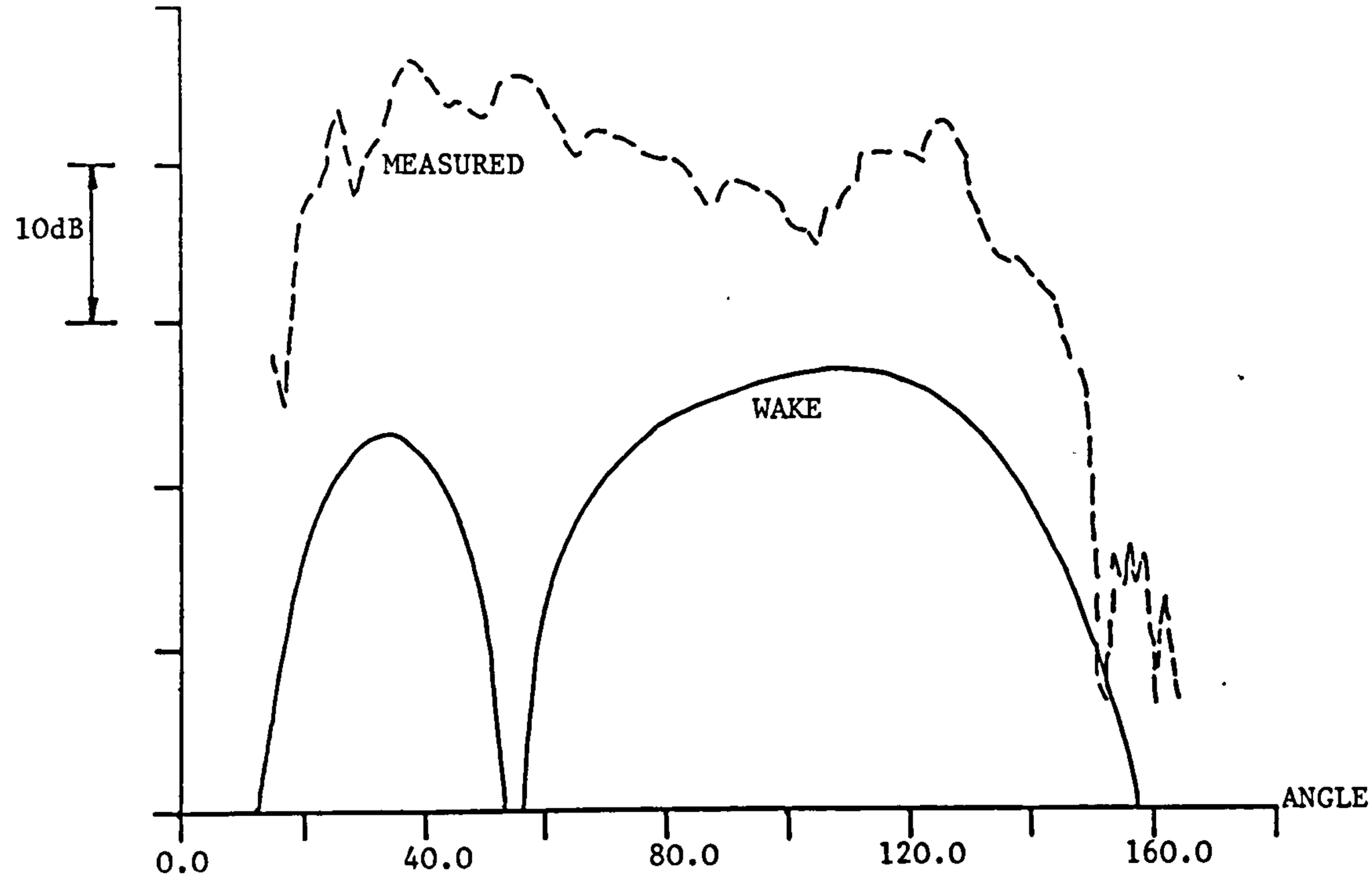

Figure 5.3 Gannet measurements vs predictions for the (1,2) interaction tone.

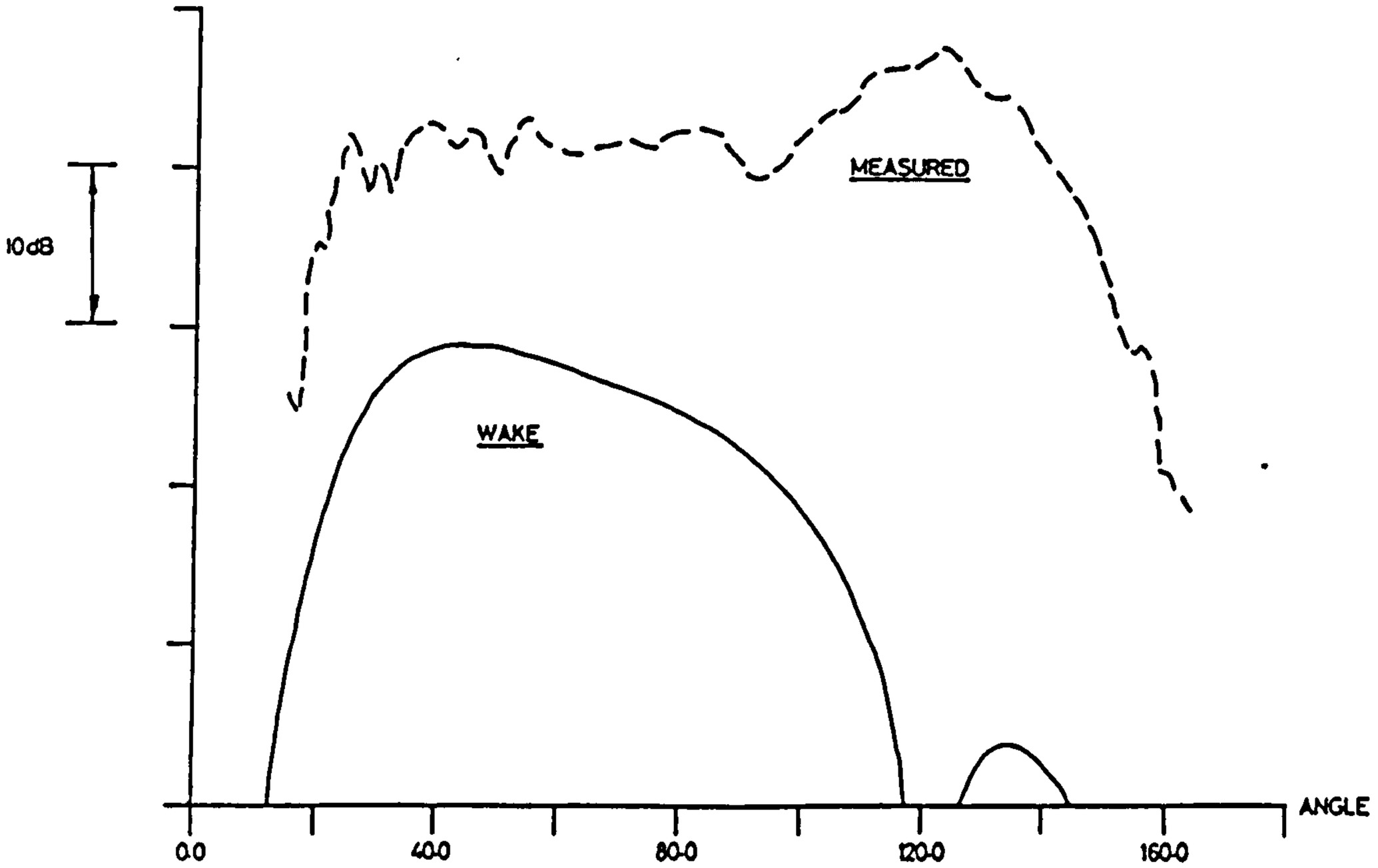

Figure 5.4 Gannet measurements vs predictions for the (2,1) interaction tone.

We now discuss the results obtain using the three different wake models described in sections 5.2 and 5.3. For the first three interaction tones on the Gannet, shown in Figures 5.2 to 5.4, the different wake models gave identical results. To understand the reason for this we consider the values of the wake wavenumber and the normalised Fourier coefficients for the Gannet. A typical value of the wake wavenumber, as defined by (5.3.10), for the first wake harmonic on the Gannet is $k_b \sim 0.05$*; the wake wavenumber obtained using the Reynolds wake model (where the wake width has a different dependence on drag coefficient from that calculated using the Schlichting and Gaussian models) differs only slightly from this and is, typically, about 10% higher. By using the series expansion for the Fresnel cosine integral from Abramowitz & Stegun (1965) we find that, for small wavenumbers, the normalised Fourier coefficients for the Schlichting wake model, defined by (5.3.12), can be approximated by

$$G(k_b) \sim 1 - \frac{5}{81} k_b^2 + O(k_b^4) \ . \qquad (5.5.1)$$

In addition, the Fourier coefficients for the Gaussian and Reynolds wake profiles, defined by (5.3.15), can be approximated by

$$G(k_b) \sim 1 - \frac{k_b^2}{4\ell n2} + O(k_b^4) \ . \qquad (5.5.2)$$

FOOTNOTE

* Here we have used the value of $b_{\frac{1}{2}}$ in the calculation of the wake wavenumber in order to obtain compatibility between the three wake models.

From (5.5.1) and (5.5.2) it is clear that all three wake profiles will give almost identical results unless $k_b = O(1)$. This shows that, for a low blade number propeller, the different wake models will only produce different results at high harmonics (typically, for $n_1 > 10$). From (5.2.31) and (5.2.44), combined with (5.3.10), we note that the dependence of the wake wavenumber on downstream distance is given by $k_b \sim (X/c)^{\frac{1}{2}}$. It then follows, from the discussion above, that for k_b to be O(1) at low harmonics on a propfan we must have $(X/c) = O(100)$. We conclude that, for all practical purposes, there will be no reduction of wake interaction noise on a propfan with increased rotor-rotor spacing; except, perhaps, at high frequencies. A plot of predicted wake interaction noise against rotor-rotor spacing is shown in Figure 5.5 for the first interaction tone on a 7 x 7 bladed propfan. The results for all three wake models overlay identically and, in addition, it is clear that there is no significant change in noise level with increased rotor separation, even when the rotors are 10 diameters apart. Experimental results obtained by Metzger & Brown (1987) confirm that there is little dependence of propfan noise on rotor-rotor spacing.

The results discussed above appear to conflict with general results obtained from work on fan noise where the wake interaction usually provides the dominant noise source. In addition it is well known that turbofan noise reduces with increasing rotor-stator separation. Accordingly, we will use the prediction scheme described in chapters 4 and 5 to predict the interaction noise generated by a model fan rig in order to explain these apparent anomalies.

5.5.2 Rotor-Stator Interactions

In this section we will compare predicted wake interaction noise levels with measurements taken from tests carried out by Rolls-Royce on

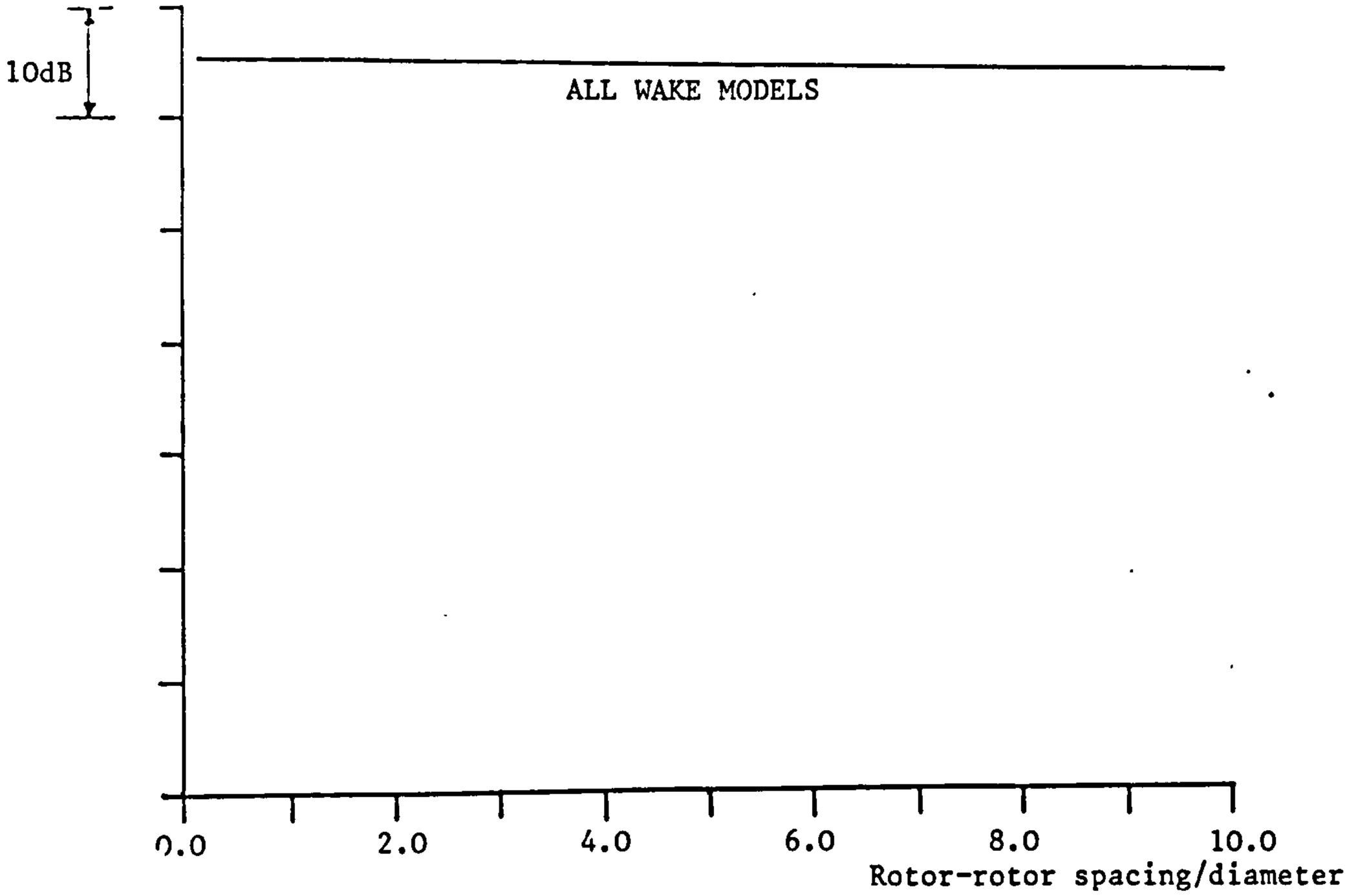

Figure 5.5 Predicted wake interaction noise vs rotor-rotor spacing for the (1,1) interaction tone on a 7 x 7 propfan.

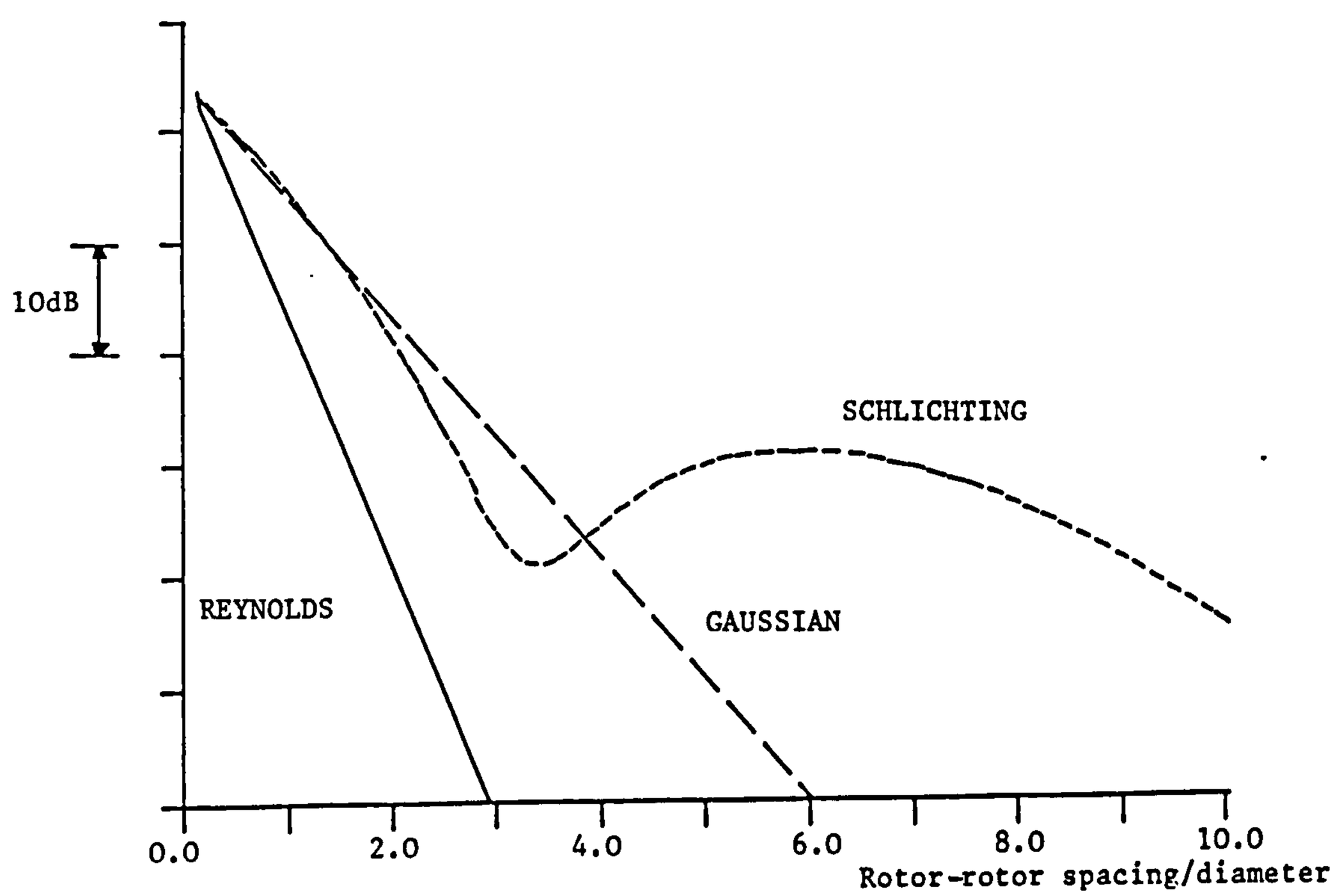

Figure 5.6 Predicted wake interaction noise vs rotor-rotor spacing for blade passing frequency on a 27-bladed fan rig.

a 27-bladed model fan rig. The tests are discussed in detail by Schwaller et al. (1984). Since we cannot expect the far field directivities to be the same on ducted and unducted configurations we will compare measured and predicted sound power levels in order to smooth out the directivity effects. In addition we consider only the rear arc data* so that rotor blockage† does not influence the results. Measurements taken of the wakes from the rotor suggest that the Schlichting or Gaussian wake models are the most appropriate. (However, these models still overpredict the wake defect velocity due to the fact that the effects of rotor swirl†† are not taken into account.)

The predictions of interaction noise at the first two harmonics of blade passing frequency for the three wake models, relative to measurements, are shown in Table 5.2. Clearly, the Schlichting and Gaussian wake

		Wake Models used in Prediction		
		Reynolds	Schlichting	Gaussian
Harmonic of Blade Passing Frequency	1	1.5	5.1	4.8
	2	-13.6	-1.0	-1.2

Table 5.2 Predicted PWL levels, relative to measurements, for the Rolls-Royce 27-bladed fan rig.

FOOTNOTES

* Rear arc data refers to measurements taken of the noise radiated from the rear of the fan rig (downstream of the stators).

† Acoustic duct modes which rotate in a direction counter to that of the rotor can be reflected back along the duct instead of propagating through the rotor; for a more detailed discussion of this phenomenon see Philpot (1975).

††On turbofan rotors the effect of blade camber is to change the direction of the airflow through the blade passages. The fluid then has non zero velocity in the direction of blade rotation. This velocity is termed the swirl velocity. On propfans swirl can, to a large extent, be neglected due to the low blade camber.

models produce similar interaction noise levels and agree with the measurements to within 5dB at blade passing frequency and to within 1dB at twice blade passing frequency. Since, as we commented above, the Schlichting and Gaussian wake models also provide the best agreement with the measured wake data, we can have some confidence in the prediction scheme for wake interaction noise. The Reynolds wake model produces noise levels which agree with the measurements to within 2dB at blade passing frequency but underpredicts by nearly 15dB at twice blade passing frequency. We now discuss the reasons for the difference in noise level obtained using the Reynolds wake model and either the Schlichting or Gaussian wake models.

Typical values of the wake wavenumber for the first wake harmonic on the fan rig are $k_b \sim 1$ for the Schlichting or Gaussian wake models, and $k_b \sim 1.6$ for the Reynolds wake model. The wake wavenumbers are much higher than those on the Gannet due to a higher number of blades (27 as opposed to 4) and higher section drag coefficients (typically 0.04 as opposed to 0.007). We can, therefore, no longer use the low wavenumber approximations to the normalised Fourier coefficients given by (5.5.1) and (5.5.2). Instead we must use the full expressions (5.3.12) and (5.3.15). A plot of the variation in noise level with increased rotor-rotor spacing, as predicted using the three wake models, is shown in Figure 5.6. From (5.3.10) this can also be viewed as a plot of the variation in noise level with k_b^2 (since $b \sim X^{\frac{1}{2}}$). We see that the Reynolds wake model produces a greater decay in noise level with k_b than either the Gaussian or Schlichting models which produce similar noise levels. However, at large rotor-rotor spacing, corresponding to $k_b \sim 6$

for the Gaussian or Schlichting wake models, the Gaussian wake model continues to produce noise levels which decay rapidly with wake wavenumber, but the decay in noise levels obtained using the Schlichting wake model is less rapid and tends to oscillate with wavenumber. The Reynolds and Gaussian wake models both produce noise levels which decay with wake wavenumber according to (5.3.15)*. The asymptotic Fourier coefficients for the Schlichting wake model are calculated in appendix 5.1 where it is shown that

$$G(k_b) \sim \frac{10}{3}\left(\frac{\pi}{2}\right)^{\frac{1}{2}} \frac{1}{k_b^{5/2}} \quad \text{as} \quad k_b \to \infty \,. \tag{5.5.3}$$

This explains why the interaction noise levels obtained using the Schlichting wake model decay only weakly at high wake wavenumbers, At these high wake wavenumbers the Fourier coefficients for the Schlichting wake profile are dominated by the contributions from the edges and the centre of the wake (where there is a discontinuity in the second derivative). In this wavenumber regime, therefore, we must view these rather artificial predictions with considerable caution. However, for current technology, low drag, fans it is unlikely that the wake wavenumbers will be high enough, in the audible frequency range, to enter this regime.

FOOTNOTE

* In (5.3.15) we must remember that the Reynolds wake is wider than the Gaussian wake, so that k_b is larger.

APPENDIX 5.1

Fourier Coefficients for the Schlichting Wake Model

From (5.3.9) the Fourier coefficients for the Schlichting wake model are defined by

$$G(k_b) = \frac{10}{9}\int_{-1}^{1} \left(1 - |\psi|^{3/2}\right)^2 e^{-ik_b\psi}\, d\psi \qquad \text{(A5.1.1)}$$

where the factor 10/9 is a normalising factor chosen so that $G(0) = 1$.

We rewrite (A5.1.1) in the form

$$G(k_b) = \frac{20}{9}\,(I_1 - 2I_2 + I_3) \qquad \text{(A5.1.2)}$$

where

$$I_1 = \int_0^1 \cos k_b\psi\, d\psi\ , \qquad \text{(A5.1.3)}$$

$$I_2 = \int_0^1 \psi^{3/2} \cos k_b\psi\, d\psi\ , \qquad \text{(A5.1.4)}$$

$$I_3 = \int_0^1 \psi^3 \cos k_b\psi\, d\psi\ . \qquad \text{(A5.1.5)}$$

The first integral I_1 can easily be evaluated as

$$I_1 = \frac{\sin k_b}{k_b}\ . \qquad \text{(A5.1.6)}$$

The third integral can be evaluated by repeated use of integration by parts leading to

$$I_3 = \frac{\sin k_b}{k_b} + \frac{3\cos k_b}{k_b^2} - \frac{6\sin k_b}{k_b^3} + \frac{6}{k_b^4}(1 - \cos k_b) \ . \qquad \text{(A5.1.7)}$$

In the second integral I_2 we substitute $\psi = \pi\theta^2/2k_b$ and again use repeated integration by parts. We then obtain

$$I_2 = \frac{\sin k_b}{k_b} + \frac{3}{2}\frac{\cos k_b}{k_b^2} - \frac{3}{2k_b^2}\left(\frac{\pi}{2k_b}\right)^{\frac{1}{2}} C\left[\left(\frac{2k_b}{\pi}\right)^{\frac{1}{2}}\right] \qquad \text{(A5.1.8)}$$

where C is the Fresnel cosine integral. From (A5.1.2) and (A5.1.6) to (A5.1.8) we find that the normalised Fourier coefficients are given by

$$G(k_b) = \frac{40}{3k_b^4}\left\{(1-\cos k_b - k_b \sin k_b) + \frac{k_b^2}{2}\left(\frac{\pi}{2k_b}\right)^{\frac{1}{2}} C\left[\left(\frac{2k_b}{\pi}\right)^{\frac{1}{2}}\right]\right\}. \qquad \text{(A5.1.9)}$$

When k_b is large we can use the large argument form of the Fresnel cosine integral from Abramowitz & Stegun (1965) which leads to

$$G(k_b) \sim \frac{10}{3}\left(\frac{\pi}{2}\right)^{\frac{1}{2}} \frac{1}{k_b^{5/2}} \text{ as } k_b \to \infty \ . \qquad \text{(A5.1.10)}$$

Note that this result can also be obtained directly from (A5.1.1) by the use of asymptotic Fourier transforms as described by Lighthill (1958).

6. POTENTIAL FIELD INTERACTIONS - INCOMPRESSIBLE FLOW

6.1 Introduction

In chapter 5 we calculated the unsteady flow generated by the wakes shed from the upstream blades of a counter-rotation propeller and the response of the downstream blades to each convected gust harmonic. Comparisons between the predicted far-field noise and measured Gannet data showed that not only were the predictions substantially below the measurements, by about 20dB in general, but also that the directivity was incorrectly predicted, resulting in under-predictions of about 50dB at some angles. Now, as we have mentioned previously, the forward and rearward rows of the Fairey Gannet propeller were run at slightly different speeds so that the different interaction tone components could be separated in terms of frequency. Bradley (1986) has shown that, for a specific interaction component, unsteady interaction noise sources on the forward blade row generate directivities different from those of unsteady interaction noise sources on the rear blade row. The only way the gross underprediction of the Gannet data can be reduced, therefore, is to introduce an unsteady interaction noise source on the forward blade row, namely that due to the interaction of the forward blades with the bound potential field (bound vortex and thickness fields) generated by the downstream blade row. It seems appropriate to include, in addition, the interaction of the downstream blades with the bound potential field generated by the forward blade row, because that is likely to generate at least as large a field as that from the interaction of the forward row with the potential field of the rear row - the latter involving a trailing edge (weakly loaded if a Kutta condition is satisfied), the former a leading edge (highly loaded).

In the previous chapter the flow was modelled as compressible throughout and the response of the downstream blades was calculated as though they were semi-infinite flat plates. Here, however, we must consider the response of both upstream and downstream airfoils. If, in calculating the response of an upstream airfoil, we retain the semi-infinite flat plate model then the airfoil is extended to upstream infinity; consequently it has no leading edge and therefore there can be no inverse square root singularity in the response. (The inverse square root singularity at the trailing edge is removed by the application of a Kutta condition.) The neglect of the standard leading edge singularity may influence the results. Since the response of a finite airfoil in compressible flow can only be calculated numerically it is difficult to determine the importance of the leading edge region. We will therefore proceed as follows.

For the present we assume the flow to be incompressible. Then the finite airfoil response can be calculated exactly. We can therefore compare the results from the semi-infinite airfoil high frequency approximation and the finite airfoil calculation in order to see whether the leading edge inverse square singularity influences the far-field noise. The extension to the compressible flow case will then be made in chapter 7 where we will take account of the results from the incompressible flow case.

In sections 6.2 and 6.3 we describe the bound potential field about each row of a counter-rotation propeller, in incompressible flow, due to blade thickness and blade circulation respectively. The potential field of each row is written in terms of harmonic components.

Next, in sections 6.4 and 6.5, we consider the response of upstream and downstream semi-infinite flat plates to each harmonic of the potential field generated by the downstream and upstream blade rows respectively.

As in chapter 5 we use the Wiener-Hopf technique in order to calculate the airfoil response. A Kutta condition is imposed at the trailing edge of the upstream plates. The response of a finite airfoil is described in section 6.6.

A comparison is then made between the finite airfoil and semi-infinite plate results, in the limit of large chord, in section 6.7. We show that, although the unsteady pressures match near the trailing edge* in the two cases, the total unsteady lift differs by a factor of $\pi/4$; the lift on a finite chord airfoil being lower.

In section 6.8 we compare far-field acoustic predictions with measured Gannet data. It is clear that the potential field interactions produce substantially higher noise levels, for the first few interaction tones, than the wake interactions. The differences between the finite airfoil and semi-infinite airfoil predictions are discussed, both by reference to the high frequency asymptotic limits, calculated in section 6.7, and the low frequency asymptotic limits, calculated in appendix 6.7.

6.2 Potential Field due to Blade Thickness

6.2.1 Velocity Potential

In order to calculate the potential flow about a blade row we consider the thickness and lift problems separately (see, for example, page 86 of Ashley & Landahl (1965)). In this section we discuss just the thickness problem.

We will assume that the airfoil cross section of the blades can be

---

FOOTNOTE

* Here we are considering an interaction between an upstream blade and the potential field of the downstream row.

approximated by an ellipse of major axis b and minor axis a (see Figure 6.1). In appendix 6.1 we show that the potential field about the ellipse, in a uniform flow of speed U_r parallel to the major axis, can be approximated by

$$\phi = \cos\alpha \left[-U_r x - U_r\, a\frac{(a+b)}{2}\frac{\partial}{\partial x}(\ell nR)\right] - \sin\alpha \left[-U_r y - U_r\, a\frac{(a+b)}{2}\frac{\partial}{\partial y}(\ell nR)\right], \tag{6.2.1}$$

where $R = (x^2 + y^2)^{\frac{1}{2}}$ and the coordinates x and y are shown in Figure 6.1. The angle α in (6.2.1) represents the blade stagger angle. On taking the Laplacian of (6.2.1) we obtain

$$\nabla^2\phi = -U_r\, a\,\frac{(a+b)}{2}\left\{\cos\alpha\,\frac{\partial}{\partial x} - \sin\alpha\,\frac{\partial}{\partial y}\right\}\nabla^2(\ell nR) \tag{6.2.2}$$

$$= \pi U_r a(a+b)[\cos\alpha\ \delta'(x)\delta(y) - \sin\alpha\ \delta(x)\delta'(y)]$$

where $\delta(x)$ is the Dirac delta function and the primes denote differentiation with respect to argument.

In the case of an infinite cascade of airfoils, centres a distance s apart, we obtain

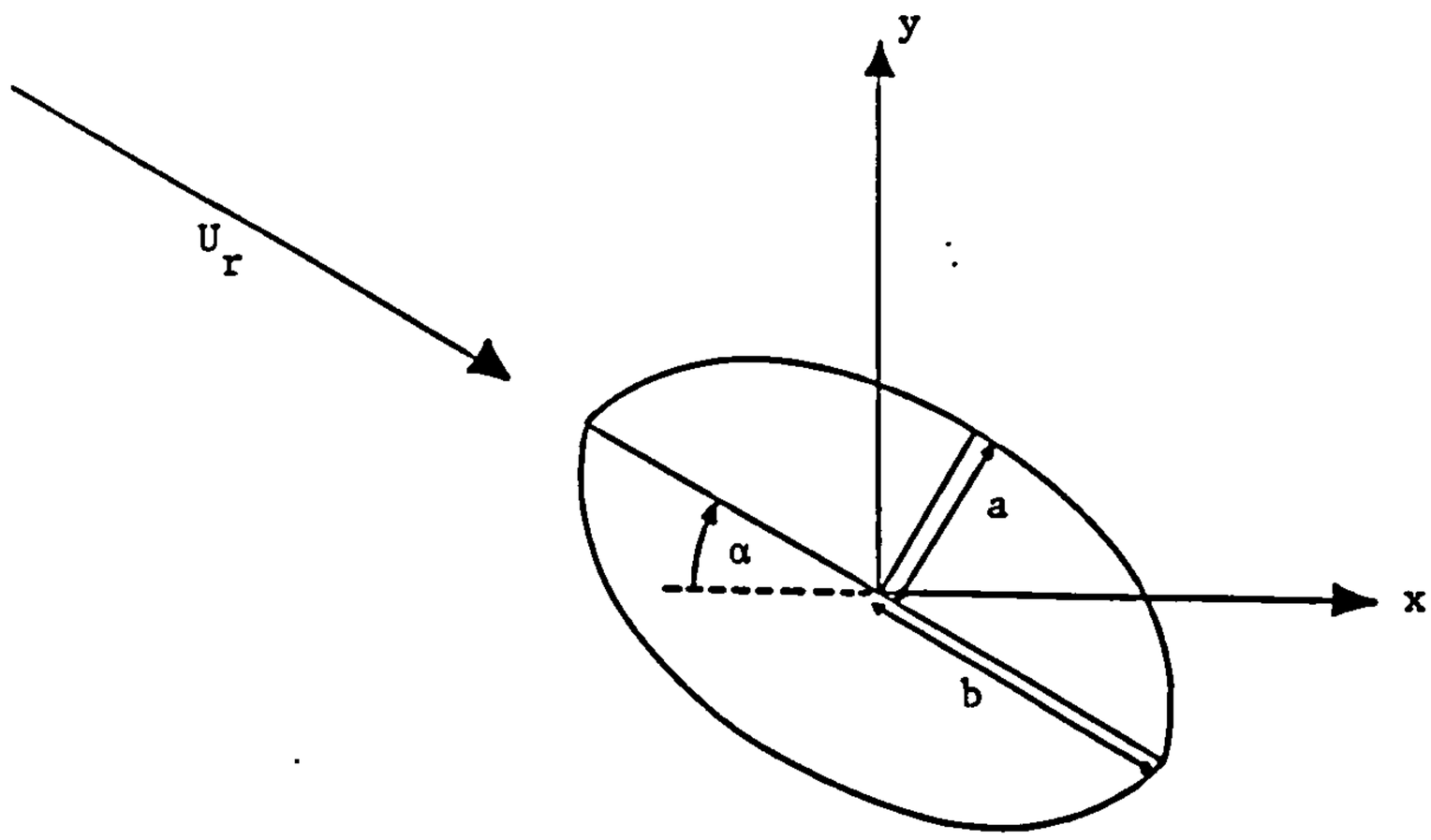

Figure 6.1 The cross section of each blade is represented by an ellipse of minor axis a and major axis b.

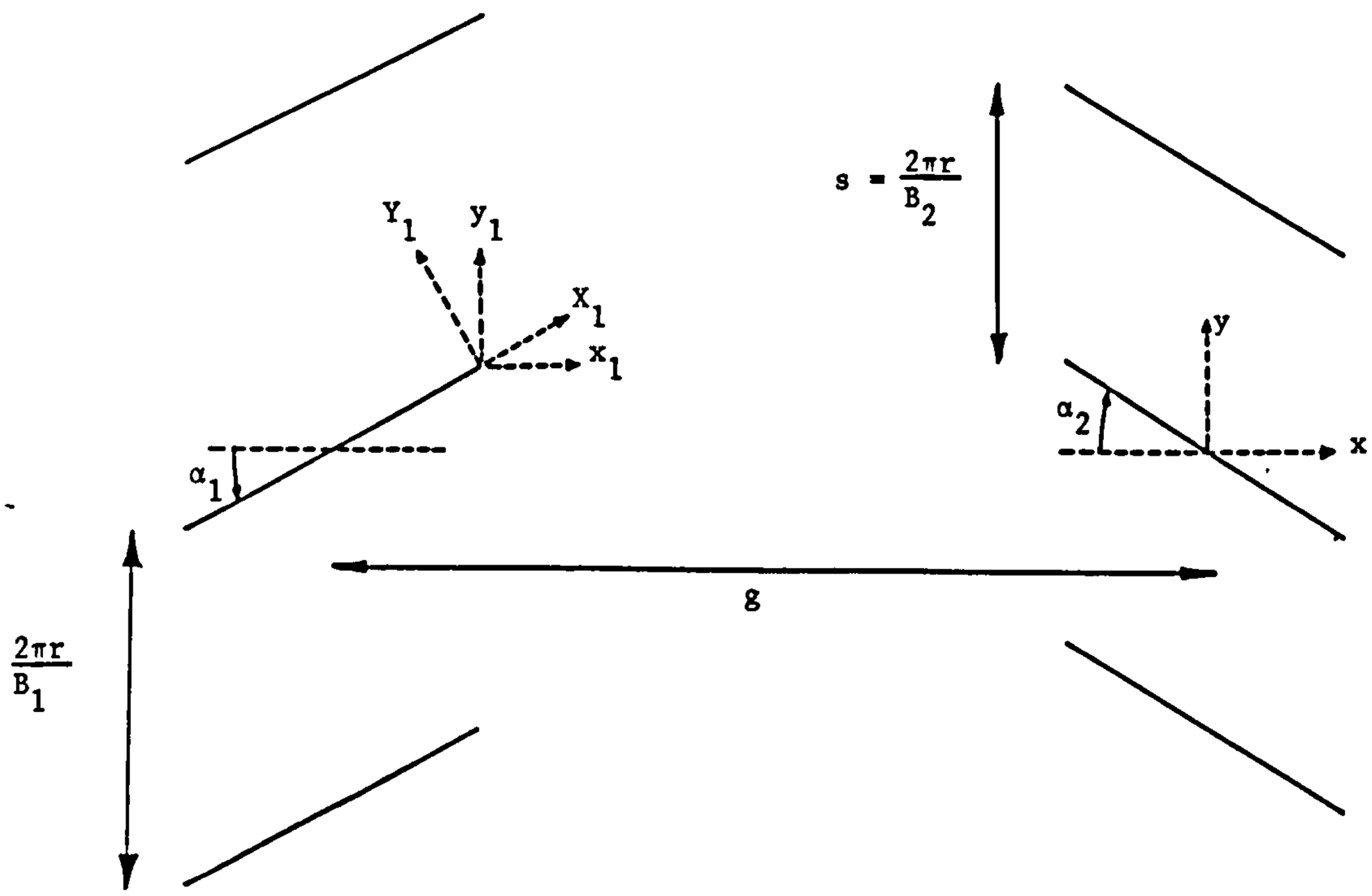

Figure 6.2 Coordinate systems for the interaction of the rear row potential field with the front row blades.

$$\nabla^2\phi = \pi U_r a(a+b) \sum_{n=-\infty}^{\infty} [\cos\alpha\ \delta'(x)\ \delta(y-ns) - \sin\alpha\ \delta(x)\ \delta'(y-ns)]. \tag{6.2.3}$$

Now, by Poisson's summation formula (see, for example, Lighthill (1958)) we know that

$$\sum_{n=-\infty}^{\infty} \delta(y-ns) = \frac{1}{s} \sum_{n=-\infty}^{\infty} \exp\left[-i2\pi \frac{ny}{s}\right] . \tag{6.2.4}$$

and, by differentiation, that

$$\sum_{n=-\infty}^{\infty} \delta'(y-ns) = \frac{-i2\pi}{s^2} \sum_{n=-\infty}^{\infty} n \exp\left[-i2\pi \frac{ny}{s}\right] . \tag{6.2.5}$$

We can then write (6.2.3) in the Fourier series form

$$\nabla^2\phi = \pi U_r \frac{a(a+b)}{s} \sum_{n=-\infty}^{\infty} \left[\cos\alpha\ \delta'(x) + \frac{i2\pi n}{s} \sin\alpha\ \delta(x)\right] \exp\left[-i2\pi n \frac{y}{s}\right] . \tag{6.2.6}$$

We try to obtain a solution to (6.2.6) in the form

$$\phi = \frac{\pi U_r a(a+b)}{s} \sum_{n=-\infty}^{\infty} [\lambda_1 \operatorname{sgn}(x) + \lambda_2]$$

$$\exp\left(-2\pi|n|\frac{|x|}{s} - i2\pi n \frac{y}{s}\right) , \tag{6.2.7}$$

where λ_1 and λ_2 are to be determined. On calculating the Laplacian of (6.2.7) and equating the coefficients of $\delta(x)$ and $\delta'(x)$ with those in (6.2.6) we obtain

$$\lambda_1 = \frac{\cos\alpha}{2} , \qquad \lambda_2 = \frac{-i \operatorname{sgn}(n)\sin\alpha}{2} , \tag{6.2.8}$$

so that ϕ is given by

$$\phi = \frac{\pi U_r a(a+b)}{2s} \sum_{n=-\infty}^{\infty} [\cos\alpha \operatorname{sgn}(x) - i \sin\alpha \operatorname{sgn}(n)]$$

$$\exp\left(-2\pi|n| \frac{|x|}{s} - i2\pi n \frac{y}{s}\right) . \tag{6.2.9}$$

6.2.2 Upwash on Upstream Airfoil

We now consider an isolated airfoil situated upstream of the cascade. The situation is shown in Figure 6.2. The upwash normal to the airfoil is given by

$$u_1 = -\sin\alpha_1 \frac{\partial\phi}{\partial x} + \cos\alpha_1 \frac{\partial\phi}{\partial y} \tag{6.2.10}$$

where α_1 is the stagger angle of the airfoil. In (6.2.9) we replace α with α_2, U_r with U_{r_2}, n with n_2, etc. (where the suffix 2 is used to denote values associated with the downstream blade row of a counter-rotation propeller, which is represented by the cascade). We take n_2 to be positive (it is clear from (6.2.9) that for n_2 negative the result is just the complex conjugate of that for n_2 positive) and x to be negative (in the upstream direction). Then, from (6.2.9) and (6.2.10),

$$u_1 = \frac{i\pi^2 U_{r_2} a_2(a_2+b_2)}{s_2^2} \sum_{n_2=-\infty}^{\infty} n_2 \exp\left[\frac{2\pi n_2}{s_2}(x_2-iy_2) + i(\alpha_2-\alpha_1)\right] . \tag{6.2.11}$$

We now define two new coordinate systems, (x_1,y_1) and (X_1,Y_1), as shown in Figure 6.2. The coordinates x_1 and y_1 are measured parallel to x and y with their origin located at the trailing edge of the upstream airfoil. The coordinates X_1 and Y_1 are measured parallel and normal to the upstream airfoil and their origin is also located at the trailing edge of the airfoil. Since the upstream airfoil represents a blade on the forward row of a counter-rotation propeller it must, of course, rotate. Similarly, the downstream cascade, which represents the rear row of a counter-rotation propeller, must also rotate. Specifically, the upstream airfoil moves in the negative y direction, with velocity $r\Omega_1$, and the cascade moves in the positive y direction, with velocity $r\Omega_2$, where Ω_1 and Ω_2 represent the angular speeds of the forward and rear rows and r is the radial station under consideration. The (x,y) and (x_1,y_1) coordinate systems are related by

$$\left.\begin{aligned} x &= x_1 - (g - c_1/2 \cos \alpha_1), \\ y &= y_1 + c_1/2 \sin\alpha_1 - r(\Omega_1 + \Omega_2)t , \end{aligned}\right\} \qquad (6.2.12)$$

where c_1 is the chord of the upstream airfoil and g is the distance (the "gap") between the midchords of the upstream and downstream airfoils. The (x_1,y_1) and (X_1,Y_1) coordinate systems are related by

$$\left.\begin{aligned} x_1 &= X_1\cos\alpha_1 - Y_1\sin\alpha_1 , \\ y_1 &= X_1\sin\alpha_1 + Y_1\cos\alpha_1 . \end{aligned}\right\} \qquad (6.2.13)$$

The cascade spacing s_2 is given by

$$s_2 = \frac{2\pi r}{B_2} \qquad (6.2.14)$$

where B_2 is the number of blades on the downstream blade row. The upwash in (6.2.11) can then be written in the form

$$u_1 = \sum_{n_2=-\infty}^{\infty} v_1 \exp[\gamma_1(X_1 - iY_1) + i\omega_1 t] \qquad (6.2.15)$$

where

$$v_1 = \frac{in_2B_2^2U r_2 a_2(a_2+b_2)}{4r^2} \exp\left[-\frac{n_2B_2}{r}\left(g - \frac{c_1 e^{-i\alpha_1}}{2}\right) + i(\alpha_2-\alpha_1)\right], \qquad (6.2.16)$$

$$\gamma_1 = \frac{n_2 B_2}{r} e^{-i\alpha_1} \qquad (6.2.17)$$

and ω_1 is the angular frequency given by

$$\omega_1 = n_2 B_2 (\Omega_1 + \Omega_2) \ . \qquad (6.2.18)$$

6.2.3 Upwash on Downstream Airfoil

Here we consider an airfoil situated downstream of the cascade. The situation is the same as in section 5.4 and is shown in Figure 5.1. The upwash normal to the airfoil chord is given by

$$u_2 = \sin\alpha_2 \frac{\partial \phi}{\partial x} + \cos\alpha_2 \frac{\partial \phi}{\partial y} \qquad (6.2.19)$$

where α_2 is the stagger angle of the downstream airfoil. (Note that, as in the previous section, the suffices 1 and 2 are used to denote values associated with the upstream and downstream airfoils respectively). In (6.2.9) we replace α with $-\alpha_1$ (since the cascade is now staggered in the opposite direction to that considered in section 6.2.1) and n with $-n_1$ (since the cascade rotates in the opposite direction to that considered in section 6.2.1). We take n_1 to be positive (as commented previously, we can take complex conjugates for n_1 negative) and x to be positive (in the downstream direction). Then, from (6.2.9) and (6.2.19),

$$u_2 = \frac{i\pi^2 U_{r_1} a_1 (a_1+b_1)}{s_1^2} \sum_{n_1=-\infty}^{\infty} n_1 \exp\left[\frac{-2\pi n_1}{s_1}(x-iy) + i(\alpha_2-\alpha_1)\right]. \qquad (6.2.20)$$

The cascade spacing s_1 is given by

$$s_1 = \frac{2\pi r}{B_1} \tag{6.2.21}$$

where B_1 is the number of blades on the downstream row. On introducing the coordinate systems (x_2,y_2) and (X_2,Y_2), which are defined by (5.4.1) and (5.4.2) and are shown in Figure 5.1, the upwash in (6.2.20) can be written in the form

$$u_2 = \sum_{n_1=-\infty}^{\infty} v_2 \exp[\gamma_2(X_2-iY_2) + i\omega_2 t] \tag{6.2.22}$$

where

$$v_2 = \frac{in_1B_1^2U r_1 a_1(a_1+b_1)}{4r^2} \exp\left[\frac{-n_1B_1}{r}\left(g - \frac{c_2 e^{i\alpha_2}}{2}\right) + i(\alpha_2-\alpha_1)\right], \tag{6.2.23}$$

$$\gamma_2 = \frac{-n_1B_1}{r} e^{i\alpha_2} \tag{6.2.24}$$

and ω_2 is the angular frequency given by

$$\omega_2 = n_1B_1(\Omega_1+\Omega_2). \tag{6.2.25}$$

6.3 Potential Field due to Blade Circulation

6.3.1 Stream Function

In section 6.2 we calculated the flow about a blade row due solely to thickness effects, i.e. the blades were assumed to be operating at zero

angle of attack, and also calculated the resulting upwash on an upstream or downstream airfoil. To complete the formulation we now need to consider the lifting flow about a row of flat plates (airfoils of infinitesimal thickness) operating at an angle of attack.

A flat plate operating at incidence to the mean flow generates lift which, by the Kutta-Joukowski law (see, for example, Ashley & Landahl (1965)), can be related to the airfoil circulation. We will therefore model each section of a blade by a point vortex with the appropriate circulation.

In terms of the stream function ψ, the x and y components of the velocity field are

$$u_x = \frac{\partial \psi}{\partial y} , \quad u_y = \frac{-\partial \psi}{\partial x} , \tag{6.3.1}$$

where the coordinate system is shown in Figure 6.3. It follows that for an infinite row of point vortices, each of circulation Γ, situated at $x = 0$, $y = ns$ where n is any integer, ψ must satisfy

$$\nabla^2 \psi = -\Gamma \, \delta(x) \sum_{n=-\infty}^{\infty} \delta(y-ns) . \tag{6.3.2}$$

From (6.2.4) we can rewrite this in Fourier series form as

$$\nabla^2 \psi = - \frac{\Gamma}{s} \, \delta(x) \sum_{n=-\infty}^{\infty} \exp\left[-i2\pi n \frac{y}{s}\right] . \tag{6.3.3}$$

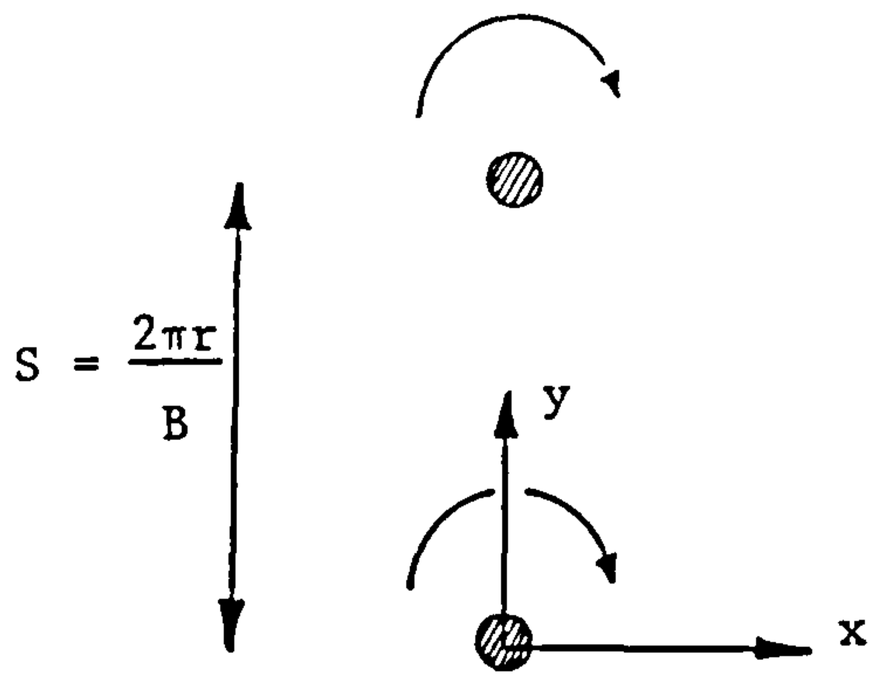

Figure 6.3 The potential field due to blade circulation can be modelled by replacing each blade section with a point vortex having the same circulation.

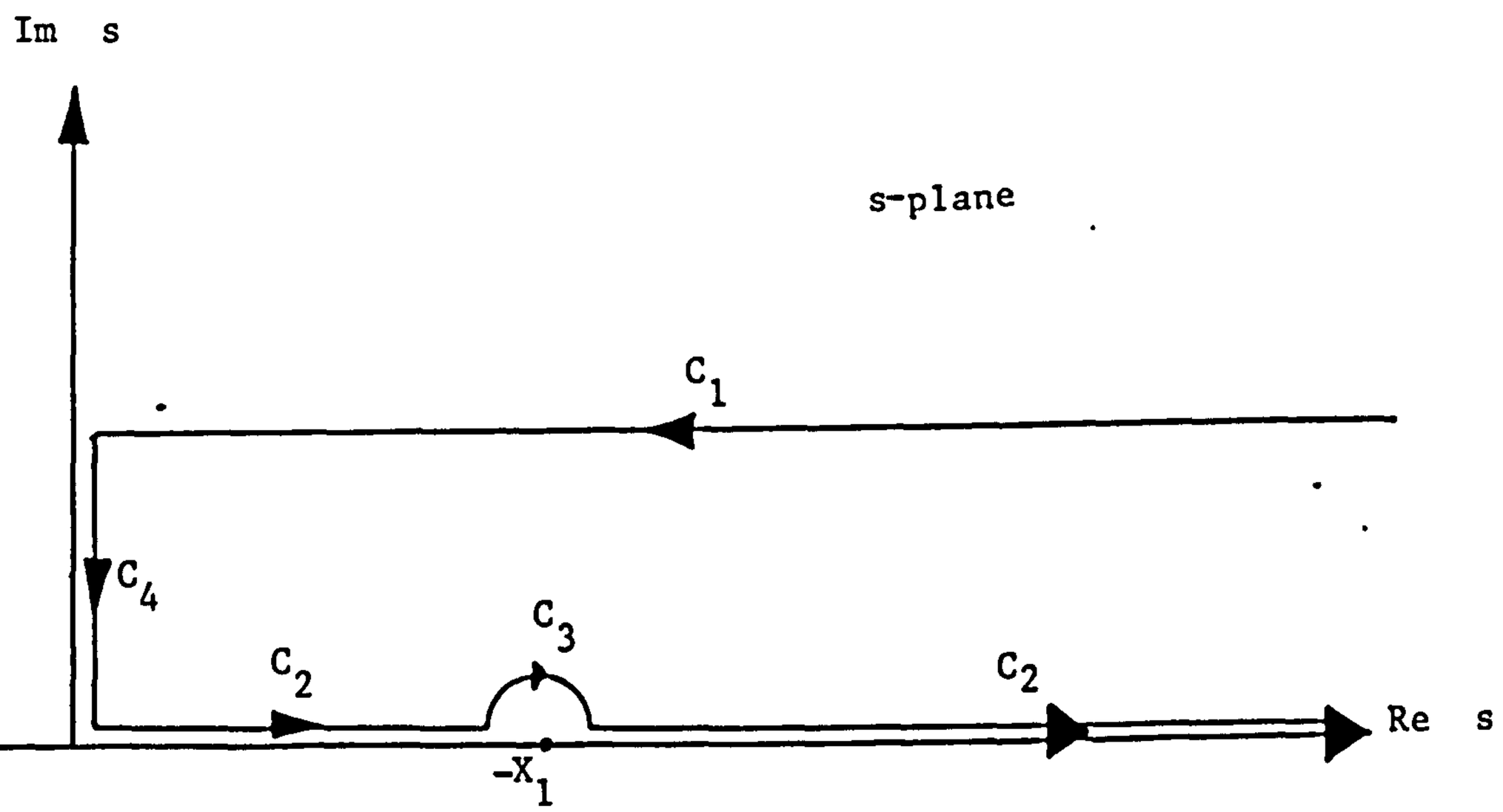

Figure 6.4 Contour used to evaluate the integral in (6.7.3).

The solution to (6.3.3) then follows immediately as*

$$\psi = \frac{\Gamma}{4\pi} \sum_{n=-\infty}^{\infty} \frac{1}{|n|} \exp\left[-2\pi|n| \frac{|x|}{s} - i2\pi n \frac{y}{s}\right] . \qquad (6.3.4)$$

6.3.2 Upwash on Upstream Airfoil

We now consider an airfoil situated upstream of the cascade: the situation is shown in Figure 6.2. The upwash normal to the airfoil is given by

$$u_1 = -\sin\alpha_1 \frac{\partial\psi}{\partial y} - \cos\alpha_1 \frac{\partial\psi}{\partial x} \qquad (6.3.5)$$

where α_1 is the stagger angle of the airfoil. By following the analysis in section 6.2.2 we find that the upwash normal to the airfoil can be written in the same form as (6.2.15), with (6.2.16) replaced by

$$v_1 = \frac{-\Gamma B_2}{4\pi r} \exp\left[\frac{-n_2 B_2}{r}\left(g - \frac{c_1}{2} e^{-i\alpha_1}\right) - i\alpha_1\right] . \qquad (6.3.6)$$

6.3.3 Upwash on Downstream Airfoil

Here we consider an airfoil downstream of the cascade as shown in Figure 5.1. The upwash normal to the airfoil is given by

---

FOOTNOTE

* It is to be understood that the summation given in (6.3.4) does not include the n = 0 contribution which is, in fact, given by $-\Gamma|x|/2s$. The n = 0 term represents the steady component (both spatially and temporally) of the velocity field and therefore has no influence on the unsteady lift to be calculated in sections 6.4 to 6.6.

$$u_2 = \sin\alpha_2 \frac{\partial\psi}{\partial y} - \cos\alpha_2 \frac{\partial\psi}{\partial x} \qquad (6.3.7)$$

where α_2 is the stagger angle of the downstream airfoil. By following the analysis in section 6.2.3 we find that the upwash normal to the airfoil can be written in the same form as (6.2.22), with (6.2.23) replaced by

$$v_2 = \frac{\Gamma B_1}{4\pi r} \exp\left[\frac{-n_1 B_1}{r}\left(g - \frac{c_2}{2} e^{i\alpha_2}\right) + i\alpha_2\right]. \qquad (6.3.8)$$

6.4 Response of Upstream Airfoil (Semi-Infinite)

In this section we consider the response of the upstream blades to the potential field generated by the rear row. Recall that (as we commented in the introduction to this chapter) the incompressible flow modelling of the potential field interaction in the current chapter is, in fact, just a prelude to the compressible flow model which will be discussed in chapter 7.

In the compressible flow case, as we found in chapter 5, the response of an airfoil to a gust cannot be calculated exactly in the general case (unless we use the numerical work of Graham (1970) or Adamczyk (1971)), but can only be given in the high frequency asymptotic limit*. For the interaction between the potential field of the downstream

FOOTNOTE

* The response can also be given in the low frequency asymptotic limit (see section 7.7).

row and an upstream blade the high frequency approximation can be interpreted physically as saying that the pressure oscillates rapidly away from the trailing edge and is, to a large degree, self-cancelling. The response should therefore be dominated by contributions from the trailing edge region (where the pressure is not simply a rapidly oscillating wave with slowly changing amplitude and phase) so that the blade can be modelled by a semi-infinite flat plate. The one area of concern in this model is the standard leading edge inverse square root singularity which has been thereby suppressed and, without resorting to a numerical solution, there is no exact way to assess the importance of this singularity in the compressible flow case.

In the incompressible flow case, however, the response of both finite and semi-infinite airfoils can be calculated. We can therefore determine, in this case, whether the leading edge provides a negligible or a non-negligible contribution to the total airfoil response. The results should indicate whether or not care should be taken in the treatment of the leading edge region in the compressible flow case.

We start, therefore, with an airfoil extending to upstream infinity and consider only the trailing edge problem. The velocity potential, ϕ, satisfies Laplace's equation

$$\nabla^2\phi = 0 \tag{6.4.1}$$

with the boundary condition

$$\frac{\partial\phi}{\partial Y_1} + v_1 e^{\gamma_1 X_1 + i\omega_1 t} = 0; \quad Y_1 = 0\pm, \quad X_1 < 0. \tag{6.4.2}$$

Also, neglecting vortex wakes for the moment, ϕ will be continuous across $Y_1 = 0$, $X_1 > 0$. Since ϕ must be an odd function of Y_1 this means that

$$\phi = 0; \quad Y_1 = 0, \quad X_1 > 0 \ . \tag{6.4.3}$$

We now have a two-part boundary value problem. The solution is obtained by using the Wiener-Hopf technique (see, for example, Noble (1958)). On imposing a Kutta condition at the trailing edge we then obtain the pressure difference across the plate as*

$$\Delta p(X_1) = -2i\rho U_{r_1} v_1 e^{i\omega_1 t}\left(1 + \frac{i\omega_1}{\gamma_1 U_{r_1}}\right)\left\{e^{\gamma_1 X_1} - w[-(-X_1)^{\frac{1}{2}}\gamma_1^{\frac{1}{2}}]\right\} \ . \tag{6.4.4}$$

The total lift acting on the airfoil is obtained by integrating (6.4.4) along the airfoil chord. There follows

$$\frac{dL_1}{dr} = \frac{-2i\rho U_{r_1} v_1 e^{i\omega_1 t}}{\gamma_1}\left(1 + \frac{i\omega_1}{\gamma_1 U_{r_1}}\right)\left[e^{-\gamma_1 c_1} - w(\gamma_1^{\frac{1}{2}} c_1^{\frac{1}{2}}) + 2i\left(\frac{\gamma_1 c_1}{\pi}\right)^{\frac{1}{2}}\right] \tag{6.4.5}$$

where c_1 is the chord of the upstream blade.

FOOTNOTE

* The use of the Wiener-Hopf technique, and the trailing edge Kutta condition, are discussed in more detail in chapter 7.

In the following section we proceed to calculate the response of a downstream blade to the bound potential field generated by the upstream blade row.

6.5 Response of Downstream Airfoil (Semi-Infinite)

Here we assume that the airfoil response is dominated by contributions from the leading edge so that the airfoil can be modelled by a plate extending to downstream infinity. The flow is again taken to be incompressible. In this case the leading edge singularity will, of course, be retained. We will not be neglecting a singularity at the trailing edge since, in practice, the trailing edge singularity is relieved by the effects of viscosity*.

We therefore consider just the leading edge problem. The velocity potential, ϕ, satisfies Laplace's equation

$$\nabla^2\phi = 0 \tag{6.5.1}$$

with the boundary condition

$$\frac{\partial\phi}{\partial Y_2} + v_2 e^{\gamma_2 X_2 + i\omega_2 t} = 0; \quad Y_2 = 0\pm, \quad X_2 > 0. \tag{6.5.2}$$

In addition ϕ is continuous across $Y_2 = 0$, $X_2 < 0$. Since ϕ is odd in Y_2 this means that

$$\phi = 0; \quad Y_2 = 0, \quad X_2 < 0 \ . \tag{6.5.3}$$

FOOTNOTE

* See the discussion on the Kutta condition in appendix 7.3.

We now have a two part boundary value problem which can be solved, as in section 6.4, by using the Wiener-Hopf technique (see, in addition, chapter 7). We then obtain the pressure difference across the plate as

$$\Delta p(X_2) = 2i\rho v_2 U_{r_2} e^{i\omega_2 t}\left\{\left(1 + \frac{i\omega_2}{\gamma_2 U_{r_2}}\right)\left[w(iX_2^{\frac{1}{2}}\gamma_2^{\frac{1}{2}}) - e^{\gamma_2 X_2}\right] - \frac{1}{\gamma_2^{\frac{1}{2}}\pi^{\frac{1}{2}}X_2^{\frac{1}{2}}}\right\} . \quad (6.5.4)$$

The total lift acting on the airfoil is obtained by integrating (6.5.4) along the airfoil. The lift, per unit span, is then given by

$$\frac{dL_2}{dr} = \frac{2i\rho v_2 U_{r_2} e^{i\omega_2 t}}{\gamma_2}\left\{\left(1 + \frac{i\omega_2}{\gamma_2 U_{r_2}}\right)\left[w(ic_2^{\frac{1}{2}}\gamma_2^{\frac{1}{2}}) - e^{\gamma_2 c_2}\right] + \frac{2i}{\pi^{\frac{1}{2}}}\gamma_2^{\frac{1}{2}}c_2^{\frac{1}{2}}\frac{\omega_2}{\gamma_2 U_{r_2}}\right\} \quad (6.5.5)$$

where c_2 is the chord of the downstream blade.

We have now calculated the response of upstream and downstream airfoils to a potential field using the basic assumption that the airfoils can be replaced by semi-infinite flat plates. In the next two sections we will discuss the ramifications of this assumption.

6.6 Response of Finite Chord Airfoil

The response of an airfoil to a gust in incompressible flow is usually calculated by way of the Sears function (see Von Karman & Sears (1938) and Sears (1940)). However, since the potential flow field is not convected with the mean flow we cannot use directly these standard results.

Instead we use the results of Kemp (1952) who made the appropriate extensions to the response calculation for a gust moving at a velocity different from that of the mean flow.

We rewrite the gust velocity on $Y_1 = 0$ in the form

$$u = w_1 \exp(i\omega_1 t - i\mu_1 X_1) \qquad (6.6.1)$$

where w_1 is the normal gust velocity at the mid chord. The relationship between w_1 and v_1 is therefore

$$w_1 = v_1 e^{-\gamma_1 c_1/2} . \qquad (6.6.2)$$

In (6.6.1) μ_1 is the normalised gust wavenumber

$$\mu_1 = i\gamma_1 \frac{c_1}{2} \qquad (6.6.3)$$

and $\bar{X}_1$ is a normalised coordinate which is related to X_1 by

$$\bar{X}_1 = \frac{X_1}{c_1/2} + 1 . \qquad (6.6.4)$$

The unsteady pressure distribution on the airfoil in incompressible flow, due to the gust defined by (6.6.1), is given by Amiet (1973) as*

FOOTNOTE

* We note that the response of an airfoil to a completely arbitrary upwash is given in integral form in chapter 13 of Ashley & Landahl (1965).

$$\Delta p(\bar{X}_1) = 2\rho U_{r_1} w_1 \left\{ \left(\frac{1-\bar{X}_1}{1+\bar{X}_1} \right)^{\frac{1}{2}} \left[C(\sigma_1)(J_o(\mu_1) - iJ_1(\mu_1)) + iJ_1(\mu_1) \right] \right.$$

$$\left. - \frac{1}{\pi} \left(1 - \frac{\sigma_1}{\mu_1} \right) (1 - \bar{X}_1^2)^{\frac{1}{2}} \; I_1'(\bar{X}_1) \right\} e^{i\omega t} \qquad (6.6.5)$$

where σ_1 is the reduced frequency defined by

$$\sigma_1 = \frac{\omega_1}{U_{r_1}} \frac{c_1}{2} \, . \qquad (6.6.6)$$

In (6.6.5) $C(\sigma_1)$ is the Theodorsen function*, which is defined by

$$C(\sigma_1) = \frac{H_1^{(2)}(\sigma_1)}{H_1^{(2)}(\sigma_1) + iH_o^{(2)}(\sigma_1)} \, , \qquad (6.6.7)$$

where $H_n^{(2)}(x)$ is a Hankel function of the second kind of order n and argument x. The integral $I_1'(\bar{X}_1)$ in (6.6.5) is defined by

$$I_1'(\bar{X}_1) = \int_{-1}^{1} \frac{e^{-i\mu_1 \xi}}{(\bar{X}_1 - \xi)(1-\xi^2)^{\frac{1}{2}}} d\xi \qquad (6.6.8)$$

and is to be interpreted as a Cauchy principal value integral.

FOOTNOTE

* Theodorsen (1935).

The total airfoil lift is obtained by integrating (6.6.5) along the airfoil. The integrations are carried out in appendix 6.2 where it is shown that

$$\frac{dL_1}{dr} = \pi\rho c_1 U_{r_1} w_1 \left\{ C(\sigma_1)[J_o(\mu_1) - iJ_1(\mu_1)] + \frac{i\sigma_1}{\mu_1} J_1(\mu_1) \right\} e^{i\omega_1 t}, \qquad (6.6.9)$$

which agrees with the result of Kemp (1952).

In this section we have obtained expressions for the pressure and lift, per unit span, or an airfoil in incompressible flow. In the following section we will examine whether these results match with those obtained in section 6.4, for a semi-infinite airfoil, when the chord length becomes large.

6.7 Finite Airfoil vs Semi-Infinite Airfoil

6.7.1 Pressure

In this section we will take the results from section 6.6, for a finite airfoil, and let the chord become large. The results will then be compared with the response calculations in section 6.4 where we considered an airfoil extending to upstream infinity.

First we consider the unsteady pressure distribution on the airfoil, due to a nonconvected gust, which is given by (6.6.5). We switch back to the X_1 coordinate which is related to $\bar{X}_1$ by (6.6.4) and, in the Cauchy integral (6.6.8), we define

$$\xi = 1 - \frac{\ell}{c_1/2} . \qquad (6.7.1)$$

From (6.6.3), (6.6.4) and (6.7.1) the Cauchy integral can be rewritten as

$$I_1'(X_1) = \frac{e^{\gamma_1 c_1/2}}{2} \int_0^{c_1} \frac{e^{-\gamma_1 \ell}}{(\ell+X_1)\left(\frac{\ell}{c_1}\right)^{\frac{1}{2}}\left(1-\frac{\ell}{c_1}\right)^{\frac{1}{2}}} d\ell \ . \qquad (6.7.2)$$

We now let $c_1 \to \infty$. Since, from (6.2.17), the real part of γ_1 is positive the inverse square root singularity in the integrand at $\ell = c_1$ can be neglected since it is damped out by the exponential decay term $e^{-\gamma_1 \ell}$. The upper limit of integration can, for the same reason, be taken as infinite. We therefore obtain

$$I_1' = c_1^{\frac{1}{2}} \frac{e^{\gamma_1 c_1/2}}{2} \int_0^{\infty} \frac{e^{-\gamma_1 \ell}}{(\ell+X_1)\ell^{\frac{1}{2}}} d\ell \ . \qquad (6.7.3)$$

This integral can be evaluated by considering the contour shown in Figure 6.4. Here

$$C = C_1 + C_2 + C_3 + C_4 \qquad (6.7.4)$$

and, by Cauchy's theorem, the integral around C is zero since there are no singularities within the contour. Now the integral along C_4 tends to zero as the length of the contour reduces to zero so that

$$\int_{C_2} = \int_{-C_1} + \int_{-C_3} . \qquad (6.7.5)$$

From Abramowitz & Stegun (1965)

$$\int_{-C_1} = \frac{-i\pi c_1^{\frac{1}{2}} e^{\gamma_1 c_1/2}}{2(-X_1)^{\frac{1}{2}}} w[-(-X_1)^{\frac{1}{2}}\gamma_1^{\frac{1}{2}}] , \qquad (6.7.6)$$

where we must take

$$\arg(X_1) = \pi . \qquad (6.7.7)$$

In addition

$$\int_{-C_3} = \frac{i\pi c_1^{\frac{1}{2}} e^{\gamma_1 c_1/2} e^{\gamma_1 X_1}}{2(-X_1)^{\frac{1}{2}}} . \qquad (6.7.8)$$

The Cauchy integral corresponds to the integral along contour C_2 so that, from (6.7.5), (6.7.6) and (6.7.8),

$$I_1' = \frac{i\pi c_1^{\frac{1}{2}} e^{\gamma_1 c_1/2}}{2(-X_1)^{\frac{1}{2}}} \left\{ e^{\gamma_1 X_1} - w[-(-X_1)^{\frac{1}{2}}\gamma_1^{\frac{1}{2}}] \right\} . \qquad (6.7.9)$$

In appendix 6.3 we show that the factor

$$C(\sigma_1)[J_o(\mu_1) - iJ_1(\mu_1)] + iJ_1(\mu_1) \qquad (6.7.10)$$

is $O(\sigma_1^{-3/2})$ for c_1 large (here we have assumed that σ_1 and μ_1 are approximately of the same order) so that, to leading order, the unsteady pressure on the airfoil is given by the Cauchy integral term in (6.6.5). From (6.6.4), with c_1 large,

$$(1-\bar{x}_1^2)^{\frac{1}{2}} = 2\left[\frac{-x_1}{c_1}\right]^{\frac{1}{2}}\left[1 + \frac{x_1}{c_1}\right]^{\frac{1}{2}} \sim 2\left[\frac{-x_1}{c_1}\right]^{\frac{1}{2}} . \qquad (6.7.11)$$

The unsteady pressure difference across the airfoil can then be approximated by

$$\Delta p(x_1) \sim -2i\rho U_{r_1} w_1 e^{\gamma_1 c_1/2} e^{i\omega_1 t}\left[1 - \frac{\sigma_1}{\mu_1}\right]\left\{e^{\gamma_1 x_1} - w[-(-x_1)^{\frac{1}{2}}\gamma_1^{\frac{1}{2}}]\right\} . \qquad (6.7.12)$$

From (6.6.2), (6.6.3) and (6.6.6) this reduces to

$$\Delta p(x_1) \sim -2i\rho U_{r_1} v_1 e^{i\omega_1 t}\left[1 + \frac{i\omega_1}{\gamma_1 U_{r_1}}\right]\left\{e^{\gamma_1 x_1} - w[-(-x_1)^{\frac{1}{2}}\gamma_1^{\frac{1}{2}}]\right\} . \qquad (6.7.13)$$

which agrees exactly with the result for the semi-infinite airfoil, given by (6.4.4), which was calculated using the Wiener-Hopf technique.

6.7.2 Lift per unit Span

In section 6.7.1 we showed that the pressure distribution on a semi-infinite plate agrees with that on a finite chord airfoil when the chord

is large and for points not close to the airfoil leading edge. We now compare the total unsteady lift per unit span obtained in the two cases.

(a) Finite Airfoil

The section lift on a finite chord airfoil in incompressible flow was given in (6.6.9). In appendix 6.3 we show that the Bessel/Hankel function combination (i.e. the term in curly brackets) tends to

$$\left(1 - \frac{\sigma_1}{\mu_1}\right) \frac{e^{-i\mu_1 + i\pi/4}}{(2\pi\mu_1)^{\frac{1}{2}}} \tag{6.7.14}$$

as c_1 becomes large. Then from (6.6.3), (6.6.6) and (6.6.9),

$$\frac{dL_1}{dr} \sim \pi^{\frac{1}{2}} \frac{\rho U_{r_1} v_1 c_1}{(\gamma_1 c_1)^{\frac{1}{2}}} \left(1 + \frac{i\omega_1}{\gamma_1 U_{r_1}}\right) e^{i\omega_1 t} \quad \text{as } c_1 \to \infty . \tag{6.7.15}$$

(b) Semi-Infinite Airfoil

The section lift on a semi-infinite airfoil in incompressible flow was given in (6.4.28). We consider each of the three terms in square brackets in turn. The first is $e^{-\gamma_1 c_1}$ which is, of course, exponentially small as c_1 becomes small (recall, from (6.2.26), that the real part of γ_1 is positive). The second term is shown by Abramowitz & Stegun (1965) to be $O[(\gamma_1 c_1)^{-\frac{1}{2}}]$ as $c_1 \to \infty$. The third term is obviously $O[(\gamma_1 c_1)^{\frac{1}{2}}]$, and is therefore the leading order term. We then have

$$\frac{dL_1}{dr} \sim \frac{4}{\pi^{\frac{1}{2}}} \frac{\rho U_{r_1} v_1 c_1}{(\gamma_1 c_1)^{\frac{1}{2}}} \left(1 + \frac{i\omega_1}{\gamma_1 U_{r_1}}\right) e^{i\omega_1 t} \quad \text{as} \quad c_1 \to \infty . \tag{6.7.16}$$

By comparison with (6.7.15) we see that the total unsteady lift per unit span on a large, but finite, chord airfoil is $\pi/4$ times that on the equivalent length c_1, as measured upstream from the trailing edge, of a semi-infinite airfoil. In section 6.7.1, however, we found that the pressure distribution was the same in both cases. We will now discuss this apparent anomaly in more detail.

6.7.3 The Factor of $\pi/4$

The two expressions, (6.7.15) and (6.7.16), show that the total unsteady lift on an airfoil section does not converge with increasing chord length; in fact the lift diverges as $c_1^{\frac{1}{2}}$. It follows that the leading edge portion of the blade is important, even when the unsteady flow field decays exponentially with distance, as was the case here. In the analysis carried out in section 6.7.1 we made a number of approximations involving the leading edge portion of the airfoil. These approximations will now be reviewed.

In (6.7.2), the vorticity integral I_1' was approximated by neglecting the inverse square root singularity at the leading edge and extending the upper limit of integration to infinity. These steps are certainly justified since there is an exponential decay factor under the integral sign which damps out the leading edge contribution. A second approximation was made in (6.7.11) where, essentially, we assumed that $X_1/c_1 \ll 1$. Near the leading edge, however, $X_1/c_1 \sim 1$ and we have shown that the leading edge region provides a non-negligible contribution to the total airfoil lift. We must therefore retain the factor $(1 + X_1/c_1)^{\frac{1}{2}}$ in (6.7.11).

The effect of the factor $(1 + X_1/c_1)^{\frac{1}{2}}$ is to reduce the unsteady pressure difference across the airfoil to zero, parabolically, at the

leading edge*. Of course, in the case of a semi-infinite airfoil the parabolic decay factor cannot exist since there is no leading edge; that is why, on neglecting the parabolic decay factor, the unsteady pressure difference across the airfoil was shown to be the same as that on a semi-infinite plate.

If we now retain the parabolic decay factor $(1 + X_1/c_1)^{\frac{1}{2}}$ in (6.7.11) the unsteady pressure difference across the airfoil is given, in the large chord limit, by

$$\Delta p(X_1) \sim -2i\rho U_{r_1} v_1 e^{i\omega_1 t}\left\{1 + \frac{i\omega_1}{\gamma_1 U_{r_1}}\right\}\left\{1 + \frac{X_1}{c_1}\right\}^{\frac{1}{2}}\left\{e^{\gamma_1 X_1} - w[-(-X_1)^{\frac{1}{2}}\gamma_1^{\frac{1}{2}}]\right\}. \tag{6.7.17}$$

The unsteady lift per unit span is then obtained by integrating (6.7.17) along the airfoil chord. The integrations are carried out in appendix 6.4. There follows

$$\frac{dL_1}{dr} \sim \pi^{\frac{1}{2}} \frac{\rho U_{r_1} v_1 c_1 e^{i\omega_1 t}}{(\gamma_1 c_1)^{\frac{1}{2}}}\left\{1 + \frac{i\omega_1}{\gamma_1 U_{r_1}}\right\} \quad \text{as} \quad c_1 \to \infty \tag{6.7.18}$$

which agrees with the result given by (6.7.15) for the lift on a finite chord airfoil (exact solution) as $c_1 \to \infty$.

FOOTNOTE

* Recall here that we are considering the leading order contribution to the airfoil response at high reduced frequencies. The contribution from the leading edge (integrable) inverse square root singularity is only $O(\sigma_1^{-1})$ times that from the parabolic decay term and is therefore neglected.

The results of this section show that, in incompressible flow, the airfoil cannot accurately be modelled by a semi-infinite plate; even though the two solutions for the resultant unsteady pressure difference across the airfoil agree precisely except in the region of the leading edge. The reason for this is that the trailing edge region does not dominate the unsteady lift induced by the gust and the two solutions, for a finite and a semi-infinite airfoil, produce different unsteady pressure distributions in the region of the leading edge*: in the case of the finite airfoil the pressure drops parabolically to zero at the leading edge when the chord is sufficiently large (or, as is appropriate here, the gust frequency is sufficiently high); in the case of the semi-infinite airfoil there is, obviously, no leading edge and the unsteady pressure just decays as $(-X_1)^{-\frac{1}{2}}$ away from the trailing edge. The difference in pressure distributions near the leading edge in the two cases wholly accounts for the factor of $\pi/4$ between the lift on the trailing edge region, of length c_1, of a semi-infinite airfoil and that on a finite airfoil of length c_1.

For a downstream gust interaction problem in incompressible flow the same result holds; for either convected or nonconvected gusts (i.e., for wake or potential field interactions). In this case a Kutta condition is imposed at the trailing edge of the finite airfoil so that the unsteady pressure drops to zero there. The semi-infinite airfoil has no trailing edge and, as in the previous case, the pressure will just decay as $X_2^{-\frac{1}{2}}$ away from the leading edge. This difference in the trailing edge behaviour again results in a factor of $\pi/4$ between the lift on the leading edge region,

---

FOOTNOTE

* For the semi-infinite airfoil the leading edge is represented by the point $X_1 = -c_1$.

of length c_2, of a semi-infinite airfoil and that on a finite airfoil of length c_2.

The main approximation made in the current section (and, indeed, in the whole of the current chapter) is the assumption of incompressible flow. This implies that the sound speed is infinite, so that a disturbance at the trailing edge of an airfoil is felt immediately at the leading edge. In practice, since the sound speed is finite, there is a time delay of $c_1/(c_o - U_{r_1})$. In order that the phase difference between leading edge and trailing edge is not significant the time delay should be small in comparison to the period $2\pi/\omega_1$. Amiet (1973) suggests a fraction of $1/\pi$ as appropriate so that, for reasonable accuracy, we require

$$\frac{\sigma_1 M_{r_1}}{1-M_{r_1}} < 1 \ . \tag{6.7.19}$$

This means that, even if the Mach number is small, the incompressible flow assumption will produce inaccurate results for high reduced frequencies (i.e. large chord or high frequency). The semi-infinite airfoil assumption will, therefore, only produce the correct response at distances from the trailing edge compatible with (6.7.19), as was shown by the agreement between (6.4.27) and (6.7.13). We note that, in a discussion of the unsteady Kutta condition , Daniels (1978) found that in incompressible flow the unsteady pressure difference across an airfoil grew algebraically at large distances upstream from the trailing edge. Daniels comments that in the compressible flow case (which is considered by Crighton (1972)) the same is not true and the pressure oscillates away from the trailing edge. However, even in compressible

flow, we must be careful about the behaviour at large upstream distances from the trailing edge.

In chapter 7 we show how a trailing edge problem, in compressible flow, can be modified to provide the correct behaviour far upstream. The solution takes the form of an asymptotic series in increasing powers of $\sigma_1^{-\frac{1}{2}}$. The same procedure cannot, however, be used in incompressible flow because then each term in the series is of the same order, i.e. $O(\sigma_1^{-\frac{1}{2}})$.

6.8 Measurement vs Prediction

In this section we use the expressions for the unsteady lift given in sections 6.4 to 6.6, along with the radiation formulae given in chapter 4, to calculate the resultant far field noise. In the case of the downstream wake interaction, which was considered in chapter 5, the noise sources were positioned on the rearward blade row; here, however, we have noise sources on both forward and rearward blade rows. Since the relative phasing of the two sources must, therefore, be corrected to account for spatial separation* we will, for the present, consider the fields separately. Throughout the discussion we will refer back to the results of chapter 5 to determine the relative predicted noise levels due to potential field and wake interactions. The predictions will be compared with the measured Gannet flyover data which were discussed in section 2.3.

We start with the semi-infinite airfoil response calculations given in sections 6.4 and 6.5. The first interaction tone generated by the

---

FOOTNOTE

* Acoustic interference between the rotor-alone tones generated by the forward and rearward rows of a counter-rotation propeller are discussed by Hanson (1985a).

Gannet is the (1,1) interaction. The far-field directivity of this tone is shown in Figure 6.5. The first thing to note is that the predicted potential field interaction noise is significantly greater than the predicted wake interaction noise: the predicted forward and rearward potential field interaction tones* are, typically, 10dB and 20dB greater than the predicted wake interaction tone respectively. The second important point follows directly from the first: the predicted rearward potential field interaction noise is greater than the predicted forward potential field interaction noise, typically by about 10dB. The predicted rearward potential field interaction noise agrees well with the measured data in the forward arc ($0 \lesssim \theta \lesssim 90^{o}$) but underpredicts by approximately 5dB in the rear arc ($90^{o} \lesssim \theta \lesssim 180^{o}$). The next two interaction tones generated by the Gannet are the (2,1) and (1,2) interaction tones, for which directivity plots are shown in Figures 6.6 and 6.7. Here we see again that the predicted potential field interaction noise levels are significantly greater than the predicted wake interaction noise levels by, typically, 15dB (and more at some angles). Note that sources on the forward blade row (due to the upstream potential field interaction) generate far-field directivities different from those of sources on the rear blade row (due to the downstream wake and potential field interactions). This agrees with the general idea of Bradley (1986) which, as we have mentioned, led us to consider the potential field interactions. The

FOOTNOTE

* The forward potential field interaction refers to the interaction between the upstream blade row and the potential field generated by the rear row. The rearward potential field interaction refers to the interaction between the downstream blade row and the potential field generated by the forward row.

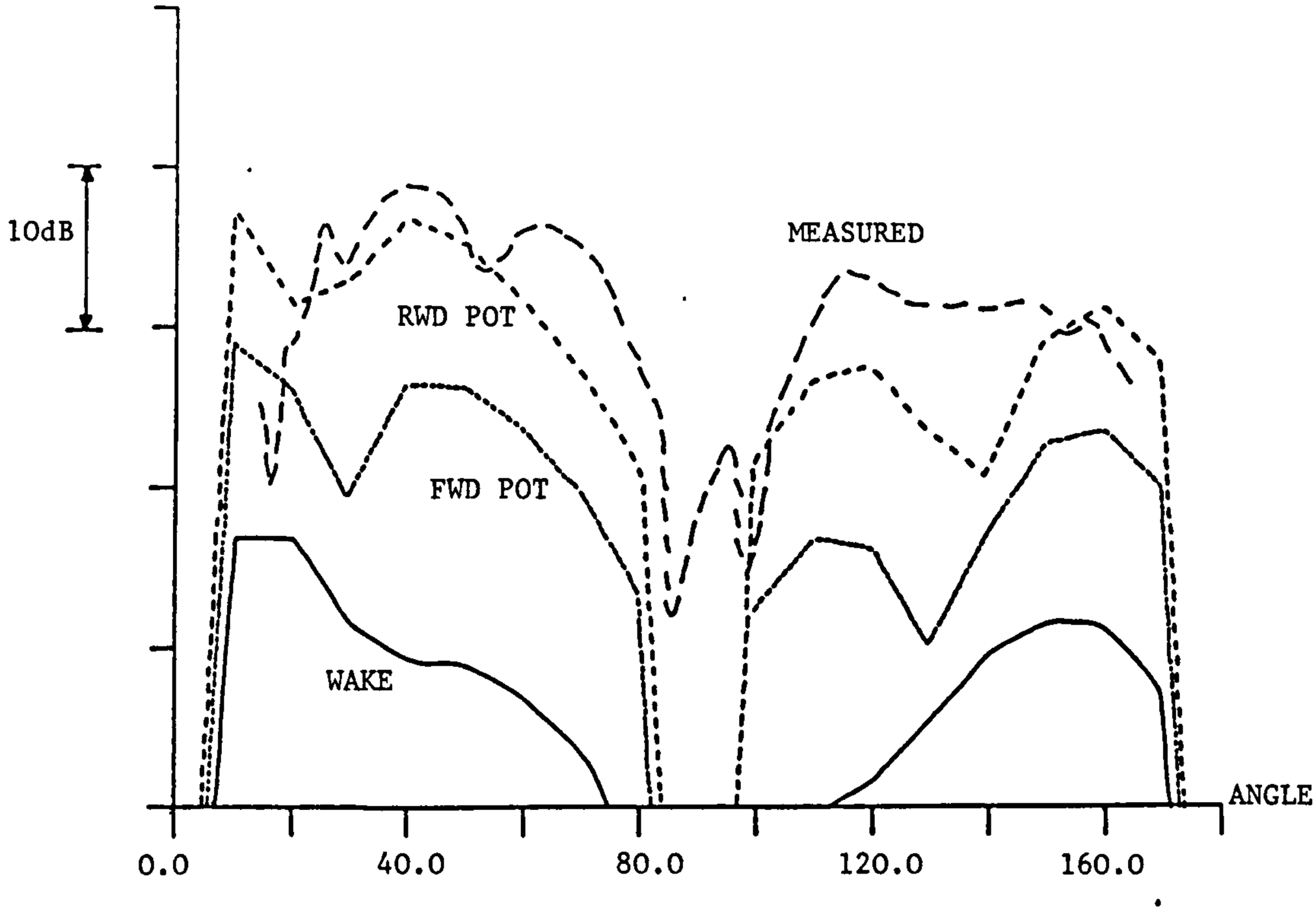

Figure 6.5 Gannet measurements vs predictions for the (1,1) interaction tone. The potential field predictions are obtained using semi-infinite airfoil response calculations in incompressible flow.

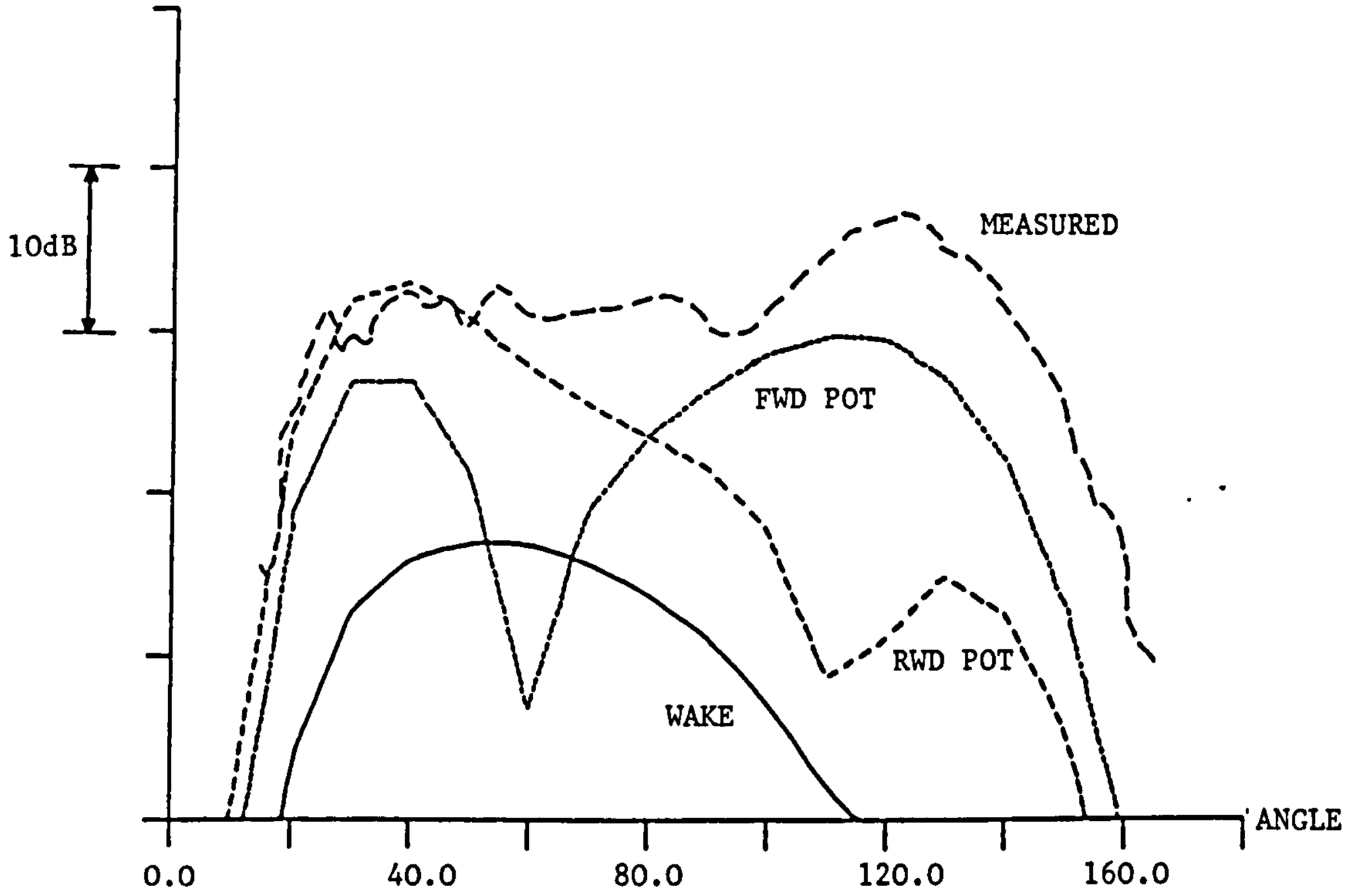

Figure 6.6 Gannet measurements vs predictions for the (2,1) interaction tone. The potential field predictions are obtained using semi-infinite airfoil response calculations in incompressible flow.

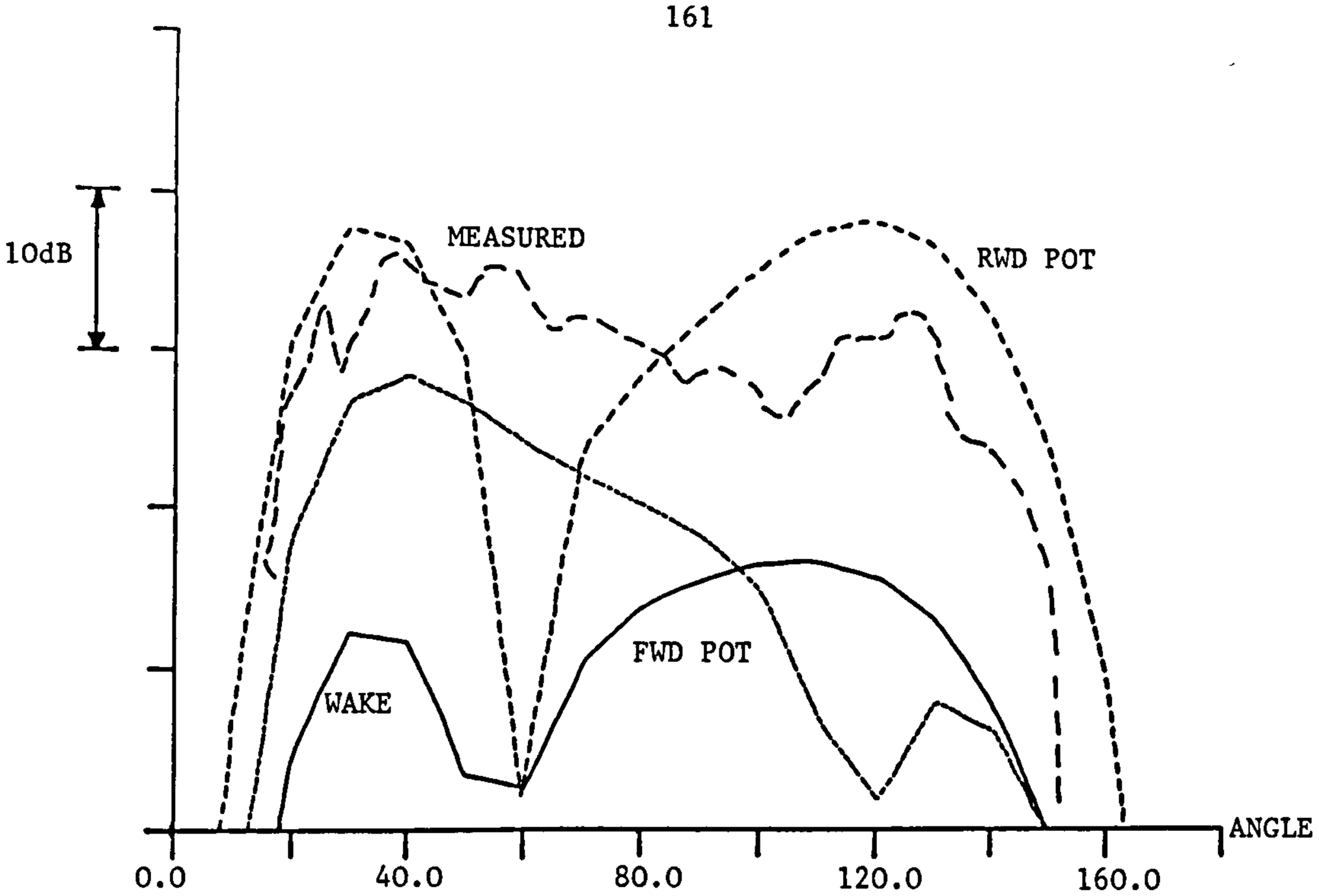

Figure 6.7 Ganner measurements vs predictions for the (1,2) interaction tone. The potential field predictions are obtained using semi-infinite airfoil response calculations in incompressible flow.

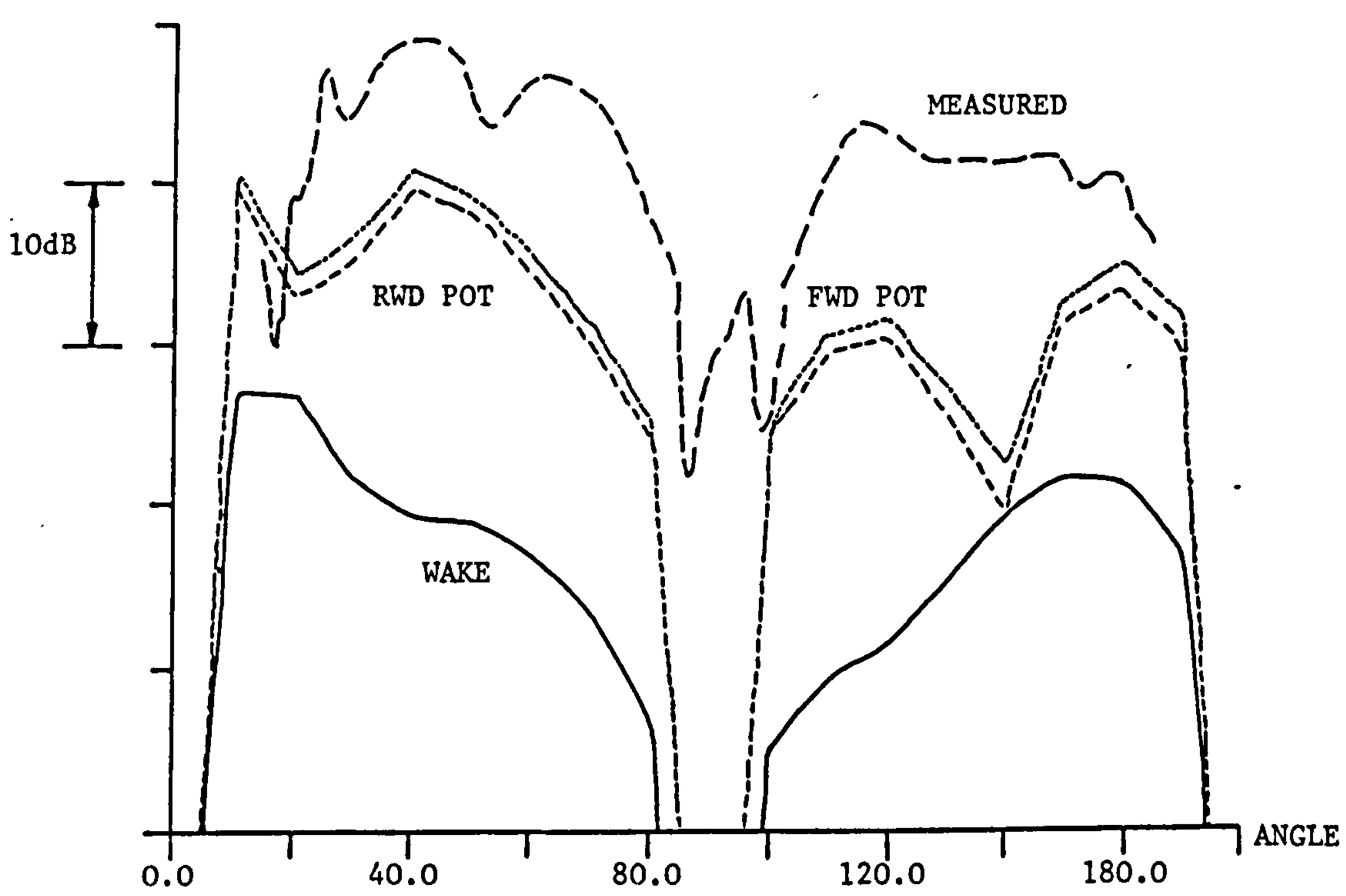

Figure 6.8 Gannet measurements vs predictions for the (1,1) interaction tone. The potential field predictions are obtained using finite chord response calculations in incompressible flow.

downstream potential field interaction is clearly the dominant source (except for the (2,1) interaction where the forward potential field interaction tone dominates in the rear arc) leading to good agreement with measurements in the forward arc and discrepancies of ± 5dB (depending on the interaction tone considered) in the rear arc.

Next we consider the finite chord calculations given in section 6.6 (these calculations are applied to both upstream and downstream potential field interactions). The far-field directivities of the (1,1), (2,1) and (1,2) interaction tones are shown in Figures 6.8, 6.9 and 6.10 respectively. By comparison with Figures 6.5, 6.6 and 6.7 we can see that the predicted upstream potential field interaction noise levels have increased, by about 3dB, and the predicted downstream potential field interaction noise levels have decreased, by about 7dB, in relation to the semi-infinite airfoil results. At first sight these results appear to conflict with the results of section 6.7 (i.e., that the semi-infinite airfoil model should give noise levels about 2dB above those obtained using the finite airfoil model); however, we must remember that the reduced frequencies of the first few Gannet interaction tones are not high, so that the results of section 6.7, which were obtained for the high reduced frequency limit, are not strictly applicable here. As an aid to understanding the results we discuss the low frequency behaviour of the airfoil response in appendix 6.5, for both the finite airfoil and the semi-infinite airfoils. There we show that the unsteady lift on the upstream blade row, as calculated using the semi-infinite airfoil model, is $O(\mu_1^{\frac{1}{2}})$, where μ_1 is small, times that calculated using the (exact) finite chord model. Consequently the far-field noise calculated using the semi-infinite airfoil model will be lower in magnitude than that calculated

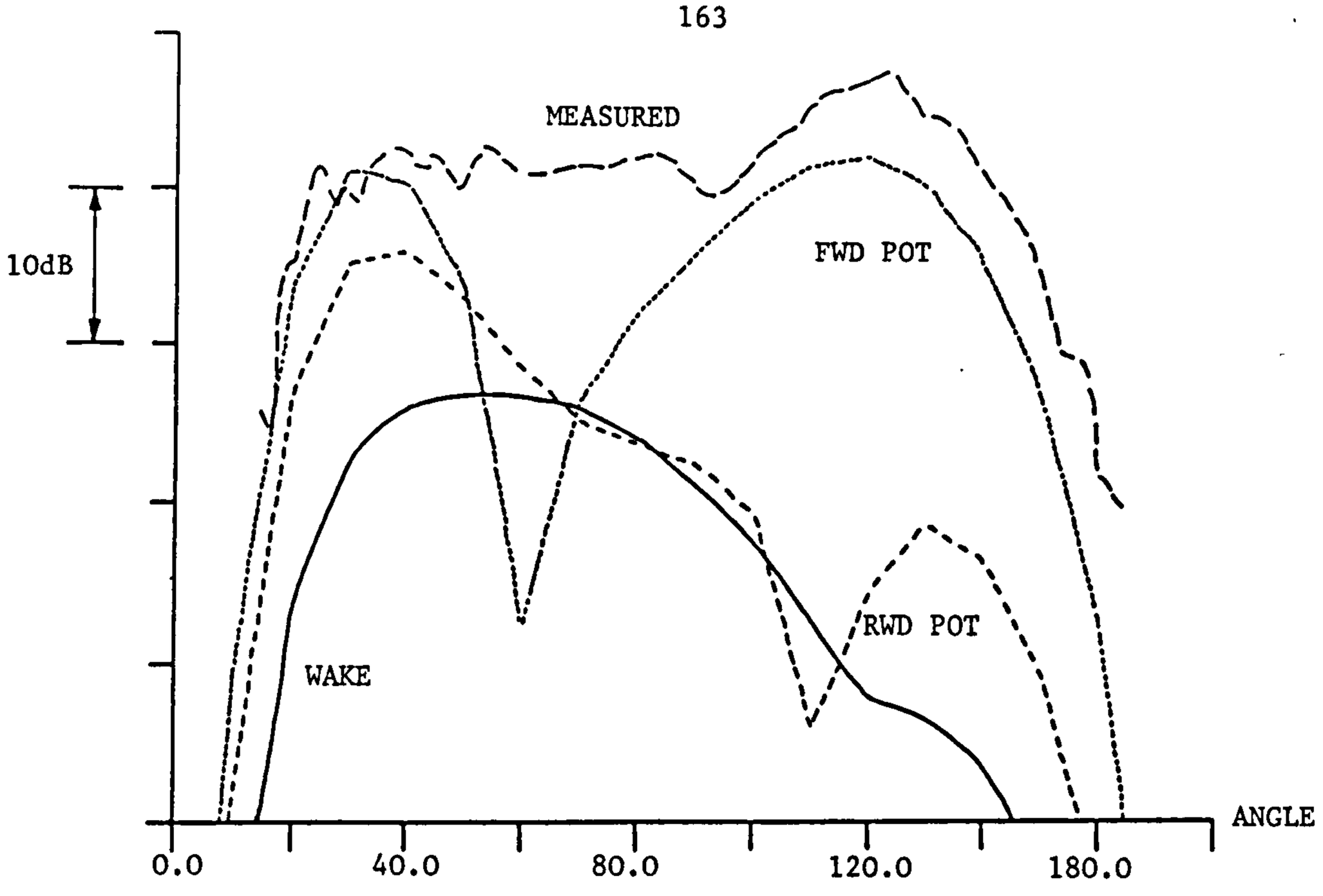

Figure 6.9 Gannet measurements vs predictions for the (2,1) interaction tone. The potential field predictions are obtained using finite chord response calculations in incompressible flow.

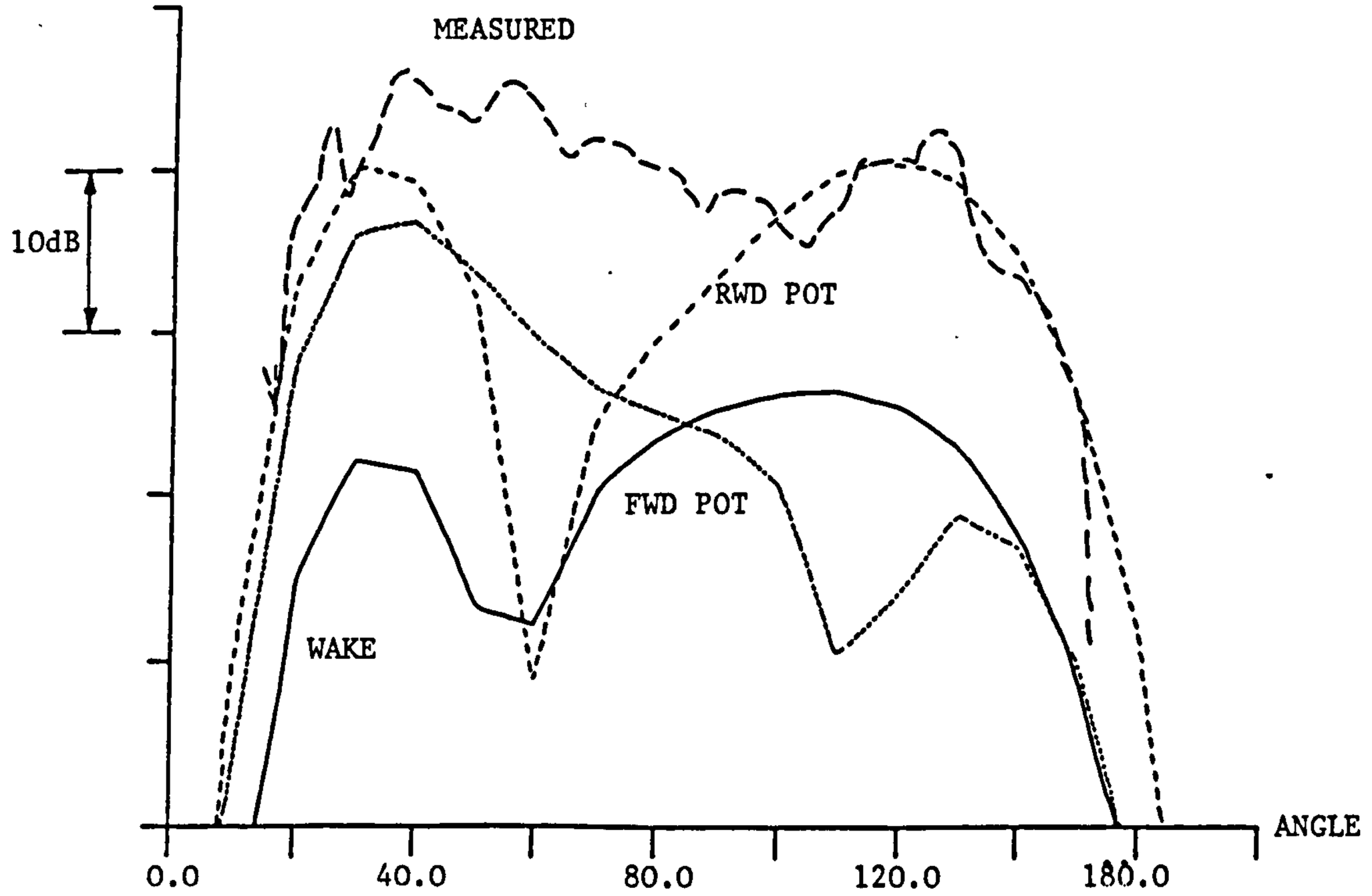

Figure 6.10 Gannet measurements vs predictions for the (1,2) interaction tone. The potential field predictions are obtained using finite chord response calculations in incompressible flow.

using the finite airfoil model in the low frequency limit. In addition we show, in appendix 6.5, that the unsteady lift on the downstream blade row, as calculated using the semi-infinite airfoil model, is $O(\mu_2^{-\frac{1}{2}})$, where μ_2 is small, times that calculated using the finite chord model. Consequently, in this case, the far field noise calculated using the semi-infinite airfoil model will be higher in magnitude than that calculated using the finite airfoil model in the low frequency limit. The differences in lift are, in each case, due to leading edge effects: for the upstream potential field interaction the finite airfoil response has an inverse square root singularity at the leading edge (which is not damped out by the decaying velocity field as it is in the high frequency case) whereas the semi-infinite airfoil response contains no singularity (there is, of course, no leading edge and a Kutta condition has been imposed at the trailing edge); for the downstream potential field interaction the unsteady pressure difference across a finite airfoil near the leading edge is $O(\mu_2^{\frac{1}{2}})$ times that across a semi-infinite airfoil near the leading edge.

These results show that for low frequency interactions in incompressible flow the semi-infinite airfoil approximation can result in substantial under-or over-predictions of the unsteady lift and hence in the radiated acoustic field. The errors can be attributed to erroneous behaviour near the leading edges of airfoils*.

For high frequency interactions in incompressible flow the semi-infinite airfoil approximation results in overprediction of the unsteady

---

FOOTNOTE

* In the case of an airfoil extending to upstream infinity the leading edge refers to the point one (real airfoil) chord length upstream from the trailing edge.

lift by a factor of $\pi/4$ and hence an overprediction of 2dB in the radiated sound field. The overprediction of the semi-infinite airfoil model here is entirely due to the behaviour away from the local airfoil edge (where the unsteady pressures agree between the two models): in the case of the finite airfoil model the pressure reduces to zero at the furthest edge; in the semi-infinite airfoil model the pressure does not reduce to zero but decays as $|X|^{-\frac{1}{2}}$ away from the local edge.

In the compressible flow case, which is discussed in the next chapter, it is not possible to calculate the airfoil response exactly* and we are forced to consider the high frequency limit. Consequently we will need to examine the leading edge behaviour, to ensure that important effects here are not neglected.

FOOTNOTE

* The airfoil response can, of course, be calculated exactly with a numerical solution such as that described by Graham (1970) or Adamczyk (1971).

APPENDIX 6.1

The Potential Field of an Ellipse

First we define a conformal mapping from a circle of radius r in the ξ plane to an ellipse, of major axis b and minor axis a, in the z-plane (see Figure 6.11). The mapping is of the form

$$z = \xi + \frac{\ell^2}{\xi} . \qquad \text{(A6.1.1)}$$

When $\xi = r$ the corresponding value of z is b and when $\xi = ir$ the value of z is ia. Using these values in (A6.1.1) and solving for r and ℓ we obtain

$$r = \frac{(a + b)}{2} , \quad \ell^2 = \frac{(b^2 - a^2)}{4} . \qquad \text{(A6.1.2)}$$

If we introduce flow of velocity U_r in the direction of the positive real axis then the complex potential, in the ξ-plane, is given by

$$w(\xi) = -U_r \xi - U_r \frac{r^2}{\xi} \qquad \text{(A6.1.3)}$$

(see, for example, Milne-Thompson (1948)). Far away from the origin the inverse of (A6.1.1) is

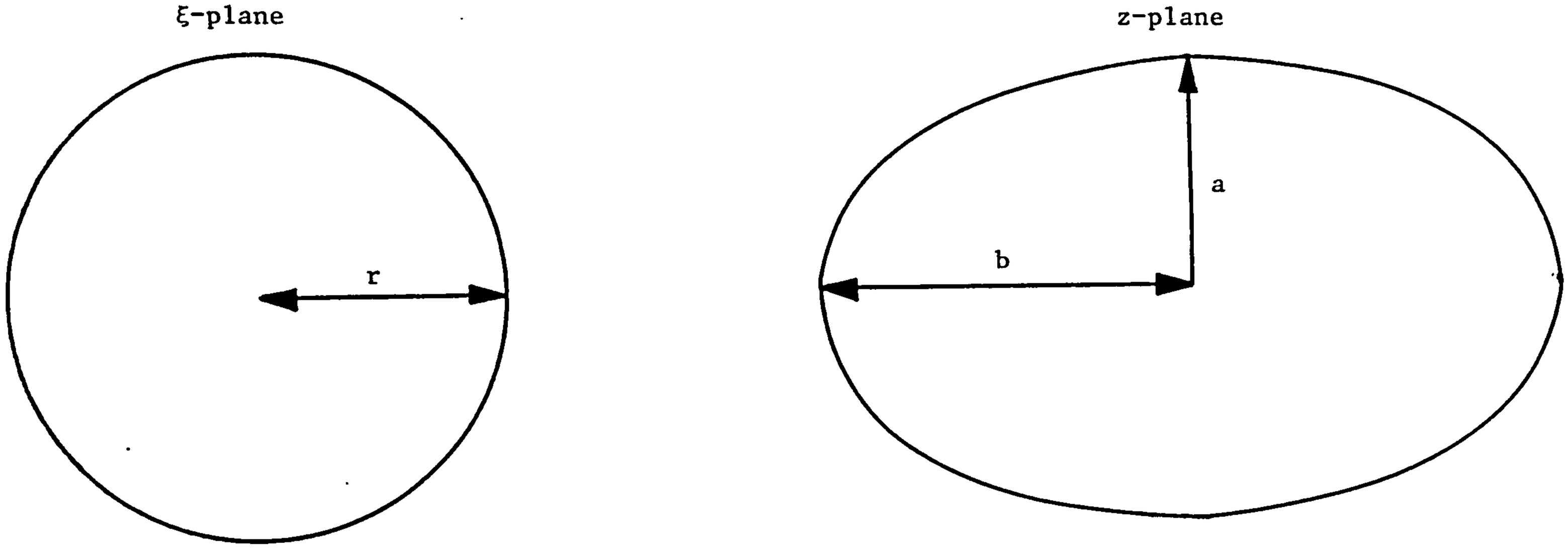

$$r = \frac{a + b}{2}$$

$$z = \xi + \frac{(b^2 - a^2)}{4\xi}$$

Figure 6.11 Conformal mapping from a circle in the ξ-plane to an ellipse in the z-plane.

$$\xi \sim z - \frac{\ell^2}{z} + \ell\, O\left[\left(\frac{\ell}{z}\right)^3\right] . \qquad \text{(A6.1.4)}$$

Then, in the z-plane, the complex potential is

$$w(z) \sim -U_r z - U_r \frac{(r^2-\ell^2)}{z} - U_r \ell\, O\left[\left(\frac{\ell}{z}\right)^3\right] . \qquad \text{(A6.1.5)}$$

From (A6.1.2) this reduces to

$$w(z) \sim U_r z - U_r \frac{a(a+b)}{2z} . \qquad \text{(A6.1.6)}$$

The velocity potential, ϕ, is given by the real part of (A6.1.6) so that

$$\phi = -U_r R\cos\Theta - U_r \frac{a(a+b)}{2R}\cos\Theta \qquad \text{(A6.1.7)}$$

where

$$z = Re^{i\Theta} = X + iY . \qquad \text{(A6.1.8)}$$

An alternative form for (A6.1.7) is given by

$$\phi = -U_r X - U_r \frac{a(a+b)}{2}\frac{\partial}{\partial X}(\ell nR) . \qquad \text{(A6.1.9)}$$

APPENDIX 6.2

Chordwise Integration (Finite Airfoil)

The pressure distribution along the airfoil is given by (6.6.5). The total lift is therefore obtained by integrating between $\bar{X}_1 = -1$ and $\bar{X}_1 = 1$ and multiplying by $c_1/2$ (since $\bar{X}_1$ represents distance scaled on the semichord). We therefore need to consider the single integral

$$I_1 = \int_{-1}^{1} \left(\frac{1 - \bar{X}_1}{1 + \bar{X}_1} \right)^{\frac{1}{2}} d\bar{X}_1 \qquad \text{(A6.2.1)}$$

and the double integral

$$I_2 = \int_{-1}^{1} (1 - \bar{X}_1^2)^{\frac{1}{2}} \int_{-1}^{1} \frac{e^{-i\mu_1 \xi}}{(\bar{X}_1 - \xi)(1 - \xi^2)^{\frac{1}{2}}} d\xi \; d\bar{X}_1 \; . \qquad \text{(A6.2.2)}$$

We now make the substitutions

$$\bar{X}_1 = -\cos\theta, \quad \xi = -\cos\phi \; . \qquad \text{(A6.2.3)}$$

The integral (A6.2.1) can then be simply evaluated as

$$I_1 = \pi \; . \qquad \text{(A6.2.4)}$$

The second integral (A6.2.2) becomes, on interchanging the order of integration,

$$I_2 = \frac{1}{2} \int_0^{\pi} e^{i\mu_1 \cos\phi} \int_0^{\pi} \frac{1-\cos 2\theta}{(\cos\phi - \cos\theta)} \, d\theta \, d\phi. \qquad \text{(A6.2.5)}$$

From page 93 of Glauert (1948) the inner integral in (A6.2.5) can be evaluated as $2\pi\cos\phi$. The outer integral then becomes

$$I_2 = \pi \int_0^{\pi} \cos\phi \; e^{i\mu_1 \cos\phi} \, d\phi = i\pi^2 J_1(\mu_1) \; . \qquad \text{(A6.2.6)}$$

The unsteady lift on the airfoil is given by, from (6.6.5),

$$\frac{dL_1}{dr} = \rho U_{r_1} w_1 c_1 e^{i\omega_1 t} \left\{ I_1 [C(\mu_1)(J_o(\mu_1) - iJ_1(\mu_1)) + iJ_1(\mu_1)] - \frac{1}{\pi}\left(1 - \frac{\sigma_1}{\mu_1}\right) I_2 \right\} \; . \qquad \text{(A6.2.7)}$$

The result (6.6.9) then follows from (A6.2.1), (A6.2.6) and (A6.2.7).

APPENDIX 6.3

High Frequency Response of a Finite Airfoil

The total unsteady lift on a finite airfoil (in incompressible flow) is given by (6.6.9). In order to approximate this at high reduced frequencies we use the asymptotic forms of the Bessel and Hankel functions given by Abramowitz & Stegun (1965). We then find that the asymptotic form of the Theodorsen function is

$$C(\sigma_1) \sim \tfrac{1}{2} + O(\sigma_1^{-1}) \quad \text{as} \quad \sigma_1 \to \infty \,. \tag{A6.3.1}$$

It follows that

$$\begin{aligned} C(\sigma_1)[J_o(\mu_1) - iJ_1(\mu_1)] + \frac{i\sigma_1}{\mu_1} J_1(\mu_1) &\sim \left(\frac{2}{\pi\mu_1}\right)^{\frac{1}{2}} \left\{[\tfrac{1}{2} + O(\sigma_1^{-1})]\right. \\ &\left. [\cos(\mu_1-\pi/4) - i\cos(\mu_1-3\pi/4)] + \frac{i\sigma_1}{\mu_1} \cos(\mu_1-3\pi/4) + O(\mu_1^{-1})\right\} \\ &= \left(\frac{2}{\pi\mu_1}\right)^{\frac{1}{2}} \left\{[\tfrac{1}{2} + O(\sigma_1^{-1})]\, e^{-i\mu_1+i\pi/4} + \frac{\sigma_1}{2\mu_1}\left(e^{i\mu_1-i\pi/4} + e^{-\mu_1+i\pi/4}\right)\right. \\ &\left. + O(\mu_1^{-1})\right\} \,. \end{aligned} \tag{A6.3.2}$$

Now μ_1 is defined by (6.6.3) and since, from (6.2.17), the real part of γ_1 is positive we must have

$$e^{i\mu_1} \to 0 \quad \text{as} \quad \mu_1 \to \infty \,. \tag{A6.3.3}$$

Then, from (A6.3.2) and (A6.3.3), we have to leading order in σ_1* that

$$C(\sigma_1)[J_o(\mu_1) - iJ_1(\mu_1)] + \frac{i\sigma_1}{\mu_1} J_1(\mu_1) \sim \left(1 - \frac{\sigma_1}{\mu_1}\right) \frac{e^{-i\mu_1 + i\pi/4}}{(2\pi\mu_1)^{\frac{1}{2}}} \,. \tag{A6.3.4}$$

Similarly, the Bessel function combination given by (6.7.10) becomes

$$C(\sigma_1)[J_o(\mu_1) - iJ_1(\mu_1)] + iJ_1(\mu_1) \sim \left(\frac{2}{\pi\mu_1}\right)^{\frac{1}{2}} \left[e^{i\mu_1 - i\pi/4} + O(\sigma_1^{-1})\right] \tag{A6.3.5}$$

$$= O(\sigma_1^{-3/2})$$

from (A6.3.3).

FOOTNOTE

* We have assumed here that σ_1 and μ_1 are of the same order.

APPENDIX 6.4

Chordwise Integration (Finite Airfoil with $c \to \infty$)

The pressure difference across an airfoil, in the large chord limit, is given by (6.7.17). In order to calculate the total lift, per unit span, we therefore need to consider the integrals

$$I_1 = \int_0^1 (1 - y)^{\frac{1}{2}} \, e^{-\gamma_1 c_1 y} \, dy \qquad \text{(A6.4.1)}$$

and

$$I_2 = \int_0^1 (1 - y)^{\frac{1}{2}} \, w(-\gamma_1^{\frac{1}{2}} c_1^{\frac{1}{2}} y^{\frac{1}{2}}) \, dy \, , \qquad \text{(A6.4.2)}$$

where we have replaced X_1 in (6.7.17) with $-c_1 y$. We calculate I_1 and I_2 for $\gamma_1 c_1$ large. The first integral I_1 can be evaluated in terms of error functions to give

$$I_1 = \frac{1}{\gamma_1 c_1} + \frac{i\pi^{\frac{1}{2}}}{2(\gamma_1 c_1)^{3/2}} e^{-\gamma_1 c_1} \, \mathrm{erf}(i\gamma_1^{\frac{1}{2}} c_1^{\frac{1}{2}}) . \qquad \text{(A6.4.3)}$$

On using the asymptotic form of the error function from Abramowitz & Stegun (1965) and neglecting terms of $O(e^{-\gamma_1 c_1})$ we find that

$$I_1 = \frac{1}{\gamma_1 c_1} + O[(\gamma_1 c_1)^{-2}] \, . \qquad \text{(A6.4.4)}$$

The second integral I_2 will be written as

$$I_2 = \left\{ \int_0^{\delta} + \int_{\delta}^{1} \right\} (1 - y)^{\frac{1}{2}} \, w(-\gamma_1^{\frac{1}{2}} c_1^{\frac{1}{2}} y^{\frac{1}{2}}) \, dy \qquad \text{(A6.4.5)}$$

where we define

$$\delta = (\gamma_1 c_1)^{-3/4} \qquad \text{(A6.4.6)}$$

for reasons that should become apparent. Since, for $\delta < y < 1$, we have

$$\left| \gamma_1^{\frac{1}{2}} c_1^{\frac{1}{2}} y^{\frac{1}{2}} \right| > \left| \gamma_1^{\frac{1}{2}} c_1^{\frac{1}{2}} \delta^{\frac{1}{2}} \right| = \left| \gamma_1^{1/8} \, c_1^{1/8} \right| , \qquad \text{(A6.4.7)}$$

we can use the asymptotic form for w in the second of the two integrals in (A6.4.5). Then

$$\int_{\delta}^{1} (1-y)^{\frac{1}{2}} \, w(-\gamma_1^{\frac{1}{2}} c_1^{\frac{1}{2}} y^{\frac{1}{2}}) \sim \frac{-i}{\pi^{\frac{1}{2}} \gamma_1^{\frac{1}{2}} c_1^{\frac{1}{2}}} \int_{\delta}^{1} \frac{(1-y)^{\frac{1}{2}}}{y^{\frac{1}{2}}} \, dy \, . \qquad \text{(A6.4.8)}$$

On making the substitution $y = \sin^2\theta$ we find that

$$\int_{\delta}^{1} \frac{(1-y)^{\frac{1}{2}}}{y^{\frac{1}{2}}} \, dy = \int_{\delta^{\frac{1}{2}}+O(\delta^{3/2})}^{\pi/2} (\cos 2\theta + 1) d\theta = \frac{\pi}{2} + O(\delta^{\frac{1}{2}}). \qquad \text{(A6.4.9)}$$

We now return to the first of the two integrals in (A6.4.5). Here we can write

$$\left| \int_0^{\delta} (1-y)^{\frac{1}{2}} \, w(-\gamma_1^{\frac{1}{2}} c_1^{\frac{1}{2}} y^{\frac{1}{2}}) dy \right| \leq \int_0^{\delta} \left| w(-\gamma_1^{\frac{1}{2}} c_1^{\frac{1}{2}} y^{\frac{1}{2}}) \right| dy \leq \delta \qquad \text{(A6.4.10)}$$

where we have used the fact that, from (6.2.17), $-\gamma_1^{\frac{1}{2}}$ (and hence $-\gamma_1^{\frac{1}{2}} c_1^{\frac{1}{2}} y^{\frac{1}{2}}$ since c_1 and y are real and positive) lies in the upper half plane where $|w|$ is bounded above by 1. Combining (A6.4.5) to (A6.4.10) we find that

$$I_2 = \frac{i\pi^{\frac{1}{2}}}{2\gamma_1^{\frac{1}{2}} c_1^{\frac{1}{2}}} + O[\delta^{\frac{1}{2}} (\gamma_1 c_1)^{-\frac{1}{2}}] + O(\delta) = \frac{-i\pi^{\frac{1}{2}}}{2\gamma_1^{\frac{1}{2}} c_1^{\frac{1}{2}}} + O\left[(\gamma_1 c_1)^{-3/4}\right] . \qquad \text{(A6.4.11)}$$

To leading order, then, the unsteady loading per unit span is, from the above results and (A6.4.17), given by

$$\frac{dL_1}{dr} \sim \pi^{\frac{1}{2}} \frac{\rho U_{r_1} v_1 c_1 e^{i\omega_1 t}}{\gamma_1^{\frac{1}{2}} c_1^{\frac{1}{2}}} \left\{ 1 + \frac{i\omega_1}{\gamma_1 U_{r_1}} \right\}. \qquad \text{(A6.4.12)}$$

APPENDIX 6.5

Low Frequency Effects

1. Total Unsteady Lift

1.1 Finite Airfoil

The unsteady lift per unit span is given by (6.6.9). In order to calculate the lift in the low frequency limit we use the small argument Bessel and Hankel function approximations from Abramowitz & Stegun (1965). Then the Theodorsen function can be approximated, at low reduced frequencies, by

$$C(\sigma_1) \sim 1 \, . \tag{A6.5.1}$$

Then, (6.6.9) reduces to

$$\frac{dL_1}{dr} \sim \pi\rho c_1 U_{r_1} w_1 \left\{ 1 + \frac{i\sigma_1}{2} - \frac{i\mu_1}{2} \right\} e^{i\omega_1 t} \, . \tag{A6.5.2}$$

From (6.6.2) w_1 can be replaced by v_1 when $\gamma_1 c_1$, or μ_1, is small. Then, to leading order, the unsteady lift is given by the quasi-steady approximation (see, for example, section 3.4.1 of Goldstein (1976))

$$\frac{dL_1}{dr} \sim \pi\rho c_1 U_{r_1} v_1 e^{i\omega_1 t} \, . \tag{A6.5.3}$$

1.2 Upstream Semi-Infinite Airfoil

Here we use the low argument approximation to the w-function in (6.4.5). For z small we have

$$w(z) \sim 1 + \frac{2iz}{\pi^{\frac{1}{2}}} - z^2 - \frac{4iz^3}{3\pi^{\frac{1}{2}}} + \ldots \qquad \text{(A6.5.4)}$$

(it is necessary here to retain the first 4 terms). Using this approximation in (6.4.5), with the exponential written in series form, we find that

$$\frac{dL_1}{dr} \sim \frac{-2i\rho U_{r_1} v_1 e^{i\omega_1 t}}{\gamma_1} \left(1 + \frac{i\omega_1}{\gamma_1 U_{r_1}}\right) \left\{ \left[1 - \gamma_1 c_1 + \frac{(\gamma_1 c_1)^2}{2}\right] \right. \qquad \text{(A6.5.5)}$$

$$\left. - \left[1 + \frac{2i(\gamma_1 c_1)^{\frac{1}{2}}}{\pi^{\frac{1}{2}}} - \gamma_1 c_1 - \frac{4i(\gamma_1 c_1)^{3/2}}{3\pi^{\frac{1}{2}}}\right] + \frac{2i(\gamma_1 c_1)^{\frac{1}{2}}}{\pi^{\frac{1}{2}}} \right\} .$$

Then, to leading order in $\gamma_1 c_1$ the unsteady lift is given by

$$\frac{dL_1}{dr} \sim \frac{8}{3\pi^{3/2}} \left(1 + \frac{i\omega_1}{\gamma_1 U_{r_1}}\right) (\gamma_1 c_1)^{\frac{1}{2}} \pi\rho c_1 U_{r_1} v_1 e^{i\omega_1 t} \qquad \text{(A6.5.6)}$$

which is $O[(\gamma_1 c_1)^{\frac{1}{2}}]$, or $O(\mu_1^{\frac{1}{2}})$, times the low frequency finite airfoil result (or quasi-steady result) given by (A6.5.3).

1.3 Downstream Semi-Infinite Airfoil

The low argument approximation to the w-function, given by (A6.5.4), is now substituted in (6.5.5). We then obtain, on using the series form for the exponential,

$$\frac{dL_2}{dr} = \frac{2i\rho v_2 U_{r_2} e^{i\omega_2 t}}{\gamma_2}\left\{\left(1 + \frac{i\omega_2}{\gamma_2 U_{r_2}}\right)\left[\left(1 - \frac{2(\gamma_2 c_2)^{\frac{1}{2}}}{\pi^{\frac{1}{2}}} + \gamma_2 c_2\right)\right.\right. \tag{A6.5.7}$$

$$\left.\left. -(1 + \gamma_2 c_2)\right] + \frac{2i}{\pi^{\frac{1}{2}}}\frac{\omega_2}{\gamma_2 U_{r_2}}(\gamma_2 c_2)^{\frac{1}{2}}\right\} .$$

To leading order in $\gamma_2 c_2$, then, the unsteady lift per unit span is given by

$$\frac{dL_2}{dr} = \frac{-4i}{(\gamma_2 c_2)^{\frac{1}{2}}\pi^{\frac{1}{2}}}\ \pi\rho c_2 U_{r_2} v_2 e^{i\omega_2 t} \tag{A6.5.8}$$

which is $O[(\gamma_2 c_2)^{-\frac{1}{2}}]$, or $O(\mu_2^{-\frac{1}{2}})$, times the low frequency finite airfoil result given by (A6.5.3)*.

2. Unsteady Pressure

2.1 Finite Airfoil

The unsteady pressure distribution across the airfoil is given by

---

FOOTNOTE

* For the downstream finite airfoil interaction the suffix 1 throughout (A6.5.3) is replaced with 2.

(6.6.5) where the singular integral I_1' is defined in (6.6.8). In (6.6.8) we will use the substitutions (A6.2.3). Then, on using the approximation

$$e^{-i\mu_1\xi} \sim 1 - i\mu_1\xi, \tag{A6.5.9}$$

we find that

$$I_1' \sim \int_0^{\pi} \frac{(1+i\mu_1\cos\phi)}{(\cos\phi-\cos\theta)}\, d\phi = i\mu_1\pi. \tag{A6.5.10}$$

If we now substitute (A6.5.10), the Bessel function low argument approximations, and the Theodorsen function approximation (A6.5.1) into (6.6.5) we obtain, to leading order in μ_1,

$$\Delta p(\bar{X}_1) \sim 2\rho U_{r_1} w_1 \left(\frac{1-\bar{X}_1}{1+\bar{X}_1}\right)^{\frac{1}{2}} e^{i\omega_1 t}. \tag{A6.5.11}$$

To $O(\mu_1)$ we can, from (6.6.2), replace w_1 with v_1. Then, on using the coordinate change given by (6.6.4) we find that

$$\Delta p(X_1) \sim 2\rho U_{r_1} v_1 e^{i\omega_1 t}\left(\frac{-X_1}{c_1+X_1}\right)^{\frac{1}{2}}. \tag{A6.5.12}$$

Equivalently, for a downstream finite airfoil, we obtain

$$\Delta p(X_2) \sim 2\rho U_{r_2} v_2 e^{i\omega_2 t} \left(\frac{c_2 - X_2}{X_2}\right)^{\frac{1}{2}} . \qquad \text{(A6.5.13)}$$

2.2 Upstream Semi-Infinite Airfoil

On using the low argument approximation for the w-function and the exponential in (6.4.4) we obtain

$$\Delta p(X_1) \sim \frac{2}{\pi^{\frac{1}{2}}} \left[1 + \frac{i\omega_1}{\gamma_1 U_{r_1}}\right] (\gamma_1 c_1)^{\frac{1}{2}} \; 2\rho U_{r_1} v_1 e^{i\omega_1 t} \left(\frac{-X_1}{c_1}\right)^{\frac{1}{2}} \qquad \text{(A6.5.14)}$$

which is $O[(\gamma_1 c_1)^{\frac{1}{2}}]$, or $O(\mu_1^{\frac{1}{2}})$, times the low frequency finite airfoil result, given by (A6.5.12), in the region of the trailing edge and has no singularity at $X_1 = -c_1$ (the leading edge).

2.3 Downstream Semi-Infinite Airfoil

The low frequency approximation to (6.5.4) is

$$\Delta p(X_2) \sim \frac{-i}{\pi^{\frac{1}{2}} (\gamma_2 c_2)^{\frac{1}{2}}} 2\rho U_{r_2} v_2 e^{i\omega_2 t} \left(\frac{c_2}{X_2}\right)^{\frac{1}{2}} \qquad \text{(A6.5.15)}$$

which is $O[(\gamma_2 c_2)^{-\frac{1}{2}}]$, or $O(\mu_2^{-\frac{1}{2}})$, times the low frequency finite airfoil results, given by (A6.5.13), in the region of the leading edge and does not reduce to zero at $X_2 = c_2$ (the trailing edge).

7. POTENTIAL FIELD INTERACTIONS - COMPRESSIBLE FLOW

7.1 Introduction

In the last chapter we calculated the unsteady flow generated by the bound potential field about the upstream and downstream blade rows of a counter-rotation propeller, and the response of the adjacent blade row to each harmonic of the unsteady velocity field. The calculations were performed assuming that the flow could be considered incompressible. This means that the modelling is inappropriate when the flow Mach numbers are, typically, greater than 0.3 (see, for example, the discussion on page 15 of Lighthill (1986)). Since the Mach numbers of interest on propfans are always above 0.3*, even at approach conditions, we need to extend the modelling in chapter 6 to include compressibility effects.

In sections 7.2 and 7.3 we describe the bound potential field about each row of a counter-rotation propeller, in compressible flow, due to blade thickness and blade circulation respectively. The potential field is written in terms of harmonic components and we show how the exponential decay of each component differs from the exponential decay given in chapter 6 for the incompressible flow case. The upwash on the forward and rearward blade rows, due to each harmonic gust, is then calculated.

In the case of compressible flow it is not possible to calculate the response of an airfoil to a gust in closed form. We therefore start by considering the high frequency limit and, in section 7.4, we calculate the response of the upstream blades to each harmonic of the potential field generated by the downstream row by using the Wiener-Hopf technique.

FOOTNOTE

* Here the Mach number is the blade helical Mach number M_r and not the flight Mach number of the aircraft.

In using this technique we are assuming that the airfoil response is dominated by contributions from the trailing edge region so that leading edge effects can be neglected. One of the important results of chapter 6 was that the leading edge region can provide a non-negligible contribution to the total unsteady lift. Therefore, in order to account for the leading edge effects we extend the iterative technique developed by Landahl (1961) and Adamczyk (1974), who considered downstream convected gust interactions, to the case of an upstream potential field interaction. This technique provides a solution, in the form of an asymptotic series, to a three part boundary value problem and is discussed in section 7.5. Following on from this we discuss the high frequency response of the downstream blades to the potential field of the upstream row in section 7.6.

Next we consider the low frequency limit and, in section 7.7, we show that, in this limit, the compressible flow problem can be reduced to an equivalent incompressible flow problem. The results from chapter 6 and the work of Osborne (1973) and Kemp (1973) then enable us to calculate the total airfoil response* to each harmonic of the potential field generated by the adjacent blade row.

In section 7.8 we compare the predicted far-field noise generated by a counter-rotation propeller (as calculated using the radiation formulae of chapter 4, with the unsteady lift provided by the results of the current chapter) with the Gannet flyover measurements† which have been described in previous chapters and, in more detail, by Bradley (1986). The

---

FOOTNOTES

* When noncompactness effects are taken into account.

† In particular, we consider the first three interaction tones.

predictions made using the high frequency approximation are shown both with and without a Kutta condition imposed at the trailing edges of the blades on the upstream row. On retaining the Kutta condition, predictions and measurements are shown to agree extremely well, typically to within 2 or 3dB. On rejecting the Kutta condition, however, the predictions are raised by between 5 and 10dB and, in some cases, the directivity of the far-field sound is altered. The predictions made using the low frequency approximation are similar to those made using the high frequency approximation. Since the first few interaction tones on the Gannet are basically low frequency interactions, the equivalence of the low and high frequency predictions for these tones suggests that only the high frequency approximation need be retained.

7.2 Potential Field due to Blade Thickness

7.2.1 Velocity Potential

In this section we will extend the analysis of section 6.2 to the compressible flow case. We again assume that the airfoil cross section of the blades can be approximated by an ellipse of minor axis a and major axis b. The compressible flow problem can be reduced to an equivalent incompressible flow problem by applying a Prandtl-Glauert transformation*; see, e.g., Landau & Lifshitz (1959) or Ward (1955). This means that the (X,Y) coordinates, which are measured parallel and normal to the airfoil chord, are scaled according to

$$\left.\begin{aligned} X' &= X, \\ Y' &= \beta Y, \end{aligned}\right\} \qquad (7.2.1)$$

FOOTNOTE

* See Prandtl (1930) and Glauert (1928).

where

$$\beta = (1 - M_r^2)^{\frac{1}{2}} \tag{7.2.2}$$

and M_r is the airfoil section relative Mach number. In addition if

$$\phi' = \beta\phi, \tag{7.2.3}$$

where ϕ is the velocity potential in the (X,Y) coordinate system, then ϕ' represents an "incompressible flow" velocity potential in the (X',Y') coordinate system about an ellipse of minor axis βa and major axis b. In the case of a staggered cascade of airfoils the separation s should also be scaled according to (7.2.1). Then, by comparison with section 6.2, we find that ϕ' satisfies

$$\nabla'^2\phi' = \pi U_r \beta a(\beta a+b) \sum_{n=-\infty}^{\infty} \frac{\partial}{\partial X'}\left[\delta(X'+ns\ \sin\alpha)\delta(Y'-ns\ \beta\ \cos\alpha)\right], \tag{7.2.4}$$

where ∇'^2 denotes the Laplacian in the (X',Y') coordinates and α is the airfoil stagger angle.

We now introduce the coordinates (x,y) which are measured normal and parallel to the cascade direction and are shown in Figure 5.1. From (7.2.1) the (x,y) and (X',Y') coordinate systems are related by

$$\left.\begin{aligned} X' &= x\ \cos\alpha - y\ \sin\alpha\ , \\ Y' &= \beta x\ \sin\alpha + \beta y\ \cos\alpha\ . \end{aligned}\right\} \tag{7.2.5}$$

This can be inverted to give

$$\left.\begin{aligned} x &= X'\cos\alpha + Y'\,\frac{\sin\alpha}{\beta}\,, \\ y &= -X'\sin\alpha + Y'\,\frac{\cos\alpha}{\beta}\,. \end{aligned}\right\} \qquad (7.2.6)$$

In appendix 7.1 it is shown that the delta function combination in (7.2.4) can be related to a delta function combination in (x,y) coordinates by

$$\delta(X'+ns\,\sin\alpha)\;\delta(Y'-ns\,\beta\cos\alpha) = \frac{1}{\beta}\delta(x)\delta(y-ns). \qquad (7.2.7)$$

Then from (7.2.6), (7.2.7) and the chain rule we find that (7.2.4) can be written in the form

$$\nabla'^2\phi' = \pi U_r a(\beta a+b) \sum_{n=-\infty}^{\infty} \left[\cos\alpha\;\delta'(x)\;\delta(y-ns) - \sin\alpha\;\delta(x)\delta'(y-ns)\right] \qquad (7.2.8)$$

where the primes on the delta functions denote differentiation with respect to argument. By using Poisson's summation formula, as in section 6.2, we then obtain

$$\nabla'^2\phi' = \frac{\pi U_r a(\beta a+b)}{s} \sum_{n=-\infty}^{\infty} \exp(-i2\pi n\,\frac{y}{s}) \qquad (7.2.9)$$

$$\left[\cos\alpha\;\delta'(x) + \frac{i2\pi n}{s}\sin\alpha\;\delta(x)\right].$$

Now from (7.2.3) and (7.2.6) the Laplacian of ϕ' in the (X',Y') coordinate system can be rewritten as

$$\nabla'^2\phi' = \frac{1}{\beta}\left[(\sin^2\alpha+\beta^2\cos^2\alpha)\ \frac{\partial^2\phi}{\partial x^2} + 2\sin\alpha\ \cos\alpha(1-\beta^2)\ \frac{\partial^2\phi}{\partial x\partial y}\right.$$

$$\left. + (\cos^2\alpha+\beta^2\sin^2\alpha)\ \frac{\partial^2\phi}{\partial y^2}\right] \quad . \tag{7.2.10}$$

We will try to obtain a solution to (7.2.9) and (7.2.10) in the form

$$\phi = \lambda_o \sum_{n=-\infty}^{\infty} [\lambda_1 \mathrm{sgn}(x) + \lambda_2] \exp\left[-i2\pi n \frac{y}{s}\right]$$

$$\exp\left[-2\pi|n|\ \frac{|x|}{s}\lambda_r - i2\pi n \frac{x}{s}\lambda_i\right] \tag{7.2.11}$$

where

$$\lambda_o = \frac{\pi U_r \beta a(\beta a + b)}{s} \tag{7.2.12}$$

and λ_1, λ_2, λ_r and λ_i are to be determined. On substituting (7.2.11) into (7.2.10) and equating the coefficients of $\delta(x)$ and $\delta'(x)$ with those in (7.2.9) we obtain, after some manipulation,

$$\lambda_1 = \frac{\cos\alpha}{2(\sin^2\alpha + \beta^2\cos^2\alpha)}, \tag{7.2.13}$$

$$\lambda_2 = \frac{-i\ \mathrm{sgn}(n)\sin\alpha}{2\beta(\sin^2\alpha + \beta^2\cos^2\alpha)}\ , \qquad (7.2.14)$$

$$\lambda_r = \frac{\beta}{(\sin^2\alpha + \beta^2\cos^2\alpha)}\ , \qquad (7.2.15)$$

$$\lambda_i = \frac{-(1-\beta^2)\sin\alpha\ \cos\alpha}{(\sin^2\alpha + \beta^2\cos^2\alpha)}\ , \qquad (7.2.16)$$

so that, finally,

$$\phi = \frac{\pi U_r a(\beta a+b)}{2s(\sin^2\alpha + \beta^2\cos^2\alpha)}[\beta\,\mathrm{sgn}(x)\cos\alpha - i\,\mathrm{sgn}(n)\sin\alpha]\ E_x E_y \qquad (7.2.17)$$

where

$$E_x = \exp\left[-\frac{2\pi\beta|n|\ |x|}{s(\sin^2\alpha + \beta^2\cos^2\alpha)} + \frac{i2\pi(1-\beta^2)nx\ \sin\alpha\cos\alpha}{s(\sin^2\alpha + \beta^2\cos^2\alpha)}\right] \qquad (7.2.18)$$

and

$$E_y = \exp\left[-i2\pi n\,\frac{y}{s}\right]\ . \qquad (7.2.19)$$

7.2.2 Upwash on upstream airfoil

We now consider an isolated airfoil situated upstream of the cascade. The situation has been previously described in section 6.2.2 and is shown

in Figure 6.2. On following the analysis in section 6.2.2 and defining Mach numbers in the x and y directions as

$$\left.\begin{aligned} M_x &= \frac{U_{r_2}}{c_o}\cos\alpha_2 \\ \text{and} \quad M_{y_2} &= \frac{U_{r_2}}{c_o}\sin\alpha_2, \end{aligned}\right\} \tag{7.2.20}$$

where c_o is the speed of sound, we find that the upwash can be written in the form

$$u_1 = v_1 \exp(\gamma_{X_1} X_1 + \gamma_{Y_1} Y_1 + i\omega_1 t) \tag{7.2.21}$$

where

$$v_1 = \frac{-n_2 B_2^2 U_{r_2} a_2}{4r^2(1-M_x^2)} (\beta_2 a_2 + b_2)(\sin\alpha_2 - i\beta_2\cos\alpha_2)(\cos\alpha_1 - i\eta_2\sin\alpha_1)$$

$$\exp\left\{\frac{-n_2 B_2}{r}\left[\eta_2\left(g - \frac{c_1}{2}\cos\alpha_1\right) + i\,\frac{c_1}{2}\sin\alpha_1\right]\right\}, \tag{7.2.22}$$

$$\gamma_{X_1} = \frac{n_2 B_2}{r}(\eta_2\cos\alpha_1 - i\sin\alpha_1), \tag{7.2.23}$$

$$\gamma_{Y_1} = \frac{-n_2 B_2}{r}(\eta_2\sin\alpha_1 + i\cos\alpha_1), \tag{7.2.24}$$

η_2 is a compressibility factor defined by

$$\eta_2 = \frac{\beta_2 + iM_x M_{y_2}}{1-M_x^2} \tag{7.2.25}$$

(note that $\eta_2 \to 1$ as M_x, $M_{y_2} \to 0$, i.e. as the flow becomes incompressible) and ω_1 is the angular frequency defined by (6.2.18).

7.2.3 Upwash on Downstream Airfoil

Here we consider an isolated airfoil situated downstream of the cascade. The situation has been previously described in section 5.4.1 (for the case of a convected gust) and is shown in Figure 5.1. On using an analysis similar to that in section 5.4.1, and defining Mach numbers in the x and y direction as

$$\left.\begin{aligned} M_x &= \frac{U_{r_1}}{c_o}\cos\alpha_1 \\ \text{and} \qquad M_{y_1} &= \frac{U_{r_2}}{c_o}\sin\alpha_1 \ , \end{aligned}\right\} \tag{7.2.26}$$

we find that the upwash on the downstream airfoil can be written in the form

$$u_2 = v_2 \exp(\gamma_{X_2} X_2 + \gamma_{Y_2} Y_2 + i\omega_2 t) \tag{7.2.27}$$

where

$$v_{2} = \frac{n_1 B_1^2 U_{r_1} a_1(\beta_1 a_1 + b_1)}{4r^2(1-M_x^2)} (\sin\alpha_1 + i\beta_1\cos\alpha_1)(\cos\alpha_2 + i\eta_1\sin\alpha_2)$$

$$\exp\left\{\frac{-n_1 B_1}{r}\left[\eta_1(g - \frac{c_2}{2}\cos\alpha_2) - i\frac{c_2}{2}\sin\alpha_2\right]\right\}, \qquad (7.2.28)$$

$$\gamma_{X_2} = \frac{-n_1 B_1}{r}(\eta_1\cos\alpha_2 + i\sin\alpha_2), \qquad (7.2.29)$$

$$\gamma_{Y_2} = \frac{-n_1 B_1}{r}(\eta_1\sin\alpha_2 - i\cos\alpha_2), \qquad (7.2.30)$$

η_1 is a compressibility factor defined by

$$\eta_1 = \frac{\beta_1 - iM_x M_{y_1}}{1-M_x^2} \qquad (7.2.31)$$

and ω_2 is the angular frequency defined by (6.2.25)

7.3 Potential Field due to Blade Circulation

7.3.1 Velocity Potential

In the incompressible flow case, discussed in chapter 6, the potential flow field due to airfoil circulation was obtained by consideration of the stream function ψ and the airfoils were modelled by point vortices. In

appendix 7.2 we show that, for a row of point vortices of circulation Γ in incompressible flow, the velocity potential ϕ satisfies

$$\nabla^2\phi = \frac{\Gamma}{2}\sum_{n=-\infty}^{\infty}\delta'(x)\,\mathrm{sgn}(y-ns) \tag{7.3.1}$$

where the row of vortices and the coordinate system are shown in Figure 6.3. We now apply a Prandtl-Glauert transformation to the (X,Y) coordinates (see Figure 7.1) as defined by (7.2.1) to (7.2.3). In the new (X',Y') coordinate system the position of the vortices has been altered. We therefore introduce coordinates $(\bar{X},\bar{Y})$ which are measured normal and parallel to the line of vortices respectively (in the scaled, or Prandtl-Glauert, coordinate system). The $(\bar{X},\bar{Y})$ coordinates are related to the (X',Y') coordinates by

$$\left.\begin{aligned}\bar{X} &= X'\cos\bar{\alpha} + Y'\sin\bar{\alpha}\ ,\\ \bar{Y} &= -X'\sin\bar{\alpha} + Y'\cos\bar{\alpha}\ ,\end{aligned}\right\} \tag{7.3.2}$$

where $\bar{\alpha}$ represents the angle between the two coordinate systems (see Figure 7.1). Now the distance between adjacent vortices (in the Prandtl-Glauert plane), as measured parallel to the X' and Y' axes, is $\beta s\cos\alpha$ and $-s\sin\alpha$ respectively, so that

$$\bar{s} = s(\sin^2\alpha + \beta^2\cos^2\alpha)^{\frac{1}{2}} \tag{7.3.3}$$

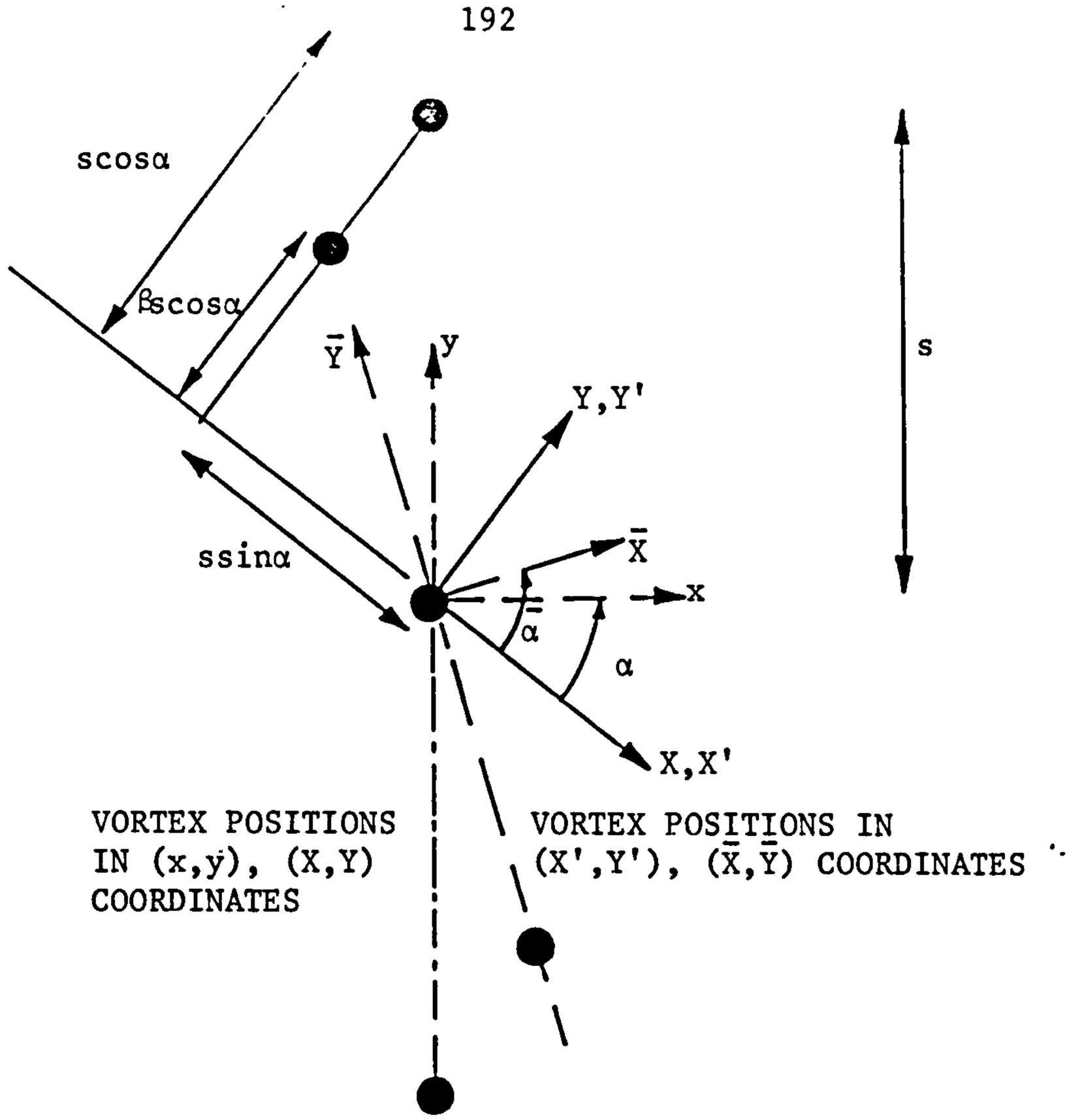

Figure 7.1 Vortex positions in original and transformed coordinate systems.

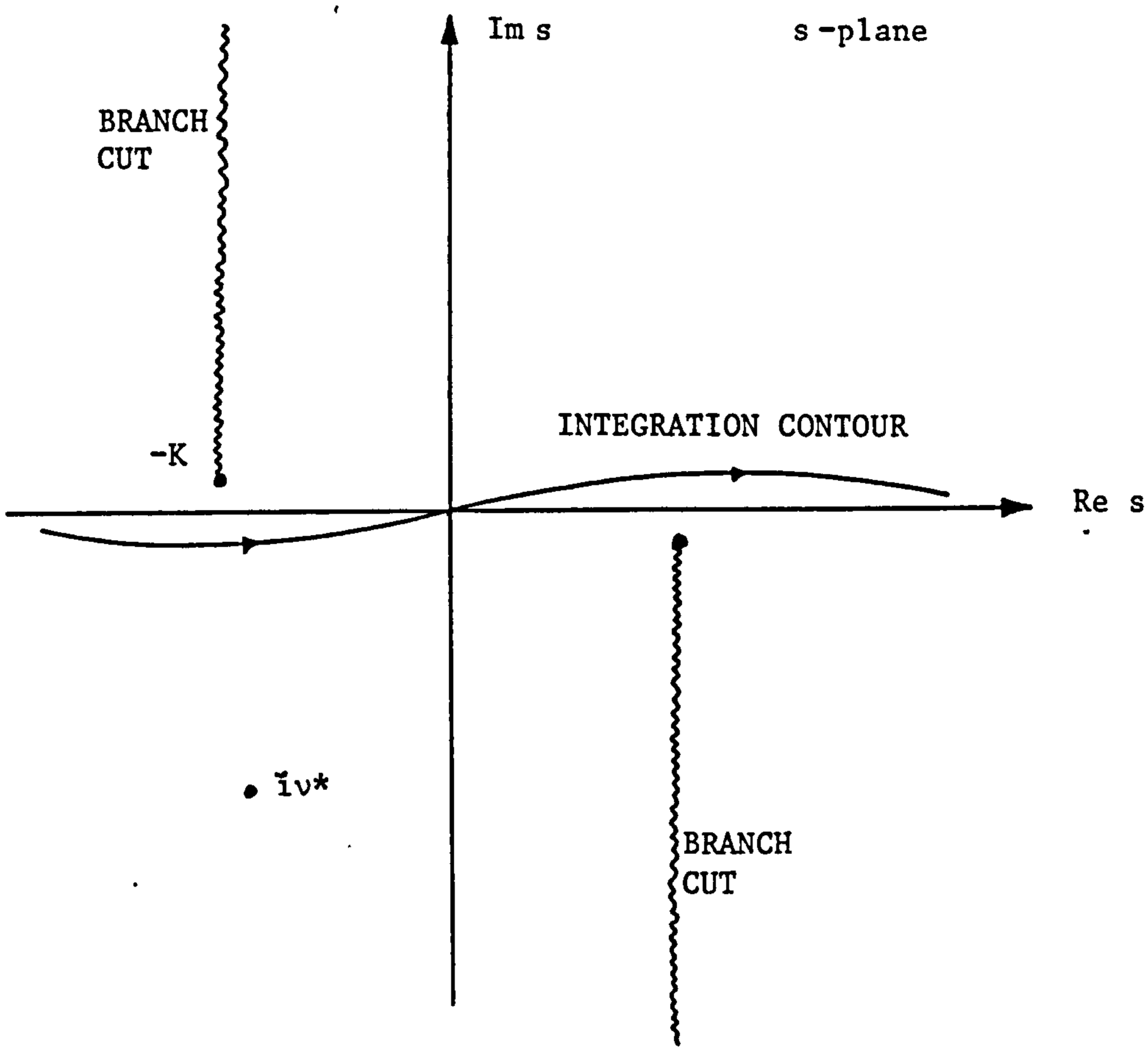

Figure 7.2 The integration contour and branch cuts in the complex plane.

is the absolute separation between adjacent vortices in the Prandtl-Glauert plane. In addition $\bar{\alpha}$ is related to α by

$$\cot\bar{\alpha} = \beta \cot\alpha \ , \tag{7.3.4}$$

whence, from (7.2.5) and (7.3.2) ,

$$\left.\begin{aligned} \bar{X} &= \frac{\beta s}{\bar{s}} x \ , \\ \bar{Y} &= -\sin\alpha\cos\alpha(1 - \beta^2)\frac{s}{\bar{s}} x + \frac{\bar{s}}{s} y \ . \end{aligned}\right\} \tag{7.3.5}$$

We can invert (7.3.5) to obtain

$$\left.\begin{aligned} x &= \frac{\bar{s}}{\beta s} \bar{X} \ , \\ y &= \sin\alpha\cos\alpha\frac{(1-\beta^2)}{\beta}\frac{s}{\bar{s}}\bar{X} + \frac{s}{\bar{s}}\bar{Y} \ . \end{aligned}\right\} \tag{7.3.6}$$

Now, from (7.3.1) the velocity potential in the Prandtl-Glauert plane must satisfy

$$\nabla'^2\phi' = \frac{\Gamma'}{2} \sum_{n=-\infty}^{\infty} \frac{\partial}{\partial\bar{X}} \delta(\bar{X})\,\mathrm{sgn}(\bar{Y} - n\bar{s}), \tag{7.3.7}$$

where Γ' is the circulation about each vortex in the new system. From (7.3.5) and (7.3.6) we can rewrite (7.3.7) as

$$\nabla'^2\phi' = \frac{\Gamma'}{2} \sum_{n=-\infty}^{\infty} \left[\frac{\bar{s}}{\beta s} \frac{\partial}{\partial x} + \sin\alpha\cos\alpha \frac{(1-\beta^2)}{\beta} \frac{s}{\bar{s}} \frac{\partial}{\partial y}\right]$$

$$\delta\left(\frac{\beta s}{\bar{s}} x\right) \operatorname{sgn}\left[-\sin\alpha\cos\alpha(1-\beta^2) \frac{s}{\bar{s}} x + \frac{\bar{s}}{s}(y-ns)\right] , \tag{7.3.8}$$

which reduces to

$$\nabla'^2\phi' = \frac{\Gamma'}{2\beta^2} \sum_{n=-\infty}^{\infty} [(\sin^2\alpha+\beta^2\cos^2\alpha)\delta'(x)\operatorname{sgn}(y-ns)$$

$$+ 2\sin\alpha\cos\alpha(1-\beta^2)\delta(x)\delta(y-ns)] . \tag{7.3.9}$$

In appendix 7.2 it is shown, from Poisson's summation formula, that

$$\sum_{n=-\infty}^{\infty} \operatorname{sgn}(y-ns) = \frac{i}{\pi} \sum_{n=-\infty}^{\infty} \frac{\exp(-i2\pi ny/s)}{n} . \tag{7.3.10}$$

By writing the series of delta functions in y in Fourier series form, as in section 7.2, we then obtain

$$\nabla'^2\phi' = \frac{i\Gamma'}{2\pi\beta^2} \sum_{n=-\infty}^{\infty} \left[(\sin^2\alpha+\beta^2\cos^2\alpha)\delta'(x) \frac{-i2\pi n}{s} \sin\alpha\cos\alpha(1-\beta^2)\delta(x)\right]$$

(7.3.11)

$$\frac{\exp(-i2\pi ny/s)}{n} .$$

Following the procedure used in section 7.2.1 we then find that ϕ is given by

$$\phi = \frac{i\Gamma}{4\pi} \text{ sgn}(x) \sum_{n=-\infty}^{\infty} \frac{1}{n} E_x E_y \qquad (7.3.12)$$

where E_x and E_y are defined in (7.2.18) and (7.2.19) respectively. The circulation Γ in (7.3.12) is related to the 'incompressible' circulation Γ' by

$$\Gamma = \frac{\Gamma'}{\beta} \qquad (7.3.13)$$

as shown, for example, by Landau & Lifshitz (1959) and Ward (1955).

7.3.2 Upwash on Upstream Airfoil

We now consider an airfoil upstream of the cascade: the situation is shown in Figure 6.2. By following the analysis in sections 6.2.2 and 7.2.2 we find that the upwash can be written in the same form as (7.2.21) with (7.2.22) replaced by

$$v_1 = \frac{-\Gamma B_2}{4\pi r}\,(\cos\alpha_1 - i\eta_2\sin\alpha_1)$$

$$\exp\left\{\frac{-\eta_2 B_2}{r}\left[\eta_2\left(g - \frac{c_1}{2}\cos\alpha_1\right) + i\,\frac{c_1}{2}\sin\alpha_1\right]\right\}. \qquad (7.3.14)$$

7.3.3 Upwash on Downstream Airfoil

Here we consider an airfoil downstream of the cascade as shown in Figure 5.1. The analysis used in sections 5.4.1, 6.2.3 and 7.2.3 is applicable. We find that (7.2.27) is again appropriate to describe the upwash, with the gust amplitude v_2 replaced by

$$v_2 = \frac{\Gamma B_1}{4\pi r}\,(\cos\alpha_2 + i\eta_1\sin\alpha_2)$$

$$\exp\left\{\frac{-\eta_1 B_1}{r}\left[\eta_1\left(g - \frac{c_2}{2}\cos\alpha_2\right) - i\,\frac{c_2}{2}\sin\alpha_2\right]\right\}. \qquad (7.3.15)$$

7.4 Response of the Upstream Row

As we mentioned in chapter 5, the response of an airfoil to a gust in compressible flow has, in general, to be calculated numerically. However, in the case of high frequency interactions, an approximate solution can be obtained by considering the airfoil to be semi-infinite and solving

only the trailing edge problem. This is similar to the problem discussed in chapter 5 except that, in this case, the gust is not convected with the mean flow. In addition, since we are considering a trailing edge, the inverse square root singularity at the edge will be removed by imposing a Kutta condition.

In chapter 6, where the incompressible flow case was considered, we found that the semi-infinite airfoil approximation can lead to errors due to the neglect of important leading edge effects. We will therefore apply a correction to the semi-infinite airfoil solution which accounts for the leading edge effects. This correction will be discussed in the following section.

In the (X_1,Y_1) coordinate system fixed to the forward blade row (see Figure 6.2) the velocity potential satisfies the convected wave equation

$$\nabla^2\phi - \frac{1}{c_o^2}\left(\frac{\partial}{\partial t} + U_{r_1}\frac{\partial}{\partial X_1}\right)^2\phi = 0 \quad . \tag{7.4.1}$$

Since ϕ has a time dependence $e^{i\omega_1 t}$ (7.4.1) reduces to

$$(1 - M_{r_1}^2)\frac{\partial^2\phi}{\partial X_1^2} + \frac{\partial^2\phi}{\partial Y_1^2} - 2ikM_{r_1}\frac{\partial\phi}{\partial X_1} + k^2\phi = 0 \tag{7.4.2}$$

where

$$k = \frac{\omega_1}{c_o}, \tag{7.4.3}$$

$$M_{r_1} = \frac{U_{r_1}}{c_o}. \tag{7.4.4}$$

The upwash is given by (7.2.21). On imposing a hard wall boundary condition we obtain

$$\frac{\partial \phi}{\partial Y_1} + v_1 e^{\gamma_{X_1} X_1 + i\omega_1 t} = 0; \quad X_1 < 0. \quad Y_1 = 0. \tag{7.4.5}$$

We now define a new velocity potential Φ, and a new set of coordinates $\bar{x}$ and $\bar{y}$, where

$$\phi(X_1, Y_1) = \Phi(\bar{x}, \bar{y}) e^{i\nu\bar{x} + i\omega_1 t}, \tag{7.4.6}$$

$$\left.\begin{aligned} \bar{x} &= X_1, \\ \bar{y} &= \kappa Y_1, \end{aligned}\right\} \tag{7.4.7}$$

and ν and κ are to be determined. On substituting (7.4.6) and (7.4.7) into (7.4.2) we obtain

$$(1 - M_{r_1}^2)\frac{\partial^2\Phi}{\partial\bar{x}^2} + \kappa^2\frac{\partial^2\Phi}{\partial\bar{y}^2} + [2i\nu(1 - M_{r_1}^2) - 2ikM_{r_1}]\frac{\partial\Phi}{\partial\bar{x}}$$

$$+ [k^2 + 2\nu kM_{r_1} - \nu^2(1 - M_{r_1}^2)]\Phi = 0 \ . \qquad (7.4.8)$$

If in (7.4.8) we set

$$\left.\begin{aligned} \kappa &= (1 - M_{r_1}^2)^{\frac{1}{2}}, \\ \nu &= \frac{kM_{r_1}}{(1 - M_{r_1}^2)}, \end{aligned}\right\} \qquad (7.4.9)$$

then (7.4.8) reduces to the Helmholtz equation

$$\frac{\partial^2\Phi}{\partial\bar{x}^2} + \frac{\partial^2\Phi}{\partial\bar{y}^2} + K^2\Phi = 0 \qquad (7.4.10)$$

where

$$K = \frac{k}{(1 - M_{r_1}^2)} \ . \qquad (7.4.11)$$

The normal velocity on the blade surface is

$$\frac{\partial \phi}{\partial Y_1} = (1 - M_{r_1}^2)^{\frac{1}{2}} \frac{\partial \Phi}{\partial \bar{y}} \, e^{i\nu\bar{x} + i\omega_1 t} \tag{7.4.12}$$

If we now define another velocity potential ψ by

$$\psi = \frac{(1 - M_{r_1}^2)^{\frac{1}{2}}}{r} \Phi \tag{7.4.13}$$

then the boundary condition, (7.4.6), reduces to

$$\frac{\partial \psi}{\partial \bar{y}} = -e^{\nu^* \bar{x}} \; ; \quad \bar{x} < 0, \; \bar{y} = 0 \; . \tag{7.4.14}$$

In (7.4.14) ν^* is defined as

$$\nu^* = \gamma_{X_1} - i\nu \; . \tag{7.4.15}$$

The pressure is given by

$$p = - \rho \left(\frac{\partial \phi}{\partial t} + U_{r_1} \frac{\partial \phi}{\partial X_1} \right) \tag{7.4.16}$$

where ρ is the density. From (7.4.6) and (7.4.13) we can rewrite this in terms of ψ as

$$p = \frac{-\rho v_1 U_{r_1}}{(1-M_{r_1}^2)^{\frac{1}{2}}} \, e^{i\nu\bar{x}+i\omega_1 t} \, p^* \, , \qquad (7.4.17)$$

where

$$p^* = ik^*\psi + \frac{\partial\psi}{\partial\bar{x}} \qquad (7.4.18)$$

and

$$k^* = \frac{k}{M_{r_1}(1. - M_{r_1}^2)} \, . \qquad (7.4.19)$$

We now look for the solution to

$$\nabla^2\psi + K^2\psi = 0 \qquad (7.4.20)$$

with the boundary condition (7.4.14).

The solution is obtained by the Wiener-Hopf technique and will be described here in detail. We define $\oplus$ and $\ominus$ Fourier transforms by

$$\Psi_{\pm}(s,\bar{y}) = \int_{-\infty}^{\infty} \psi(\bar{x},\bar{y}) \, H(\pm\bar{x}) e^{is\bar{x}} \, d\bar{x} \qquad (7.4.21)$$

where $H(\bar{x})$ is the Heaviside unit function. The inverse transform is given by

$$\psi(\bar{x},\bar{y}) = \frac{1}{2\pi}\int_{-\infty}^{\infty} \Psi(s,\bar{y})e^{-is\bar{x}}\,ds \ . \qquad (7.4.22)$$

On Fourier transforming the Helmholtz equation, (7.4.20), we obtain

$$\Psi''(s,\bar{y}) + \chi^2\Psi(s,\bar{y}) = 0 \ , \qquad (7.4.23)$$

where we use primes to denote differentiation with respect to $\bar{y}$ and

$$\chi = (K^2 - s^2)^{\frac{1}{2}} \ . \qquad (7.4.24)$$

Here we choose the branch of the square root so that

$$\chi \to -i|s| \quad \text{as} \quad s \to \pm\infty \ . \qquad (7.4.25)$$

The branch cuts in the complex plane are shown in Figure 7.2. The wave-number K is taken to have a small imaginary part.

We now consider the region $\bar{x} > 0$ where we assume continuity of pressure across the wake. From (7.4.17) p* is also continuous across the wake so that, on Fourier transforming (7.4.18), we obtain

$$i(k^* - s)[\Psi_+(s,0-) - \Psi_+(s,0+)] = 0 \ .$$

Since ψ must be an odd function of $\bar{y}$ this leads to

$$\Psi_+(s,0+) = 0. \tag{7.4.26}$$

If we now take the Fourier transform of p* in the region $\bar{x} < 0$ we obtain

$$-2i(k^* - s)\, \Psi_-(s,0+) = \Delta P^*_-(s) \tag{7.4.27}$$

where we have again used the fact that ψ is odd in $\bar{y}$ and ΔP^*_- represents the transform of the jump in p* across the airfoil.

The boundary condition, (7.4.14), can be Fourier transformed to give

$$\Psi'_-(s,0) = -\int_{-\infty}^{0} e^{\nu^*\bar{x}+isx}\, dx \tag{7.4.28}$$

$$= \frac{i}{(s - i\nu^*)}$$

where the integral converges provided that

$$\mathrm{Im}(s) < \mathrm{Re}(\nu^*) \,. \tag{7.4.29}$$

From (7.4.23) and the requirement that the fields decay at infinity we obtain

$$\Psi(s,\bar{y}) = C(s)e^{-i\chi\bar{y}} \qquad (7.4.30)$$

where we have taken $\bar{y}$ to be positive. (For $\bar{y}$ negative we can again use the fact that ψ is odd in $\bar{y}$.) On differentiating (7.4.30) and setting $\bar{y} = 0+$ we obtain

$$\Psi'(s,0) = -i\chi\Psi(s,0+) \ . \qquad (7.4.31)$$

On substituting (7.4.26) and (7.4.28) into (7.4.31) we find that

$$\Psi_+'(s,0) + \frac{i}{(s - i\nu^*)} = -i\chi\Psi_-(s,0+) \ . \qquad (7.4.32)$$

We now write χ in the form

$$\chi = (K + s)^{\frac{1}{2}}(K - s)^{\frac{1}{2}} \qquad (7.4.33)$$

so that, on dividing through by $(K - s)^{\frac{1}{2}}$, (7.4.32) becomes

$$\frac{\Psi_+'(s,0)}{(K - s)^{\frac{1}{2}}} + \frac{i}{(s - i\nu^*)(K - s)^{\frac{1}{2}}} = - i(K + s)^{\frac{1}{2}}\Psi_-(s,0+) \ . \qquad (7.4.34)$$

Here the first term on the left hand side is a $\oplus$ function and the right hand side is a $\ominus$ function. We can rewrite the second term on the left hand

side as

$$\frac{i}{(s - i\nu^*)(K - i\nu^*)^{\frac{1}{2}}} + \frac{i}{(s - i\nu^*)}\left[\frac{1}{(K - s)^{\frac{1}{2}}} - \frac{1}{(K - i\nu^*)^{\frac{1}{2}}}\right] \qquad (7.4.35)$$

where the first term is $\ominus$ function (since, from (7.2.35) and (7.4.15), $i\nu^*$ lies in the upper half plane) and the second term is a $\oplus$ function. We thus rewrite (7.4.34) as

$$\frac{\Psi_+'(s,0)}{(K - s)^{\frac{1}{2}}} + \frac{i}{(s - i\nu^*)}\left[\frac{1}{(K - s)^{\frac{1}{2}}} - \frac{1}{(K - i\nu^*)^{\frac{1}{2}}}\right] \qquad (7.4.36)$$

$$= -i(K + s)^{\frac{1}{2}}\Psi_-(s,0+) - \frac{i}{(s - i\nu^*)(K - i\nu^*)^{\frac{1}{2}}}$$

where the left hand side is a $\oplus$ function and the right hand side is a $\ominus$ function. By the usual arguments resulting from Liouville's theorem, both sides of (7.4.36) are equal to an entire function E(s) which must be identically equal to zero (otherwise $\Psi_+'(s,0)$ would diverge as $s \to \infty$ implying that ψ has a singularity at the origin). From (7.4.27) and the right hand side of (7.4.36) we then obtain

$$\Delta P^*_-(s) = \frac{2i(k^* - s)}{(K - i\nu^*)^{\frac{1}{2}}(K + s)^{\frac{1}{2}}(s - i\nu^*)} . \qquad (7.4.37)$$

We now apply the inverse Fourier transform, as defined by (7.4.22), whence

$$\Delta p^*(\bar{x}) = \frac{i}{\pi(K - i\nu^*)^{\frac{1}{2}}} \int_{-\infty}^{\infty} \frac{(k^* - s)e^{-is\bar{x}}}{(K + s)^{\frac{1}{2}}(s - i\nu^*)} ds \ . \tag{7.4.38}$$

On wrapping the integration contour around the branch cut in the upper half plane we obtain

$$\Delta p^*(\bar{x}) = \frac{2e^{iK\bar{x}+i\pi/4}}{\pi(K - i\nu^*)^{\frac{1}{2}}} \int_{0}^{\infty} \frac{(k^* + K - is')e^{\bar{x}s'}}{s'^{\frac{1}{2}}(s' + iK - \nu^*)} ds'$$

$$- \frac{2(k^* - i\nu^*)}{(K^2 + \nu^{*2})^{\frac{1}{2}}} e^{\bar{x}\nu^*} \tag{7.4.39}$$

where the final term represents the contribution from the pole at $s = i\nu^*$. Alternatively,

$$\Delta p^*(\bar{x}) = \frac{2e^{iK\bar{x}-i\pi/4}}{\pi(K - iv^*)^{\frac{1}{2}}} [I_1 + (v^* + ik^*)I_2] \tag{7.4.40}$$

$$- 2\frac{(k^* - iv^*)}{(K^2 + v^{*2})^{\frac{1}{2}}} e^{\bar{x}v^*}$$

where

$$I_1 = \int_0^\infty \frac{e^{\bar{x}s'}}{s'^{\frac{1}{2}}} ds' = \frac{\pi^{\frac{1}{2}}}{|x'|^{\frac{1}{2}}} \tag{7.4.41}$$

and, from Abramowitz & Stegun (1965),

$$I_2 = \int_0^\infty \frac{e^{\bar{x}s'}\, ds'}{s'^{\frac{1}{2}}(s' + iK - \nu^*)} = \frac{\pi}{(iK - \nu^*)^{\frac{1}{2}}} w[i|\bar{x}|^{\frac{1}{2}}(iK - \nu^*)^{\frac{1}{2}}] \tag{7.4.42}$$

where we have used $\bar{x} = -|\bar{x}|$ since $\bar{x}$ is negative on the airfoil. Then, combining (7.4.40) to (7.4.42), we obtain

$$\Delta p^*(\bar{x}) = \frac{-2i(\nu^* + ik^*)}{(K^2 + \nu^{*2})^{\frac{1}{2}}} \left\{ e^{iK\bar{x}}\, w[i|\bar{x}|^{\frac{1}{2}}(iK - \nu^*)^{\frac{1}{2}}] - e^{\nu^*\bar{x}} \right\} \tag{7.4.43}$$

$$+ \frac{2e^{iK\bar{x} - i\pi/4}}{\pi^{\frac{1}{2}}(K - i\nu^*)^{\frac{1}{2}}|\bar{x}|^{\frac{1}{2}}} .$$

We now impose a Kutta condition at the trailing edge of the airfoil. In appendix 7.3 we show that this is equivalent to removing the inverse square root singularity at the trailing edge. Then, from (7.4.17) and (7.4.15), the pressure jump across the airfoil is given by

$$\Delta p(\bar{x}) = \frac{2i\rho v_1 U_{r_1} (\nu^* + ik^*)}{(1 - M_{r_1}^2)^{\frac{1}{2}}(K^2 + \nu^{*2})^{\frac{1}{2}}} \left\{ e^{i(\nu+K)\bar{x}} w[i|\bar{x}|^{\frac{1}{2}}(iK-\nu^*)^{\frac{1}{2}}] - e^{\gamma_{X_1}\bar{x}} \right\} e^{i\omega_1 t} . \tag{7.4.44}$$

We now define the reduced frequency

$$\sigma = \frac{kc_1}{2M_{r_1}} , \tag{7.4.45}$$

where c_1 is the chord of the upstream airfoil, and the normalised gust frequency

$$\mu = i\gamma_{X_1} \frac{c_1}{2} . \tag{7.4.46}$$

We also move the origin to the midchord of the upstream airfoil and normalise by the semichord so that

$$\bar{x} = \frac{c_1}{2}(x - 1); \quad -1 \leq x \leq 1 . \tag{7.4.47}$$

Then, from (7.4.9), (7.4.11), (7.4.15) and (7.4.19), we can rewrite (7.4.44) in the form

$$\Delta p(x) = \frac{-2i\rho v_1 U_{r_1} (\sigma - \mu)}{(1 - M_{r_1}^2)^{\frac{1}{2}} (i\sigma^* + i\mu)^{\frac{1}{2}} (i\tilde{\sigma} - i\mu)^{\frac{1}{2}}} \left\{ e^{i\sigma^*(x-1)} w[i(1-x)^{\frac{1}{2}}(i\mu+i\sigma^*)^{\frac{1}{2}}] \right.$$

$$\left. - e^{-i\mu(x-1)} \right\} e^{i\omega_1 t} \qquad (7.4.48)$$

where we have defined

$$\sigma^* = \frac{\sigma M_{r_1}}{(1 - M_{r_1})} \qquad (7.4.49)$$

and

$$\tilde{\sigma} = \frac{\sigma M_{r_1}}{(1 + M_{r_1})} \; . \qquad (7.4.50)$$

The total lift on the airfoil is obtained by integrating (7.4.48) along the airfoil chord (and multiplying by the semichord). We also need to include the phase term $e^{-ik_x x}$ which was introduced in chapter 4 and represents the noncompactness effects. The 'effective' unsteady lift per unit span, i.e. the point force which generates the same far-field sound (the actual unsteady lift per unit span is obtained by setting the chordwise wavenumber k_x equal to zero), is then given by

$$\frac{dL_1}{dr} = \frac{\rho v_1 U_{r_1} c_1(\sigma - \mu)e^{i\omega_1 t - ik_x}}{(1 - M_{r_1}^2)^{\frac{1}{2}}(\mu + k_x)(i\mu + i\sigma^*)^{\frac{1}{2}}(i\tilde{\sigma} - i\mu)^{\frac{1}{2}}}$$

$$\left\{ e^{-i\pi/4} \frac{(i\mu + i\sigma^*)^{\frac{1}{2}}}{(\sigma^* - k_x)^{\frac{1}{2}}} \left[1 - e^{-i2(\sigma^* - k_x)} w(-(1 - i)(\sigma^* - k_x)^{\frac{1}{2}}) \right] \right.$$

$$\left. - e^{i2(\mu + k_x)} + w[i2^{\frac{1}{2}}(i\mu + i\sigma^*)^{\frac{1}{2}}] e^{-i2(\sigma^* - k_x)} \right\} . \qquad (7.4.51)$$

If in (7.4.48) and (7.4.51) we let $M_{r_1} \to 0$ (the reduced frequency is, in this case, written as $\sigma = \omega_1 c_1 / 2U_{r_1}$), which is the incompressible flow limit, then we obtain the results (6.4.4) and (6.4.5)*. This serves as a partial check on the results of this section.

In the current section we have dealt with just the trailing edge problem and consequently any leading edge effects have been neglected. Since, in chapter 6, we showed that leading edge effects can be important we will discuss a correction to the present results to account for these effects. This discussion forms the basis for the next section.

7.5 Leading Edge Correction

We will use a technique developed by Landahl (1961) and Adamczyk (1974), and discussed by Amiet (1973, 1975), for downstream convected gust

---

FOOTNOTE

* Note that particular care must be taken with the low argument limit of the first w-function in (7.4.50) as $\sigma^* \to 0$ in order to remove the inverse square root singularity $(\sigma^* - k_x)^{-\frac{1}{2}}$ with $k_x = 0$.

interactions. This involves an iterative technique for the solution of a three part boundary value problem. The situation is shown in Figure 7.3 with the upwash specified on $-c_1 \leqslant \bar{x} \leqslant 0$. The first iteration involves solving the trailing edge problem with the upwash specified on $-\infty < \bar{x} \leqslant 0$; this is the case discussed in the previous section. The second iteration involves correcting the upstream boundary condition on $-\infty < \bar{x} \leqslant -c_1$ without affecting the boundary condition on the airfoil, i.e. on $-c_1 \leqslant \bar{x} \leqslant 0$. We therefore require the "new" pressure difference across $-\infty < \bar{x} \leqslant -c_1$ to be minus the pressure difference obtained on the first iteration, and the upwash on $-c_1 \leqslant \bar{x} < \infty$ to be zero. This second iteration induces an error in the boundary condition on $0 \leqslant \bar{x} < \infty$ which could be corrected by a third iteration and so on. (In fact, we are likely to obtain a finite, but non zero, pressure jump at $\bar{x} = 0$ corresponding to the airfoil trailing edge.)

We define a new coordinate $\tilde{x}$ centred on the airfoil leading edge so that

$$\tilde{x} = \bar{x} + c_1. \tag{7.5.1}$$

The pressure jump Δp_2 across $-\infty < \tilde{x} \leqslant 0$ is minus that obtained in the previous section so that

$$\Delta p_2(\tilde{x}) = -\Delta p(\bar{x}) = -\Delta p(\tilde{x} - c_1). \tag{7.5.2}$$

Then, from (7.4.17) and (7.4.18),

$$\Delta p_2^*(\tilde{x}) = -e^{-i\nu c_1}\, \Delta p^*(\tilde{x} - c_1) .$$

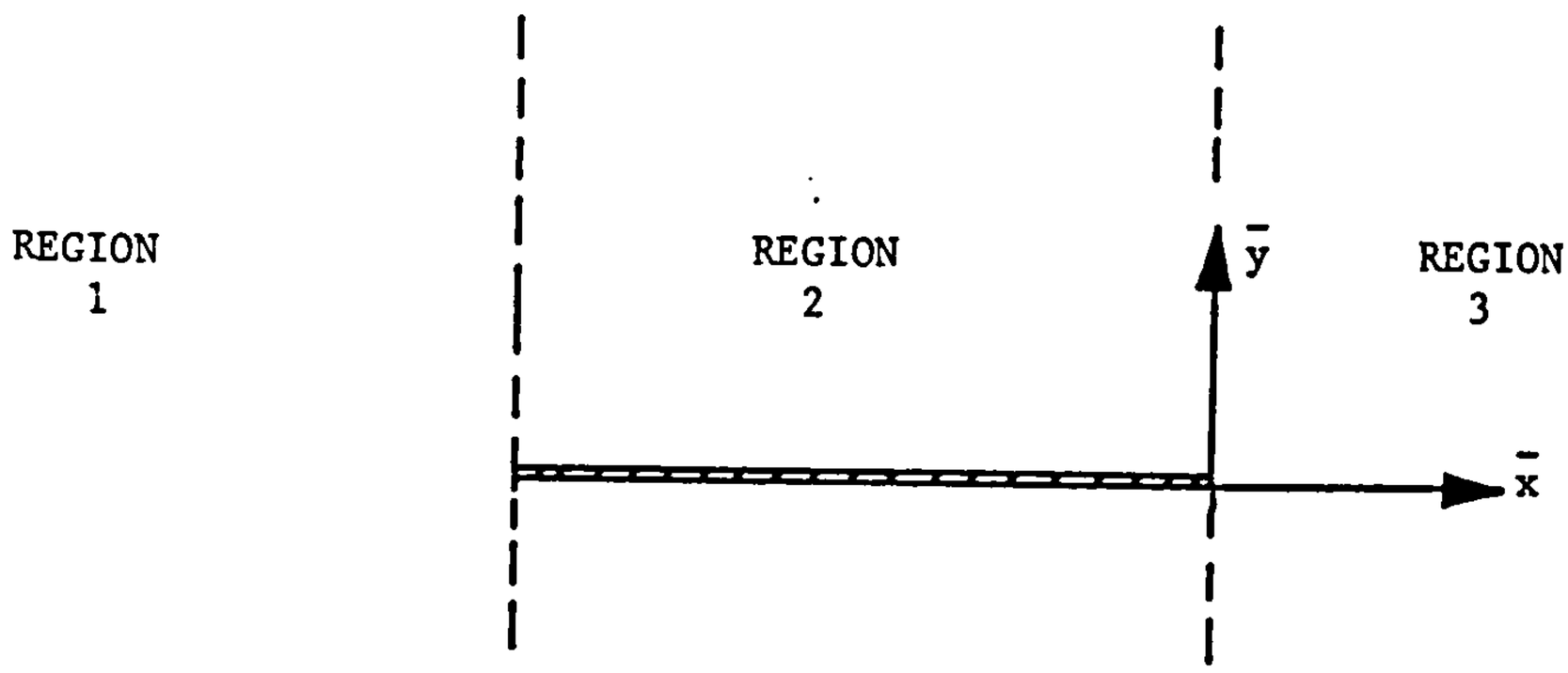

STAGE 1: TRAILING EDGE PROBLEM

$$\frac{\partial \psi}{\partial \bar{y}} + v_1 e^{\gamma_{X_1} \bar{x}} = 0$$

$$\frac{\partial \psi}{\partial \bar{y}} + v_1 e^{\gamma_{X_1} \bar{x}} = 0$$

$\Delta p = 0,$

KUTTA CONDITION

STAGE 2: LEADING EDGE CORRECTION

$$\Delta p_2 = -\Delta p$$

$$\frac{\partial \psi_2}{\partial \bar{y}} = 0$$

$$\frac{\partial \psi_2}{\partial \bar{y}} = 0$$

Figure 7.3 Three part boundary value problem.

(We will use the suffix 2 throughout this section to denote "second iteration" values.) From (7.4.43) we then obtain

$$\Delta p_2^*(x) = \frac{2i(\nu^* + ik^*)}{(K^2 + \nu^{*2})} e^{-i\nu c_1} \left\{ e^{iK(\tilde{x}-c_1)} w[i|\tilde{x}-c_1|^{\frac{1}{2}}(iK-\nu^*)^{\frac{1}{2}}] - e^{\nu^*(\tilde{x}-c_1)} \right\} \tag{7.5.3}$$

(recall, from the discussion following (7.4.43), that the inverse square root singularity term has been removed in order to satisfy the Kutta condition). Since we are considering a high frequency problem kc_1 and $\gamma_{X_1} c_1$ are both large. Then, from (7.4.9), (7.4.11) and (7.4.15), the argument of the w function in (7.5.3) is also large on $\tilde{x} < 0$ so that, from Abramowitz & Stegun (1965), we can use the approximation

$$w[i|\tilde{x} - c_1|^{\frac{1}{2}}(iK - \nu^*)^{\frac{1}{2}}] \sim \frac{1}{\pi^{\frac{1}{2}}|\tilde{x} - c_1|^{\frac{1}{2}}(iK - \nu^*)^{\frac{1}{2}}} \quad . \tag{7.5.4}$$

(In order to use this approximation we have used the fact that $|\arg(iK - \nu^*)^{\frac{1}{2}}| < \pi/2$.) In addition, since $\gamma_{X_1} c_1$ is large, the last term in (7.5.3) is, from (7.4.15), exponentially small on $\tilde{x} < 0$. Consequently, this term will be neglected. The jump in p_2^* across $\tilde{x} < 0$ can therefore be approximated by

$$\Delta p_2^*(\tilde{x}) \sim \frac{2i(\nu^* + ik^*)e^{-i\nu c_1 + iK(\tilde{x}-c_1)}}{\pi^{\frac{1}{2}}(iK - \nu^*)^{\frac{1}{2}}(K^2 + \nu^{*2})^{\frac{1}{2}}|\tilde{x} - c_1|^{\frac{1}{2}}} \quad . \tag{7.5.5}$$

The boundary condition is that of no upwash so that

$$\frac{\partial \psi_2}{\partial \tilde{y}} = 0 \; ; \quad \tilde{x} > 0 \; . \tag{7.5.6}$$

In (7.5.6) we have, for consistency, replaced $\bar{y}$ with $\tilde{y}$.

The problem is therefore defined by the Helmholtz equation, (7.4.20), with the boundary condition (7.5.6) and the jump in p_2^* across $\tilde{x} < 0$ given by (7.5.5). The solution is again obtained by the Wiener-Hopf technique with $\oplus$ and $\ominus$ Fourier transforms defined by (7.4.1) and the inverse transform defined by (7.4.22).

The Fourier transform of $\Delta p_2^*(\tilde{x})$ is given by

$$\Delta P_{2_-}^*(s) = \frac{2i(\nu^* + ik^*)e^{-i\nu c_1 - iKc_1}}{\pi^{\frac{1}{2}}(iK - \nu^*)^{\frac{1}{2}}(K^2 + \nu^{*2})^{\frac{1}{2}}} \int_{-\infty}^{0} \frac{e^{i(s+K)\tilde{x}}}{(c_1 - \tilde{x})^{\frac{1}{2}}} d\tilde{x} \; . \tag{7.5.7}$$

We now use the fact that Kc_1 is large. On normalising $\tilde{x}$ in (7.5.7) by c_1 we find that the integrand oscillates rapidly. Then the integral is dominated by contributions from near $\tilde{x} = 0$ and, by following Murray (1974), we can approximate (7.5.7), to leading order in $\frac{1}{c_1(K+s)}$, by

$$\Delta P^*_{2_-}(s) = \frac{2(\nu^* + ik^*)e^{-i(\nu+K)c_1}}{\pi^{\frac{1}{2}}c_1^{\frac{1}{2}}(iK - \nu^*)^{\frac{1}{2}}(K^2 + \nu^{*2})^{\frac{1}{2}}(s + K)} . \qquad (7.5.8)$$

From this point we proceed with the Wiener-Hopf technique in the usual manner and the pressure jump $\Delta p_2(x)$ is finally obtained as

$$\Delta p_2(x) = \frac{2^{\frac{1}{2}} i\rho v_1 U_{r_1} (\sigma - \mu) e^{i\omega_1 t + i\tilde{\sigma}(1-x) - 4i\bar{\sigma}}}{\pi^{\frac{1}{2}}(1 - M_{r_1}^2)^{\frac{1}{2}}(i\mu + i\sigma^*)(i\tilde{\sigma} - i\mu)^{\frac{1}{2}}} \qquad (7.5.9)$$

$$\left\{ w[-2^{\frac{1}{2}} e^{-i\pi/4} \sigma^{\frac{1}{2}}(1 + x)^{\frac{1}{2}}] - \frac{2^{\frac{1}{2}} e^{-i\pi/4}}{\pi^{\frac{1}{2}} \sigma''^{\frac{1}{2}}} \frac{1}{(1 + x)^{\frac{1}{2}}} \right\}$$

where we have reintroduced the normalised frequencies σ, μ, σ^* and $\tilde{\sigma}$ given by (7.4.45), (7.4.46), (7.4.49) and (7.4.50) and, in addition, we define

$$\bar{\sigma} = \frac{M_{r_1}}{1 - M_{r_1}^2} \sigma , \qquad (7.5.10)$$

$$\sigma'' = \frac{(1 + M_{r_1})}{M_{r_1}(1 - M_{r_1})} \sigma . \qquad (7.5.11)$$

We note, from (7.5.9), that we have restored the inverse square root singularity at the airfoil leading edge (recall that the pressure distrib-

ution on the airfoil is now given by the sum of (7.4.48) and (7.5.9)). Comparing (7.4.48) and (7.5.9) we see that, apart from the exponential decay term $e^{-i\mu x}$ in p and the inverse square root singularity $(1 + x)^{-\frac{1}{2}}$ in p_2, the first and second stage solutions are basically of the same form apart from the factor $(i\mu + i\sigma^*)^{-\frac{1}{2}}$ in p_2. Since we are considering a high frequency problem both μ and σ (and hence σ^*) are large. This suggests that, in the high frequency limit, the first correction to the trailing edge problem is $O(\sigma^{-\frac{1}{2}})$ smaller than the leading order term.

The total lift, per unit span, on the airfoil is obtained by integrating (7.5.9) along the airfoil chord (and multiplying by the semichord). As in the previous section we will include the phase term $e^{-ik_x x}$ which was introduced in chapter 4 and represents noncompactness effects. After some manipulation we obtain

$$\frac{dL_{1_2}}{dr} = \frac{-\rho v_1 U_{r_1} c_1 (\sigma - \mu) e^{i\omega_1 t + ik_x - i2\sigma^*}}{2^{\frac{1}{2}} \pi^{\frac{1}{2}} (1 - M_{r_1}^2)^{\frac{1}{2}} (i\mu + i\sigma^*)(i\tilde{\sigma} - i\mu)^{\frac{1}{2}}}$$

$$\left\{ \left[\frac{1 - w(-2e^{-i\pi/4} \sigma^{\frac{1}{2}}) e^{-i2(\tilde{\sigma}+k_x)}}{(\sigma^* - k_x)} \right] \right. \tag{7.5.12}$$

$$\left. + 2^{\frac{1}{2}} \left[\frac{1 - w(-2^{\frac{1}{2}} e^{-i\pi/4} (\tilde{\sigma} + k_x)^{\frac{1}{2}}) e^{-i2(\sigma+k_x)}}{(\tilde{\sigma} + k_x)^{\frac{1}{2}}} \right] \left[\frac{1}{\sigma''^{\frac{1}{2}}} - \frac{\bar{\sigma}^{-\frac{1}{2}}}{(\sigma^* - k_x)} \right] \right\} .$$

The total "effective" lift (i.e. the magnitude of the lift that determines the amplitude of the far-field sound) is then given by the sum of (7.4.50)

and (7.5.12). Note that, as we suggested in the last paragraph, the first correction to the trailing edge problem is $O(\sigma^{-\frac{1}{2}})$ smaller than the leading order term - even when the inverse square root singularity at the airfoil leading edge is included. We conclude that, in the high frequency limit, the semi-infinite airfoil model is a valid approximation and provides accurate results to leading order in σ. Recall that, as we found in chapter 6, the same conclusion does not hold in the incompressible flow case where the semi-infinite airfoil approximation leads to errors in the unsteady pressure, away from the trailing edge, which affect the final result for the total fluctuating lift, per unit span, acting across the airfoil.

7.6 Response of the Downstream Row

In the previous two sections we considered the interaction of the potential field, generated by the downstream blade row, with the upstream airfoils. We now consider the interaction of the potential field, generated by the upstream blade row, with the downstream airfoils. As in section 7.4 we consider the high frequency limit and model the airfoil as a semi-infinite flat plate extending to downstream infinity. The Kutta condition is inappropriate here since there is no trailing edge. We could, of course, follow the procedure discussed in the previous section for a three part boundary value problem and add a correction to the leading edge response so that the final solution satisfies the trailing edge Kutta condition. However, the airfoil response is likely to be dominated by the leading edge inverse square root singularity so that the trailing edge region should be relatively unimportant. Moreover, as we showed in section 7.5, the correction terms are $O(\sigma^{-\frac{1}{2}})$ smaller than those resulting from the semi-infinite airfoil approximation. We will therefore

consider just the leading edge problem.

On following the analysis at the start of section 7.4 we can reduce the problem to that of finding a potential $\psi(\bar{x},\bar{y})$ which satisfies the Helmholtz equation

$$\nabla^2\psi + K^2\psi = 0 \ , \tag{7.6.1}$$

where

$$K = \frac{k}{(1 - M_{r_2}^2)} \tag{7.6.2}$$

and $k = \omega_2/c_o$ with ω_2 defined by (6.2.25), with the boundary condition

$$\frac{\partial\psi}{\partial\bar{y}} = - e^{\nu^*\bar{x}} \ ; \quad \bar{y} = 0, \quad \bar{x} > 0 \ . \tag{7.6.3}$$

The coordinates $\bar{x}$ and $\bar{y}$ are given by

and

$$\left.\begin{aligned} \bar{x} &= X_2 \\ \bar{y} &= (1 - M_{r_2}^2)^{\frac{1}{2}} Y_2, \end{aligned}\right\} \tag{7.6.4}$$

where X_2 and Y_2 are shown in Figure 5.1, and in (7.6.3) the wavenumber ν^* is given by

$$\nu^* = \gamma_{X_2} - i\nu \tag{7.6.5}$$

where

$$\nu = \frac{kM_{r_2}}{(1 - M_{r_2}^2)} \quad . \tag{7.6.6}$$

We write the pressure in the form

$$p = \frac{-\rho v_2 U_{r_2}}{(1 - M_{r_2}^2)^{\frac{1}{2}}} e^{i\omega_2 t + i\nu\bar{x}} \; p^* \tag{7.6.7}$$

where

$$p^* = ik^*\psi + \frac{\partial \psi}{\partial \bar{x}} \tag{7.6.8}$$

and

$$k^* = \frac{k}{M_{r_2}(1 - M_{r_2}^2)} \, . \tag{7.6.9}$$

The solution is again obtained by the Wiener-Hopf technique whence

$$\Delta p^*(\bar{x}) = \frac{2(\nu^* + ik^*)}{(iK - \nu^*)^{\frac{1}{2}}(iK + \nu^*)^{\frac{1}{2}}} \left\{ e^{-iK\bar{x}} \, w[i\bar{x}^{\frac{1}{2}}(iK + \nu^*)^{\frac{1}{2}}] - e^{\bar{x}\nu^*} \right\} \tag{7.6.10}$$

$$- \frac{2e^{-iK\bar{x}}}{\pi^{\frac{1}{2}}(iK - \nu^*)^{\frac{1}{2}}\bar{x}^{\frac{1}{2}}}$$

where all the complex wavenumber square roots are now defined with a

branch cut along the negative real axis. The pressure jump Δp is then found from (7.6.7) and (7.6.10). If we introduce the reduced frequency

$$\sigma = \frac{kc_2}{2M_{r_2}}, \tag{7.6.11}$$

where c_2 is the chord of the downstream airfoil section, the normalised gust frequency

$$\mu = i\gamma_{X_2}\frac{c_2}{2}. \tag{7.6.12}$$

and a normalised coordinate x, which is related to $\bar{x}$ by

$$\bar{x} = \frac{c_2}{2}(x + 1), \tag{7.6.13}$$

then the pressure jump can be written in the form

$$\Delta p(x) = \frac{-2\rho v_2 U_{r_2} e^{i\omega_2 t}}{(1 - M_{r_2}^2)^{\frac{1}{2}}(i\mu + i\sigma^*)^{\frac{1}{2}}}$$

$$\left\{\frac{i(\sigma - \mu)}{(-i\mu + i\tilde{\sigma})^{\frac{1}{2}}}\left[e^{-i\tilde{\sigma}(x+1)}w(i(x + 1)^{\frac{1}{2}}(-i\mu + i\tilde{\sigma})^{\frac{1}{2}}) - e^{-i\mu(x+1)}\right]\right. \tag{7.6.14}$$

$$\left. - \frac{e^{-i\tilde{\sigma}(x+1)}}{\pi^{\frac{1}{2}}(x + 1)^{\frac{1}{2}}}\right\}$$

where σ^* and $\tilde{\sigma}$ are defined as

$$\sigma^* = \frac{M_{r_2}\sigma}{(1 - M_{r_2})} \tag{7.6.15}$$

and

$$\tilde{\sigma} = \frac{M_{r_2}\sigma}{(1 + M_{r_2})} \quad . \tag{7.6.16}$$

The total lift, per unit span, on the airfoil is obtained by integrating (7.6.14) along the airfoil chord. As in the previous sections we include the phase term $e^{-ik_x x}$, introduced in chapter 4, which represents the noncompactness effects. We then obtain

$$\frac{dL_2}{dr} = \frac{\rho v_2 U_{r_2} c_2 e^{ik_x + i\omega_2 t}}{(1 - M_{r_2}^2)^{\frac{1}{2}}(i\mu + i\sigma^*)^{\frac{1}{2}}(\mu + k_x)}$$

$$\left\{ \frac{e^{-i\pi/4}(\sigma + k_x)}{(\tilde{\sigma} + k_x)^{\frac{1}{2}}} \left[1 - w(-(1 - i)(\tilde{\sigma} + k_x)^{\frac{1}{2}}) e^{-i2(\tilde{\sigma}+k_x)} \right] \right. \tag{7.6.17}$$

$$\left. + \frac{(\sigma - \mu)}{(i\tilde{\sigma} - i\mu)^{\frac{1}{2}}} \left[w(i2^{\frac{1}{2}}(i\tilde{\sigma} - i\mu)^{\frac{1}{2}}) e^{-i2(\tilde{\sigma}+k_x)} - e^{-i2(\mu+k_x)} \right] \right\} .$$

If in (7.6.14) and (7.6.17) we let $M_{r_2} \to 0$ ($\sigma = \omega c_2/2U_r$, $\sigma^* \to 0$, $\tilde{\sigma} \to 0$),

which is the incompressible flow limit, we regain the results (6.5.4) and (6.5.5).

7.7 Low Frequency Response

The response calculations in the three previous sections have been specifically aimed at the high frequency limit since, in general, this is the regime which is most appropriate to the interactions on high blade number counter-rotation propellers. However, there are occasions on which interactions take place at low reduced frequencies (some of these will be discussed in the following section). It is therefore necessary to consider low frequency interactions. In the case of convected gust interactions, i.e. wake interactions, which were discussed in chapter 5, we only considered the high frequency limit. Our reasons for discussing low frequency potential field interactions and not low frequency wake interactions is that, as became clear in chapter 6, the potential field interactions are much more significant than wake interactions at low frequencies*.

The response of an airfoil to a nonconvected gust in compressible flow, in the low frequency limit, has already been provided by Osborne (1973) and Kemp (1973) who followed on from the basic theory of Amiet & Sears (1970). However, their approach, and notation, was somewhat different from ours. Furthermore, we require not the total airfoil lift but the effective lift when acoustic noncompactness effects are taken into account. In addition, for the sake of completeness, we wish to relate the

---

FOOTNOTE

* This conclusion has been obtained just by consideration of the data from the Fairey Gannet flyover tests. Since there are major differences between Gannet propeller blades and advanced propeller blades the same conclusion does not necessarily apply to the propfan.

compressible flow results to the incompressible flow results which were given in chapter 6. We shall therefore solve the problem in detail.

Our starting point is the boundary value problem described by (7.4.14) to (7.4.20). (We note, in passing, that the coordinate transformation given by (7.4.6), (7.4.7) and (7.4.9), which reduces the wave equation to a Helmholtz equation, is equivalent to the combined Galilean-Lorentz transformation used by Amiet & Sears (1970) and Osborne (1973)). In order to apply the results to both upstream and downstream interactions we introduce the upwash

$$w(x,t) = w_o e^{i\omega t - i\mu x} \qquad (7.7.1)$$

where μ and x are defined by (7.4.46) and (7.4.47) for upstream interactions and by (7.6.12) and (7.6.13) for downstream interactions. The coordinate x is centred on the midchord in both cases. The upwash amplitudes v_1 and v_2 in (7.4.17) and (7.6.7) respectively can then be replaced by relating them to w_o as appropriate. We scale all lengths on the semichord. We then require the solution to

$$\nabla^2\phi' + K'^2\phi' = 0 \qquad (7.7.2)$$

with the boundary condition

$$\frac{\partial\phi'}{\partial y} = -e^{-i\mu' x} \quad \text{on } -1 \leq x \leq 1 \qquad (7.7.3)$$

where

$$K' = \frac{\sigma M_r}{(1 - M_r^2)} \tag{7.7.4}$$

and

$$\mu' = \mu + \frac{\sigma M_r^2}{(1 - M_r^2)} \quad . \tag{7.7.5}$$

The pressure jump across y = 0 is given by

$$\Delta p = \frac{-\rho w_o U_r}{(1 - M_r^2)^{\frac{1}{2}}} \exp\left[\frac{i\sigma M_r^2 x}{(1 - M_r^2)} + i\omega t\right] \Delta p' \quad . \tag{7.7.6}$$

where

$$\Delta p' = i\sigma'\phi' + \frac{\partial \phi'}{\partial x} \quad , \tag{7.7.7}$$

$$\sigma' = \frac{\sigma}{(1 - M_r^2)} \quad . \tag{7.7.8}$$

Since we are considering the low frequency limit we assume that K' is small and neglect K'^2. The Helmholtz equation (7.7.2) then reduces to Laplace's equation. The problem is then completely analogous to that considered by Kemp (1952) in the case of incompressible flow. The pressure distribution across the airfoil for this case is given by Amiet (1973) and was described in chapter 6. We then obtain

$$\Delta p' = -2\left\{\left(\frac{1-x}{1+x}\right)^{\frac{1}{2}}\left[C(\sigma')(J_o(\mu') - iJ_1(\mu')) + iJ_1(\mu')\right]\right.$$

$$\left. - \frac{1}{\pi}\left(1 - \frac{\sigma'}{\mu'}\right)(1-x^2)^{\frac{1}{2}} I'\right\} \qquad (7.7.9)$$

where I' is the singular integral

$$I' = \int_{-1}^{1} \frac{e^{-i\mu'\xi}}{(x-\xi)(1-\xi^2)^{\frac{1}{2}}}\, d\xi \quad . \qquad (7.7.10)$$

We see, from (7.7.6) and (7.7.9), that the total lift acting on the airfoil section is not the same as that given by Kemp (1952) (with the transformed temporal and spatial reduced frequencies, σ' and μ') because of the phase factor $\exp[i\sigma M_r^2 x/(1-M_r^2)]$ in (7.7.6). In addition we need to include the noncompactness phase factor $\exp(-ik_x x)$ in order to obtain the "effective" lift (or dipole strength) as observed in the far acoustic field. (Since we are considering the low frequency limit the noncompactness effects are likely to be small. However, for the sake of consistency, we retain all first order wavenumber terms.) The chordwise integrations, including these phase terms, are carried out in appendix 7.4 where it is shown that the "effective" unsteady lift, per unit span, acting across the airfoil is given by

$$\frac{dL}{dr} = \frac{\rho w_o U_r c \pi e^{i\omega t}}{(1 - M_r^2)^{\frac{1}{2}}} \left\{ [J_o(\mu') - iJ_1(\mu')][C(\sigma')(J_o(\eta') - iJ_1(\eta')) + iJ_1(\eta')] \right.$$

(7.7.11)

$$\left. + \frac{i(\sigma + k_x)}{(\mu' - \eta')} [J_o(\eta')J_1(\mu') - J_1(\eta')J_o(\mu')] \right\}$$

where

$$\eta' = \frac{M_r^2 \sigma}{(1 - M_r^2)} - k_x \ . \qquad (7.7.12)$$

If, as in the three previous sections, we let M_r tend to zero we find that the compressible flow result (7.7.11) tends to the incompressible flow result given by (6.6.9)

The above analysis should be accurate to O(K'). However, Miles (1950a, 1950b) has questioned the validity of the O(K') approximation when an infinite wake is present. Problems arise when logarithmic terms such as $\ell n(K')$ appear in the solution. By direct expansion of the exact Poissio integral equation, Miles derives results for $\sigma << 1$ and $M_r << 1$. Amiet (1974) showed that in the case of a convected sinusoidal gust, the Miles solution differed from the Osborne (1973) solution by an $O(kM^2)$ phase term. One piece of further work, therefore, would be to update the results of this section by calculating the Miles/Amiet correction for a nonconvected gust.

In the following section we proceed to make comparisons between counter-rotation propeller noise interaction tones, as calculated using the results for airfoil response from this chapter, and measured data.

7.8 Measurement vs Prediction

In the previous sections of this chapter we have calculated the unsteady lift* generated on both upstream and downstream blade rows due to the interaction of the blades on each row with the bound potential field of the adjacent blade row. We showed, in chapter 4†, how the far-field acoustic pressure could be calculated once the unsteady lift is known. In this section we will compare the Gannet flyover measurements with the predicted acoustic field using the results from both the current chapter and chapter 4. We shall also refer back to the comparisons between measurements and predictions which were shown in chapter 5, where just the downstream wake interaction was considered, and chapter 6, where the potential field interactions were considered but the flow was assumed to be incompressible.

We start with the high frequency response calculations given in sections 7.4 to 7.6. Since the validity of the Kutta condition in unsteady flow is a matter of controversy at the moment (see the discussion in appendix 7.3) we calculate the response of the upstream blades to the potential field of the downstream blades both with and without the Kutta condition imposed. (As we show in appendix 7.3, this corresponds to rejecting or retaining the inverse square root term in (7.4.43).)

The first interaction tone generated by the Gannet is the (1,1)

FOOTNOTES

* As we pointed out during the analysis, we have in fact calculated the effective (chordwise) point loading that gives the same far-field acoustic pressure as the (chordwise) distributed loading when interference effects are taken into accout.

† See also Hanson (1985a).

interaction. The far-field directivity of this tone is shown in Figure 7.4. The predicted far-field noise, due to the upstream and downstream potential field interactions with a Kutta condition imposed at the trailing edge of the upstream blades, is typically 5dB higher in the forward arc ($0 \leq \theta \leq 90^{o}$), and up to 10dB higher in the rear arc ($90^{o} \leq \theta \leq 180^{o}$), than was calculated in the incompressible flow case (see Figure 6.5) and compares extremely well with the measured data. (Since the upstream and downstream potential field interactions are spatially separated the phase relationship between the two sources is not just that given in the current chapter but must be corrected in the manner described by Hanson (1985a). For the present we consider the sources separately.) The next two interaction tones generated by the Gannet are the (2,1) and (1,2) interactions for which directivity plots are shown in Figures 7.5 and 7.6. Here, as for the (1,1) interaction, the predicted noise levels are between 5dB and 10dB higher than was calculated in the incompressible flow case (see Figures 6.6 and 6.7) and agree well with the measurements, although there is a small discrepancy in the rear arc for the (1,2) interaction.

In Figures 7.4 to 7.6 we have also plotted the predicted far-field noise due to the upstream potential field interaction* using the high frequency response calculation with no Kutta condition imposed at the trailing edges of the blades. In this case the predictions are, typically, 5 to 10dB higher than the predictions for which a Kutta condition was imposed at the trailing edges. In addition there appears

---

FOOTNOTE

* i.e. the interaction of the upstream blades with the potential field generated by the downstream blade row.

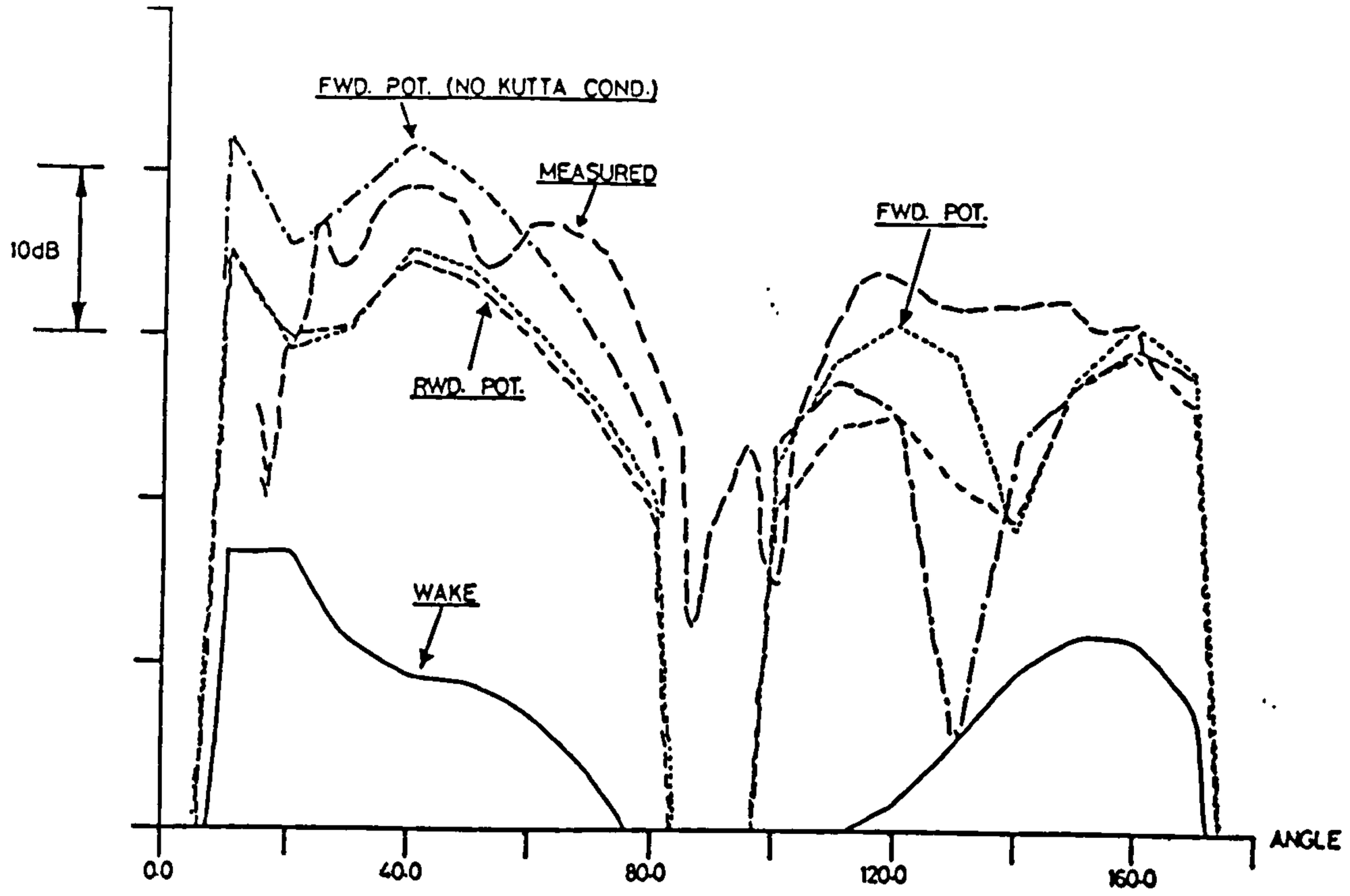

Figure 7.4 Gannet measurements vs predictions for the (1,1) interaction tone. The potential field predictions are obtained using semi-infinite airfoil response calculations in compressible flow.

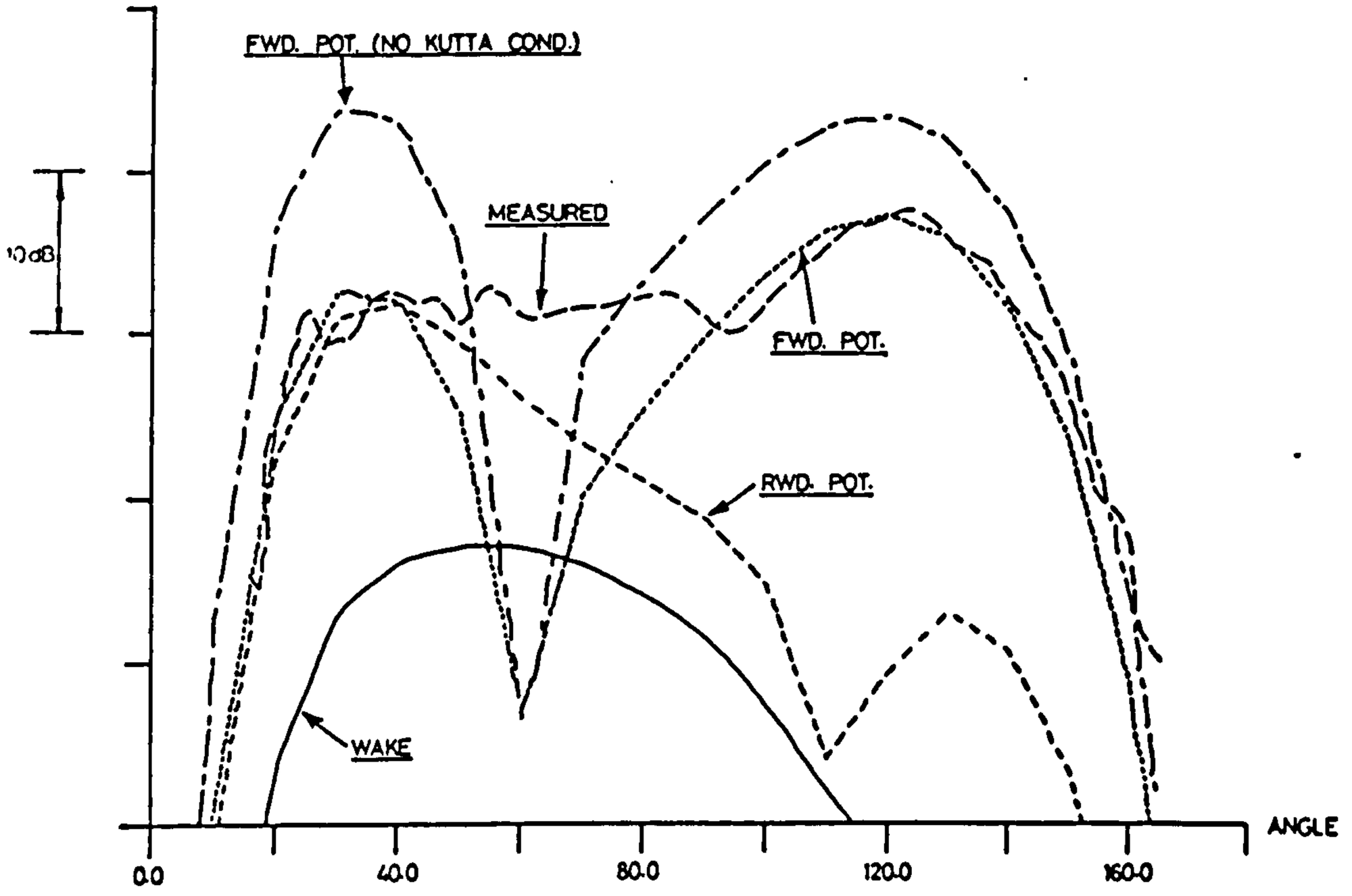

Figure 7.5 Gannet measurements vs predictions for the (2,1) interaction tone. The potential field predictions are obtained using semi-infinite airfoil response calculations in compressible flow.

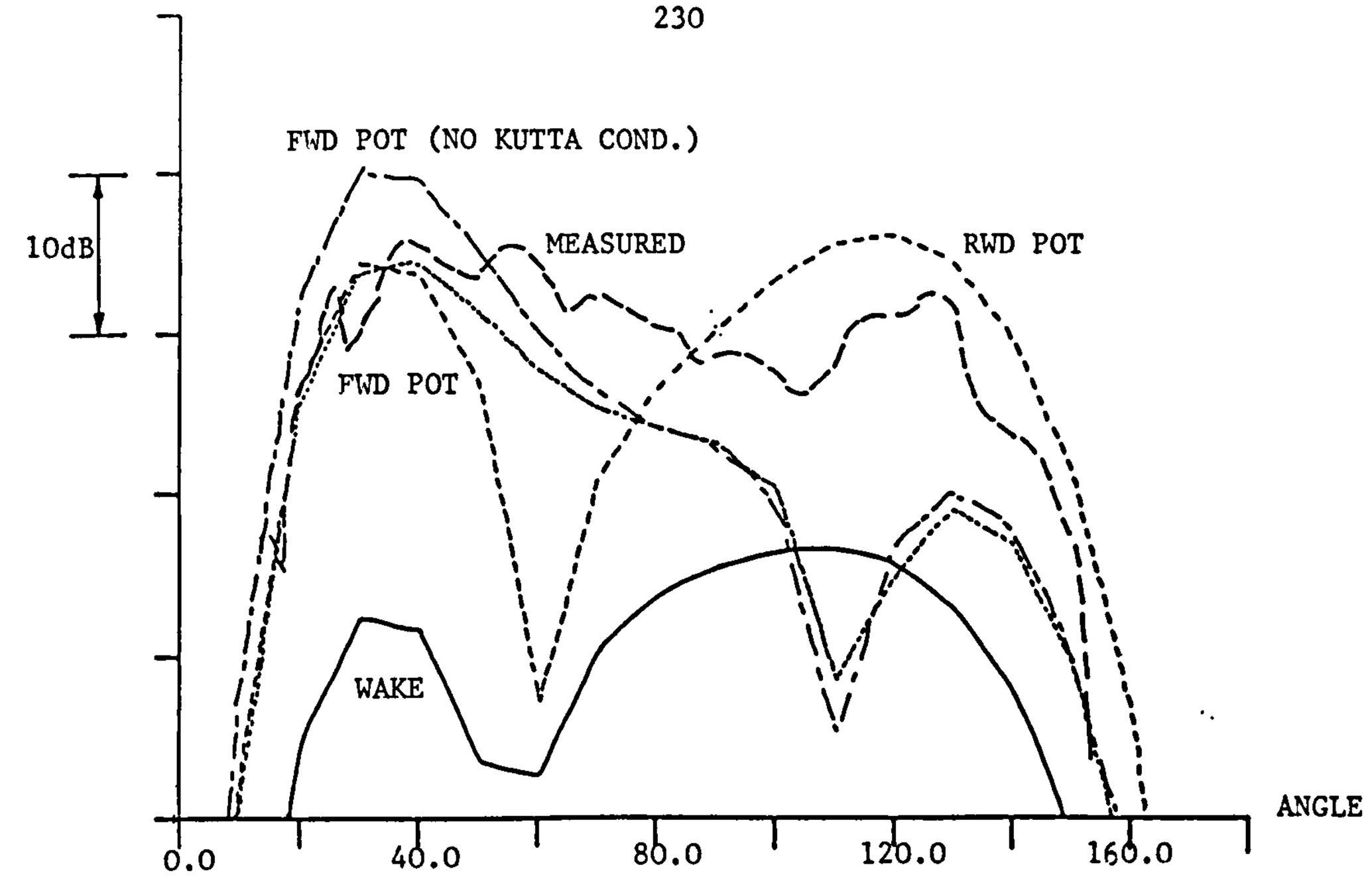

Figure 7.6 Gannet measurements vs predictions for the (1,2) interaction tone. The potential field predictions are obtained using semi-infinite airfoil response calculations in compressible flow.

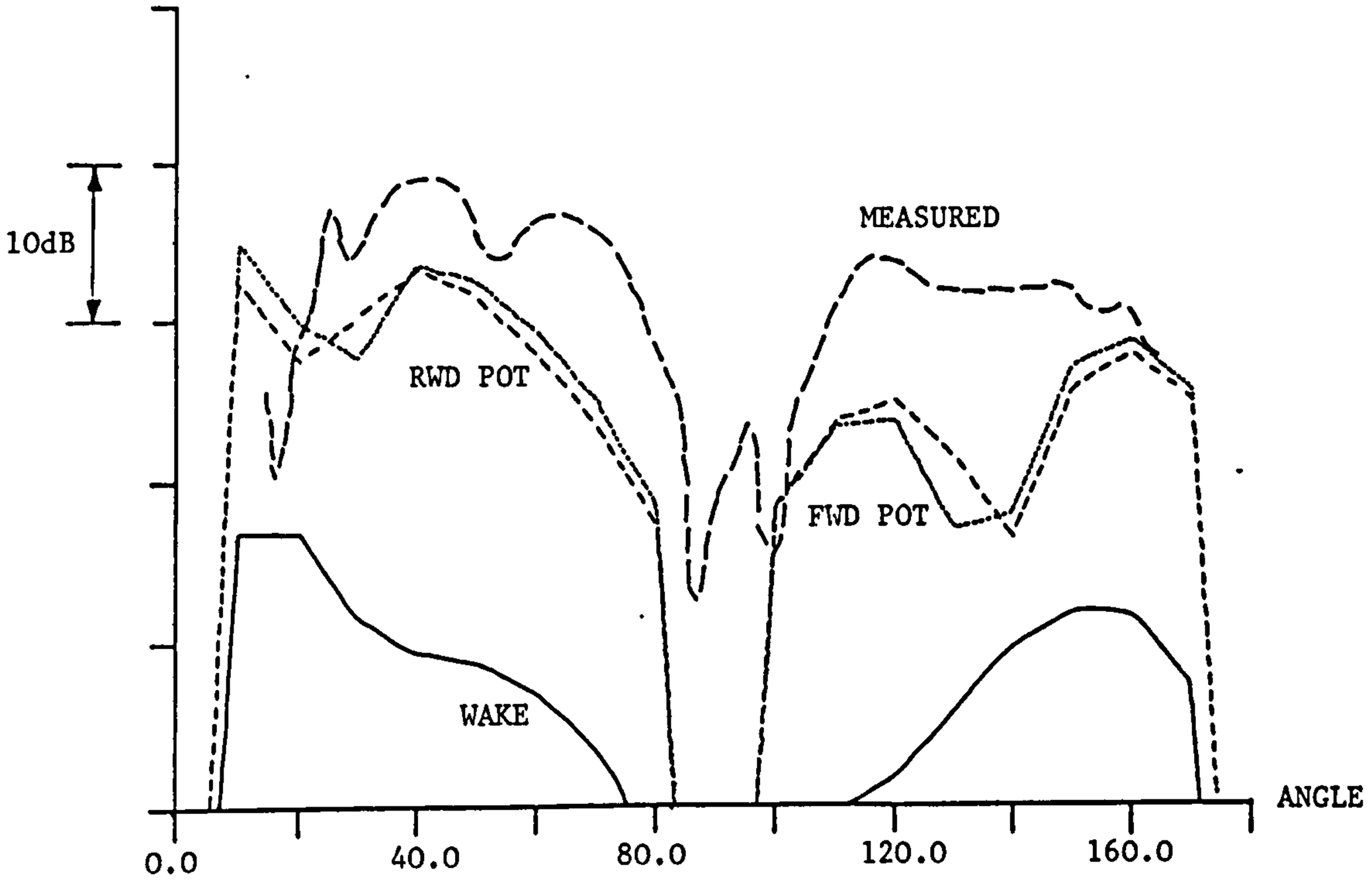

Figure 7.7 Gannet measurements vs predictions for the (1,1) interaction tone. The potential field predictions are obtained using low frequency airfoil response calculations in compressible flow.

to be some change in directivity, particularly for the (1,1) interaction where the forward arc levels are raised and the rear arc levels are lowered when no Kutta condition is imposed. These results seem to agree qualitatively with those of Howe (1976), who found that the application of a Kutta condition reduces the level of acoustic radiation, and Rienstra (1981), who found that the sound field diffracted by an airfoil has directivity properties which are strongly dependent on the trailing edge condition. The results presented here seem to indicate that it is appropriate to apply the trailing edge Kutta condition for the interaction frequencies we have considered on the Gannet. This follows the suggestion of Crighton (1981) that far-field acoustic measurements, along with theory, may be the optimum way of determining the correct trailing edge condition.

The high frequency response calculations, with a Kutta condition imposed at the trailing edge of the upstream blades, agree extremely well with far-field acoustic measurements. From a point of interest however we will now consider the low frequency response calculations which were discussed in section 7.7. The predicted far-field noise, using the low frequency approximation, due to the upstream and downstream potential field interactions, and the measured data, are shown in Figures 7.7, 7.8 and 7.9 for the (1,1), (2,1) and (1,2) interactions respectively. By comparison with Figures 7.4, 7.5 and 7.6 we can see that there is close agreement between the low frequency predictions and the high frequency predictions (with, of course, a Kutta condition imposed at the trailing edge of the upstream blades) which, as we have already shown, agree extremely well with the measured data. It seems, therefore, appropriate to retain the high frequency approximation since it agrees with the low

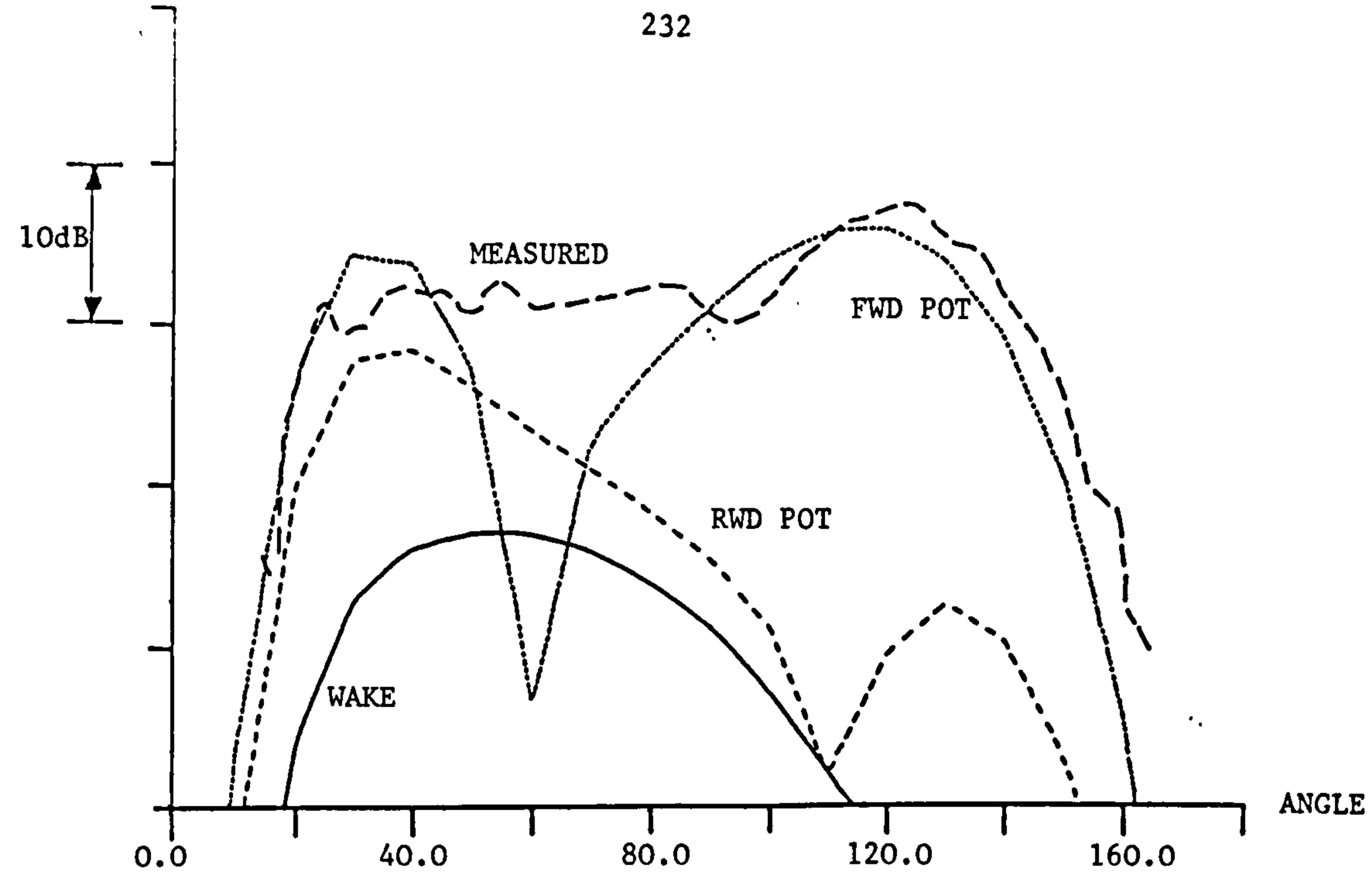

Figure 7.8 Gannet measurements vs predictions for the (2,1) interaction tone. The potential field predictions are obtained using low frequency airfoil response calculations in compressible flow.

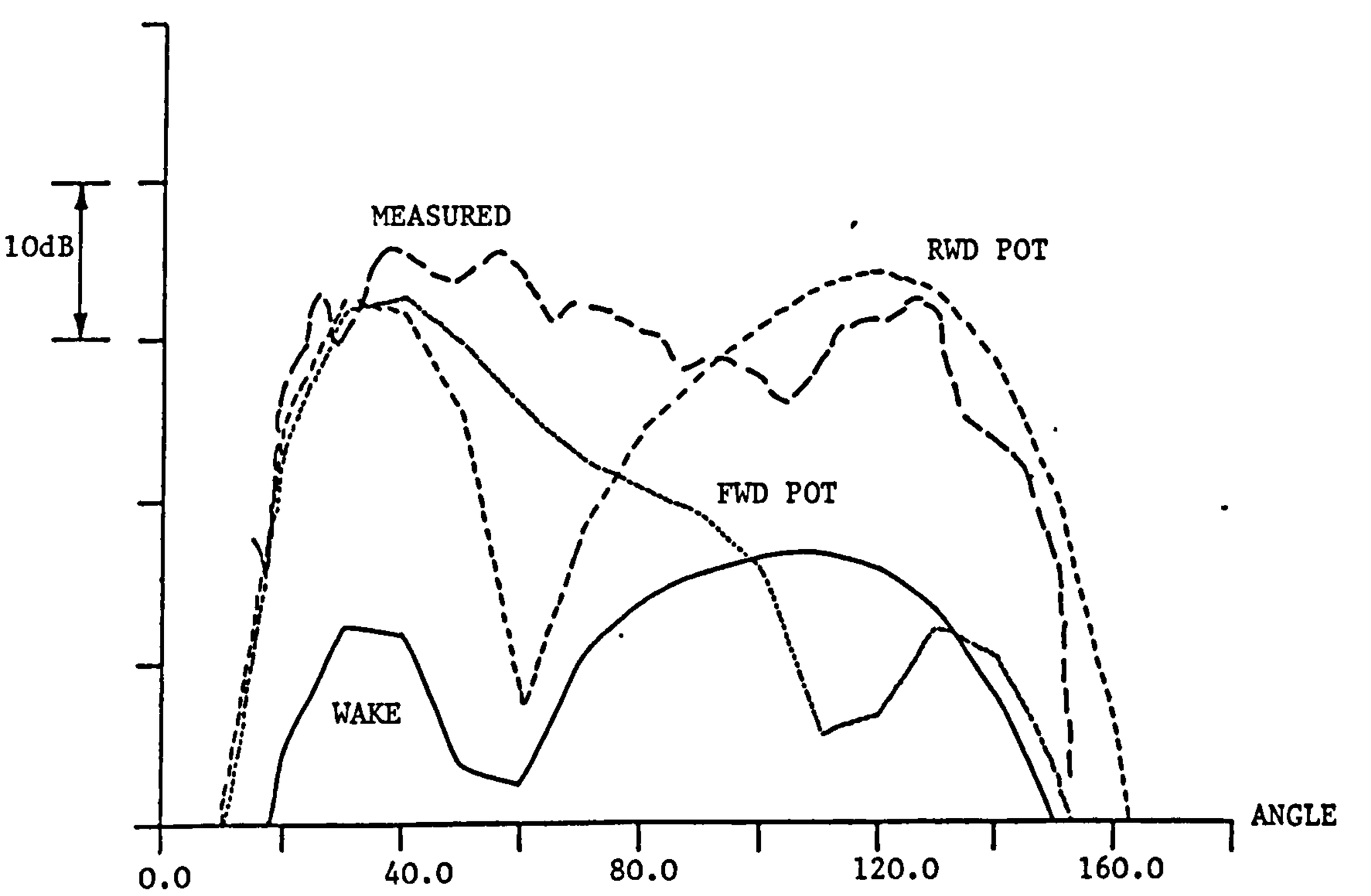

Figure 7.9 Gannet measurements vs predictions for the (2,1) interaction tone. The potential field predictions are obtained using low frequency airfoil response calculations in compressible flow.

frequency Gannet measurements and is, by definition, accurate in the high frequency asymptotic limit.

Finally, we note that the potential field predictions, which agree with measured far-field noise levels, are typically 20dB (and more at some angles) above the predicted noise levels due to the wake interactions which were discussed in chapter 5. This shows that, although wake interactions are likely to be important when the rotor-rotor spacing on a counter-rotation propeller is large (since the bound potential field decays exponentially with distance as shown in sections 7.2 and 7.3), potential field interactions may provide the dominant low frequency interaction noise sources when the rotor-rotor spacing is small.

APPENDIX 7.1

Dirac Delta Functions

Here we consider the delta function combination

$$\delta(X' + ns\ \sin\alpha)\ \delta(Y' - ns\ \beta\cos\alpha) \tag{A7.1.1}$$

representing the locations of the airfoil mid-chords in section 7.2.1.

We now define

$$\left.\begin{aligned} \tilde{X} &= X' + ns\ \sin\alpha\ , \\ \tilde{Y} &= Y' - ns\ \beta\cos\alpha\ . \end{aligned}\right\} \tag{A7.1.2}$$

From (7.2.5) we can relate $\tilde{X}$ and $\tilde{Y}$ to x and y by

$$\left.\begin{aligned} \tilde{X} &= x\ \cos\alpha - (y - ns)\sin\alpha\ , \\ \tilde{Y} &= \beta x\ \sin\alpha + \beta(y - ns)\cos\alpha\ . \end{aligned}\right\} \tag{A7.1.3}$$

We can invert (A7.1.3) to give

$$\left.\begin{aligned} x &= \tilde{X}\ \cos\alpha + \frac{\tilde{Y}}{\beta}\ \sin\alpha\ , \\ y &= -\tilde{X}\ \sin\alpha + \frac{\tilde{Y}}{\beta}\ \cos\alpha + ns\ . \end{aligned}\right\} \tag{A7.1.4}$$

Now

$$\frac{\partial(x,y)}{\partial(\tilde{X},\tilde{Y})} = \begin{bmatrix} \cos\alpha & -\sin\alpha \\ \frac{\sin\alpha}{\beta} & \frac{\cos\alpha}{\beta} \end{bmatrix} \tag{A7.1.5}$$

and the Jacobian is given by

$$\det\left[\frac{\partial(x,y)}{\partial(\tilde{X},\tilde{Y})}\right] = \frac{1}{\beta} . \tag{A7.1.6}$$

Then, from (A7.1.2) to (A7.1.6),

$$\int_{-\infty}^{\infty}\int_{-\infty}^{\infty} \delta(\tilde{X})\delta(\tilde{Y})\, dxdy = \int_{-\infty}^{\infty}\int_{-\infty}^{\infty} \delta(\tilde{X})\delta(\tilde{Y})\, \det\left[\frac{\partial(x,y)}{\partial(\tilde{X},\tilde{Y})}\right] d\tilde{X}d\tilde{Y} = \frac{1}{\beta} . \tag{A7.1.7}$$

Since $\tilde{X} = 0$ and $\tilde{Y} = 0$ if, and only if, $x = 0$ and $y = ns$, (A7.1.7)

implies that

$$\delta(\tilde{X})\delta(\tilde{Y}) = \frac{1}{\beta}\, \delta(x)\delta(y - ns) . \tag{A7.1.8}$$

APPENDIX 7.2

Velocity Potential for a Point Vortex in Incompressible Flow

In chapter 6 it was shown that the harmonics, n, of the stream function ψ, for a row of point vortices in incompressible flow, satisfy

$$\frac{\partial \psi}{\partial x} = -\frac{\Gamma}{2s}\,\mathrm{sgn}(x)\,\exp\left[-2\pi|n|\,\frac{|x|}{s} - i2\pi n\,\frac{y}{s}\right] \qquad \text{(A7.2.1)}$$

where the situation is shown in Figure 6.3. Since the stream function ψ and the velocity potential ϕ are related by

$$\frac{\partial \psi}{\partial x} = -\frac{\partial \phi}{\partial y}\ , \qquad \text{(A7.2.2)}$$

(A7.2.1) implies that

$$\phi = \frac{i\Gamma}{4\pi n}\,\mathrm{sgn}(x)\,\exp\left[-2\pi|n|\,\frac{|x|}{s} - i2\pi n\,\frac{y}{s}\right] \qquad \text{(A7.2.3)}$$

(recall that we are considering individual harmonic components). The Laplacian of ϕ is then given by

$$\nabla^2\phi = \frac{i\Gamma}{2\pi}\,\delta'(x)\sum_{n=-\infty}^{\infty}\frac{1}{n}\exp\left[-i2\pi n\,\frac{y}{s}\right] \qquad \text{(A7.2.4)}$$

where we have restored the summation.

We now define

$$F(\xi) = \frac{1}{\xi} \exp\left[-i2\pi\xi \frac{y}{s}\right] . \qquad \text{(A7.2.5)}$$

The Fourier transform of $F(\xi)$ is

$$G(\nu) = \int_{-\infty}^{\infty} F(\xi) \exp(-i2\pi\xi\nu)d\xi$$

$$= \int_{-\infty}^{\infty} \frac{1}{\xi} \exp\left[-2\pi\xi\left(\nu + \frac{y}{s}\right)\right] d\xi \qquad \text{(A7.2.6)}$$

$$= -i\pi \operatorname{sgn}\left(\nu + \frac{y}{s}\right) .$$

From (A7.2.6) and Poisson's summation formula (see appendix 3.1) we can write (A7.2.4) in the form

$$\nabla^2\phi = \frac{\Gamma}{2} \delta'(x) \sum_{n=-\infty}^{\infty} \operatorname{sgn}(y - ns). \qquad \text{(A7.2.7)}$$

APPENDIX 7.3

The Kutta Condition

In our analysis the airfoils have been modelled as flat plates (finite or semi-infinite). As we have found, the pressure jump across the plate has inverse square root singularities at the edges of the plate. In order to alleviate the singularity at the trailing edge we must introduce a vortex sheet, extending to downstream infinity, across which the tangential velocities jump but the pressure is continuous. If the strength of the vortex sheet is fixed in order to cancel exactly the trailing edge singularity, then a Kutta condition is said to be satisfied. (A more detailed discussion of the Kutta condition in unsteady flow is provided by Crighton (1985).) The use of a Kutta condition in unsteady flow is a matter of controversy at the present. For the moment, however, we will assume that a Kutta condition is satisfied.

We look for a potential ψ_K which satisfies the Helmholtz equation (7.4.20) and is odd in $\bar{y}$. Then, downstream of the trailing edge, there is a jump in the potential across the vortex wake so that

$$\psi_K = \pm\, G e^{i\nu_K \bar{x}} \quad ; \quad \bar{y} = 0 \pm \,, \quad \bar{x} > 0 \,, \tag{A7.3.1}$$

where ν_K and G are to be determined. Now $p_K^*(\bar{x})$ is continuous across $\bar{y} = 0$ since $p_K(\bar{x})$ is continuous (the definitions of p_K^* and p_K are the same as in section 7.4 except that we have introduced a suffix 'K' on those parameters related to the velocity potential ψ_K), so that (7.4.18)

and (A7.3.1) together imply that

$$\nu_K = -k^* \ . \qquad \text{(A7.3.2)}$$

Since there is no additional upwash the boundary condition is

$$\frac{\partial \psi_K}{\partial \bar{y}} = 0 \ ; \quad \bar{y} = 0 \ , \quad \bar{x} < 0 \ . \qquad \text{(A7.3.3)}$$

As in section 4 we now have a two part boundary value problem which we will solve by using the Wiener-Hopf technique*. We then obtain, on $\bar{x} < 0$,

$$\Delta p_K^*(\bar{x}) = \frac{-2G(K + k^*)^{\frac{1}{2}} e^{iK\bar{x}+i\pi/4}}{\pi^{\frac{1}{2}}(-\bar{x})^{\frac{1}{2}}} \ . \qquad \text{(A7.3.4)}$$

This shows that the effect of the Kutta condition here is merely to remove the inverse square root singularity at the trailing edge, i.e. we select

$$G = \frac{1}{(K + k^*)^{\frac{1}{2}}(K - i\nu^*)^{\frac{1}{2}}} \qquad \text{(A7.3.5)}$$

so that the sum of (7.4.43) and (A7.3.4) has no term in $|\bar{x}|^{\frac{1}{2}}$.

FOOTNOTE

* Crighton (1977, chapter 9) shows how the Wiener-Hopf technique can be used to solve a trailing edge problem in unsteady compressible flow with a Kutta condition imposed.

APPENDIX 7.4

Chordwise Integration (Low Frequency)

From (7.7.6), (7.7.9) and (7.7.10) we find, on including the noncompactness phase term $e^{-ik_x x}$, that the chordwise integrals are

$$I_1 = \int_{-1}^{1} \left(\frac{1-x}{1+x}\right)^{\frac{1}{2}} e^{i\eta' x}\, dx \,, \qquad \text{(A7.4.1)}$$

where η' is defined in (7.7.12), and

$$I_2 = \int_{-1}^{1} e^{i\eta' x} (1-x^2)^{\frac{1}{2}} \int_{-1}^{1} \frac{e^{-i\mu'\xi}}{(x-\xi)(1-\xi^2)^{\frac{1}{2}}}\, d\xi dx \,, \qquad \text{(A7.4.2)}$$

where μ' is defined in (7.7.5). On making the substitution $x = -\cos\theta$ the first integral (A7.4.1) is easily evaluated as

$$I_1 = \pi[J_o(\eta') - iJ_1(\eta')] \,. \qquad \text{(A7.4.3)}$$

We use the same substitution in the second integral (A7.4.2) and change the order of integration. In Watson (1952) it is shown that $e^{-i\eta'\cos\theta}$ can be expanded as a series of Bessel functions:

$$e^{-in't\cos\theta} = J_o(n't) + 2\sum_{n=1}^{\infty} (-i)^n J_n(n't)\cos n\theta \ . \qquad \text{(A7.4.4)}$$

We then consider the integral

$$I^{(n)} = \int_0^{\pi} \frac{\cos n\theta \ \sin^2\theta}{(\cos\phi - \cos\theta)}\, d\theta \qquad \text{(A7.4.5)}$$

$$= \frac{1}{4}\int_0^{\pi} \frac{[2\cos n\theta - \cos(n+2)\theta - \cos(n-2)\theta]}{(\cos\phi - \cos\theta)}\, d\theta \ .$$

where we have replaced ξ with $-\cos\phi$.

Before proceeding we note, from Glauert (1948, p.93), that

$$\int_0^{\pi} \frac{\cos m\theta}{(\cos\theta - \cos\phi)}\, d\theta = \pi \frac{\sin m\phi}{\sin\phi}. \qquad \text{(A7.4.6)}$$

Then

$$I^{(0)} = \frac{1}{2}\int_0^{\pi} \frac{(1 - \cos 2\theta)}{(\cos\phi - \cos\theta)}\, d\theta = \pi\cos\phi \ , \qquad \text{(A7.4.7)}$$

$$I^{(1)} = \frac{1}{4}\int_0^{\pi} \frac{(\cos\theta - \cos 3\theta)}{(\cos\phi - \cos\theta)}\, d\theta = \frac{\pi}{2} - \pi\sin^2\phi \qquad \text{(A7.4.8)}$$

and, for $n \geq 2$,

$$I^{(n)} = \frac{-\pi}{4\ \sin\phi}[2\ \sin n\phi - \sin(n+2)\phi - \sin(n-2)\phi] = -\pi\sin\phi\sin n\phi. \qquad (A7.4.9)$$

The integral (A7.4.2) is then given by

$$I_2 = \pi \int_0^{\pi} e^{i\mu'\cos\phi} \left[\cos\phi J_o(\eta') - iJ_1(\eta') - 2\sum_{n=1}^{\infty}(-i)^n J_n(\eta')\sin\phi\sin n\phi\right] d\phi. \qquad (A7.4.10)$$

The integrals in (A7.4.10) can be evaluated in terms of Bessel functions (Watson 1952) so that

$$I_2 = i\pi^2\left[J_o(\eta')J_1(\mu') - J_1(\eta')J_o(\mu') + \frac{2}{\mu'}\sum_{n=1}^{\infty} nJ_n(\eta')J_n(\mu')\right]. \qquad (A7.4.11)$$

Kemp (1973) has shown that the series of Bessel functions in (A7.4.11) can be summed as

$$\sum_{n=1}^{\infty} nJ_n(\eta')J_n(\mu') = \frac{\eta'\mu'}{2(\mu'-\eta')}[J_o(\eta')J_1(\mu') - J_1(\eta')J_o(\mu')] \qquad (A7.4.12)$$

whence, on substituting (A7.4.12) in (A7.4.11),

$$I_2 = \frac{i\pi^2\mu'}{(\mu'-\eta')}[J_o(\eta')J_1(\mu') - J_1(\eta')J_o(\mu')] \ . \qquad \text{(A7.4.13)}$$

On using (A7.4.3) and (A7.4.13) in the integral of (7.7.6), and multiplying by c/2, we obtain the result (7.7.11) which, apart from the wavenumber k_x, agrees with the result of Kemp (1973).

8. FURTHER WORK

8.1 Introduction

In chapters 2 to 7 we have described a technique for predicting both the rotor-alone and the aerodynamic interaction components of the sound field generated by a counter-rotation propeller. We now proceed to discuss ways in which the model could be improved or extended.

8.2 Approximations

We start by reviewing some of the assumptions and/or approximations that have been made during the course of the work.

One of the most important assumptions made at the outset was of the validity of linear theory. However, since nonlinear effects have already been reviewed in detail in section 2.5, we will not discuss them further here.

An approximation made in the problem of aerodynamic interactions was that the blades could be replaced by flat plates. This involves switching the boundary conditions from the true airfoil surface to a mean surface. Hawkings (1978) showed that this change in boundary conditions could be represented by an "unsteady thickness" noise source. Glegg (1986) showed that unsteady thickness was important on a model helicopter rotor, mainly due to directivity effects*. However, our preliminary calculations indicate that this noise source is not important on the Gannet, and is therefore unlikely to be important on prop-fans.

FOOTNOTE

* Unsteady loading on flat plate helicopter rotor blades generates noise on the rotor axis with a null in the rotor plane. The unsteady thickness source radiates mainly in the plane of the rotor, thus removing the null.

In the gust/airfoil interaction calculations in chapters 5 to 7 we assumed that the gust is not distorted by the potential flow field about the rotor. However, Goldstein & Atassi (1976) used rapid distortion theory to calculate the response of a two-dimensional airfoil to a low frequency sinusoidal gust in incompressible flow, and showed that the airfoil potential field has an important influence on the airfoil response. The work was extended by Goldstein (1979) to include compressibility effects, although the principal result takes the form of a variable coefficient wave equation for which a solution is not available in closed form. Kerschen & Balsa (1981) showed that a number of simplifications could be made to Goldstein's work, although some numerical methods were still necessary. The use of subsonic thin airfoil theory enabled Kerschen & Myers (1983) to provide further approximations and hence obtain a closed form solution. This work has since been extended by Myers & Kerschen (1984, 1986) to include a more accurate description of speed of sound fluctuations and to include the effects of airfoil camber. All these effects relating to potential field distortion of the gust could, in principle, be incorporated into our prediction scheme.

The decomposition of rotor wakes into harmonic gusts in chapter 5 is performed assuming that the wakes are discrete. For high solidity rotors we must therefore consider wake merging effects. This should be straightforward provided we use the Gaussian wake model which forms the solution to a linear equation given by (5.2.35). We can therefore simply superpose the wake profiles. However, the Schlichting wake model forms the solution to a nonlinear equation given by (5.2.22) and it would obviously be inappropriate to superpose solutions in this case.

Another assumption, which is invalid for high solidity rotors, is that the rotor response can be calculated by treating each blade as an

isolated airfoil, rather than as an element of a periodic cascade of blades. The response of cascades to sinusoidal gusts has been discussed previously by Fleeter (1973) and in chapter 5 of Goldstein (1976). However, their results are given in terms of the numerical solution of simpler integral equations and it may therefore, for our purposes, be more appropriate to seek solutions in closed form for some limiting cases; for example, under the high frequency assumption made in chapters 5, 6 and 7 it should be possible to treat leading and trailing edge cascade problems as if the cascade were semi-infinite, and the corresponding Wiener-Hopf problems are now being examined by D. Innes (private communication).

8.3 Installation Effects

The prediction method described in chapters 2 to 7 is applicable, mainly, to an isolated powerplant. We now discuss some additional effects present on installed powerplants.

The effects of upstream or downstream pylons or wings can be predicted using the formulation already described in chapters 4 to 7.

Tanna et al. (1981) and Dittmar (1986) have shown that incidence effects can be important. These effects could be included in the prediction scheme, for small angles of incidence, by writing the incident velocity field as the sum of a constant velocity component (normal to the propeller disc) and an azimuthal velocity component which varies sinusoidally around the disc.

We next consider the effect of boundary layer shielding. Dittmar et al. (1984) conducted wind tunnel experiments in an attempt to reproduce effects which had been noted on earlier flight tests with a propfan

mounted on a Jet Star aircraft. The experiments showed that the boundary layer did indeed provide substantial shielding. A number of analytical studies have been carried out to predict the shielding effect. McAninch (1983) described a simple model, involving a shear layer to represent the boundary layer, to show the effects of Mach number, frequency and observer position. Further work was described by McAninch & Rawls (1984) who used two models: the first was two-dimensional and the fuselage was represented by a flat plate; the second was three-dimensional and the fuselage was represented by a circular cylinder. The parallel flow assumption is applied and several methods are used to solve the resulting differential equation for acoustic pressure. Hanson (1984) used an infinitesimally thin boundary layer and an incident plane wave; the shielding effect was described purely in terms of classical refraction. A more representative description of the incident field was used by Hanson & Magliozzi (1985) who used Hanson's (1985b) near-field propeller noise theory to predict the sound field; the framework was three-dimensional and accounted for boundary layer refraction and scattering effects. Tam (1986) has used two models to examine boundary layer shielding; the first is inviscid and accounts for refraction effects; the second is an eddy viscosity model which accounts for turbulence damping effects. The theoretical work described above is, in all cases, used in conjunction with a harmonic wave representing the incident sound field and is therefore ideally suited to incorporation in the prediction method described here.

8.4 Extensions

We now outline some extensions to the work described in previous chapters.

Noise fields on upstream and downstream rotors have been treated

independently thus far. There is, however, a need to sum all sources. Different sources on the same blade row can simply be added (provided, of course, that we ensure the phase descriptions are correct). To sum front and rear blade row fields we must account not only for phase differences at source but also for spatial separation. This is quite straightforward and has been described by Hanson (1985a).

We should consider also the effects of blade sweep. The radiation formulae described in chapters 2 and 4 include phase terms representing blade sweep effects. However, the airfoil response calculations described in chapters 5 to 7 were performed for unswept blades. Graham (1970) showed how the convected wave equation for a three-dimensional disturbance incident on an airfoil of infinite span can be transformed into a two-dimensional Helmholtz equation*. Martinez & Widnall (1980) used this transformation to consider a high frequency oblique gust interaction problem. Their work can easily be used to extend the descriptions in chapters 5 to 7 for application to counter-rotation propellers with swept blades.

In chapters 5 to 7 we calculated the response of an airfoil to an incident gust on a two-dimensional basis, i.e., we calculated the response of a section of an infinite span airfoil. This calculation should be reasonably accurate along most of the blade span where blade chord, thickness and twist are changing quite slowly. However, in the region of the blade tips the two-dimensional response calculation is obviously incorrect. Martinez & Widnall (1983) have examined the tip edge effect for a high frequency gust interaction problem, and obtained a correction

---

FOOTNOTE

* The transformation that we used in chapter 7 is, basically, a simplification of Graham's transformation.

factor that could possibly be used to correct the response calculations in chapters 5 to 7. Another view of the tip interaction problem is given in recent work of Cargill (1987) who has solved exactly the linearised equations at a free stream Mach number of precisely unity; this study explicitly displays the effects associated with the side edge of the tip.

In calculating steady loading noise in chapter 2 we considered the blade forces generated by airfoil section lift. The resolved components of these forces correspond to the torque and thrust forces considered by Gutin (1936). However, experimental results (Hanson 1986; Vaczy & McCormick 1987) show that advanced propellers generate strong leading edge and tip vortices which produce a radial suction force (the effects of interactions between the tip vortex and a downstream blade row are discussed below). Hanson (1986) has shown how this source can be included in a frequency domain prediction technique.

8.5 Further Topics

We discuss finally two further pieces of important work that need to be included in the prediction scheme.

First, consider the interaction between the tip vortex generated by a propeller and a downstream blade row or wing. Miller et al. (1981) conducted experiments on general aviation propellers which showed that the tip vortex could be important with regard to cabin noise. Block (1986), Harris & Cuthbertson* (1987) and Dittmar & Stang (1987) have carried out tests on counter-rotation propellers in which the rear blade row

---

FOOTNOTE

* Harris & Cuthbertson did not publish the results from the cropped blade row tests. We note, however, that the two rows were run at different speeds in order to separate out the different harmonic components.

was cropped in order to avoid chopping of the tip vortices from the upstream blades by the downstream row. Block's tests were carried out on a counter-rotation propeller with equal blade numbers fore and aft: cropping the rear row produced no clear acoustic benefit. Dittmar & Stang conducted tests on a 9 x 8 counter-rotation propeller, for which the different harmonic components were separated out in terms of frequency: the levels of both rotor-alone tones and interaction tones were reduced by cropping the rear row. Since the tip vortex interaction appears to represent an important noise source it would seem appropriate to include it in the prediction scheme. Various models of the tip vortex have been described in the literature: Spreiter & Sacks (1951) considered the trailing vortex from a lifting wing; Widnall (1970) considered the potential field about an oblique line vortex as a sum of harmonics - incompressible or compressible two-dimensional response functions can be used and it is also possible to extend the vortex model to include a viscous core; Widnall & Wolf (1980) considered different tip vortex structures, using the inviscid rollup model of Betz, in incompressible flow for application to low frequency gust interactions with swept airfoils; Martinez & Widnall (1983) considered interactions in compressible flow between a high frequency harmonic gust and a noncompact airfoil - the airfoil response and radiation calculations, however, differ from those used in chapters 5 to 7 and must therefore be calculated independently; a vortex model which includes a viscous core has been described by Amiet (1986) - this model appears to predict rotor/vortex interaction noise quite well at low frequencies as shown by Schlinker & Amiet (1983). Since the models described above were all formulated for harmonic gusts they are well suited for application to the prediction techniques described here.

Lastly, consider near-field effects. The acoustic radiation formulae obtained in chapters 2 and 4 were derived for an observer situated in the far-field. The equivalent frequency domain formulae for an observer in the near field of a single-rotation propeller have been derived by Hanson (1985b). The equivalent near-field formulae for a counter-rotation propeller can easily be derived from the results of Hanson (1983). Wright (1971) and Hanson (1985b) have shown that considerable errors results from the application of far-field radiation formulae in the near-field, particularly at low tip speeds. However, the near-field formulae are quite complicated and involve both Hankel and Bessel functions, as well as spanwise and chordwise integration, in addition to an infinite wavenumber transform. In order to obtain near-field predictions, without using large amounts of CPU time, the asymptotic techniques discussed in chapter 3 can be applied to the near field radiation formulae. In this case we take mB to be large with the observer distance fixed. Work is now well underway to develop near-field asymptotics along these lines, with cabin noise and structural fatigue as important applications.

REFERENCES

Abramowitz, M. & Stegun, I. A. (1965). Handbook of Mathematical Functions. Dover.

Adamczyk, J. J. (1971). Passage of an isolated airfoil through a three-dimensional disturbance. Ph.D. thesis, Univ. Connecticut.

Adamczyk, J. J. (1974). The passage of an infinite swept airfoil through an oblique gust. N.A.S.A. Contr. Rep. 2395.

Amiet, R. K. (1973). Review of unsteady airfoil lift theories. United Aircraft Research Lab. Rep. M210885-2.

Amiet, R. K. (1974). Compressibility effects in unsteady thin airfoil theory. A.I.A.A.J. 12(2), 252-255.

Amiet, R. K. (1975). Effects of compressibility in unsteady airfoil lift theories. Proc. Symp. "Unsteady Aerodynamics". Univ. Arizona, 18-20 Mar.

Amiet, R. K. (1986). Airfoil gust response and the sound produced by airfoil-vortex interaction. J. Sound Vib. 107(3), 487-506.

Amiet, R. K. & Sears, W. R. (1970). The aerodynamic noise of small perturbation subsonic flows. J. Fluid Mech. 44(2), 227-235.

Aravamudan, K. S., Lee, A. & Harris, W. L. (1978). A simplified Mach number scaling law for helicopter rotor noise. J. Sound Vib., 57(4), 555-570.

Ashley, H. & Landahl, M. T. (1965). Aerodynamics of Wings and Bodies. Dover.

Banach, H. J. & Reynolds, H. J. (1981). Turboprop engine propulsion for the 1990's. A.I.A.A. Paper 1648.

Barger, R. L. (1980). Theoretical prediction of nonlinear propagation effects on noise signatures generated by subsonic or supersonic propeller or rotor blade tips. N.A.S.A. Tech. Paper 1660.

Block, P. J. W. (1985). Noise radiation patterns of counter-rotation and unsteadily loaded single-rotation propellers. J. Aircraft 22(9), 776-783.

Block, P. J. W. (1986a). Experimental study of the effects of installation on single- and counter-rotation propeller noise. N.A.S.A. Tech. Paper 2541.

Block, P. J. W. (1986b). Pusher propeller noise directivity and trends. A.I.A.A. Paper 1929.

Block, P. J. W. & Gentry, G. L. (1986). Directivity and trends of noise generated by a propeller in a wake. N.A.S.A. Tech. Paper 2609.

Block, P. J. W., Klatte, R. M. & Druez, P. M. (1986). Counter-rotation propeller noise directivity and trends. A.I.A.A. Paper 1927.

Borchers, I. U., Scholten, R. & Gehlhar, B. W. (1986). Experimental results of the noise radiation of propellers in non-uniform flows. A.I.A.A. Paper 1928.

Boussinesq, J. (1877). Théorie de l'écoulement tourbillant.Mém. prés. Acad. Sci. XXIII, 46.

Bradley, A. J. (1986). A study of the rotor/rotor interaction tones from a contra rotating propeller driven aircraft. A.I.A.A. Paper 1894.

Brady, G. W. (1951). Propellers for high powers and transonic speeds. Presented at the Third Anglo-American Aeronautical Conference.

Bryan, G. H. (1920). The acoustics of moving sources with application to airscrews. British A.R.C.R. & M. No. 684.

Caradonna, F. X. & Isom, M. P. (1972). Subsonic and transonic potential flow over helicopter blades. A.I.A.A.J. 10, 1606-1612.

Cargill, A. M. (1987). Tip effects on the sound generated by gust-aerofoil interaction at transonic speeds. To be submitted to J. Fluid Mech.

Chester, C. R. (1971). Techniques in Partial Differential Equations. McGraw-Hill Kogakusha.

Crighton, D. G. (1972). Radiation properties of the semi-infinite vortex sheet. Proc. Roy. Soc. Lond. A330, 185-198.

Crighton, D. G. (1977). Introduction to Wiener-Hopf methods in acoustics and vibration. David W. Taylor Naval Ship Research and Development Center Rep. 0112.

Crighton, D. G. (1981). Acoustics as a branch of fluid mechanics. J. Fluid Mech. 106, 261-298.

Crighton, D. G. (1985). The Kutta condition in unsteady flow. Ann. Rev. Fluid Mech. 17, 411-445.

Curle, N. (1955). The influence of solid boundaries on aerodynamic sound. Proc. Roy. Soc. A231, 505-514.

Daly, B. B. (1958). Noise level in fans. J. Inst. Heating Ventilating Eng. 26, 29-45.

Daniels, P. G. (1978). On the unsteady Kutta condition. Quart. J. Mech. Appl. Math. 31, 49-75.

Deming, A. F. (1937). Noise from propellers with symmetrical sections at zero blade angle. N.A.C.A. Tech. Note 605.

Deming, A. F. (1938). Noise from propellers with symmetrical sections at zero blade angle II. N.A.C.A. Tech. Note 679.

Deming, A. F. (1940). Propeller rotation noise due to torque and thrust. J. Acoust. Soc. Am. 12, 173-182.

Diprose, K. V. (1955). Some propeller noise calculations showing the effect of thickness and planform. R.A.E. Tech. Note M.S.19.

Dittmar, J. H. (1984). Observations from varying the lift and drag inputs to a noise prediction method for supersonic helical tip speed propellers. N.A.S.A. Tech. Memo. 83797.

Dittmar, J. H. (1986). Cruise noise of counter-rotation propeller at angle of attack in wind tunnel. N.A.S.A. Tech. Memo. 88869.

Dittmar, J. H., Burns, R. J. & Leciejewski, D. J. (1984). An experimental investigation of the effect of boundary layer refraction on the noise from a high speed propeller. N.A.S.A. Tech. Memo. 83764.

Dittmar, J. H. & Stang, D B. (1987). Noise reduction for model counter-rotation propeller at cruise by reducing aft-propeller diameter. N.A.S.A. Tech. Memo. 88936.

Dobrzynski, W. M. (1986). The effect on radiated noise of non-zero propeller rotational plane attitude. A.I.A.A. Paper 1926.

Dodd, K. N. & Roper, G. M. (1958). A Deuce program for propeller noise calculations. R.A.E. Tech. Note M.S.45.

Dugan, J. F., Bencze, D. P. & Williams, L. J. (1977). Advanced turboprop technology development. A.I.A.A. Paper 1223.

Dugan, J. F., Gatzen, B. S. & Adamson, W. M. (1978). Prop-Fan propulsion - its status and potential. S.A.E. Paper 780995.

Ffowcs Williams, J. E. (1979). On the role of quadrupole source terms generated by moving bodies. A.I.A.A. Paper 0576.

Ffowcs Williams, J. E. & Hawkings, D. L. (1969a). Sound generation by turbulence and surfaces in arbitrary motion. Phil. Trans. Roy. Soc. A264, 321-342.

Ffowcs Williams, J. E. & Hawkings, D. L. (1969b). Theory relating to the noise of rotating machinery. J. Sound Vib. 10(1), 10-21.

Filleul, N. le S. (1966). An investigation of axial flow fan noise. J. Sound Vib. 3(2), 147-165.

Fleeter, S. (1973). Fluctuating lift and moment coefficients for cascaded airfoils in a non-uniform compressible flow. J. Aircraft 10(2), 93-98.

Fujii, S., Nishiwaki, H. & Takeda, K. (1986). Noise and performance of a counter-rotation propeller. J. Aircraft 23(9), 719-724.

Garrick, I. E. & Watkins, C. E. (1954). A theoretical study of the effect of forward speed on the free space sound pressure field around propellers. N.A.C.A. Rep. 1198.

Gatzen, B. S. (1982). Turboprop design - now and the future. I.C.A.S. Paper 452.

Glauert, H. (1926). The Elements of Airfoil and Airscrew Theory. Macmillan.

Glauert, H. (1928). The effect of compressibility on the lift of an airfoil. Proc. Roy. Soc. A 118, 113-119.

Glegg, S. A. L. (1982). Fan noise. In "Noise and Vibration" (R. G. White and D. J. Mead, eds.). Ellis Horwood.

Glegg, S. A. L. (1986). Broadband propeller noise prediction in the plane of the rotor. A.I.A.A. Paper 1964.

Godston, J. & Reynolds, C. (1985). Future Prop-Fans - tractor or pusher. A.I.A.A. Paper 1189.

Goldstein, M. E. (1976). Aeroacoustics. McGraw-Hill.

Goldstein, M. E. (1979). Unsteady vortical and entropic disturbances of potential flows round arbitrary obstacles. J. Fluid Mech. 93, 209-224.

Goldstein, M. E. & Atassi, H. (1976). A complete second order theory for the unsteady flow about an airfoil due to a periodic gust. J. Fluid Mech. 74, 741-765.

Goldstein, S. (1933). On the two-dimensional steady flow of a viscous fluid behind a solid body. Proc. Roy. Soc. A 142, 545-562.

Goldstein, S. (1938). Modern Developments in Fluid Mechanics. Clarendon Press.

Görtler, H. (1942). Berechnung von aufgaben der freien turbulenz auf grund eines neuen näherungsansatzes. ZAMM 22, 244-254.

Graham, J. M. R. (1970). Similarity rules for thin airfoils in non-stationary flows. J. Fluid Mech. 43, 753-766.

Gutin, L. (1936). On the sound field of a rotating propeller. Physik. Zeitschr. der Sowjetunion 9(1), 57-71. (Translated as 1948 N.A.C.A. Tech. Memo. 1195).

Hanson, D. B. (1979). The aeroacoustics of advanced turbopropellers. In "Mechanics of Sound Generation in Flows" (E.-A. Müller, ed.). Springer-Verlag.

Hanson, D. B. (1980a). Helicoidal surface theory for harmonic noise of propellers in the far field. A.I.A.A.J. 18(10), 1213-1220.

Hanson, D. B. (1980b). Influence of propeller design parameters on far field harmonic noise in forward flight. A.I.A.A.J. 18(11), 1313-1319.

Hanson, D. B. (1983). Compressible helicoidal surface theory for propeller aerodynamics and noise. A.I.A.A.J. 21(6), 881-889.

Hanson, D. B. (1984). Shielding of Prop-Fan cabin noise by the fuselage boundary layer. J. Sound Vib. 92(4), 591-598.

Hanson, D. B. (1985a). Noise of counter-rotation propellers. J. Aircraft 22(7), 609-617.

Hanson, D. B. (1985b). Near field frequency domain theory for propeller noise. A.I.A.A.J. 23(10), 499-504.

Hanson, D. B. (1986). Propeller noise caused by blade tip radial forces. A.I.A.A. Paper 1892.

Hanson, D. B. & Fink, M. R. (1979). The importance of quadrupole sources in prediction of transonic tip speed propeller noise. J. Sound Vib. 62(1), 19-38.

Hanson, D. B. & Magliozzi,B. (1985). Propagation of propeller tone noise through a fuselage boundary layer. J. Aircraft 22(1), 63-70.

Hanson, D. B. & Patrick, W. P. (1985). Near wakes of advanced turbo-propellers. I.U.T.A.M. Symp. "Aero- and Hydro-acoustics". Ecole Central de Lyon, Lyon, Jul.

Harris, R. W. & Cuthbertson, R. D. (1987). U.D.F.^{TM}/727 flight test program. A.I.A.A. Paper 1733.

Hawkings, D. L. (1978). Theoretical models of helicopter rotor noise. Specialists Meeting "Helicopter Acoustics". N.A.S.A. Langley, Hampton, Virginia, 22-24 May.

Hawkings, D. L. (1979). Noise generation by transonic open rotors. In "Mechanics of Sound Generation in Flows" (E.-A. Müller, ed.). Springer-Verlag.

Hawkings, D. L. & Lowson, M. V. (1974). Theory of open supersonic rotor noise. J. Sound Vib. 36(1), 1-20.

Hawkings, D. L. & Lowson, M. V. (1975). Tone noise of high speed rotors. A.I.A.A. Paper 0450.

Hicks, C. W. & Hubbard, H. H. (1947). Comparison of sound emission from two blade, four blade and seven blade propellers. N.A.C.A. Tech. Note 1354.

Holbrook, G. E. & Rosen, G. (1978). Evolution of the turboprop for high speed air transportation. A.S.M.E. Paper G.T.-201.

Howe, M. S. (1976). The influence of vortex shedding on the generation of sound by convected turbulence. J. Fluid Mech. 76, 711-740.

Howell, G. P., Bradley, A. J., McCormick, M. A. & Brown, J. D. (1986). Dedopplerisation and acoustic imaging of aircraft flyover noise measurements. J. Sound Vib. 105(1), 151-167.

Hubbard, H. H. (1948). Sound from dual-rotating and multiple single-rotating propellers. N.A.C.A. Tech. Note 1654.

Hubbard, H. H. & Lassiter, L. W. (1952). Sound from a two-blade propeller at supersonic tip speeds. N.A.C.A. Rep. 1079.

Jackson, A. H. & Gatzen, B.S. (1976). Multi-mission uses for Prop-Fan propulsion. Conf. "Variable Geometry and Multicycle Engines". A.G.A.R.D. 48th Meeting, Paris.

Kemp, N. H. (1952). On the lift and circulation of airfoils in some unsteady flow problems. J. Aeron. Sci. 19(10), 713-714.

Kemp, N. H. (1973). Closed form lift and moment for Osborne's unsteady thin-airfoil theory. A.I.A.A.J. 11(9), 1358-1360.

Kerschen, E. J. & Balsa, T. F. (1981). Transformation of the equation governing disturbances of a two-dimensional compressible flow. A.I.A.A.J. 19, 1367-1370.

Kerschen, E. J. & Myers, M. R. (1983). Incidence angle effects on convected gust airfoil noise. A.I.A.A. Paper 0765.

Korkan, K. D., Von Lavante, E. & Bober, L. J. (1986). Numerical evaluation of propeller noise including nonlinear effects. A.I.A.A.J. 24(6), 1043-1045.

Kurbjun, M. C. (1955). Noise survey of a 10-foot four blade turbine driven propeller under static conditions. N.A.C.A. Tech. Note 3422.

Lamb, H. (1932). Hydrodynamics, 6th ed. Cambridge Univ. Press.

Landahl, M. (1961). Unsteady Transonic Flow. Pergamon Press.

Landau, L. D. & Lifshitz, E. M. (1959). Fluid Mechanics. Pergamon Press.

Lange, R. H. (1984). A review of advanced turboprop transport activities. In "Aerodynamics and Acoustics of Propellers". A.G.A.R.D. Conf. Proc. No. 366.

Lighthill, M. J. (1952). On Sound generated aerodynamically. I. General theory. Proc. Roy. Soc. A211, 546-587.

Lighthill, M. J. (1958). Fourier Analysis and Generalised Functions. Cambridge Univ. Press.

Lighthill, M. J. (1972). The fourth annual Fairey lecture: the propagation of sound through moving fluids. J. Sound Vib. 24(4), 471-492.

Lighthill, M. J. (1986). An Informal Introduction to Theoretical Fluid Mechanics. Clarendon Press.

Lowson, M. V. (1965). The sound field for singularities in motion. Proc. Roy. Soc. A 286, 559-572.

Lowson, M. V. (1966). Basic mechanisms of noise generation by helicopters, V./S.T.O.L. aircraft and ground effect machines. J. Sound Vib. 3(3), 454-466.

Lynam, E. J. H. & Webb, H. A. (1919). The emission of sound by airscrews. British A.R.C. R. & M. No. 624.

Lyon, R. H. (1971). Radiation of sound by airfoils that accelerate near the speed of sound. J. Acoust. Soc. Am. 49(3 part 2), 894-905.

Lyon, R. H., Mark, W. D. & Pyle, R. W. (1973). Synthesis of helicopter rotor tips for less noise. J. Acoust. Soc. Am. 53(2), 607-618.

Magliozzi, B. (1984). Advanced turboprop noise: a historical review. A.I.A.A. Paper 2261.

Majjigi, R. K. & Gliebe, P. R. (1985). Development of a rotor wake/vortex model, vol. 1 final technical report. N.A.S.A. Contr. Rep. 174849.

Martinez, R. & Widnall, S. E. (1980). Unified aerodynamic-acoustic theory for a thin rectangular wing encountering a gust. A.I.A.A.J. 18(6), 636-645.

Martinez, R. & Widnall, S. E. (1983a). Aerodynamic theory for wing with side edge passing subsonically through a gust. A.I.A.A.J. 21(6), 808-815.

Martinez, R. & Widnall, S. E. (1983b). An aeroacoustic model for high speed unsteady blade-vortex interaction. A.I.A.A.J. 21(9), 1225-1231.

McAninch, G. L. (1983). A note on propagation through a realistic boundary layer. J. Sound Vib. 88(2), 271-274.

McAninch, G. L. & Rawls, J. W. (1984). Effects of boundary layer refraction and fuselage scattering on fuselage surface noise from advanced turboprop propellers. A.I.A.A. Paper 0249.

Metzger, F. B. (1980). Progress and trends in propeller/Prop-Fan noise technology. A.I.A.A. Paper 0856.

Metzger, F. B. (1984). The state of the art in Prop-Fan and turboprop noise. In "Aerodynamics and Acoustics of Propellers". A.G.A.R.D. Conf. Proc. No. 366.

Metzger, F. B. & Brown, P. C. (1987). Results of acoustic tests of a Prop-Fan model. A.I.A.A. Paper 1894.

Metzger, F. B. & Rohrbach, C. (1979). Aeroacoustic design of the propfan. A.I.A.A. Paper 0610.

Metzger, F. B. & Rohrbach, C. (1985). Benefits of blade sweep for advanced turboprops. A.I.A.A. Paper 1260.

Miles, J. W. (1950a). On the compressibility correction for subsonic unsteady flow. J. Aeron. Sci. 17(3), 181-182.

Miles, J. W. (1950b). Quasi-stationary airfoil theory in subsonic compressible flow. Quart. Appl. Math. 8, 350-358.

Miller, B. A., Dittmar, J. H. & Jeracki, R. J. (1981). The propeller tip vortex - a possible contributor to aircraft cabin noise. N.A.S.A. Tech. Memo. 81768.

Miller, C. J. & Sullivan, J. P. (1985). Noise constraints effecting optimal propeller designs. S.A.E. Paper 850871.

Milne-Thompson, L. M. (1948). Theoretical Aerodynamics. Macmillan.

Mitchell, G. A. & Mikkelson, D. C. (1982). Summary and recent results from the N.A.S.A. advanced high-speed propeller research program. N.A.S.A. Tech. Memo. 82891.

Morfey, C. L. (1972). The sound field of sources in motion. J. Sound Vib. 23(3), 291-295.

Morfey, C. L. & Fisher, M. J. (1970). Shock wave radiation from a supersonic ducted rotor. J. Roy. Aeron. Soc. 74, 579-585.

Morfey, C. L. & Tanna, H. K. (1971). Sound radiation from a point force in circular motion. J. Sound Vib. 15(3), 325-351.

Morgan, J. D. (1982). Nonlinear effects in high speed rotor noise. J. Sound Vib. 85(4), 501-511.

Morse, P. M. & Ingard, K. U. (1968). Theoretical Acoustics. McGraw-Hill.

Murray, J. D. (1974). Asymptotic Analysis. Oxford Univ. Press.

Myers, M. R. & Kerschen, E. J. (1984). Effect of airfoil mean loading on convected gust interaction noise. A.I.A.A. Paper 2324.

Myers, M. R. & Kerschen, E. J. (1986). Influence of airfoil camber on convected gust interaction noise. A.I.A.A. Paper 1873.

Noble, B. (1958). Methods Based on the Wiener-Hopf Technique for the Solution of Partial Differential Equations. Pergamon Press.

Oestreicher, H. L. (1951). The effect of motion on the acoustic radiation of a sound source. Centr. Air. Docum. Off. (Washington) Tech. Data Digest 16(9), 16-19.

Oestreicher, H. L. (1957). Field of a spatially extended moving sound source. J. Acoust. Soc. Am. 29(11), 1223-1232.

Olver, F. W. J. (1974). Introduction to Asymptotics and Special Functions. Academic Press.

Osborne, C. (1973). Unsteady thin-airfoil theory for subsonic flow. A.I.A.A.J. 11(2), 205-209.

Paris, E. T. (1932). A note on the sound generated by a rotating airscrew. Phil. Mag. 13, 99-111.

Philpot, M. G. (1975). The role of rotor blade blockage in the propagation of fan noise interaction tones. A.I.A.A. Paper 0447.

Pierce, A. D. (1981). Acoustics: an Introduction to its Physical Principles and Applications. McGraw-Hill.

Prandtl, L. (1925). Über die ausgebildete turbulenz. ZAMM 5, 136-139.

Prandtl, L. (1930). Über strömungen deren geschwindigkeiten mit der schallgeschwindigkeit vergleichbar sind. J. Aero. Res. Inst. Tokyo 63, 14 et seq.

Raj, R. & Lakshminarayana, B. (1973). Characteristics of the wake behind a cascade of airfoils. J. Fluid Mech. 61(4), 707-730.

Ravindranath, A. & Lakshminarayana, B. (1981). Rotor wake mixing effects downstream of a compressor rotor. A.S.M.E. Paper G.T. - 98.

Rayleigh, Lord (1877). The Theory of Sound. Macmillan.

Regier, A. A. & Hubbard, H. H. (1953). Status of research on propeller noise and its reduction. J. Acoust. Soc. Am. 25(3), 395-404.

Reichardt, H. (1942). Gesetzmäßigkeiten der freien Turbulenz. V.D.I. - Forschungsheft 414.

Reynolds, B. D. (1979). Characteristics of the wake of a lightly loaded compressor or fan rotor. A.I.A.A. Paper 0550.

Rienstra, S. W. (1981). Sound diffraction at a trailing edge. J. Fluid Mech. 108, 443-460.

Roberts, J. P. & B ranek, L. L. (1952). Experiments in external noise reduction of a small pusher-type amphibian airplane. N.A.C.A. Tech. Note 2727.

Rohrbach, C. & Metzger, F. B. (1975). The Prop-Fan - a new look in propulsors. A.I.A.A. Paper 1208.

Sagerser, D. A. & Ludemann, S. G. (1985). Large-scale advanced propfan (LAP) program progress report. A.I.A.A. Paper 1187.

Schlichting, H. (1930). Über das ebene windschattenproblem. Ing-Arch. 1, 533-571.

Schlichting, H. (1955). Boundary Layer Theory. McGraw-Hill.

Schlinker, R. H. & Amiet, R. K. (1983). Rotor-vortex interaction noise. A.I.A.A. Paper 0720.

Schwaller, P. J. G., Parry, A. B., Oliver, M. J. & Eccleston, A. (1984). Farfield measurements and mode analysis of the effects of vane/blade ratio on fan noise. A.I.A.A. Paper 2280.

Sears, W. R. (1940). Some aspects of non-stationary airfoil theory and its practical application. J. Aeron. Sci. 8, 104-108.

Sharland, I. J. & Leverton, J. W. (1968). Propeller and helicopter and hovercraft noise. In "Noise and Acoustic Fatigue in Aeronautics". (E. J. Richards and D. J. Mead, eds.). J. Wiley and Sons.

Silverstein, A., Katzoff, S. & Bullivant, W. K. (1939). Downwash and wakes behind plain and flapped airfoils. N.A.C.A. Rep. 651.

Spreiter, J. R. & Sacks, A. H. (1951). The rolling up of the trailing vortex sheet and its effect on the downwash behind wings. J. Aeron. Sci. 18(1), 21-32.

Strack, W. C., Knip, G., Weisbrich, A. L., Godston, J. & Bradley, E. (1982). Technology and benefits of aircraft counter rotation propellers. N.A.S.A. Tech. Memo. 82983.

Stuckey, T. J. & Goddard, J. O. (1967). Investigation and prediction of helicopter rotor noise part I Wessex whirl tower results. J. Sound Vib. 5(1), 50-80.

Succi, G. P. (1980). Noise and performance of propellers for light aircraft. M.I.T. Rep. 154.

Sundar, R. M. (1985). Ph.D. thesis. Purdue University.

Sundar, R. M. & Sullivan, J. P. (1986). An experimental investigation of propeller wakes using a laser Doppler velocimeter. A.I.A.A. Paper 0080.

Tam, C. K. W. (1983). On linear acoustic solutions of high speed helicopter impulsive noise problems. J. Sound Vib. 89(1), 119-134.

Tam, C. K. W. (1986). Propagation of acoustic waves through a turbulent boundary layer. Proc. I.M.A.C.S. Symp. "Computational Acoustics". Yale Univ., 6-8 Aug.

Tam, C. K. W. & Salikuddin, M. (1986). Weakly nonlinear acoustic and shock wave theory of the noise of advanced high speed turbopropellers. J. Fluid Mech. 164, 127-154.

Tanna, H. K., Burrin, R. H. & Plumblee, H. E. (1981). Installation effects on propeller noise. J. Aircraft 18(4), 303-309.

Tanna, H. K. & Morfey, C. L. (1971). Sound radiation from point sources in circular motion. J. Sound Vib. 16(3), 337-348.

Theodorsen, T. (1935). General theory of aerodynamic instability and the mechanism of flutter. N.A.C.A. Tech. Rep. 496.

Trebble, W. J. G. (1983a). Investigation of effect of blade-tip shape on aerodynamic performance and noise characteristics of a 0.7m diameter propeller. R.A.E. Tech. Memo. Aero. 1974.

Trebble, W. J. G. (1983b). Investigation of the aerodynamic performance and noise characteristics of a 1/5th scale model of the Dowty-Rotol R212 propeller. R.A.E. Tech. Memo. Aero. 1983.

Trebble, W. J. G. (1984). Investigation of the aerodynamic performance and noise characteristics of a Dowty-Rotol R212 propeller at full scale in the 24 ft wind tunnel. R.A.E. Tech. Memo. Aero. 2012.

Trebble, W. J. G ., Williams, J. & Donnelly, R. P. (1981). Comparative acoustic wind-tunnel measurements and theoretical correlations on subsonic aircraft propellers at full-scale and model-scale. R.A.E. Tech. Memo. Aero. 1909.

Trebble, W. J. G., Williams, J. & Donnelly, R. P. (1984). Some aero-acoustic windtunnel measurements, theoretical predictions and flight test correlations on subsonic aircraft propellers. In "Aerodynamics and Acoustics of Propellers". A.G.A.R.D. Conf. Proc. 366.

Trillo, R. L. (1966). An empirical study of hovercract propeller noise. J. Sound Vib. 3(3), 476-509.

Vaczy, C. M. & McCormick, D. C. (1987). A study of the leading edge vortex and tip vortex on Prop-Fan blades. A.S.M.E. Paper G.T.-234.

Van de Vooren, A. I. & Zandbergen, P. J. (1963). Noise field of a rotating propeller in forward flight. A.I.A.A.J. 1(7), 1518-1526.

Van Dyke, M. (1975). Perturbation Methods in Fluid Mechanics. Parabolic Press.

Von Karman, T. & Sears, W. R. (1938). Airfoil theory for non-uniform motion. J. Aeron. Sci. 5, 379-390.

Ward, G. N. (1955). Linearized Theory of Steady High-Speed Flow. Cambridge Univ. Press.

Watkins, C. E. & Durling, B. J. (1956). A method for calculation of free space sound pressures near a propeller in flight including considerations of the chordwise blade loading. N.A.C.A. Tech. Note 3809.

Watson, G. N. (1952). Theory of Bessel Functions, 2nd ed. Cambridge Univ. Press.

Whitham, G. B. (1956). On the propagation of weak shock waves. J. Fluid Mech. 1, 290-318.

Whitham, G. B. (1974). Linear and Nonlinear Waves. Wiley Interscience.

Widnall, S. E. (1970). Helicopter noise due to blade vortex interaction. J. Acoust. Soc. Am. 50(1 part 2), 354-365.

Widnall, S. E. & Wolf, T. L. (1980). Effect of tip vortex structure on helicopter noise due to blade vortex interaction. J. Aircraft 17(10), 705-711.

Wright, S. E. (1971). Discrete radiation from rotating periodic sources. J. Sound Vib. 17(4), 437-498.

Young, R. H. (1951). Contra-rotating axial flow fans. J. Inst. Heating Ventilating Eng. 18(187), 448-477.